SEARCH FOR ANOMALOUS PRODUCTION OF PROMPT LIKE-SIGN LEPTON PAIRS AT $\sqrt{s} = 7$ TEV WITH THE ATLAS DETECTOR

Dominick Olivito

A DISSERTATION

in

Physics and Astronomy

Presented to the Faculties of the University of Pennsylvania

in

Partial Fulfillment of the Requirements for the

Degree of Doctor of Philosophy

2012

Evelyn Thomson, Associate Professor, Physics

Supervisor of Dissertation

A. T. Charlie Johnson, Professor, Physics

Graduate Group Chairperson

Dissertation Committee

I. Joseph Kroll, Professor, Physics

Burt Ovrut, Professor, Physics

Masao Sako, Associate Professor, Physics

Evelyn Thomson, Associate Professor, Physics

H. H. Williams, Professor, Physics

SEARCH FOR ANOMALOUS PRODUCTION OF PROMPT LIKE-SIGN LEPTON PAIRS AT $\sqrt{s} = 7$ TEV WITH THE ATLAS DETECTOR

Acknowledgements

I would like to thank first and foremost my family, my parents Dominick and Cindy Olivito and my siblings Jonathan and Kimberly. They have been a source of constant support even while I have been living an ocean away these past four-plus years. My girlfriend Ellen has also been an enormous source of encouragement and support. The last two years have been great, and I'm excited about what the future will bring for us.

I owe a large debt to my undergraduate advisors at the Ohio State University, Richard Hughes and Brian Winer. They gave me a start in this field and inspired me to get excited about it at a time when I was uncertain what direction to take.

There are many people at the University of Pennsylvania who have collectively made my time here truly unique. There are my fellow graduate students at Penn, who have been some of the central people in my life over the last six and a half years as both colleagues and friends. They include John Alison, who despite his best attempts at procrastination managed to beat me by a week, Ryan Reece, Josh Kunkle, Liz Hines, Chris Lester, Brett Jackson, Doug Schaefer, Rami Vanguri, Alex Tuna, and Kurt Brendlinger. And outside the Penn group, there is John Penwell, bearer of TRT spirit and instigator of TRT BBQs for many years, and Emily Thompson, a fellow 80's music and whiskey enthusiast, along with many others.

My closest work has been with other members of the TRT DAQ team, an outstanding group that I have been privileged to work with. My early mentor was Mike Hance, the very much deserving three-time TRT champion. He was really the trail blazer for both the TRT DAQ and also my performance work on isolation, for which I owe him a great deal. Following after me was Jonathan Stahlman, who did an excellent job in quickly mastering the TRT DAQ, freeing me to do the actual work for this thesis. Technically my elder in terms of TRT tenure, but in many respects still a young whippersnapper, Jamie Saxon has been a great asset both for the TRT and for dealing with impenetrable French bureaucracies. There is Sarah Heim, with whom I cut my teeth on analysis and who is poised to steward the TRT DAQ through the upcoming long shutdown. And finally there's Peter Wagner, my longtime TRT DAQ partner.

The TRT community was great and is a major reason why the subdetector performs so well. There is Anatoli Romaniouk, whose mastery of the TRT and tenaciousness drove us to make the TRT DAQ one of the smoothest-running systems on ATLAS. Christoph Rembser's enthusiasm for the TRT and especially the TRT BBQs has pulled us through more than a couple tricky situations. And the TRT DCS group at Krakow, Zbyszek Hajduk, Elzbieta Banas, and Jolanta Olszowska, were always available and provided excellent support to keep the TRT and electronics running.

There are the Penn postdocs who stewarded the TRT through the early LHC running: Saša Fratina, who tirelessly helped us at every stage to calibrate the detector and understand the data, and Jim Degenhardt, who brought his legendary cool to TRT Run Coordination. Among the other Penn postdocs, there was Mauro Donega, who got me started with electron work, Tae Min Hong, who helped me learn the statistics for this thesis, and Rustem Ospanov. In the Penn electronics group, there were Rick Van Berg and Mitch Newcomer, the electronics gurus who taught me an immense amount and always had a theory (or five) for every strange problem we encountered, as well as Paul Keener.

From this analysis, I would like to thank my colleagues, who were a pleasure to work with and from whom I learned a lot about physics and analysis techniques. They include Else Lytken and Anthony Hawkins at Lund, Kenji Hamano and Nick Rodd at Melbourne, and especially the Berkeley group: Beate Heinemann, Martina Hurwitz, Louise Skinnari, and Jean-Francois Arguin.

I would like to thank my advisor, Evelyn Thomson, who helped me chart my course for physics analysis and gave me the freedom and support to follow my own ideas. Brig Williams has been an invaluable resource on every aspect of experimental particle physics, from the detector to performance to analysis. I have always been impressed by his ability to follow the details of my work seemingly at the same time as everyone else in our (large) group and provide incisive feedback, for which I am tremendously grateful. I've had many good discussions with Joe Kroll and Elliot Lipeles. And I'd also like to thank Burt Ovrut and Masao Sako for serving on my thesis committee, and Burt also for his compelling lectures on field theory.

Our field is truly a collaborative one, and I have benefited from great work by many others in commissioning, operations, performance, and analysis, who I do not have room to mention here but have all helped me get to this point.

ABSTRACT

SEARCH FOR ANOMALOUS PRODUCTION OF PROMPT LIKE-SIGN LEPTON PAIRS AT $\sqrt{s} = 7$ TEV WITH THE ATLAS DETECTOR

Dominick Olivito

Evelyn Thomson

An inclusive search for anomalous production of two prompt, isolated leptons with the same electric charge is presented. The search is performed in a data sample corresponding to 4.7 fb^{-1} of integrated luminosity collected in 2011 at $\sqrt{s} = 7$ TeV with the ATLAS detector at the LHC. Pairs of high-p_{T} leptons ($e^{\pm}e^{\pm}$, $e^{\pm}\mu^{\pm}$, and $\mu^{\pm}\mu^{\pm}$) are selected, and the dilepton invariant mass distribution is examined for any deviation from the Standard Model expectation. No excess is found, and upper limits on the production of like-sign lepton pairs due to contributions from physics beyond the Standard Model are placed as a function of the dilepton mass within a fiducial region close to the experimental selection criteria. The 95% confidence level upper limits on the cross section of anomalous $e^{\pm}e^{\pm}$, $e^{\pm}\mu^{\pm}$, or $\mu^{\pm}\mu^{\pm}$ production range between 1.7 fb and 64.1 fb depending on the dilepton mass and flavor combination. The same data are interpreted in the context of a search for a narrow doubly-charged resonance, using the doubly-charged Higgs boson as a benchmark model. The masses of doubly-charged Higgs bosons are constrained depending on the branching ratio into these leptonic final states. Assuming pair production, coupling to left-handed fermions, and a branching ratio of 100% for each final state, masses below 409 GeV, 375 GeV, and 398 GeV are excluded for $e^{\pm}e^{\pm}$, $e^{\pm}\mu^{\pm}$, and $\mu^{\pm}\mu^{\pm}$, respectively.

Contents

List of Tables

List of Figures

Chapter 1

Introduction

This thesis documents a search for like-sign dilepton production beyond Standard Model expectations, carried out using pp collision data taken by the ATLAS detector at $\sqrt{s} = 7$ TeV. To motivate this search, Chapter 2 briefly reviews the Standard Model of particle physics along with some outstanding questions in the field and some particulars of hadron collider experiments. It introduces and motivates some hypothetical extensions of the Standard Model which this search would have sensitivity to.

Chapters 3 and 4 describe the relevant aspects of the experimental apparatus used for this search, covering first the Large Hadron Collider then the ATLAS detector. Chapter 5 provides details on lepton reconstruction and identification in ATLAS, focusing on electrons and muons and the aspects critical for this search.

Chapter 6 gives a fairly detailed overview of the analysis strategy used in this search as well as the main backgrounds to contend with. Chapter 7 describes the data and simulated samples used in this search, and Chapter 8 details the lepton and event selection applied.

Chapter 9 explains the estimation of backgrounds in detail, and Chapter 10 covers the systematic uncertainties assessed on the signal and background yields. The resulting comparison of data with prediction is shown in Chapter 11, and no significant deviations are observed.

Chapter 12 uses these results to set model-independent cross section limits on the production of like-sign dileptons beyond the Standard Model expectations, while Chapter 13 interprets the same data in the context of a narrow doubly-charged resonance decaying to leptons, setting cross-section and mass limits. Chapter 14 contains ideas on how to improve this search for posterity. And finally, Chapter 15 concludes.

The analyses detailed in this thesis are published in [1] and [2].

Chapter 2

Theoretical Motivations

The Standard Model (SM) of particle physics is the most precise and one of the most successful theories devised to describe nature. This chapter starts with a brief overview of the elements of this theory, outstanding issues, and the application to physics at hadron colliders. Standard Model processes which give rise to like-sign dileptons form a background to the searches that are described later, and those are discussed in more detail. Finally, a selection of theories which extend the Standard Model and give rise to like-sign dilepton signatures are presented.

2.1 The Standard Model of Particle Physics

The Standard Model of particle physics [3, 4, 5] is a description of the fundamental particles which make up the universe along with their interactions. The particles are divided into two types based on their spin (intrinsic angular momentum). Particles with half-integer spin are fermions, which are further divided into quarks and leptons, and these are typically thought of as matter particles. They obey the Pauli exclusion principle and more than one cannot occupy the same quantum state. Particles with integer spin are bosons, and these are typically thought of as the force carriers. Bosons are not subject to the exclusion principle, so they can, and indeed prefer to, occupy the same quantum state.

The interactions among these fundamental particles are derived from the Standard Model Lagrangian. It respects a $SU(3) \times SU(2) \times U(1)$ gauge symmetry, rendering it invariant under local gauge transformations of this group. $SU(3)$ is the group of QCD color charge, $SU(2)$ is the group of weak isospin, and $U(1)$ is the group of weak hypercharge. The leptons, belonging to an $SU(3)$ singlet, interact directly only with the force carriers of $SU(2) \times U(1)$: the W and Z bosons and the photon, γ. These electroweak (EW) interactions thus represent the primary backgrounds to the searches considered in this thesis.

2.1.1 Outstanding Questions

The SM is known to be incomplete as it does not contain gravity, one of the four fundamental forces. Besides this obvious omission, there are several other outstanding questions of varying degrees of importance. Some of these are presented here to motivate the potential theories for beyond the SM (BSM) physics discussed below.

2.1.1.1 Electroweak Symmetry Breaking

In the SM with electroweak symmetry intact, all particles are massless. Explicit mass terms are forbidden in the Lagrangian due to gauge invariance. The canonical solution to this problem is the Higgs mechanism, which introduces a complex scalar doublet. One neutral component acquires a vacuum expectation value (vev), the state known as the Higgs boson, and the other three degrees of freedom become Goldstone bosons which give masses to the $W^{\pm}$ and Z bosons. The same field can also give mass to the quarks and charged leptons via Yukawa couplings.

The discovery of a new boson was recently announced [6, 7], and first results indicate that it is consistent with expectations from the SM Higgs boson. Now a detailed program of measurements is underway to determine the couplings of this new particle to test the SM hypothesis. This question is also intimately tied to the mechanism of EW symmetry breaking, by which the gauge bosons acquire mass. The discovery of this particle, though, confirms the existence of the Higgs sector, and many BSM theories predict a more complicated Higgs sector with more states.

2.1.1.2 Hierarchy Problem

Most theorists believe that new interactions not described in the SM exist at higher energy scales, especially at energies approaching the fundamental Planck scale. As the Planck scale is 10^{17} times larger than the EW scale which current experiments are able to probe, one question is why potential new particles do not contribute strongly to quantum loop diagrams. The most famous example of this problem is the Higgs boson mass, which receives corrections from loops that include all massive SM particles. If particles of order the Planck mass were to contribute to these loops, those corrections would dominate and presumably drive the Higgs mass up to the Planck scale.

However, that is not what is observed. The question of why this does not occur is termed the hierarchy problem. Besides fine-tuning, which is possible but less than elegant, several solutions have been proposed. One class deals with supersymmetry, a new discrete symmetry relating fermions and bosons which acts to cancel out these unwanted loop contributions. Another class uses strong dynamics analogously to QCD, with technicolor [8] being the prime example[1]. And there are other proposed mechanisms, such as in the Little Higgs model discussed below in Section 2.4.1.3.

2.1.1.3 Neutrino Masses

The observation of neutrino oscillations showed that neutrinos have mass [9]. In the SM, however, neutrino masses are forbidden. The lack of right-handed neutrinos prevents Dirac mass terms, while the conservation of lepton number prevents Majorana mass terms [10]. The "seesaw mechanism" is invoked by several models intending to explain neutrino masses. In the simplest form (type I), right-handed (Majorana) neutrinos are added to the SM, with a heavy mass scale (often corresponding to a Grand Unified Theory scale). The left-handed neutrino masses are inversely proportional to the right-handed masses, hence the name seesaw.

2.1.1.4 Generations of Matter

In the SM, there are three generations of quarks and of leptons. Experimentally, the number of (interacting) neutrino generations is constrained to three by the measurement of the Z width at LEP [11]. For quarks, the constraints are less stringent, especially for quark-like objects which do not have the same chiral interactions as the known quarks. A more detailed discussion can be found below in Section 2.4.3.

2.2 Physics at Hadron Colliders

True to its name, the Large Hadron Collider (LHC) collides hadrons at unprecedented center-of-mass energies. A hadron is a bound state of three quarks, with the common stable varieties being the familiar proton and neutron that are found in the nuclei of atoms. The data used for this analysis is from proton-proton (pp) collisions. A proton consists of two up quarks and a down quark, and colliding protons effectively means colliding these constituents (partons). While the proton energy is known and fixed, the energy of the parton that participates in the collision is some fraction of the proton energy and follows a probabilistic distribution, known as the Parton Distribution Function (PDF) [12]. In addition to the three "valence" quarks listed above, there are other particles which can participate instead in a collision due to quantum fluctuations. These include gluons, the carriers

[1] Note that if the newly discovered boson is confirmed to be the SM Higgs boson, technicolor will be strongly disfavored.

of the strong force, and "sea" quarks which temporarily appear. The PDFs also contain the likelihood for these other partons to participate in interactions.

Another significant feature of physics at hadron colliders is that the remaining partons in each proton which do not participate in a collision continue along in the direction of the beam (considered the z-direction for this discussion[2]), carrying an unknown fraction of the proton's original momentum. Conservation of momentum still applies, but experimentally, it is impossible to use this constraint in the z-direction. Instead, transverse variables are used, defined in the plane orthogonal to the z-axis. Measuring the momentum balance in the transverse plane allows one to infer the momentum of undetected particles using the transverse missing energy:[3]

$$E_{\mathrm{T}}^{\mathrm{miss}} = -\sum_i p_T^i \tag{2.1}$$

where the sum is over the particles in a given collision event and p_T^i is the transverse momentum of the ith particle.

To measure angular distributions, the rapidity y is defined:

$$y = \frac{1}{2}\ln\left(\frac{E + p_z}{E - p_z}\right) \tag{2.2}$$

This quantity has the property that, under a boost in the z-direction of velocity β, $y \to y - \tanh^{-1}\beta$. Thus differences in rapidity or differential distributions like $\frac{dN}{dy}$ are Lorentz invariant. In the case of $p \gg m$,

$$y \approx -\ln(\tan(\theta/2)) \equiv \eta \tag{2.3}$$

where $\cos(\theta) = p_z/p$. This quantity η is called the pseudorapidity. It can be measured independently of the mass and momentum of a particle, and for the particles created in the LHC collisions and which are stable enough to propagate in the detector, $p \gg m$ is a very good approximation.

Another critical concept is that of luminosity, $\mathcal{L}$, which is a measure of the rate of interactions for a collider. Given the cross section of a process of interest, σ, the number of observed events will be:

$$N = \sigma \int \mathcal{L}(t)dt \tag{2.4}$$

Typical units for luminosity are $\mathrm{cm}^{-2}\mathrm{s}^{-1}$. When integrated over time, however, luminosities are typically expressed in inverted units of cross sections, e.g. inverse picobarns (pb^{-1}). The luminosity of the Large Hadron Collider is discussed in Section 3.2.

---

[2] A more detailed description of the coordinate system used by the ATLAS detector is given in Section 4.1.

[3] Technically this formula is for a momentum, but the quantity takes its name from the fact that, experimentally, typically the transverse energies of particles are what are measured precisely.

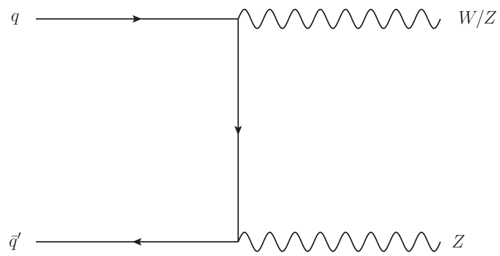

(a) t-channel

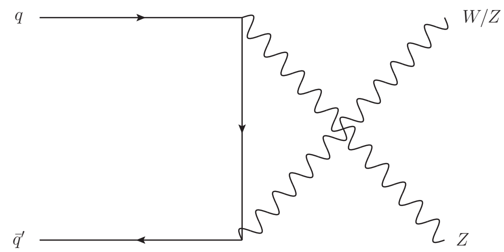

(b) u-channel

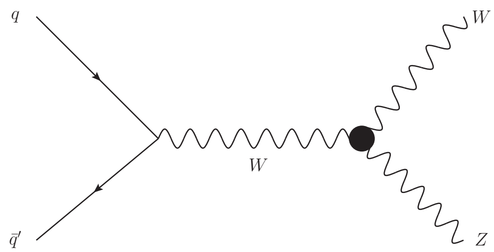

(c) s-channel

Figure 2.1: Example diboson production diagrams for $W^{\pm}Z/ZZ$. The s-channel process where a W boson is exchanged contains a triple gauge coupling which is forbidden in the SM for ZZ.

2.3 Like-Sign Dilepton Production in the Standard Model

In the SM, there are a handful of processes which can produce prompt like-sign dileptons. The ones with the highest cross-sections are $W^{\pm}Z$ and ZZ diboson production, where both bosons decay leptonically. The dominant production mechanism for these at the LHC is from quark-antiquark initial states, as depicted in Fig. 2.1, with further contributions from gluon fusion.

In addition, there are a few rarer processes which have not yet been measured but which are predicted by the SM at rates which are not completely negligible for this search. One such process is like-sign W pair production where both W bosons decay leptonically. This occurs through double parton scattering as well as electroweak processes like vector boson fusion, with a couple example diagrams shown in Fig. 2.2. The others are $t\bar{t}W$ and $t\bar{t}Z$, vector bosons produced in association with top quark pairs, where the boson and at least one of the top quarks decay leptonically.

There are several processes which can give rise to non-prompt leptons, through semi-leptonic decays of heavy flavor quarks, as well as hadronic signatures which appear similar to leptons in the detector. These are covered in detail in Chapter 9.

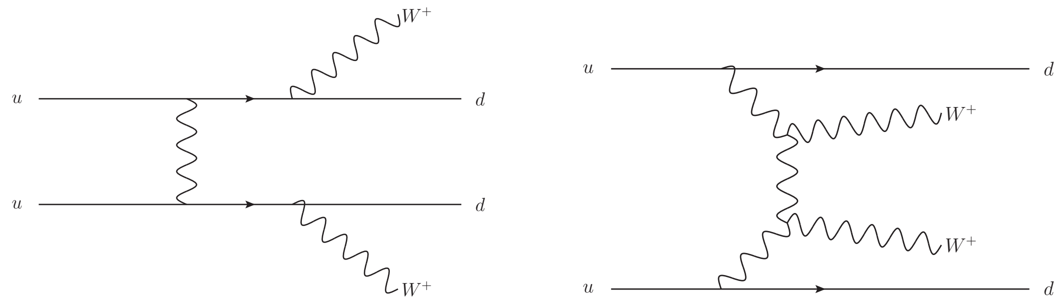

(a) (b)

Figure 2.2: Example production diagrams for $W^{\pm}W^{\pm}$.

2.4 Like-Sign Dilepton Production in Theories Beyond the Standard Model

The search for anomalous, prompt like-sign lepton production is a promising one because of the relatively low SM backgrounds, as detailed above, and because many extensions of the SM predict new phenomena with signatures including these. An incomplete list of such models is given below.

2.4.1 Doubly-Charged Scalars

Several extensions of the SM include doubly-charged scalar states. Often these occur as a doubly-charged Higgs boson in a multiplet with other Higgs states [13], but they can also occur in other different contexts. For all the cases below, the production and decay of these particles is essentially the same.

The dominant production mode is pair production in the s-channel, from a quark initial state with a Z/γ^* mediating, as shown in Fig. 2.3. The typical decays, and those that will be of interest in this analysis, are to pairs of like-sign charged leptons. The two leptons can be of any flavor in general, with specific constraints on the branching ratios arising in various models. Decays to pairs of like-sign W bosons are also possible once the mass of the scalar is larger than $2m_W$, depending on the model. Additionally, decays can include a singly-charged Higgs boson in some models, if kinematically allowed. These possibilities are not considered here.

The partial decay width to leptons is given by

$$\Gamma(\Phi^{\pm\pm} \to \ell^{\pm}\ell'^{\pm}) = k\frac{h^2_{\ell\ell'}}{16\pi}m(\Phi^{\pm\pm}), \tag{2.5}$$

where $\Phi^{\pm\pm}$ is the doubly-charged scalar, $k = 2$ if both leptons have the same flavor ($\ell = \ell'$) and $k = 1$

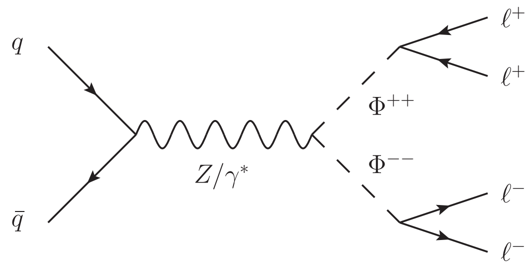

Figure 2.3: Diagram of doubly charged scalar production and decay to like-sign lepton pairs.

if they have a different flavor. The factor $h_{\ell\ell'}$ is the coupling parameter. For experimental purposes, the decays are considered prompt if $c\tau < 10\ \mu$m, corresponding to $h_{\ell\ell'} > 10^{-6}$ for $m(\Phi^{\pm\pm}) = 300$ GeV.

Experimental constraints exist from direct searches at previous experiments [11], ATLAS [14], and CMS [15]. The coupling parameters $h_{\ell\ell'}$ are also constrained by various low energy experiments as summarized in [13].

2.4.1.1 Higgs Triplets

Some models predict a $SU(2)_L$ triplet including a neutral Higgs boson plus singly and doubly-charged scalars. The typical motivation for this is to explain the neutrino masses. In what is called the type II seesaw mechanism, the neutral Higgs boson obtains a vacuum expectation value, and the neutrino masses are proportional to this value [13]. Higgs triplets can appear in left-right symmetric models as well as the Little Higgs model, described in the next sections.

2.4.1.2 Left-right Symmetric Models

Left-right symmetric models (LRSM) contain the gauge group $SU(2)_L \times SU(2)_R \times U(1)_{B-L}$. A Higgs triplet occurs naturally in some models, and the main motivation is generating neutrino mass terms in conjunction with right-handed Majorana neutrinos. Obviously the $SU(2)_R$ symmetry is broken in nature, which can be accomplished spontaneously.

Left-right symmetry can occur in various SUSY models. To break the $SU(2)_R$ symmetry and have a physical mass spectrum for the Higgs particles, R-parity (defined below in Section 2.4.5) must be violated [16].

2.4.1.3 Little Higgs

The Little Higgs models are motivated by solving the hierarchy problem without strong dynamics or low-scale SUSY (assumed to be perturbative at EW scale) [17]. The Higgs boson appears as a pseudo-Nambu-Goldstone boson, and the Higgs mass is protected from divergences by approximate global symmetries. New states are introduced around the TeV scale to cut off the most important divergences: loop corrections from the top quark, $SU(2)$ gauge bosons, and the Higgs itself. In addition, there is a more complicated Higgs sector with some models having new states near the EW scale in mass, including a Higgs triplet with a doubly-charged scalar.

2.4.1.4 Zee-Babu Model

The Zee-Babu model is the minimal extension of the SM providing neutrino masses and consistent with experimental constraints [10, 18, 19]. It adds two complex singlet scalar fields, one singly-charged and one doubly-charged. Dirac neutrino mass terms are generated at the 2-loop level, with the neutrino masses proportional to the Yukawa couplings of the new scalars and inversely proportional to their masses squared, which restricts the available parameter space.

2.4.2 Like-sign Top Quarks

One motivation for signatures involving like-sign top quarks comes from the anomaly observed in the top quark forward-backward asymmetry by the CDF experiment [20, 21]. A potential mechanism to generate the large asymmetry is through the t-channel exchange of a Z' boson with strong flavor-changing neutral current (FCNC) couplings with the top and up quarks. A similar t-channel exchange would then also produce like-sign top quarks, when starting from a uu initial state instead of $u\bar{u}$, as shown in Fig. 2.4a. Measurements by the D0 and CMS collaborations, however, are consistent with SM predictions and exclude the level of asymmetry observed by CDF [22, 23].

Like-sign top quark final states can also result from the decay of a charge 4/3 color triplet or color sextet [24], as shown in Fig. 2.4b. The existence of such particles would have implications for the evolution of the strong coupling strength and thus grand unified theories.

Limits on this final state have been placed recently by ATLAS [25] and CMS [26] using more tailored searches.

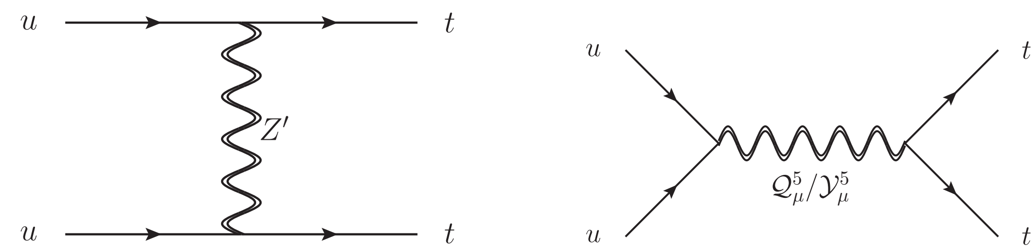

(a) FCNC Z'

(b) Color triplet/sextet

Figure 2.4: Production diagrams for like-sign top quarks, via a Z' boson with strong FCNC couplings (a) or charge 4/3 color triplet/sextet (b).

2.4.3 Fourth Generation Quarks

Sequential fourth generation quarks are disfavored with discovery of Higgs-like boson with a mass of about 125 GeV and cross-sections consistent with the SM. A fourth generation quark would significantly enhance the gg-fusion production mechanism of the Higgs boson [27]. For bottom-type fourth generation quarks (denoted b'), a typical signature would be b' quark pair production to $WtWt$ to leptons.

Another more viable possibility is vector-like quarks, whose left- and right-handed components transform the same under $SU(2)$ [28]. Typically these would only couple to the third generation due to constraints on light quark couplings, but these models can have contributions to quark mixing cancel and remove some constraints. Signatures including like-sign leptons would be pair production of b' decaying to $ZbZb$ or pair production of t' decaying to $ZtZt$.

Limits on these type of models have been placed recently by ATLAS [29, 30, 31] and CMS [32, 33] using dedicated searches.

2.4.4 Heavy Neutrinos

New heavy Majorana right-handed neutrinos could explain the light left-handed neutrino masses via the seesaw mechanism. One class of models in which these arise are left-right symmetric models. As mentioned above, these along with a Higgs triplet can generate the left-handed neutrino masses in what is termed the type II seesaw mechanism [34]. Such models include three new gauge bosons: $W_R^\pm$ and Z'. One promising channel for direct detection is $pp \to W_R \to \ell N \to \ell\ell' qq'$, where N is a heavy neutrino, and the last decay takes place via an off-shell W_R boson [35]. As N is not charged, the second lepton charge is uncorrelated with the first and like-sign lepton pairs will be produced half of the time. This decay chain is shown in Fig. 2.5. The same final state can also be described by a

4-fermion effective operator for N production [36]. Limits on this production have been placed by a dedicated ATLAS search [37].

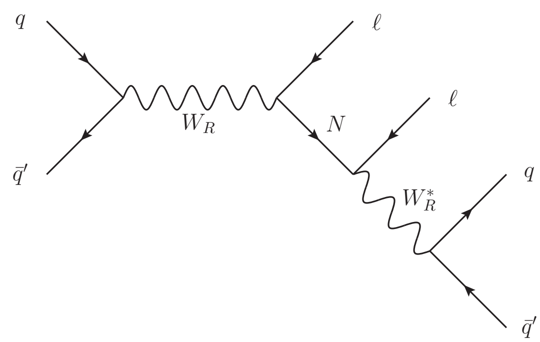

Figure 2.5: Diagram of a like-sign lepton final state in a left-right symmetric model with W_R and heavy neutrinos, N.

2.4.5 Supersymmetry

One of the main motivations for SUSY is to explain the hierarchy problem. By postulating a symmetry between fermions and bosons, all the known SM particles receive a superpartner state, and the contributions of the two to the loop corrections of the Higgs boson mass cancel to all orders [38]. These additional superpartners have not been observed with identical masses, so SUSY must be a broken symmetry.

Much of the phenomenology of SUSY models comes from the manner in which SUSY is broken. The breaking mechanism, whether gravity-mediated, gauge-mediated, or otherwise, typically introduces a large number of parameters into the model, including masses, mixing angles, and CP violating phases. Experimental results form constraints on many of the flavor parameters of a model, but there is still a large amount of freedom especially in the masses of the various states, which leads to a variety of potential experimental signatures. Another critical aspect is the conservation or violation of R-parity. SM particles have R-parity of +1, while supersymmetric partners have R-parity of -1, and if conserved, this forbids mixing between the SM particles and the SUSY sparticles. It also preserves baryon number and total lepton number, and it guarantees the existence of a "lightest supersymmetric particle" (LSP) which must be stable and thus cannot decay to SM particles.

Like-sign leptons can be produced in one of several ways, depending on the allowed decays. One example is gluino pair production, if the gluinos can decay to charginos via the process $\tilde{g} \to q\bar{q}'\tilde{C}_i$. As the gluinos do not carry electric charge, the chargino charges are random, so with two charginos produced there is a 50% chance of them being like-sign. The chargino could subsequently decay as $\tilde{C}_i \to \ell \tilde{N}_j$, where $\tilde{N}_j$ is a neutralino. Similarly, trilepton final states can occur if one gluino decays via $\tilde{g} \to q\bar{q}\tilde{N}_i$ to a neutralino. Then the neutralino could decay as $\tilde{N}_i \to \ell\tilde{\ell} \to \ell\bar{\ell}\tilde{N}_j$. Other signatures can give rise to like-sign leptons, for instance decays involving gluinos to stop squarks. For all the signatures mentioned here, the leptons would typically be produced in association with hadronic jets and likely also $E_{\mathrm{T}}^{\mathrm{miss}}$.

ATLAS and CMS have performed several searches constraining various regions of SUSY phase space. Results from recent searches using like-sign leptons or more than two leptons are described in [39, 40] for ATLAS and in [26, 41, 42] for CMS.

Chapter 3

The Large Hadron Collider

The gargantuan LHC is the most powerful particle collider to date and one of the most complex machines ever built. This chapter describes some of the basics of the LHC and the accelerator complex that feeds into it, including the most relevant aspects for luminosity production. More complete information can be found in [43].

3.1 LHC and Accelerator Complex

The LHC is located at CERN, the European Organization for Nuclear Research, and straddles the border between France and Switzerland near Geneva. Located about 100 m underground, it has a circumference of 26.7 km and sits with a tilt of 1.4% toward Lake Geneva. Two beams of protons circulate, with beam 1 circulating in the clockwise direction and beam 2 counter-clockwise. The beams are housed in separate beam pipes and have separate magnetic fields out of necessity, but they are located within the same physical magnet assembly in a twin-bore design, largely due to space constraints from reusing the tunnel of the Large Electron Positron collider (LEP). The LHC has eight equally spaced interaction regions, numbered IR1–8, four of which are used to collide the beams and therefore house experiments. The ATLAS and CMS detectors, located at IR1 and IR5 respectively, are general purpose experiments. The LHCb detector, located at IR8, is a lower luminosity b-physics experiment, and the ALICE detector at IR2 primarily studies heavy ion collisions. The beam dump system, used to safely extract the beams from the LHC, is located at IR6.

Besides having had the LEP tunnel available to install the LHC, CERN also has an extensive accelerator complex which has been used for past experiments and parts of which were adapted to provide the early boosting stages for the LHC. The ion source is a duoplasmatron, which makes protons from hydrogen atoms by bombarding them with free electrons to strip off the valence electrons. The protons are first accelerated by the Linac2, a linear accelerator, up to energies of 50 MeV. They are fed into the Proton Synchrotron Booster (PSB) which accelerates them to energies of 1.4 GeV for the next stage, the Proton Synchrotron (PS). The PS came online in 1959 and has received many upgrades over time, and its primary purpose now is to supply protons or ions for the various experiments at CERN, including the LHC. It accelerates protons to 25 GeV and injects bunches of up to $1.6 \cdot 10^{11}$ particles into the next stage, the Super Proton Synchrotron (SPS). The last stage prior to injection in the LHC, the SPS now serves as a booster for the LHC but in the past (1981–1984) was operated as the Sp$\bar{\text{p}}$S, a p$\bar{\text{p}}$ collider. There the protons are accelerated to 450 GeV and injected into the LHC. The energy ramp in the LHC from 450 GeV to the the current operating energy of 8 TeV takes about 20 minutes.

The original LHC design energy was 7 TeV per beam to give collisions at $\sqrt{s} = 14$ TeV. This forms requirements on many of the LHC parameters, but in particular, the energy is proportional to the current in the LHC dipole magnets. The superconducting magnets are all cooled with liquid helium to a temperature of 1.9 K. They can quench and rapidly heat up if some part of them leaves the superconducting state, due to too high of a field, too quick of a field change, defects, or energy deposition. After an unexpected and catastrophic quench damaged several magnets in one sector of the LHC in 2008, problematic solder connections were repaired and additional quench protection was put into place. Upon restarting in 2009 and first high energy running (above 450 GeV) in 2010, it was decided to operate the LHC at 3.5 TeV per beam to minimize the risk of another catastrophic event. In 2012, the energy was increased to 4 TeV per beam, and after further work in the 2013–2014 long shutdown, the LHC is expected to run at 6.5–7 TeV per beam.

3.2 Luminosity Production

One of the primary goals of LHC operations is to maximize the amount of luminosity delivered to the experiments. This depends on the peak luminosity, the luminosity lifetime, and the availability of the LHC for physics collisions. These in turn depend on machine parameters.

Equation 3.1 gives the instantaneous luminosity, $\mathcal{L}$, provided by the LHC:

$$\mathcal{L} = \frac{N_b^2 n_b f_{\text{rev}} \gamma_r}{4\pi \epsilon_n \beta^*} F \tag{3.1}$$

Here N_b is the number of particles per bunch, n_b is the number of bunches per beam, f_{rev} is the beam revolution frequency, and γ_r the relativistic gamma factor. The number of bunches, n_b, of course depends on the bunch spacing in the LHC; the design spacing is 25 ns but due to various stability issues, higher luminosity can currently be achieved with 50 ns. The parameter ϵ_n is the normalized

Table 3.1: Some LHC parameters for $\sqrt{s} = 8$ TeV collisions in October 2012 at IP1 (for the ATLAS detector).

Parameter	Value
N_b	$1.6 \cdot 10^{11}$
n_b	1368
f_{rev}	11.25 kHz
γ_r	4260
ϵ_n	2.5 μm
β^*	0.6
F	0.82
θ_c	290 μrad
σ_z	9.4 cm
σ^*	19 μm
Bunch spacing	50 ns
$\mathcal{L}$	$7.2 \cdot 10^{33}$ cm^{-2}s^{-1}

transverse beam emittance, which is the average spread of the beam in position and momentum phase space. The parameter β^* is the beta function at the interaction point (IP), which is a measure of the transverse beam size. Its value is the distance from the IP at which the beam is twice the size of that at the IP. And F is a geometric luminosity reduction factor at the IP, given by:

$$F = \left(1 + \left(\frac{\theta_c \sigma_z}{2\sigma^*}\right)^2\right)^{-1/2} \tag{3.2}$$

Here θ_c is the crossing angle at the IP, σ_z is the RMS bunch length, and σ^* is the transverse RMS beam size at the IP. Table 3.1 shows the values of these parameters in October 2012, when the peak instantaneous luminosity was about $7.2 \cdot 10^{33}$ cm^{-2}s^{-1}. Figure 3.1 shows the peak luminosity versus time for the pp physics runs in 2010, 2011, and most of 2012, as recorded by the ATLAS detector.

The beams decay from the maximum luminosity throughout a given LHC fill due to loss of particles in collisions and increasing emittance along with various other effects. The luminosity lifetime, τ_L, is defined as the time required for the luminosity to drop to $1/e$ of its peak value. Then the integrated luminosity for a run, $\mathcal{L}_{\text{int}}$, is given by:

$$\mathcal{L}_{\text{int}} = \mathcal{L}_0 \tau_L \left[1 - e^{-T_{\text{run}}/\tau_L}\right] \tag{3.3}$$

where $\mathcal{L}_0$ is the initial peak luminosity and T_{run} is the length of the run. The final piece is the operational availability of the machine for physics runs. The minimum theoretical turn around time

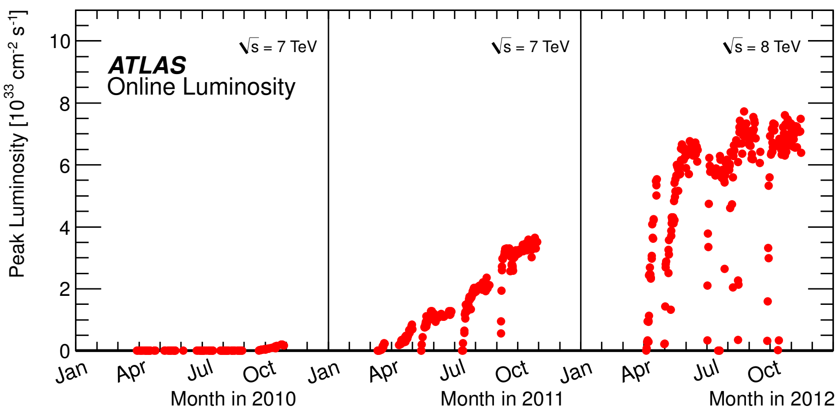

Figure 3.1: Peak luminosity delivered by the LHC as a function of time, as measured by the ATLAS detector.

for the LHC, after dumping the beams in a physics run to colliding them again for physics, is around 70 minutes. This includes about 20 minutes to ramp the magnets down, time for injection and system checks, and 20 minutes to ramp the magnets up again. In practice, many runs are dumped early due to various issues which require time to solve, and so an availability of 30-40% for physics running is more feasible. In 2011, the availability for *pp* physics averaged over the full year was about 32% [44].

The downside of the high instantaneous luminosity delivered by the LHC is that each crossing typically produces multiple interactions, so the detectors must be able to separate a rare high-p_{T} scattering interaction of interest from the overlap of many common low-p_{T} interactions. The average number of these low-p_{T} "pileup" interactions is shown in Fig. 3.2 for the 2011 and 2012 *pp* physics runs. In 2011, the number typically ranged from 5–15, going up to 20 at peak luminosities. For 2012, typical values are 10–30, with tails above 35. Coping with this large number of pileup interactions is a constant experimental challenge and is discussed in later chapters.

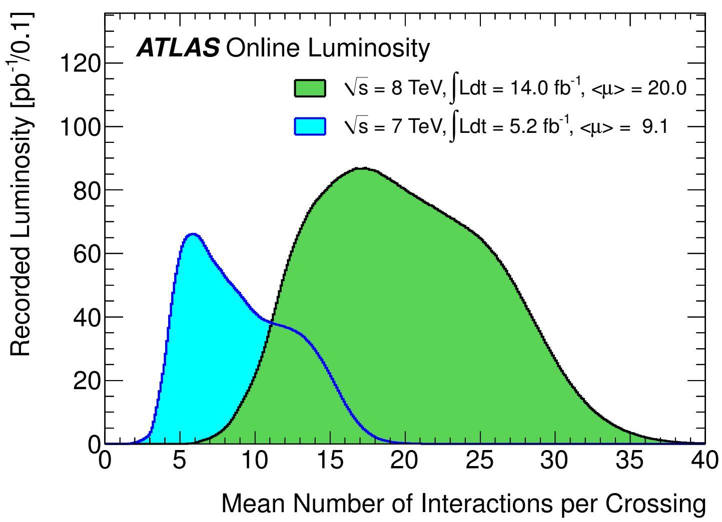

Figure 3.2: Luminosity-weighted distributions of the mean number of interactions per bunch crossing for the 2011 and 2012 pp physics runs.

Chapter 4

The ATLAS Detector

Rivaling the complexity of the LHC are the detectors built to study its collisions, the largest and most general of these being ATLAS (**A** **T**oroidal **L**HC **A**pparatu**S**) and CMS (the **C**ompact **M**uon **S**olenoid). In this chapter, the basics of the ATLAS detector are described, and then the subdetectors are described in some detail, with particular attention paid to those most relevant for this search.

4.1 General Overview

The ATLAS detector [45] consists of an inner tracking system, calorimeters, and a muon spectrometer. The inner detector (ID), directly surrounding the interaction point, is composed of a silicon pixel detector, a silicon microstrip detector, and a transition radiation tracker, all contained within a 2 T axial magnetic field. It covers the pseudorapidity[4] range $|\eta| < 2.5$ and is enclosed by a calorimeter system consisting of electromagnetic and hadronic sections. The electromagnetic part is a lead/liquid-argon sampling calorimeter, divided into a barrel ($|\eta| < 1.475$) and two end-cap sections ($1.375 < |\eta| < 3.2$). The barrel ($|\eta| < 0.8$) and extended barrel ($0.8 < |\eta| < 1.7$) hadronic calorimeter sections consist of iron and scintillator tiles, while the end-cap ($1.5 < |\eta| < 3.2$) and forward ($3.1 < |\eta| < 4.9$) calorimeters are composed of copper or tungsten and liquid-argon.

The calorimeter system is surrounded by a large muon spectrometer (MS) built with air-core toroids. This spectrometer is equipped with precision chambers (composed of monitored drift tubes and cathode strip chambers) to provide precise position measurements in the bending plane in the range $|\eta| < 2.7$. In addition, resistive plate chambers and thin gap chambers with a fast response time are used primarily to trigger muons in the rapidity ranges $|\eta| \leq 1.05$ and $1.05 < |\eta| < 2.4$, respectively.

[4] ATLAS uses a right-handed coordinate system with its origin at the nominal interaction point (IP) in the center of the detector and the z-axis along the beam line. The x-axis points from the IP to the center of the LHC ring, and the y-axis points upward. Cylindrical coordinates (r, ϕ) are used in the transverse plane, ϕ being the azimuthal angle around the beam line. The pseudorapidity is defined in terms of the polar angle θ as $\eta = -\ln\tan(\theta/2)$.

The resistive plate chambers and thin gap chambers also provide position measurements in the non-bending plane, which are used to improve the pattern recognition and the track reconstruction.

The ATLAS trigger system has a hardware-based Level-1 trigger followed by a software-based high-level trigger (HLT) [46]. The Level-1 muon trigger searches for hit coincidences between different muon trigger detector layers inside geometrical windows that define the muon transverse momentum and provide a rough estimate of its position. It selects muons in the pseudorapidity range $|\eta| < 2.4$. The Level-1 electron trigger selects local energy clusters of cells in the electromagnetic section of the calorimeter. For low-energy electron clusters, low activity in the hadronic calorimeter nearby in the η-ϕ plane is required. The high-level trigger selection is based on similar reconstruction algorithms as those used offline.

The following sections provide more detail on the components of the ATLAS detector most relevant for this search. More complete information on the ATLAS detector can be found in [45].

4.2 Inner Detector

The ID contains three subdetectors. Moving radially outward from the interaction point, these are the silicon pixels, the silicon microstrips (SCT), and the Transition Radiation Tracker (TRT), a gaseous straw tube detector. The silicon detectors provide precise measurements of the charged particle tracks from interactions, in particular determining their transverse momentum and reconstructing primary and secondary vertices in a given event. The TRT lies at larger radius and provides a large number of less precise measurements, bringing a larger lever arm to improve momentum resolution as well as providing particle identification for electrons.

The silicon detectors both cover the pseudorapidity range $|\eta|$ <2.5, with layers of sensors arranged in concentric cylinders in the barrel region and on disks perpendicular to the beam direction in the endcaps. The TRT extends to $|\eta|$ <2.0, with layers of straw tubes running parallel to the beam line in the barrel detector and perpendicular to the beam line in the endcaps. Illustrations of the barrel and an endcap for the ID detectors are shown in Figs. 4.1 and 4.2.

The ID can reconstruct tracks of charged particles down to p_{T} of 0.5 GeV (0.1 GeV in special software configurations). The intrinsic single hit resolution for the pixel detector is 10 μm in R-ϕ and 115 μm in the $z(R)$-direction in the barrel (endcaps), while for the SCT it is 17 μm in R-ϕ and 580 μm in z/R. The TRT provides only two-dimensional information: R-ϕ in the barrel and z-ϕ in the endcaps, with a resolution of about 120 μm. The p_{T} resolution is roughly $0.05\% \cdot p_{\mathrm{T}} \oplus 1\%$.

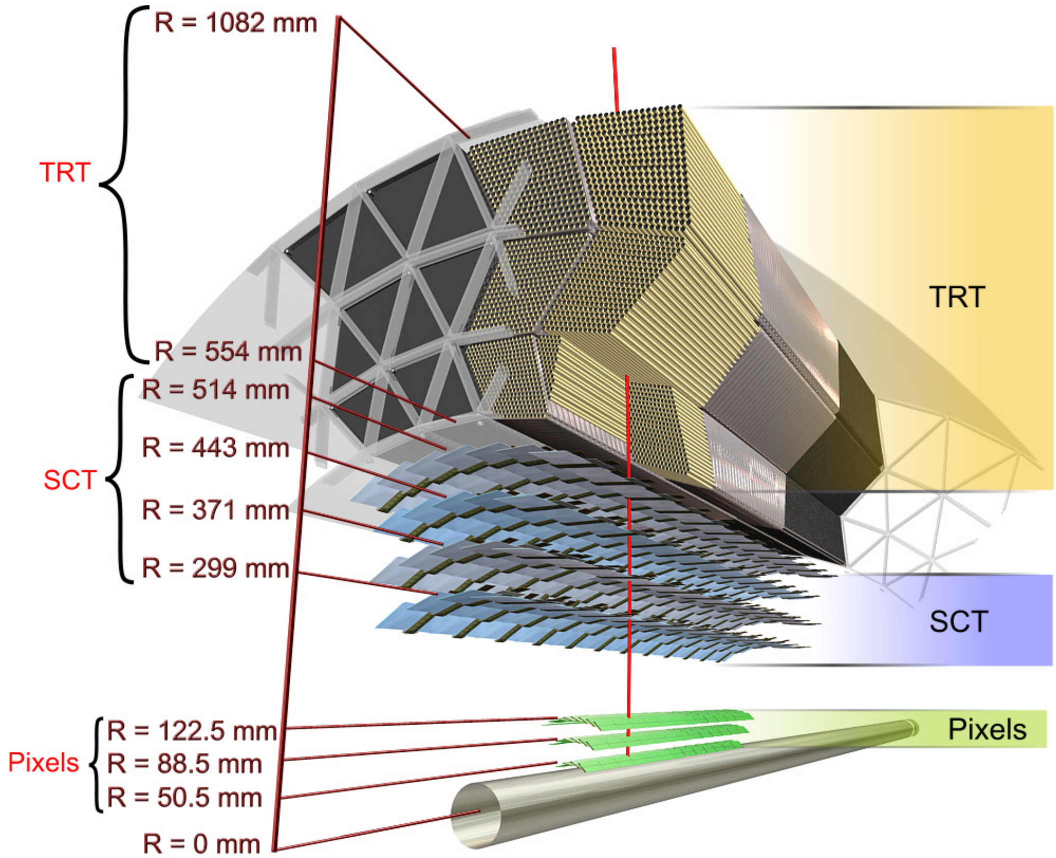

Figure 4.1: Depiction of the ATLAS ID barrel, showing the radius of each detector layer.

4.2.1 Transition Radiation Tracker

The TRT is a novel detector combining almost continuous tracking with the particle identification capabilities of transition radiation [47, 48]. Its design allows for a low-material, low-cost extension of the ID to large radius, compared with silicon sensors. The University of Pennsylvania group has played a large role in the design, installation, and commissioning of the readout electronics and data acquisition for the TRT, as well as in calibration work to optimize the performance of the TRT for reconstruction and particle identification.

The detector elements are hollow "straw" tubes made of polyimide and carbon fiber, cylindrically shaped and 4 mm in diameter, with a tungsten wire running down the center. The straw tube is kept at a potential of roughly -1500 V relative to the wire, creating a strong electric field. Its basic principle of detection is observing ionization electrons from charged particles traversing the straw tubes. When a charged particle passes through the straw, it ionizes the gas, and the ionization electrons drift inward

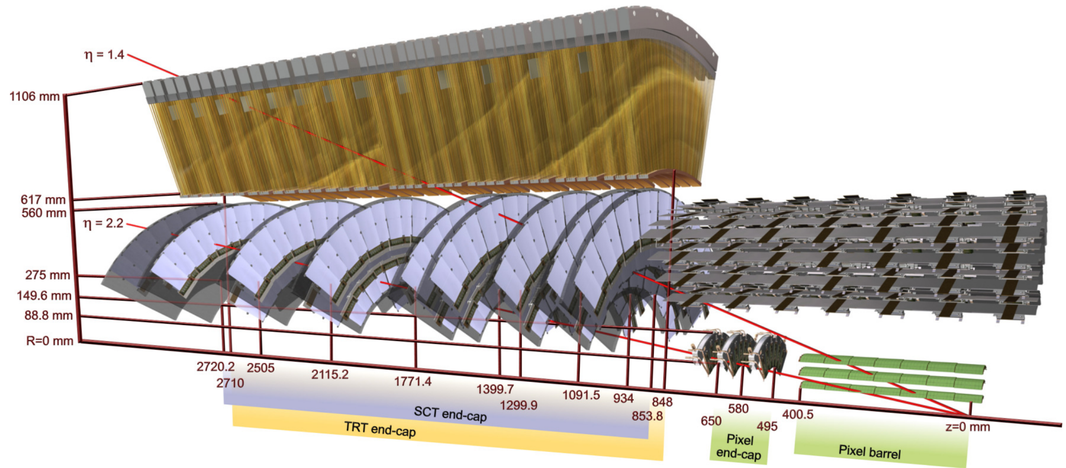

Figure 4.2: Depiction of one of the ATLAS ID endcaps, with the radius and z-position of each detector layer.

toward the wire. The high electric field near the wire causes an avalanche effect which amplifies the drift electron signal, with typical gains of $2.5 \cdot 10^4$. This current travels along the wire to electronics at the end which process the analog pulse, as described below. The timing of the first ionization electrons to arrive at the wire can be used to infer the distance of closest approach for the charged particle relative to the wire. An empirical function, called the R-T relation, is used to convert the drift time measurement to track-to-wire distance. This function is determined from data and is one of the primary calibrations performed for the TRT (the other being the determination of the timing offsets among the various channels).

Transition radiation (TR), exploited in the TRT for particle identification, refers to a photon emitted by a charged particle when traversing the boundary between two materials of different dielectric constants. The energy of the photon is in the x-ray range, several keV, so when absorbed by an atom it leads to a much larger signal amplitude compared to minimally ionizing particles. The rate of emission is in general proportional to the Lorentz γ-factor of the particle ($\gamma = E/m$), while the emission angle is proportional to $1/\gamma$. The rate of emission can be enhanced by coherence effects when many such transitions happen sequentially, so the design of the TRT was optimized to maximize these effects. A polymer foil or foam is used as the radiator material in different detector regions, ensuring a large number of boundary transitions between the polymer and the active gas mixture.

The actual probability for a transition radiation photon to be emitted as a function of γ thus depends strongly on the design choices of the detector, and this is reflected in Fig. 4.3. It shows the high threshold hit probability versus γ for electrons and pions in different detector regions. The high

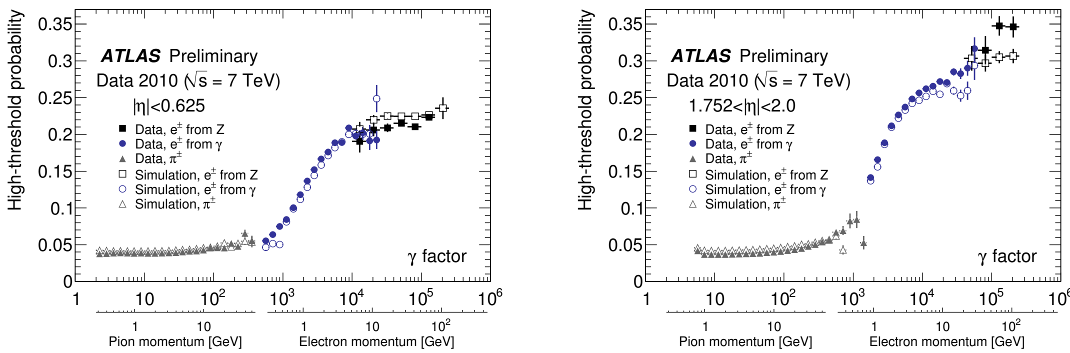

(a) Barrel (b) High η Endcaps

Figure 4.3: Probability to observe a high threshold hit (described in Section 4.2.1.1) as a function of Lorentz γ-factor, measured for the TRT barrel (a) and high η endcaps (b). For electrons, the high threshold hits are from transition radiation, while for pions, typically the hits are from large ionization energy deposits due to Landau $\mathrm{d}E/\mathrm{d}x$ fluctuations.

threshold is described below in Section 4.2.1.1. For electrons, it is effectively measuring TR, while for pions, high threshold hits are typically from large ionization energy deposits due to Landau dE/dx fluctuations. The different responses are a product of both the detector design and the incidence angle of the particles in the detector.

Being a gaseous detector, the choice of active gas for the TRT straw tubes directly impacts its capabilities. A Xenon-based gas mixture (70% Xe, 27% CO_2, 3% O_2) was chosen, as opposed to an Argon-based one, for a two key reasons. First and foremost, it has a high probability of absorbing TR photons, necessary for using TR for particle identification. The absorption probability for Argon is sufficiently small that the particle identification capabilities are mostly lost. Second, compared to an Argon gas mixture, a Xenon mixture allows for a more precise determination of the ionization electron drift time and hence track-to-wire distance, due to the different pulse shape and also a slower drift velocity in Xenon.

The TRT barrel consists of 73 straw tube layers, aligned parallel to the beam line, with radiator material interspersed between these. The barrel straws are divided in the middle by a glass separator and read out at each end. In the endcaps, the straw tubes are arranged in "wheels" perpendicular to the beam line with 8 straw layers per wheel and 20 wheels per endcap. Radiator materials are located between each straw layer. A typical charged particle passing through the TRT volume will produce hits in about 36 straws, depending on the part of the detector traversed. From Fig. 4.3, depending on the detector region, 20–30% of these hits will be high threshold hits for electrons with momentum greater than 10 GeV. In total, the TRT barrel has 52,544 straws and each endcap has 122,880.

4.2.1.1 TRT Data Acquisition

For the analog signals from the TRT wires to be used for charged particle reconstruction, they must be digitized and sent off the detector for trigger decisions and eventual storage, which is accomplished with the TRT Data Acquisition (DAQ) system [49]. Electronics mounted on the detector, called the front end (FE) electronics, shape the analog pulses received from the straw wires and digitize the output into discrete bins in time. The data from each LHC bunch crossing (BC) is stored in a buffer. Electronics in a separate service cavern, known as the back end (BE) electronics, communicate with the rest of the ATLAS DAQ system and transmit configurations and commands to the FE. Upon receipt of a trigger command, the BE transmits the trigger to the FE, where the buffered data for the BC of interest is sent to the BE for further processing and eventually to the ATLAS DAQ system. The signals between the BE and FE electronics are relayed through patch panel (PP) boards, which are located inside the ATLAS detector in the barrel toroid volume. The individual electronics are described in more detail below.

4.2.1.1.1 Front End Electronics The FE electronics consist of a type of analog chip and a type of digital chip, both of which were designed by the University of Pennsylvania instrumentation group. The analog ASDBLR (Amplifier, Shaper, Discriminator, BaseLine Restorer) receives the raw analog signal from the straw wire and performs the functions in its name. For discrimination, two thresholds are applied: a low threshold, corresponding to roughly 300 eV, which is sensitive to ionization from minimally-ionizing particles, and a high threshold, typically around 7 keV, which is used to detect transition radiation. The DTMROC (Digital Time Measurement ReadOut Chip) receives the discriminated output of the ASDBLR and digitizes the result into 3.12 ns time bins for the low threshold and 25 ns time bins for the high threshold. Each ASDBLR receives inputs from up to 8 straws, and each DTMROC handles 2 ASDBLRs.

These FE chips are mounted on printed circuit boards (PCBs), also designed by the University of Pennsylvania instrumentation group. In the barrel, the boards are mounted perpendicular to the straws at the longitudinal ends of the detector. Space is limited and so the PCBs contain the analog ASDBLRs on one side and the digital DTMROCs on the opposite side, with 7–15 DTMROCs on each PCB depending on the location radially in the detector. In the endcaps, the boards are mounted again perpendicular to the straw direction, this time at the outer radius of the TRT. More space is available, and the ASDBLRs are mounted on separate PCBs from the DTMROCs. There are 4 DTMROCs on each PCB, with “triplets” of 3 PCBs connected together to give a total of 12 DTMROCs. Due to the other detectors and especially the large number of services which would need to be removed to access the TRT FE electronics, they are generally considered inaccessible for the installed lifetime of the TRT.

4.2.1.1.2 Back End Electronics At the back end, there are two types of electronics boards: Timing, Trigger, and Control (TTC) boards[5] and ReadOut Driver (ROD) boards. They are PCBs which use the VME standard to communicate with each other and a network-linked single-board computer located in the same VME crate. The TTC boards send a clock and commands to the DTMROCs, including configurations, triggers, and resets. The ROD boards receive the data from the DTMROCs after each trigger. They use a Huffman encoding scheme [50] to compress the data losslessly and transmit the data onward to the rest of the ATLAS DAQ system. Each physical ROD board is logically divided into two halves, with barrel ROD halves processing data for 104 DTMROCs and each endcap ROD, 120 DTMROCs. There is one TTC board for every two physical RODs, for a total of 48 TTC boards and 96 ROD boards.

4.2.1.1.3 Patch Panels The patch panel boards include both TTC PPs, which relay the TTC board commands to the DTMROCs, and the ROD PPs, which transmit the front end data to the ROD boards. The TTC PPs are passive, while the ROD PPs take the electrical transmission data from the DTMROCs and convert it to optical using Gigabit Optical Link (GOL) chips. There is one ROD PP per logical ROD, while for the TTC PPs, there are 2 per TTC board in the endcaps and 4 per TTC board in the barrel, yielding a total of 128 TTC PPs and 192 ROD PPs. Unlike the FE boards, these PP boards are generally accessible during intervention periods due to their location in the barrel toroid volume.

4.2.1.1.4 Fast-OR Trigger The TRT can be configured to provide a coarse-granularity track trigger, called the Fast-OR trigger [51]. Due to its granularity, it is not suitable for collisions where many charged particle tracks are expected, but it has been used extensively during commissioning periods to trigger on cosmic ray muons. These muons tracks, in turn, were used for ID alignment especially in the period before LHC collisions, allowing ATLAS to begin physics data taking with well-aligned tracking detectors.

In addition to digitizing the ASDBLR output signals into discrete time bins, the DTMROCs can send on a separate ("command out") line a fast digitized signal indicating a hit on any of the connected straws. As there is only one command out line per FE board, the information received at the BE

[5] Note that TTC is also used generally within ATLAS to refer to the system and electronics boards which distribute the clock and trigger signals. These boards are distinct from the TRT-specific TTC board described here, so in ambiguous contexts, this board is sometimes referred to as the TRT-TTC.

corresponds to whether any DTMROC on a given board registered a hit, summing over ∼200 straws.[6] The trigger can be programmed to use either the low or high threshold in the DTMROCs. For triggering on cosmic rays, the high threshold is used, running with a reduced value corresponding to about 1 keV to obtain a high threshold hit efficiency of roughly 30%.

The purity of the trigger (fraction of triggered events with a reconstructed track) was estimated to be about 94% with an efficiency of about 75%. The trigger rate is about about 8 Hz in the barrel region and 13 Hz in the endcaps. In total, the TRT Fast-OR trigger increased the sample of tracks available for ID alignment by over an order of magnitude compared to the cosmic ray triggers available from other subdetector systems.

4.2.1.1.5 Operation For recording LHC collisions to be used as physics data, the TRT DAQ is integrated with the ATLAS Trigger and Data Acquisition (TDAQ) system. From the TRT side, this entails receiving the ATLAS clock, triggers, and resets from the Central Trigger Processor (CTP) in the TRT TTC boards and transmitting these to the FE. When the data arrives in the RODs, it is sent to ReadOut System (ROS) computers as a buffer for the high level trigger. A set of software known as the online software is used to control and monitor the BE electronics via the VME interface. This software includes several automatic checks and procedures which allow minor errors in data-taking to be automatically recovered, maximizing the time available for physics data and minimizing the requirements placed on the ATLAS shift crew. As an example, changes in the ATLAS clock can sometimes induce desynchronization in the TRT electronics, which would result in incorrect or no data being sent to the ROS computers. This condition is automatically detected by the TRT online software and corrected through a "resynchronization" procedure.

4.3 Calorimetry

Calorimeters are used to stop and measure particles which interact electromagnetically (electrons and photons) or via the strong nuclear force (hadrons) by causing them to shower and lose their energy. Muons typically interact minimally with the calorimeters so are not stopped. The ATLAS calorimeters are sampling calorimeters, meaning they alternate layers of dense materials which produce the showers with layers of absorber materials which measure the deposited energy. The ATLAS calorimeters are depicted in Fig. 4.4.

[6]Technically, an analog current sum is sent to the TTC PP from the FE board, with an amplitude proportional to the number of DTMROCs which registered hits. However, the present TTC PPs have no configurable threshold for discriminating this signal, and the threshold is fixed at 1 DTMROC per FE board by resistors.

Electromagnetic (EM) calorimetry is provided by a lead/liquid-argon (LAr) sampling calorimeter, divided into a barrel ($|\eta| < 1.475$) and two end-cap sections ($1.375 < |\eta| < 3.2$). Further coverage is provided by a copper-tungsten/LAr calorimeter in the forward region for high η ($3.1 < |\eta| < 4.9$). These calorimeters stop and measure the energies of electrons and photons by inducing electromagnetic showers via bremsstrahlung and pair production, respectively. Liquid argon was chosen as the active medium for its hardness against radiation as well as linear behavior and stability with time.

The barrel is located outside the solenoid magnet but in the same cryostat, to minimize the amount of material upstream of the calorimeter. Each endcap is housed in a separate cryostat. It features an accordion geometry designed for full azimuthal coverage with no gaps. In the pseudorapidity range used for precision measurements ($|\eta| < 2.47$), the LAr calorimeter consists of three longitudinal layers. These are shown in Fig. 4.5 for the central barrel region, along with their dimensions and depths. The first longitudinal layer is finely segmented in η and less so in ϕ, allowing a precise determination of the η direction of particles. The second longitudinal layer contains cells roughly the same size in η and ϕ and contains most of the depth of the calorimeter. The third layer is coarsely segmented and adds some small additional depth to the detector. The region $|\eta| < 1.8$ also features a LAr presampler to determine the energy loss in front of the calorimeter. Figure 4.6 shows the material in radiation lengths (X_0) for the barrel and endcap calorimeters, where an electromagnetic radiation length is defined as the distance over which an electron loses all but $1/e$ of its energy via bremsstrahlung. There are at least 25 radiation lengths across the full coverage except in the transition region ($1.37 < |\eta| < 1.52$), which is typically excluded from analyses.

Hadronic calorimetry is designed to stop and measure the energy of hadronic particles interacting via the strong nuclear force. It is provided in the barrel ($|\eta| < 0.8$) and extended barrel ($0.8 < |\eta| < 1.7$) regions with an iron and scintillator tile calorimeter. This technology was chosen to maximize the calorimeter depth at minimal cost. The endcaps ($1.5 < |\eta| < 3.2$) are covered by copper/LAr calorimeters, and the higher η region is covered by the same forward calorimeter described above. The material in terms of nuclear interaction lengths (λ), the mean free distance traveled by a hadronic particle before undergoing an inelastic nuclear interaction, is shown as a function of η for each calorimeter layer in Fig. 4.7. The total ranges from around 11–19 depending on detector region.

4.4 Muon Spectrometer

The ATLAS muon system is designed to measure the trajectories of charged particle tracks outside the calorimeter volume. As all charged particles except muons are typically stopped fully in the calorimeters, the particles reconstructed by the MS are predominantly muons.

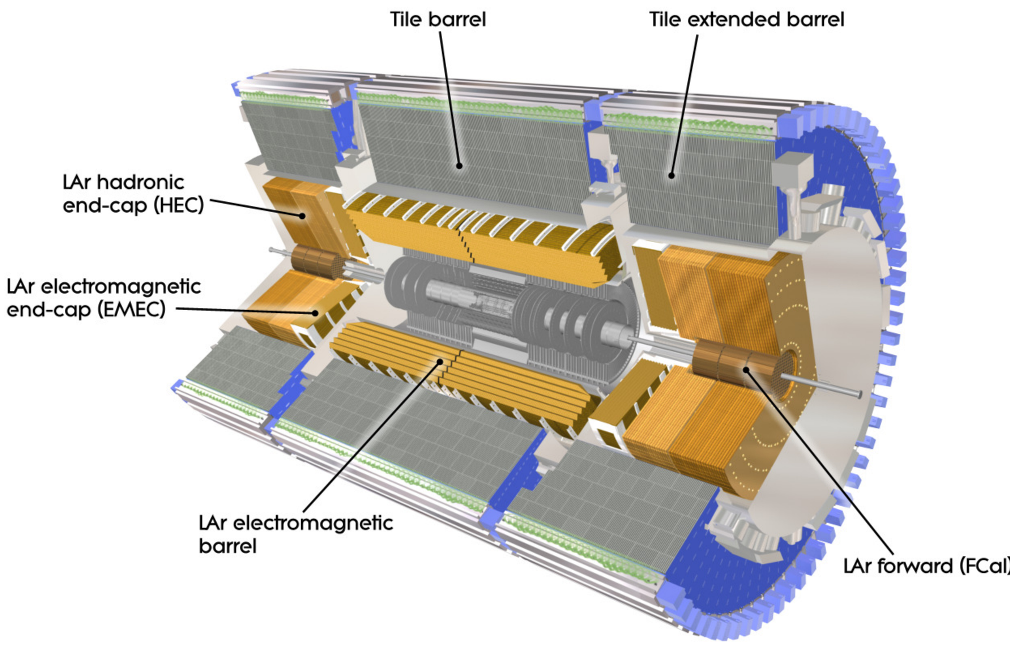

Figure 4.4: Cut-away view of the ATLAS calorimeters.

The primary feature is an air-core toroid magnet, which allows minimizing the material in the MS volume and thus multiple scattering effects. The MS then consists of chambers arranged in three concentric layers in the barrel and wheels in the endcaps. The main elements are depicted in Fig. 4.8.

The precision chambers consist of Monitored Drift Tubes (MDTs) in the barrel and most of the endcaps, with three layers of chambers across most of the range $|\eta| < 2.7$. Each chamber contains 3–8 layers of MDTs. To cope with the larger particle flux at high η, the innermost endcap wheel uses instead Cathode Strip Chambers (CSCs) to cover the region $2.0 < |\eta| < 2.7$. These chambers provide precision hit information in the bending plane of the muons, with a typical resolutions of about 80 μm for a single drift tube (35 μm for an MDT chamber) and 40 μm for a CSC chamber.

Separate chambers are used as inputs for the L1 muon triggers and also to provide hit information in the non-bending plane. In the barrel region ($|\eta| < 1.05$), Resistive Plate Chambers (RPCs) are used, while in the endcaps ($1.05 < |\eta| < 2.4$), Thin Gas Chambers (TGCs) are used. The position resolution in the non-bending plane for these chambers is 3–7 mm, and the timing spread is around 15–25 ns, allowing bunch crossing determination.

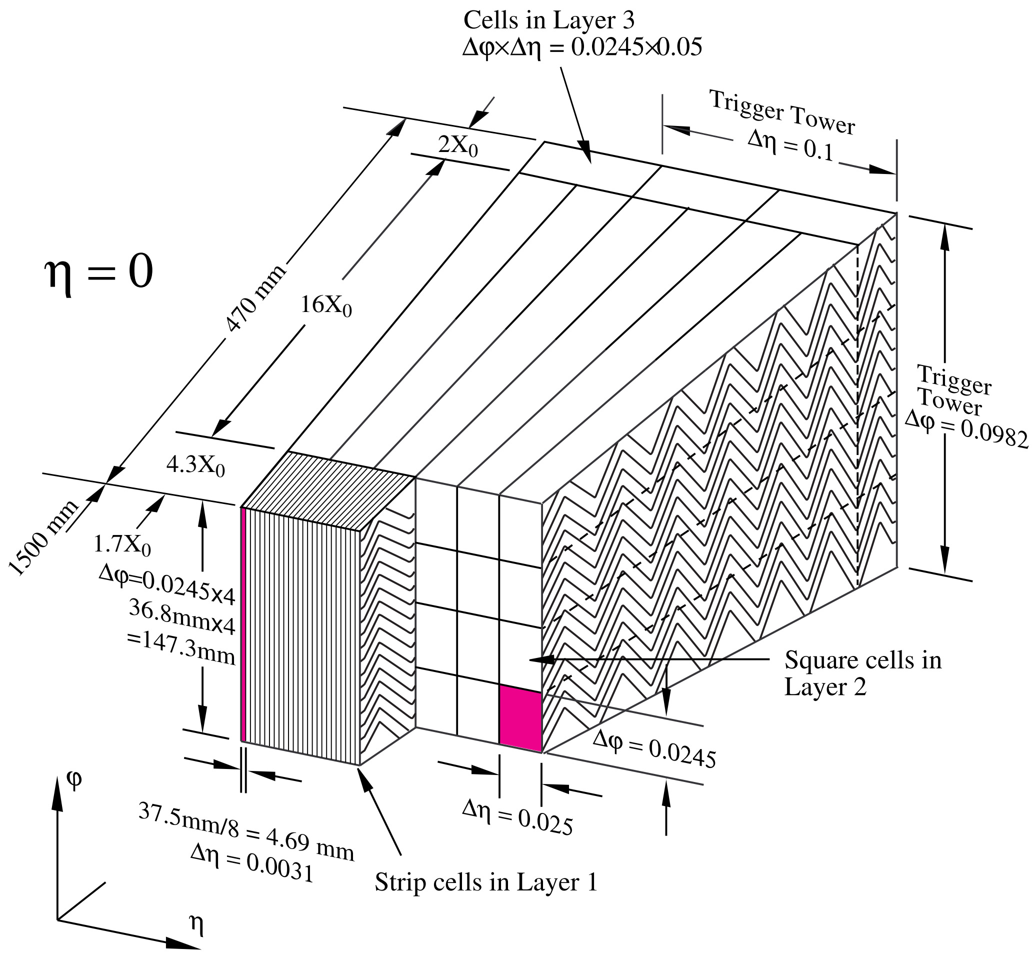

Figure 4.5: Drawing of the LAr EM calorimeter showing the cells in each longitudinal layer for the central barrel region ($\eta = 0$).

4.5 Trigger

The ATLAS trigger consists of three levels in total. The first level, Level-1 (L1), is implemented in hardware and uses coarse granularity information from a subset of subdetectors to make quick first decisions, taking less than 2.5 μs per event. It looks for calorimeter energy deposits (to find electrons, photons, τ leptons, and QCD jets), muon segments in the MS, or event-level calorimeter quantities like $E_{\mathrm{T}}^{\mathrm{miss}}$. The next two levels are Level-2 (L2) and the Event Filter (EF), which are implemented in software and are collectively referred to as the high-level trigger (HLT). L2 is based on a region-of-interest (RoI) concept, taking the objects found at L1 and using information from all subdetectors in a limited $\eta - \phi$ region around each object of interest along with coarse software reconstruction. The

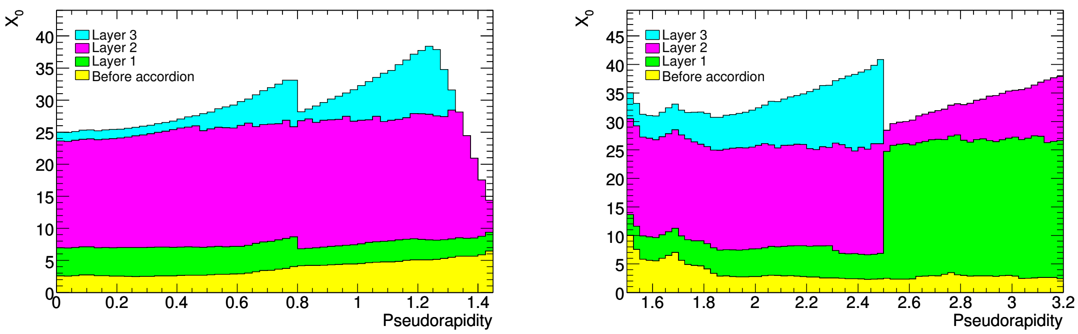

(a) Barrel

(b) Endcaps

Figure 4.6: Depth in radiation lengths (X_0) of the layers of the electromagnetic calorimeter as a function of η, for the barrel (a) and endcaps (b).

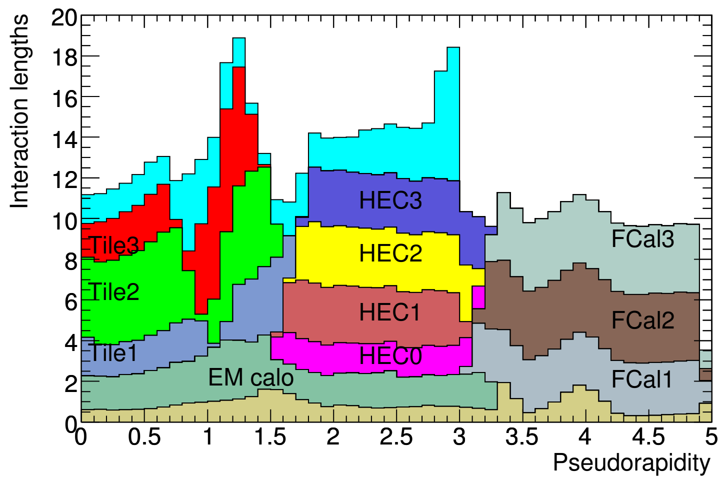

Figure 4.7: Hadronic interaction lengths (λ) of the material in each calorimeter layer, as a function of η. Also shown is the material upstream of the calorimeter (bottom) and material in front of the first muon spectrometer layer (stacked on top, for $|\eta| < 3.0$).

EF has access to full event data and runs reconstruction and algorithms which are very similar to those run in offline reconstruction.

From the nominal 40 MHz collision rate of the LHC with 25 ns bunch spacing, L1 reduces this to 75–100 kHz, L2 reduces it further to about 3.5 kHz, and the output of the EF is written to permanent storage at an average rate of about 400 Hz. The rate of a given trigger increases with the instantaneous luminosity of the LHC, and given the limited bandwidth at each level of the trigger system, priorities must be established as to which triggers are employed. Priority is typically given to triggers which

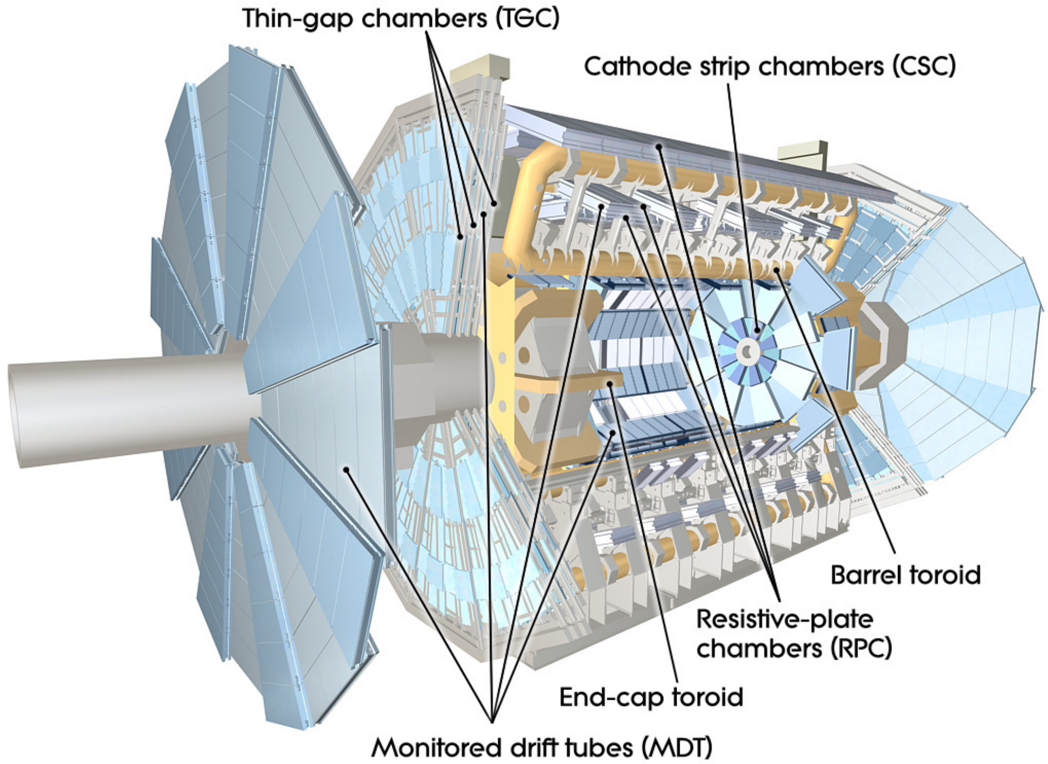

Figure 4.8: Cut-away view of the ATLAS muon spectrometer detectors.

collect the physics datasets for analyses such as this one, with the largest share of the bandwidth being consumed by single electron or muon triggers with thresholds typical of leptons from W or Z boson production. Other triggers which collect events for control regions are often run with a prescale[7] to fit the bandwidth allotment.

[7]A prescale of N for a given trigger implies that one event is kept for every N events passing the trigger, and the rest are rejected.

Chapter 5

Lepton Reconstruction and Identification in ATLAS

Much of the design of the ATLAS detector was centered around reconstructing, identifying, and precisely measuring electrons and muons, as these light leptons provide a relatively clean probe of both SM and BSM physics. This chapter contains details on the reconstruction of these objects.

5.1 Electrons

The lightest charged lepton, electrons leave tracks in the ATLAS ID and are typically stopped in the LAr EM calorimeter. Thus the signature is an energy deposit (cluster) in the EM calorimeter with a track from the ID pointing to it.

Electron reconstruction is seeded by clusters, which are found using a sliding window algorithm [52]. The search window size used corresponds to 3×5 cells in $\eta \times \phi$ in the second sampling of the calorimeter, and windows with at least 2.5 GeV of energy are kept. Clusters are then formed with a fixed size of 3×7 cells in $\eta \times \phi$ in barrel and 5×5 in the endcaps. The cluster finding efficiency is essentially 100% for electrons with $p_{\mathrm{T}} > 15$ GeV.[8]

Tracks are reconstructed independently in the ID, with all tracks being fit with a default pion hypothesis. They are extrapolated to the calorimeter and loose track-cluster matching is required in order to form an electron candidate. Specifically, the track must satisfy $\Delta\eta < 0.05$ and an asymmetric requirement of $\Delta\phi$ less than 0.05 or 0.1 with respect to the cluster position.[9] The track matching efficiency is about 99% for electrons with $p_{\mathrm{T}} > 20$ GeV, dropping to about 94% after making require-

[8]For electrons, the actual quantity used is not the p_{T} of the track but rather the transverse energy, E_{T}, of the cluster, as the calorimeter measurement is more precise in the energy range of interest. However, for simplicity, p_{T} is used throughout this thesis.

[9]The distribution of $\Delta\phi$ has a longer tail toward the side where the track bends due to bremsstrahlung, hence the looser requirement.

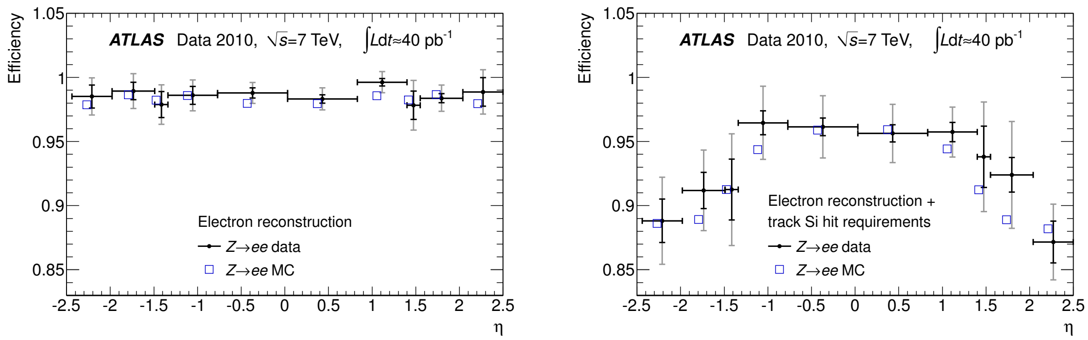

(a) Reconstruction (b) Reconstruction + silicon requirements

Figure 5.1: Efficiency of the electron reconstruction after track matching (left) and after silicon hit requirements on tracks (right), measured in 2010 data and MC.

ments on the number of silicon tracker hits. Figure 5.1 shows the η dependence of these efficiencies, with most of the drop coming at higher $|\eta|$ after requiring silicon hits. In 2011 data, the uncertainty on these efficiencies is about 0.6–1.2% depending on η.

At this basic level, a large number of QCD jets are classified as electron candidates. This can happen if a charged pion is reconstructed as an electron, if a photon conversion (from a π^0 meson decay, for instance) is reconstructed as an electron instead of a photon, or if a real electron is produced in the semi-leptonic decay of a heavy flavor quark (b- or c-quarks). The desired signal is typically from "prompt" decays of particles with short enough lifetimes not to propagate in the detector. These include W and Z bosons, $t\bar{t}$ production, and hypothetical new particles. In order to reduce the unwanted jet contribution, electron identification is applied, consisting of a number of cuts on sensitive variables.

The first category of identification variables is shower shapes. The energy deposits by true electrons in the calorimeters, compared to hadrons, tend to be narrower in the transverse direction and not penetrate as deeply. Thus both transverse and longitudinal variables are used. Because of the longitudinal segmentation of the LAr calorimeter, each sampling layer can be considered individually for transverse shapes, and several variables are constructed from the first and second samplings. Longitudinally, the most important variable is the fraction of cluster energy which has punched through the EM calorimeter and been deposited in the hadronic calorimeter.

Track information is used as well, requiring high quality tracks to reject combinatoric backgrounds. Requirements include a minimum number of hits in each ID subdetector, a cut on the transverse impact parameter (d_0, defined as the distance of closest approach in the transverse plane of the fitted track to the primary vertex), and a hit in the innermost pixel layer (b-layer) to reduce photon conver-

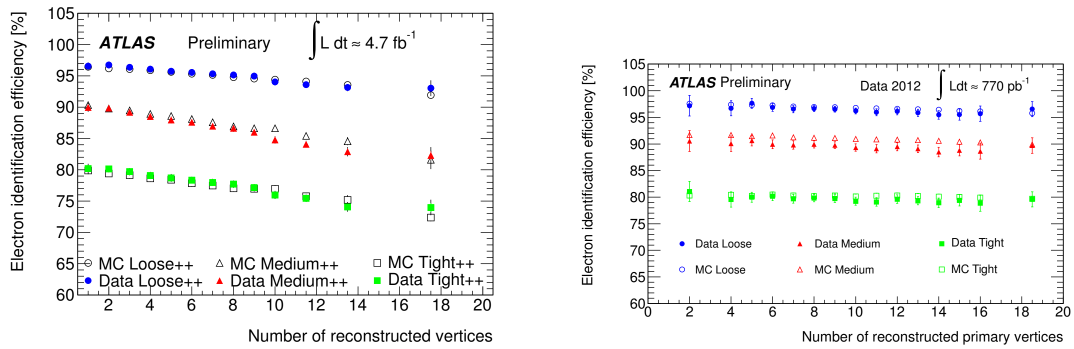

(a) 2011 (b) 2012

Figure 5.2: Efficiency of the electron identification operating points as a function of the number of reconstructed primary vertices, for 2011 (a) and 2012 (b) data and MC. The cut values were re-optimized for 2012 to reduce the pileup dependence. In the text, the 2011 operating points of *Loose++*, *Medium++*, and *Tight++* are referred to simply as *Loose*, *Medium*, and *Tight*.

sion backgrounds. A separate cut explicitly rejects electron candidates which have been reconstructed as photon conversions. Transition radiation from the TRT is used as well to separate electrons from hadrons, as discussed in Section 4.2.1 and described in detail below in Section 5.1.2.

The next class of variables are the track-cluster matching variables which check the compatibility of the two measurements. The track η is compared with η measured in the first LAr sampling, exploiting the fine segmentation. Track ϕ is compared with the cluster ϕ from the second sampling. And the ratio of cluster energy to track momentum (E/p) provides a further discriminant.

The requirements described above form the inputs for the standard electron identification in ATLAS, which has three operating points: *Loose*, *Medium*, and *Tight*.[10] Each tighter operating point adds requirements to the previous, so the objects selected by *Medium* are a strict subset of those selected by *Loose*, and likewise for *Tight*. A full list of the requirements in the *Tight* operating point, which is used in this analysis, is found in [52].

For electrons with p_{T} of 25 GeV, *Loose* has an average efficiency of 95%, compared with 85% for *Medium* and around 75% for *Tight*, with the lower efficiencies being offset by higher background rejection. The efficiencies for each operating point are shown as a function of the number of reconstructed primary vertices[11] (N_{PV}) in Fig. 5.2 for 2011 and 2012. For 2012, the cut values were re-optimized to reduce the pileup dependence. The uncertainty on the *Tight* efficiencies for the 2011 dataset used range from 0.5–2.0% depending on p_{T} and η.

[10] Internally to ATLAS, the *Loose*, *Medium*, and *Tight* discussed here refer to *Loose++*, *Medium++*, and *Tight++* in the 2011 data.

[11] As described later in Section 5.1.3.2, N_{PV} is proportional to the number of additional interactions in the bunch crossing of interest and thus the pileup.

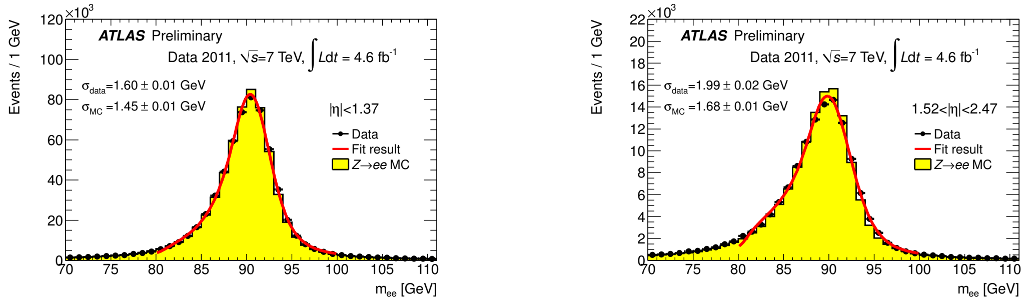

(a) Barrel (b) Endcaps

Figure 5.3: Invariant mass spectra for e^+e^- events showing the $Z \to ee$ peak for pairs of electrons both in the barrel and both in the endcaps. Crystal Ball fits and resulting σ parameters are shown for data and MC.

The electron energy resolution is parametrized by the functional form:

$$\frac{\sigma_E}{E} = \frac{a}{\sqrt{E}} \oplus \frac{b}{E} \oplus c \tag{5.1}$$

where a is the sampling term, b is the noise term, and c is the constant term. The parameters a and b are taken from MC, while the constant term c is measured in data averaged over large detector regions. In 2010 it was found to be about 1.2% in the barrel and 1.8% in the endcaps, with total uncertainties of about 0.6%. The intrinsic resolution should be 0.7% or better and will be achieved through more detailed calibration including finer granularity. The total dielectron resolution in the $Z \to ee$ peak is shown in Fig. 5.3 for the barrel and endcaps and is about 1.6 to 2.0 GeV. The electron energy scale is determined using the $Z \to ee$ peak, resulting in corrections applied to data of up to 0.5% in the barrel and 1.0% in the endcaps. The uncertainty depends on p_{T} and η, ranging from 0.4–1.6%, and through 2011, the energy scale was stable with respect to time and pileup at level of about 0.1%.

The next subsections provide more information about discriminating variables important for this analysis.

5.1.1 Bremsstrahlung Fitting

Electrons traversing the ID often lose energy through bremsstrahlung due to the amount of material. This is shown in Fig. 5.4 as the number of radiation lengths as a function of η, and for the silicon detectors alone (Pixel+SCT) varies from about 0.2–1.0 in the range $0.0 < |\eta| < 2.47$. Hard emissions of bremsstrahlung can make an electron abruptly change direction, in turn reducing the probability that the track will be reconstructed correctly or at all by the default track fitter, a global χ^2 algorithm.

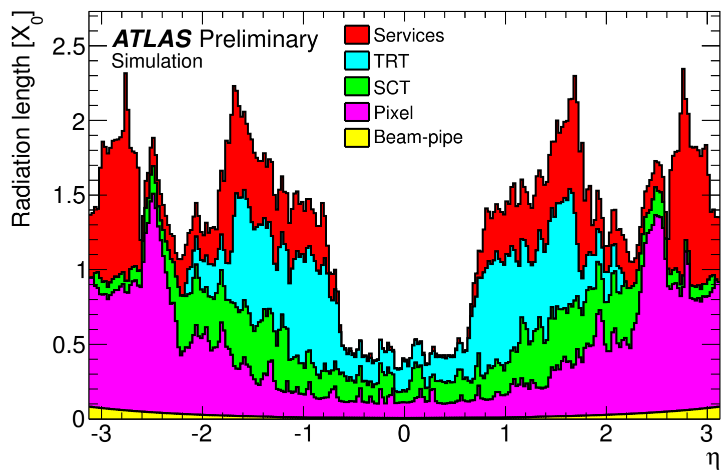

Figure 5.4: Material in the ID, broken down by subsystem, in number of radiation lengths as a function of η.

To account for this effect, electron tracks are refitted with a Gaussian Sum Filter (GSF) algorithm [53], a non-linear generalization of a Kalman Filter [54]. The Kalman Filter is a recursive linear algorithm for signal processing which can be adapted to track fitting. In the Kalman Filter, the track parameters are represented by a state vector. As the track is extrapolated to each new measurement surface, the parameters and associated uncertainties are updated using the measurement and a Gaussian error. The GSF algorithm essentially consists of a number of Kalman Filters running in parallel, each using a Gaussian function to represent a different component of the electron energy loss spectrum.

For this analysis, electron tracks which are already found with the default fitter are refit with the GSF. The primary benefit is that track parameters in the bending plane are improved, including the transverse impact parameter d_0, ϕ, and the transverse momentum p_{T}. Figure 5.5 shows the improvement in d_0 and d_0 significance ($d_0/\sigma(d_0)$) from using the GSF-refitted tracks. The resolution for this quantity is improved,[12] making it a more effective discriminant against heavy flavor semi-leptonic decays and other backgrounds.

[12]Typical values for the estimated error on d_0 in electron track fits are around 20 μm, with a long tail of larger values.

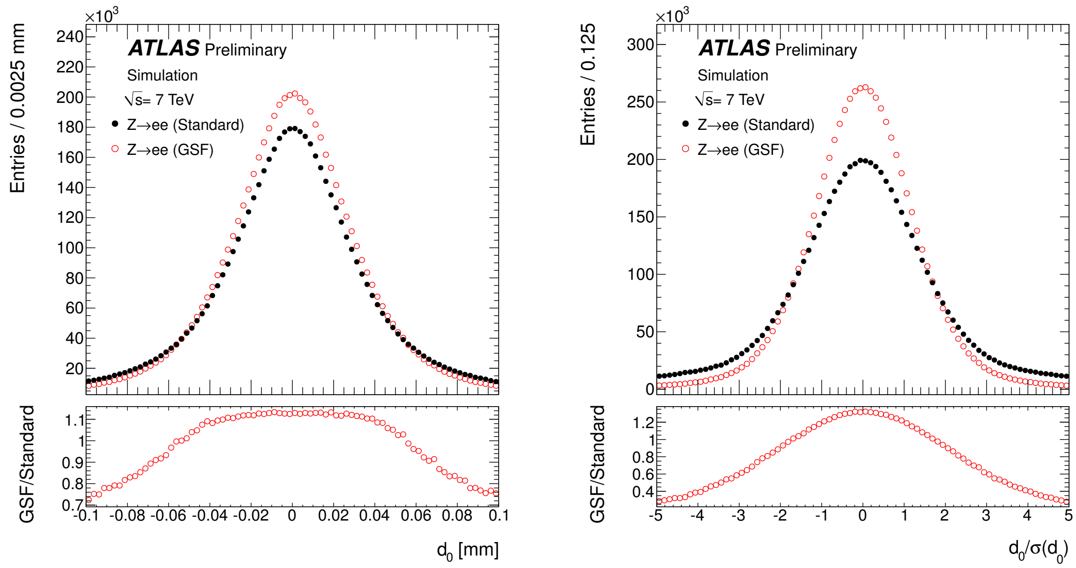

(a) d_0 (b) d_0 significance

Figure 5.5: Distribution of the transverse impact parameter (a) and of the transverse impact parameter significance (b) for both GSF (open red) and standard (solid black) truth-matched MC electrons from Z-boson decays. The bottom plots show the ratio of the entries of the GSF and standard electrons per bin.

5.1.2 Transition Radiation

As described in Section 4.2.1, the TRT provides transition radiation (TR) capabilities to discriminate electrons from charged hadrons [55]. Figure 5.6 shows the observed shapes of the TRT high threshold (HT) hit fraction distribution, normalized to unit area, for electrons and pions in data. Clear separation is seen between these shapes, and the discrimination is quantified in Fig. 5.7, which shows the pion misidentification rate as a function of $|\eta|$ for a cut on the HT fraction with a fixed electron efficiency of 90%. The rejection power depends on $|\eta|$ because of the variation in detector geometry and radiator spacing, and it varies from a factor of about twenty in the barrel to 50–100 in the endcaps. The bin $0.8 < |\eta| < 1.0$ corresponds to the barrel-endcap transition region and is thus not as effective. The TRT can thus provide significant rejection using TR, and this information is largely uncorrelated with the calorimeter cluster. The cut values used in the *Tight* operating point are closer to 95% efficient, varying with $|\eta|$.

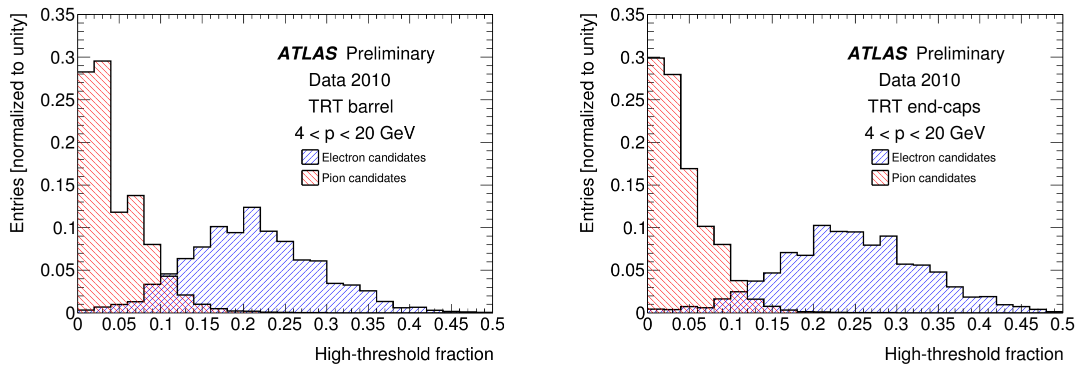

(a) Barrel (b) Endcaps

Figure 5.6: TRT high threshold hit fractions, normalized to unit area, for electrons and pions in data.

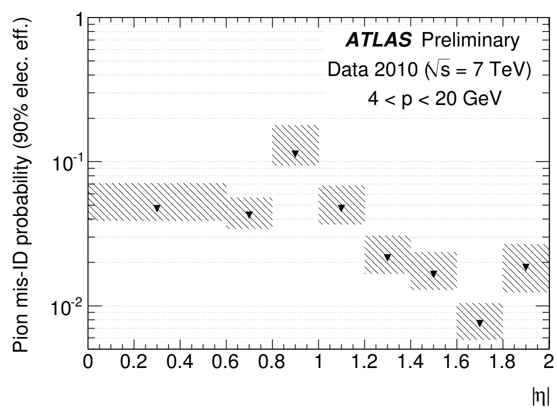

Figure 5.7: Pion misidentification rate as a function of $|\eta|$ for a cut on the HT fraction with a fixed electron efficiency of 90%.

5.1.3 Isolation

A key feature of leptons from electroweak decays, as well as those in many BSM models, is that they are "isolated," i.e. typically separated in $\eta - \phi$ space from other energetic particles in the event. This is exploited experimentally to further reduce backgrounds from QCD jets, including semi-leptonic decays, as these tend to have nearby hadronic activity.

In ATLAS, separate isolation variables are constructed using tracking and calorimeter information. Generally, track isolation is robust against pileup but only includes charged particles, while calorimeter isolation includes charged and neutral energy but is more susceptible to pileup effects. Details on each of these are given below.

5.1.3.1 Track Isolation

Track isolation variables are formed by simply summing the p_T of the charged tracks within a cone of fixed size in ΔR[13] centered around the electron track, typically using $\Delta R < 0.2$, 0.3, or 0.4. The electron track itself is excluded from the sum. A cut of $p_\mathrm{T} > 1$ GeV is applied to the tracks along with tracking quality cuts. The transverse and longitudinal impact parameters of the tracks are also required to be consistent with the primary vertex of the event to reject tracks from pileup interactions, passing cuts of $|d_0| < 1.5$ mm and $|z_0| < 1.0$ mm. These track isolation variables are denoted "ptconeXX," with $\Delta R < 0.\mathrm{XX}$. Figure 5.8 shows the mean of ptcone30 as a function of the number of reconstructed primary vertices for electrons from $Z \to ee$, and no significant dependence is observed, confirming the robustness of these variables.

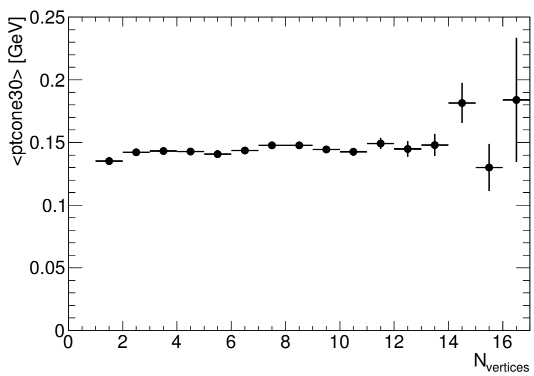

Figure 5.8: Mean of ptcone30 as a function of the number of reconstructed vertices, for electrons from $Z \to ee$. No significant dependence is observed.

5.1.3.2 Calorimeter Isolation

The electron calorimeter isolation variables, "EtconeXX," are formed by summing up the energy of all calorimeter cells, EM and hadronic, within $\Delta R < 0.\mathrm{XX}$ of the electron cluster barycenter. A central core is subtracted out: the cells in the EM calorimeter corresponding to a central core area of 5×7 cells in $\eta \times \phi$ in the second LAr sampling. Figure 5.9 shows a cartoon of the cells included in the isolation sum for Etcone40. Figure 5.10 shows a typical Etcone40 distribution for electrons in data, fit with a Crystal Ball function. In the discussions below, a Crystal Ball distribution, which consists of a Gaussian core with a power law tail, is often fit to the Etcone distribution to extract the peak and width (denoted m0 and sigma, respectively, in Fig. 5.10). Explicitly, the Crystal Ball distribution

[13] $\Delta R = \sqrt{\Delta\eta^2 + \Delta\phi^2}$

is defined as:

$$f_{CB}(x;\sigma,\alpha,n,\mu) = N \cdot \begin{cases} \exp\left(-\frac{(x-\mu)^2}{2\sigma^2}\right) & \text{for } \frac{x-\mu}{\sigma} > -\alpha \\ \left(\frac{n}{n-\alpha^2-\sigma^{-1}(|\alpha|(x-\mu))}\right)^n \exp\left(-\frac{\alpha^2}{2}\right) & \text{for } \frac{x-\mu}{\sigma} \leq -\alpha \end{cases} \tag{5.2}$$

where x represents Etcone, μ is the Gaussian mean, σ the Gaussian width, and α and n control the power-law tail.

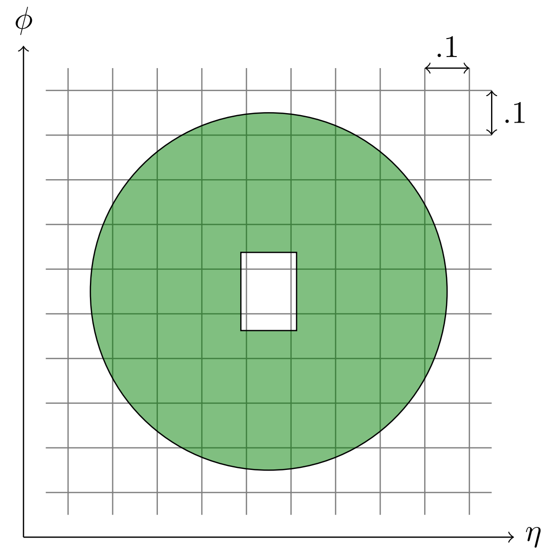

Figure 5.9: The Etcone isolation variables are calculated using calorimeter cells in a cone around the object axis, ignoring a central core of 5x7 cells in (η,ϕ) in the center of the cone. A cone size of $\Delta R = 0.40$ is depicted here.

The Etcone variables suffer undesirable effects from at least two sources, which are discussed in more detail below along with the corrections applied for them. The first of these is residual leakage of the electron object energy into the isolation cone after the central core has been subtracted, and the second is pileup.

5.1.3.2.1 Energy Leakage The Etcone variables exclude a rectangular core of cells centered on the object axis in an attempt to reduce the dependence of the Etcone isolation energy on the object p_{T}. This simple approach is sufficient to remove roughly 95–99% of the object p_{T} from the isolation cone. However, the remaining 1-5% of the object's p_{T} leaks outside this central region, and is almost entirely absorbed into the isolation energy. This leads to a slow growth in the Etcone isolation energy as a linear function of p_{T}.

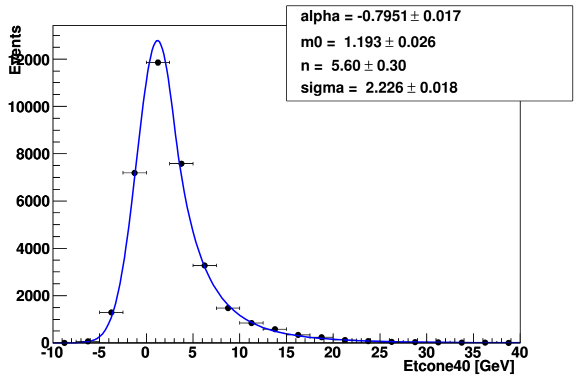

Figure 5.10: A typical Etcone40 distribution for electrons in data from $Z \to ee$, fit using a Crystal Ball function with fit parameters displayed. Leakage corrections, described in the text, have been applied.

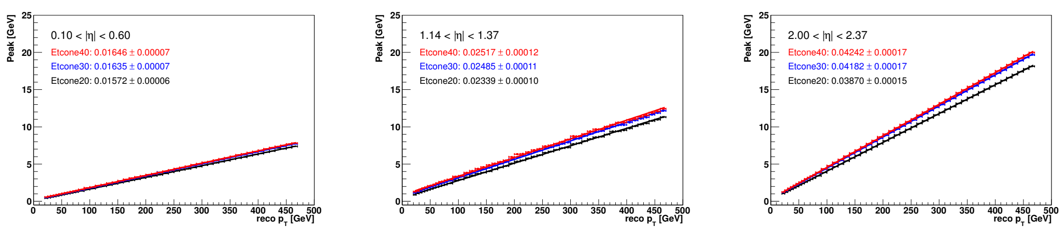

(a) $0.10 < |\eta| < 0.60$ (b) $1.14 < |\eta| < 1.37$ (c) $2.00 < |\eta| < 2.37$

Figure 5.11: Peak of Etcone for different cone sizes as a function of p_{T} in MC single particle events, for different $|\eta|$ bins. The points are fit with linear functions, and the slope parameter is displayed along with its error.

This effect is displayed in Fig. 5.11, which shows the peak of the Etcone distribution for different cone sizes as a function of electron p_{T} in different bins of $|\eta|$, measured in single particle MC.[14] The linear effect is clear, with a strong dependence on $|\eta|$ due to the material upstream of the calorimeter and a weak dependence on the cone size. The points are fit with a linear function, and both the slope and offset of this function are used in a p_{T}-dependent correction. This correction becomes important for electrons with $p_{\mathrm{T}} \gtrsim 100$ GeV, as the measured isolation energy from leakage alone would be at least 1–4 GeV.

5.1.3.2.2 Pileup Particles from interactions other than the hard scatter of interest can contribute to the isolation sum in the Etcone variables. Effects arising from other interactions in the same bunch

[14] In single particle MC, the propagation of just a single particle through the detector is simulated, and it is often used to study expected detector response in detail.

crossing as the hard scattering process are denoted "in-time pileup," while effects from previous bunch crossings are denoted "out-of-time pileup." Typically, in-time pileup increases the energy of the Etcone variables, while out-of-time pileup can increase or decrease it, as is discussed below. Both in-time and out-of-time pileup tend to increase the width of the Etcone distribution.

The effect of in-time pileup is straightforward: particles from additional interactions in the same bunch crossing deposit energy in the calorimeter which is then included in the isolation sum, and the amount of extra energy deposited depends on average on the number of additional interactions. One way of measuring the number of additional interactions is by counting the number of reconstructed primary vertices.[15] Figure 5.12 shows the peak of the Etcone distribution for different cone sizes as a function of N_{PV}. The observed energy increases with N_{PV} as expected, with larger cone sizes more susceptible to pileup. At high values of N_{PV}, the trend becomes nonlinear mostly due to vertex merging as fewer true vertices are reconstructed. The same effect can be seen in Fig. 5.13, which shows N_{PV} as a function of the average number of additional interactions per beam crossing (calculated using the measured luminosity and the pp inelastic cross section).

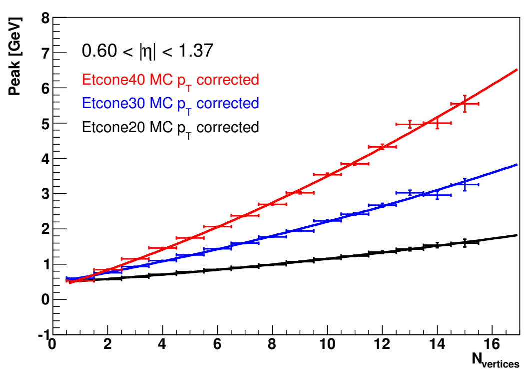

Figure 5.12: Peak of Etcone for different cone sizes as a function of the number of reconstructed vertices for electrons from $Z \to ee$ in 2011 data and MC for a specific $|\eta|$ bin. The points are fit with quadratic functions. Corrections for leakage have been applied.

The energy deposits from previous bunch crossings (out-of-time pileup) can influence the isolation energy in the bunch crossing of interest due to the long LAr calorimeter pulse shaping time. A typical pulse is depicted in Fig. 5.14. It has a sharp peak shortly after the initial deposit, then a long, negative undershoot lasting for $\sim$500 ns after the initial deposit. Because of this long shaping time, energy

[15]The number of reconstructed primary vertices is typically smaller than the true number of additional interactions due to a few effects. Some vertices do not produce enough tracks in the ID acceptance to be reconstructed, while others can "merge" in the reconstruction if the separation in z between the vertices is small. The typical resolution in z for a vertex reconstructed from 70 tracks is about 40 μm and about 80 μm for a vertex reconstructed from 20 tracks [56].

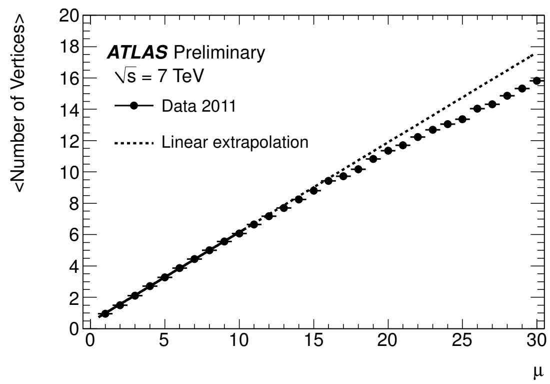

Figure 5.13: Average number of reconstructed primary vertices as a function of the average number of interactions per beam crossing in 2011 data.

deposits from previous bunch crossings within this ∼600 ns window will affect the observed pulse shape and thus measured energy. For bunch crossings $\gtrsim$ 150 ns after an energy deposit, the negative tail will tend to reduce the measured energy. The integral under the pulse shape, however, is 0, so that if the same amount of energy is deposited every N ns, where N $\ll$ 600, the analog sum of the out-of-time pileup will cancel with the in-time pileup, and the effective shift in the measured energy will be 0.

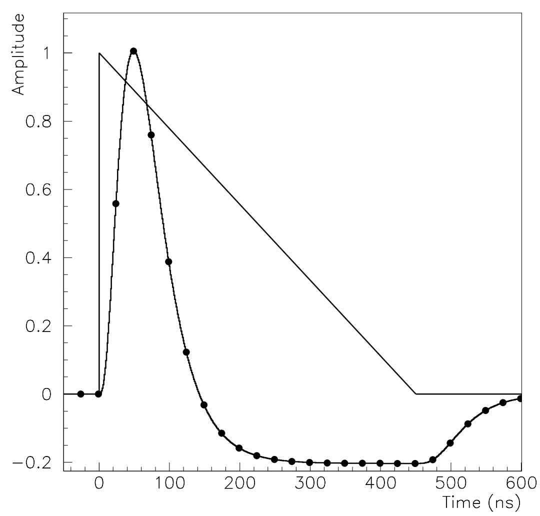

Figure 5.14: Cartoon of a typical pulse shape in the LAr front end electronics. The shaped pulse has a sharp peak followed by a long undershoot.

The actual LHC bunch structure, however, is more complicated than this [43]. The bunches are arranged in “trains” of varying length, partially dependent on the spacing between individual bunches. For most of 2011 and all of 2012, the LHC ran with 50 ns bunch spacing and trains extending up to 144 bunches in length, with large gaps between the trains and small gaps of 200 ns between every 36 bunches. An example of the bunch train structure in 2011 is shown in Fig. 5.15, showing filled bunches as a function of the bunch crossing identifier (bcid). Each bcid represents a 25 ns increment, so 50 ns bunch spacing corresponds to spacing of 2 in terms of bcid. In addition to the finite train length, there are also bunch-to-bunch variations in intensity, so different bunches within a train have varying luminosity.

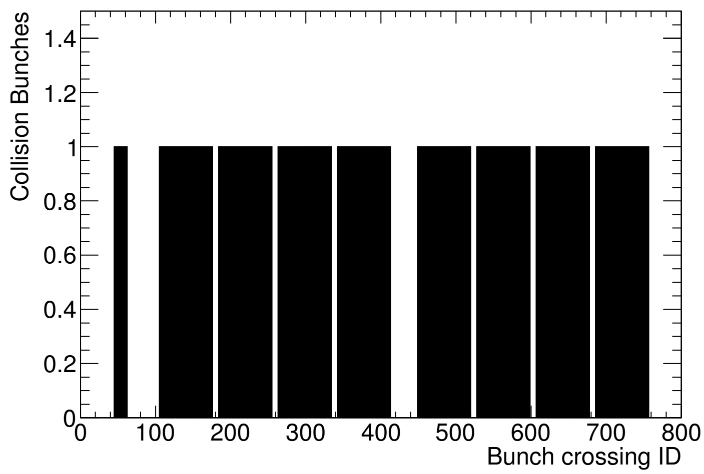

Figure 5.15: Colliding bunches for a typical LHC bunch train structure in the 2011 pp run, shown for the first 800 bunch crossing identifiers. Between around bcid 100 and 420, a large train can be seen with 144 filled bunches and 3 small gaps. The spacing of 2 bcids between each filled bunch cannot be seen on this plot due to the zoom level.

Figure 5.16 shows the impact of this effect, plotting the peak of Etcone40 as a function of bcid for a subset of the LHC bunches. The first bunches in the train, around bcid 100, show a large isolation energy. This comes from constructively adding the large peak in the early part of the signal from Fig. 5.14. For pulses later in the train, from about 500 ns in (about 20 bcids), and before the first small gap, the full cancellation described above takes place on average. After the small gaps, around bcid 190 and 270, there is incomplete cancellation and the peak structure can be seen again, although it is somewhat reduced compared to around bcid 100. Then about 500 ns after the small gaps, complete cancellation occurs again.

Different pileup correction strategies have been tried. In 2011 and for this analysis, the typical

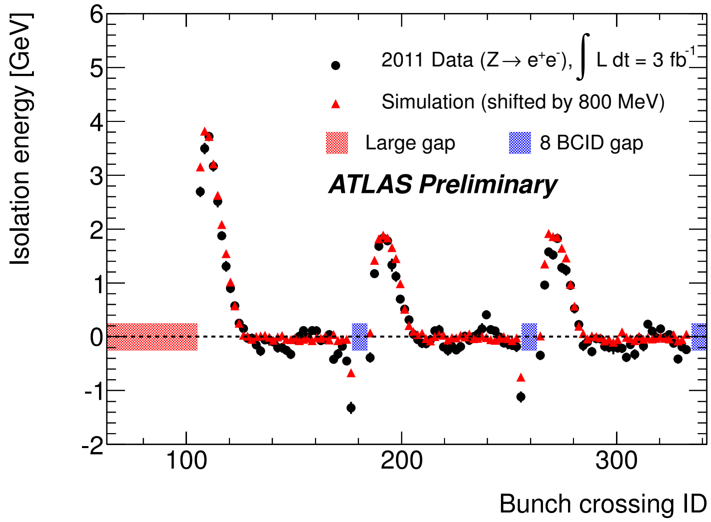

Figure 5.16: Peak of Etcone40 as a function of bunch crossing identifier for electrons from $Z \rightarrow ee$ in 2011 data and MC, for a subset of the LHC bunches. The gaps in the LHC bunch structure are also shown.

correction applied just uses the N_{PV} dependence measured as in Fig. 5.12 and N_{PV} for the event of interest to subtract off an average amount of energy from the isolation cone. This corrects on average for the effect of in-time pileup. No explicit correction was made for out-of-time pileup. Another correction developed in the context of photons and used more for the 2012 data for electrons is the "ambient energy density" correction [57], which attempts to estimate the measured energy density on an event-by-event basis and use this to correct the isolation energy. The out-of-time effect described here is a general issue for the energy measurement for all LAr cells, and for 2012 data, an average correction is now applied to cell energies based on the measured luminosity of each LHC bunch to minimize this.

5.2 Muons

Heavier than electrons, muons interact minimally in the calorimeters and are typically the only charged particles to pass through and leave tracks in the MS. Tracks are reconstructed independently in the ID and MS [58]. In the MS, track segments are first built in each muon station, and these segments are linked to form a track. The MS track is then extrapolated back to the ID, accounting for multiple scattering and energy loss in the calorimeters,[16] matched to an ID track, and in the algorithm used for this analysis, the track parameters are combined statistically using the covariance matrices of each track fit. A muon with matched ID and MS tracks is called a combined muon.

The reconstruction efficiency for combined muons using this algorithm is shown in Fig. 5.17. It is around 96% across most of the detector, with a lower efficiency of about 80% in the very central region, where there are coverage gaps for ID services, and in the barrel-endcap transition regions. It is flat to 1–2% as a function of p_{T} for $p_{\mathrm{T}} > 20$ GeV, and the uncertainty on this measurement is around 1%.

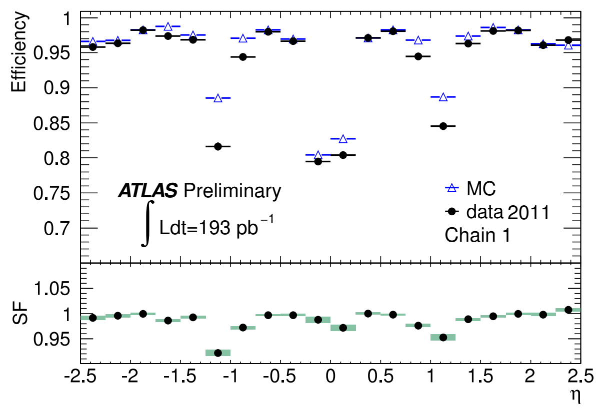

Figure 5.17: Combined muon reconstruction efficiencies for the algorithm used in this analysis, as a function of η.

The single muon momentum resolution ranges from about 2% at 20 GeV to about 10% at 1 TeV, degrading due to finite curvature resolution. The dimuon resolution in the $Z \rightarrow \mu\mu$ peak is shown in Fig. 5.18 and varies from about 1.6–2.5 GeV across η. The differences between data and MC are mainly due to residual misalignments in data. The uncertainty on the momentum resolution is small for the muon p_{T} range considered in this analysis and has a negligible impact.

[16] On average, muons lose about 3 GeV of energy in the calorimeters, so muons below that threshold typically do not make it to the MS.

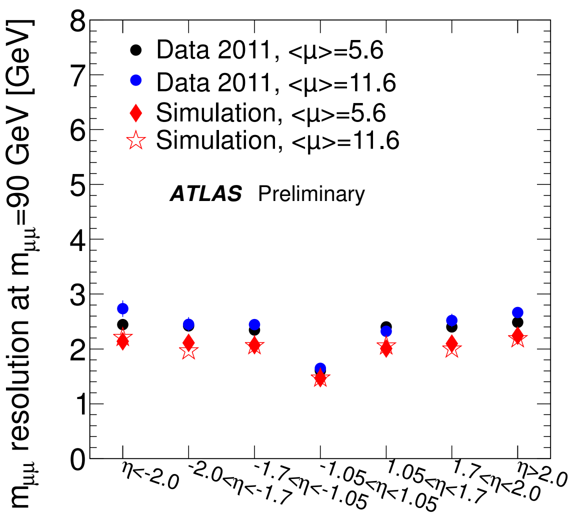

Figure 5.18: Dimuon resolution for the $Z \to \mu\mu$ peak as a function of muon η.

Chapter 6

Analysis Overview

The analysis presented in the following chapters is an *inclusive* search for like-sign dilepton production in excess of SM expectations. Here inclusive means that no requirements are made on the event activity beyond the selected pair of leptons; specifically, there are no cuts based on additional leptons, hadronic activity, or $E_{\mathrm{T}}^{\mathrm{miss}}$. Requirements are placed only on the selected leptons and the mass of the dilepton system. The full selection is described in Chapter 8.

Backgrounds to this search arise from three principal sources: SM production of prompt, like-sign lepton pairs (prompt background); production of opposite-sign lepton pairs where the charge of one lepton is misidentified (charge-flip background) or where a photon produced in association with the opposite-sign leptons converts into an e^+e^- pair; and hadrons or leptons from hadronic decays (non-prompt background).

The prompt background consists mainly of diboson production of $W^{\pm}Z$ and ZZ where both bosons decay leptonically. Other smaller backgrounds come from $t\bar{t}W^{\pm}$ and $t\bar{t}Z$, $t\bar{t}$ production in association with a vector boson, and like-sign W vector boson scattering. These backgrounds are predicted from simulation as described in Chapter 7.

The processes contributing to the charge-flip background are the SM sources of opposite-sign dileptons, dominantly Drell-Yan along with $W^{\pm}W^{\mp}$ and $t\bar{t}$ production with leptonic decays. Conversions of prompt photons are also included in this category, arising from $W\gamma$ and $Z\gamma$ production. These backgrounds are taken from simulation but the normalization is taken from data, as discussed in Section 9.2.

Non-prompt leptons may originate from QCD jets via several sources. For electrons, these include hadrons misidentified as electrons, photon conversions, and semi-leptonic decays of heavy-flavor (b, c) quarks. For muons, these include semi-leptonic b- or c-hadron decays and muons from π and K

mesons that decay in the detector volume. The non-prompt background includes all background processes where at least one of the leptons is non-prompt. The dominant sources are W+jets and QCD multijets with smaller contributions arising from Z+jets and $t\bar{t}$. To assess this background, a data-driven method is employed, as described in Section 9.3.

Systematic uncertainties are assessed in Chapter 10. Data is compared with prediction in Chapter 11, and as no significant deviations from the SM expectations are observed, limits are set on the anomalous production of like-sign lepton pairs in Chapter 12. Chapter 13 presents another interpretation of the same data, a scan in narrow mass bins to search for a resonance using a doubly-charged Higgs boson as the benchmark model. And Chapter 14 describes potential extensions of this analysis.

The internal ATLAS documentation for these analyses can be found in [59] and [60].

Chapter 7

Data and Simulated Samples

This analysis is carried out using the full 2011 ATLAS data sample, corresponding to an integrated luminosity of 4.7 fb^{-1} after data quality requirements. The data were triggered using single lepton triggers, which look for at least one electron or at least one muon. For electrons, p_{T} thresholds of 16 GeV at Level-1 and 20–22 GeV in the HLT were applied, with the latter increasing through 2011 as shown in Table 7.1. To ensure no efficiency loss for electrons with very high p_{T}, a trigger with a threshold of 45 GeV is also used which has no requirement on the hadronic calorimeter energy deposits near the electron in the η-ϕ plane at Level-1. For muons, the p_{T} thresholds were 10–11 GeV at Level-1 and 18 GeV at the HLT.

Table 7.1: Electron trigger evolution through 2011. The ATLAS internal data periods are given, along with the start and end dates (day/month), integrated luminosity, and trigger p_{T} thresholds. All triggers required the *Medium* electron ID. In periods L–M of the 2011 run, the *Medium* ID was tightened with additional requirements, and a requirement on the nearby hadronic calorimeter activity was added to the Level-1 electron trigger.

Run Period	Start Date	End Date	$\int \mathcal{L}dt$	p_{T} Threshold
Periods B–J	21/03/11	04/08/11	1.7 fb^{-1}	20 GeV
Period K	04/08/11	22/08/11	0.6 fb^{-1}	22 GeV
Periods L–M	07/09/11	30/10/11	2.4 fb^{-1}	22 GeV

MC simulation is used to estimate some of the background contributions and to determine the selection efficiency and acceptance for possible new physics signals. The dominant SM processes that contribute to prompt like-sign dilepton production are WZ and ZZ, with smaller contributions from like-sign W production ($W^{\pm}W^{\pm}$) and production of a W or Z boson in association with a top quark pair ($t\bar{t}W$, and $t\bar{t}Z$). These are all estimated using MC simulation. For processes with a Z boson, the contribution from $\gamma^* \to \ell^+\ell^-$ due to internal or external bremsstrahlung of final-state quarks or leptons is also simulated for $m(\ell^+\ell^-) > 0.1$ GeV. Sherpa [61] is used to generate WZ and ZZ events, while $W^\pm W^\pm$, $t\bar{t}W$, and $t\bar{t}Z$ production is modeled using MadGraph [62] for the matrix element and Pythia [63] for the parton shower and fragmentation. The $W^\pm W^\pm$ sample includes the $W^\pm W^\mp W^\pm$ process.

The normalization of the WZ and ZZ MC samples is based on cross sections determined at next-to-leading order (NLO) in QCD with MCFM [64]. The cross sections times branching fractions for $W^\pm Z \to \ell^\pm \nu \ell^\pm \ell^\mp$ and $ZZ \to \ell^\pm \ell^\mp \ell^\pm \ell^\mp$ after requiring two charged leptons (electrons, muons or taus) with the same electric charge and with $p_{\mathrm{T}} > 20$ GeV and $|\eta| < 2.5$, are 372 fb and 91 fb, respectively.

For $t\bar{t}W$ and $t\bar{t}Z$ production, the higher-order corrections are calculated in [65] and [66, 67, 68], respectively. The full higher-order corrections for $W^\pm W^\pm$+2 jets production have not been calculated. However, for parts of the process, the NLO QCD corrections have been shown to be small [69, 70]. Based on this, no correction is applied to the LO cross section.

Opposite-sign dilepton events due to Z/γ^*, $t\bar{t}$, and $W^\pm W^\mp$ production constitute a background if the charge of one of the leptons is misidentified. The Z/γ^* process is generated with Pythia, and the cross section is calculated at next-to-next-to-leading order (NNLO) using PHOZPR [71]. The ratio of this cross section to the leading-order cross section is used to determine a mass dependent QCD K-factor which is applied to the result of the leading-order simulation [72]. Higher-order electroweak corrections (beyond the photon radiation included in the simulation) are calculated using Horace [73, 74], yielding an electroweak K-factor due to virtual heavy gauge boson loops. The production of $t\bar{t}$ is modeled using MC@NLO [75], with Herwig [76] used for parton showering and hadronization. The normalization is obtained from approximate NNLO QCD calculations using Hathor [77]. The production of $W^\pm W^\mp$ is generated using Herwig, and the cross section is normalized to the NLO value calculated with MCFM. The production of $Z\gamma \to \ell\ell\gamma$ and $W\gamma \to \ell\nu\gamma$ constitutes a background if the photon converts to an e^+e^- pair. Alpgen [78] is used to generate $W\gamma$ production, and the cross section is normalized to be consistent with the ATLAS $W\gamma$ cross-section measurement for $p_{\mathrm{T}}(\gamma) > 15$ GeV [79]. The $Z\gamma$ process is implicitly accounted for in simulation of the Z/γ^* process.

In addition, a variety of new physics signals are simulated in order to study the efficiency and acceptance of the selection criteria. Pair production of doubly-charged Higgs bosons ($pp \to H^{\pm\pm}H^{\mp\mp}$) via a virtual Z/γ^* exchange is generated using Pythia for $H^{\pm\pm}$ mass values between 50 GeV and 1000 GeV [13]. Production of a right-handed W boson (W_R) decaying to a charged lepton and a right-handed neutrino (N_R) [36, 80] and pair production of heavy down-type fourth generation quarks (d_4)

decaying to tW are generated using Pythia. Like-sign top-quark pair production can occur in models with flavor-changing neutral currents, e.g. via a t-channel exchange of a Z' boson with utZ' coupling. Since the left-handed coupling is highly constrained by $B_d^0 - \bar{B}_d^0$ mixing [81], only right-handed top quarks (t_R) are considered. A sample is generated with the Protos [82] generator, based on an effective four-fermion operator $uu \to tt$ corresponding to Z' masses $\gg$ 1 TeV [24]. The parton shower and hadronization are performed with Pythia.

Parton distribution functions taken from CTEQ6L1 [83] are used for the MadGraph, Alpgen, and $H^{\pm\pm}H^{\mp\mp}$ samples, and MRST2007 LO** [84] is used for the Pythia and Herwig samples. For the $t\bar{t}$ MC@NLO sample, CTEQ6.6 [85] parton distribution functions are used, while for the generation of diboson samples with Sherpa the CTEQ10 [86] parametrization is used. Uncertainties on the quoted cross sections are discussed in Sections 10.2.1–10.2.3.

The detector response to the generated events is simulated with the ATLAS simulation framework [87] using Geant4 [88], and the events are reconstructed with the same software used to process the data. Simulated minimum bias interactions generated with Pythia are overlaid on the hard scatter events to closely emulate the pileup present in the data. The simulated response is corrected for the small differences in efficiencies, momentum scales, and momentum resolutions between data and simulation, using scale factors and smearing techniques described in later chapters.

Chapter 8

Event Selection

This analysis is carried out using the full 2011 ATLAS data sample. Data quality requirements are imposed, requiring that all relevant subsystems were recording data and had no major problems, giving an integrated luminosity of 4.7 fb^{-1} for this dataset. The events used were triggered with single lepton triggers. For electrons, the trigger threshold increased during 2011 from 20 to 22 GeV, while for muons, the threshold was constant at 18 GeV. The events are required to have the reconstructed primary vertex with the highest $\sqrt{\sum p_{\mathrm{T}}^2}$ value determined with three or more tracks. Leptons are selected using the criteria summarized in Table 8.1 and described in more detail in Sections 8.1–8.3. Then pairs of leptons passing these criteria are formed, as described in Section 8.4. Multiple pairs of like-sign leptons can be selected in a given event (for instance, in the case of $ZZ \to \ell^+\ell^-\ell^+\ell^-$), and each pair is considered in the analysis.

Table 8.1: Summary of selection requirements for electron and muon candidates.

Requirement	Electrons	Muons
Leading p_{T}	25 GeV	20 GeV
Subleading p_{T}	20 GeV	20 GeV
η	$\|\eta\| < 2.47$ excluding $1.37 < \|\eta\| < 1.52$	$\|\eta\| < 2.5$
Impact Parameters	$\|d_0\| < 1.0$ mm $\|d_0\|/\sigma(d_0) < 3$ $\|z_0 \sin\theta\| < 1.0$ mm	$\|d_0\| < 0.2$ mm $\|d_0\|/\sigma(d_0) < 3$ $\|z_0 \sin\theta\| < 1.0$ mm
Isolation	Track and calo isolation $\Delta R(e, \text{jet}) > 0.4$	Track isolation $\Delta R(\mu, \text{jet}) > 0.4$
Specific Cuts	*Tight* ID Object quality in LAr GSF-refitted	Combined muon Hit quality in ID $Q_{ID} == Q_{MS}$

8.1 Electron Selection

For electrons the trigger threshold of $p_{\mathrm{T}} > 22$ GeV in the later part of the 2011 run dictates the analysis threshold of $p_{\mathrm{T}} > 25$ GeV for the leading lepton,[17] while the subleading is required to have $p_{\mathrm{T}} > 20$ GeV. The η range $|\eta| < 2.47$ is used, excluding the calorimeter transition region of $1.37 < |\eta| < 1.52$ where electrons are poorly measured.

Electrons are required to pass the *Tight* ID described in Section 5.1 and are refitted with the GSF algorithm as described in Section 5.1.1. Object quality cuts are applied to reject clusters from calorimeter noise.

The impact parameter requirements, defined with respect to the primary vertex in the event, are $|d_0| < 1.0$ mm, $|d_0|/\sigma(d_0) < 3$, and $|z_0 \sin\theta| < 1.0$ mm. The first is the cut applied in *Tight* and was not further optimized, but the cut on $|d_0|/\sigma(d_0)$ was optimized as described below. The cut on $|z_0 \sin\theta|$ was chosen to be as tight as possible while maintaining very high efficiency, to reject potential beam backgrounds.

Both track and calorimeter isolation cuts are applied, using the variables described in Section 5.1.3. The track isolation requirement is ptcone30/$p_{\mathrm{T}} < 0.1$, and the calorimeter isolation requirement is Etcone20 < 3 GeV + (p_{T} - 20 GeV) $\times$ 0.037, where the calorimeter isolation has been corrected for leakage and pileup. The optimization of these cuts is described below. Separation from jets of $\Delta R(e, \mathrm{jet}) > 0.4$ is also required, with the jet selection described below in Section 8.3.

In data, the electron energy is scaled as described in Section 5.1, and in MC, the electron energy is smeared to reproduce the larger resolution observed in data. Scale factors are also applied in MC to match the electron efficiency measured in data. The scale factors for the electron reconstruction, *Tight* ID, and trigger efficiencies are standardized and provided by the ATLAS electron/photon combined performance group (e/gamma). They vary from about 0.99 to 1.03 depending on the electron η and 0.95 to 1.0 depending on p_{T}. The efficiency and scale factors for the impact parameter and isolation cuts are measured for this analysis and are given below in Section 8.1.2.

8.1.1 Electron Cut Optimization

The impact parameter cuts, particularly $|d_0|/\sigma(d_0) < 3$, help to reject backgrounds from non-prompt electrons and charge-flip. The shapes of $d_0/\sigma(d_0)$ for prompt, charge-flip, and heavy flavor decay electrons are shown in Fig. 8.1 for GSF electrons in MC. Both charge-flip and heavy flavor decay electrons have wider distributions with longer tails. Figure 8.2 shows the prompt electron efficiency

[17] The efficiency for the $p_{\mathrm{T}} > 22$ GeV cut reaches a plateau at about 25 GeV in the offline calibrated p_{T}.

versus the rejection of charge-flip and heavy flavor electrons cutting on $|d_0|/\sigma(d_0)$, for both standard and GSF electrons, for a single electron selection. In this type of plot, one looks to maximize both prompt electron efficiency and background rejection, so points further to the top and right are more optimal. This figure shows that the GSF track fit clearly improves the effectiveness of this cut with respect to both backgrounds considered.

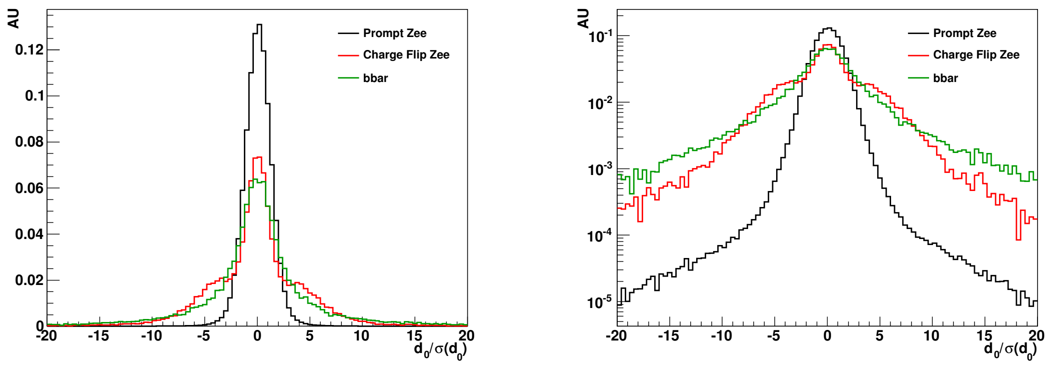

(a) Linear y-axis (b) Log y-axis

Figure 8.1: Shapes of $d_0/\sigma(d_0)$ for GSF-refitted prompt electrons, charge-flip electrons, and electrons from heavy flavor decays, taken from MC, after *Medium* selection. The left shows a linear scale while the right shows a log scale.

The chosen calorimeter isolation cut was motivated as follows. A small cone size (20) was chosen to minimize the impact of pileup as well as potential radiative effects at very high p_{T}. With the leakage correction applied, the calorimeter isolation is independent of p_{T} for signal electrons to first order, but strong dependence remains for fakes. As this is an inclusive search and not optimized for a specific p_{T} range, a sliding cut was adopted to reject more background at lower p_{T} and become highly efficient at high p_{T}. Instead of using a typical cut on Etcone20/p_{T} which loosens very quickly as p_{T} increases, a sliding cut with a smaller slope and an offset from zero is used. To study the isolation cut, single electron samples from data are used. For signal, electrons from W decays are selected using a standard set of cuts, and background (QCD jets) is selected by using a reverse selection based on the TRT high threshold. Figure 8.3 shows a histogram of the isolation variable versus p_{T} with the chosen analysis cut. Then Fig. 8.4 shows a histogram and profile for the background sample, again with the analysis cut. It is this p_{T} dependence of the background that motivates the specific slope used.

To gain additional rejection at low p_{T}, where most of the fakes arise, a sliding cut on track isolation cut is used. The ptcone variables for electrons include cuts on $|d_0|$ and $|z_0|$ as part of the track selection, making them relatively insensitive to pileup conditions. Given this, cone sizes of 20,

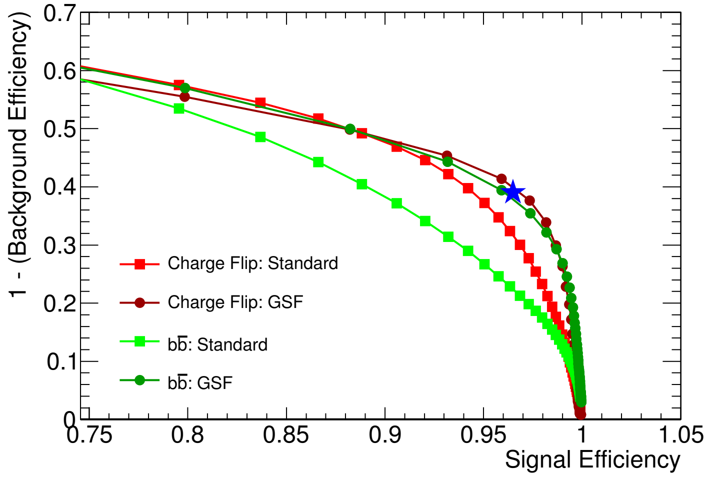

Figure 8.2: Efficiency for prompt electrons versus rejection of charge-flips (red) and electrons from heavy flavor decays (green) for cutting on $d_0/\sigma(d_0)$, taken from MC, after *Medium* selection. The lighter curves show the performance of this cut for the standard electron reconstruction while the darker curves show the performance for the GSF-refitted electrons. The blue star shows the operating point selected for this analysis. The efficiencies and rejections shown are for a single electron selection.

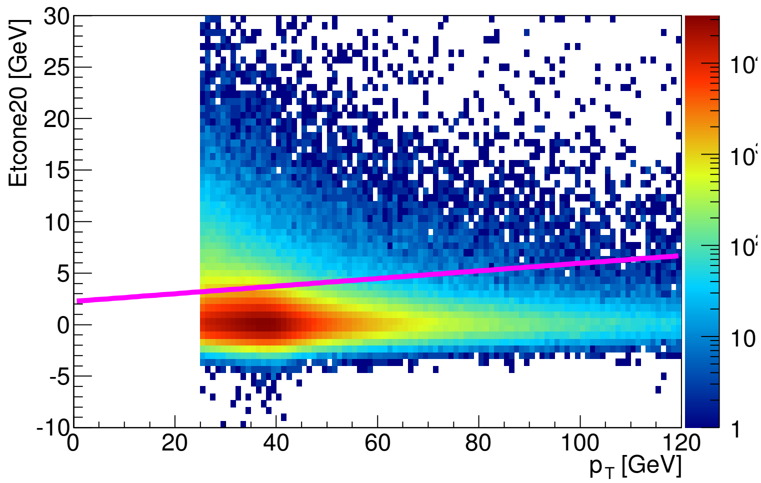

Figure 8.3: Histogram of isolation energy versus p_{T} for electrons from W decays. The analysis cut is shown as a purple line.

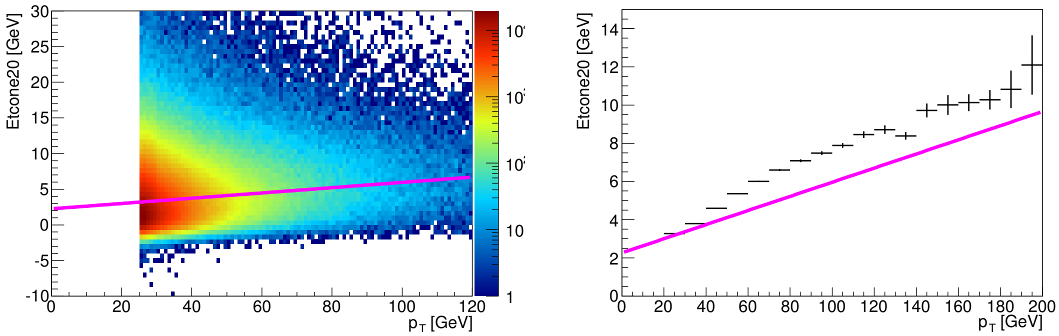

(a) Histogram (b) Profile

Figure 8.4: Histogram (a) and profile (b) of isolation energy versus p_{T} for background electrons, using the selection described in the text. The analysis cut is shown as a purple line.

30, and 40 were considered, and a cut on ptconeXX/p_{T} was optimized to reject heavy flavor electron background at the analysis p_{T} threshold of 20 GeV. The resulting single object efficiency and rejection curves from this MC study are shown in Fig. 8.5, after the cut on calorimeter isolation. Cone sizes of 30 and 40 perform equally well. The smaller cone size is used, with a cut of ptcone30/$p_{\mathrm{T}} < 0.1$. The shape of this distribution for Z MC and $b\bar{b}$ MC is shown in Fig. 8.6, after the other analysis cuts including calorimeter isolation.

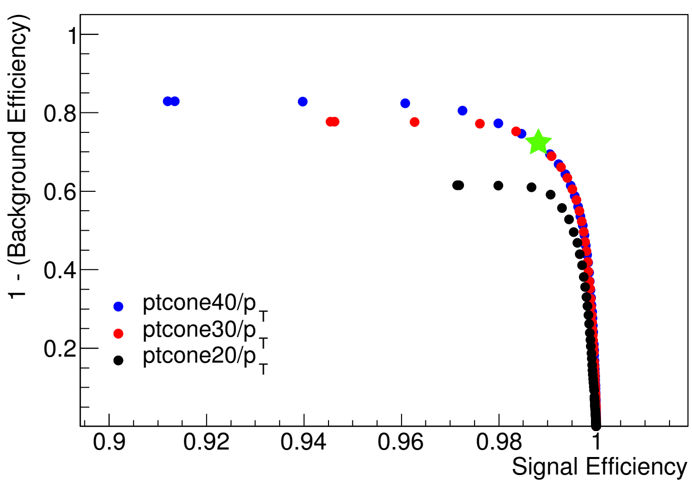

Figure 8.5: Efficiency versus heavy flavor rejection for cutting on ptconeXX/p_{T}. Efficiency is taken from Z MC while the rejection is taken from $b\bar{b}$ MC. The other analysis cuts, including calorimeter isolation, are already applied, and an p_{T} threshold of 20 GeV is used. The green star shows the operating point selected for this analysis.

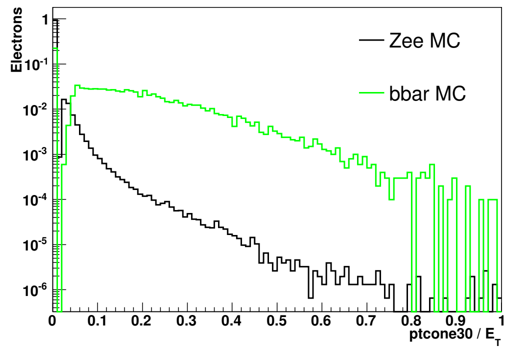

Figure 8.6: Shapes of ptcone30/p_{T} for electrons from Z MC and $b\bar{b}$ MC, showing the clear separation.

8.1.2 Electron Efficiency

The efficiency of the additional electron requirements beyond *Tight* (impact parameters and isolation) are computed using a tag-and-probe technique on $Z \to ee$. In this technique, strict requirements are placed on one lepton (the "tag") and the dilepton system to obtain a pure sample, then the other lepton (the "probe") is studied using an unbiased selection for the measurement of interest. For this case of computing efficiencies relative to *Tight*, both the tag and the probe are required to pass *Tight*, they are required to have opposite electric charge, and the dielectron system must have an invariant mass in the Z mass window ($80 < m(ee) < 100$ GeV). With this selection, the background from QCD multijets has been shown to be negligible.

The resulting efficiencies for these additional cuts are shown in Fig. 8.7 as functions of η (averaged over p_{T}) and p_{T} (averaged over η). The efficiency versus η varies between 94–96%, with the largest inefficiencies coming from the $|d_0|/\sigma(d_0)$ and calorimeter isolation cuts. The efficiency rises versus p_{T} from about 93% to 96%, effectively reaching a plateau above 50 GeV. There is a small ($\sim$1%) efficiency drop observed due to the $|d_0|/\sigma(d_0)$ cut, but this and the other cuts are checked to higher p_{T} in simulation in Fig. 8.8 with no drop seen. Thus the slight decrease in efficiency seen in data is believed to be related to the kinematics of $Z \to ee$ decays.

The same measurement is done in an MC $Z \to ee$ sample, and the ratio of the data efficiency to the MC efficiency is taken as a scale factor to apply to be applied to MC. The resulting scale factors are shown in Fig. 8.9. As a function of p_{T}, they are compatible with 1 with a maximum variation of less than 1%, and versus η there are total variations of up to about 1%. The scale factors are also computed versus pileup sensitive variables including N_{PV} and are observed to be flat to within 1%.

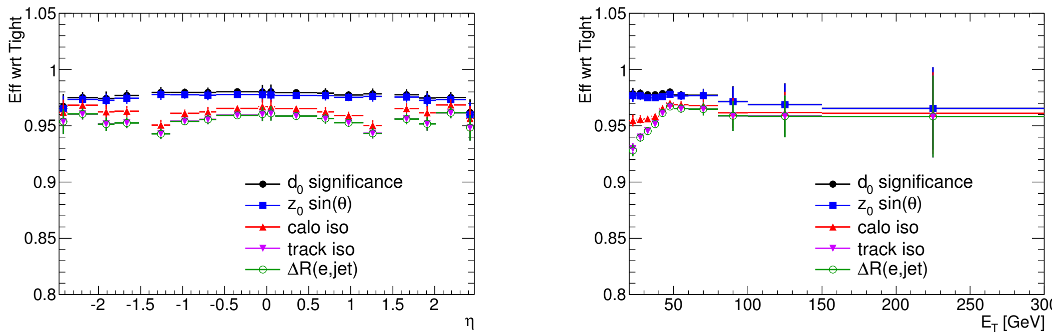

(a) (b)

Figure 8.7: Electron efficiency wrt. *Tight* versus η (a) and p_{T} (b) measured in data using Z tag-and-probe, for the additional selection cuts used in this analysis.

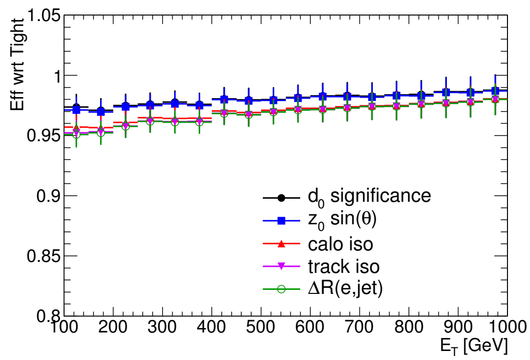

Figure 8.8: Electron efficiency wrt. *Tight* versus p_{T} measured in MC using a simulated high-p_{T} sample, for the additional selection cuts used in this analysis.

The η variation is used for these scale factors and additional systematics of 1% are assigned to cover the variation with p_{T} and pileup.

The scale factors in Fig. 8.9 apply for all MC samples using full ATLAS simulation, which includes all backgrounds in this analysis and some of the signal models. Some of the signal models are simulated using the ATLAS fast simulation AtlFastII (AF2), which has slightly different performance. The scale factors for different MC production campaigns and for full vs fast simulation are shown in Fig. 8.10. Differences of about 1% are observed between full and fast simulation (the black and red points), so separate scale factors are used for the fast simulation samples, with again an additional systematic uncertainty of 1% assigned. The reason for this difference is an observed shift in the calorimeter isolation distribution, depicted in Fig. 8.11, which causes the applied cut to be more efficient in fast

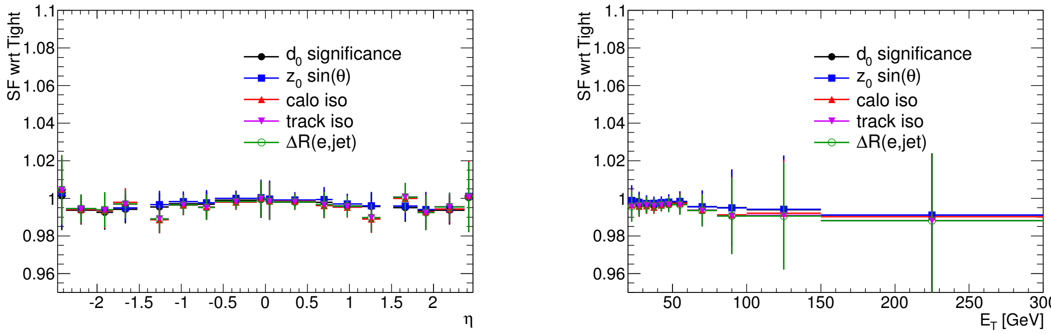

(a) (b)

Figure 8.9: Electron scale factors wrt. *Tight* versus η (a) and p_{T} (b) measured using Z tag-and-probe, for the additional selection cuts used in this analysis.

simulation.

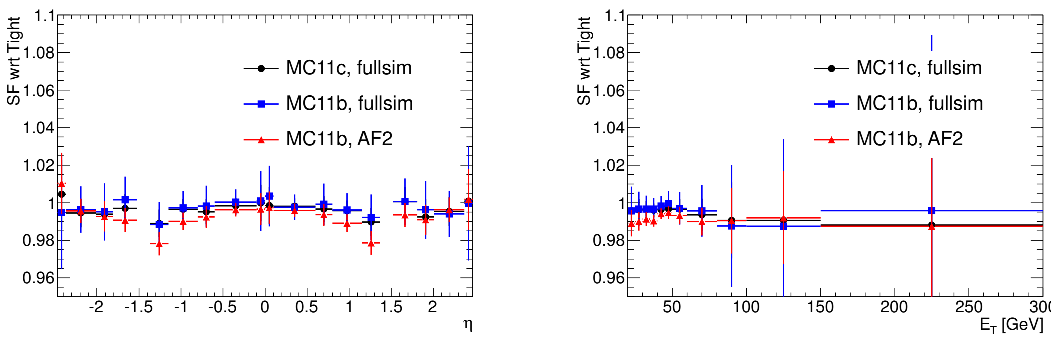

(a) (b)

Figure 8.10: Electron scale factors wrt. *Tight* versus η (a) and p_{T} (b) measured using Z tag-and-probe, for the additional selection cuts used in this analysis, compared for MC samples using different simulations.

8.2 Muon Selection

For muons the trigger threshold of $p_{\mathrm{T}} > 18$ GeV allows an analysis cut of $p_{\mathrm{T}} > 20$ GeV for both leading and subleading muons.[18] The η range $|\eta| < 2.5$ is used. Only combined muons are used, and track quality cuts are applied to the ID track to ensure it is well-reconstructed. The electric charge

[18]In previous iterations of this analysis, a subleading p_{T} requirement of 10 GeV was considered. But it was not motivated by any particular signal model, and the lower threshold significantly increased the non-prompt background, so 20 GeV was chosen.

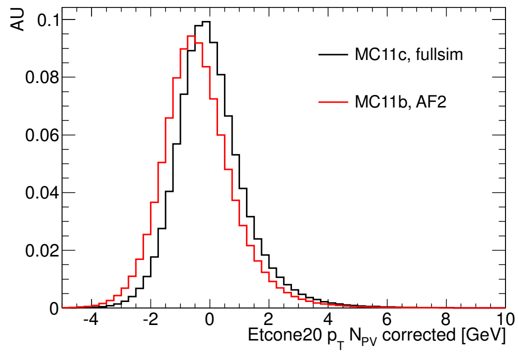

Figure 8.11: Comparison of the calorimeter isolation variable used for electrons between full simulation and AtlFastII MC samples.

measured from the tracks in the ID and MS is required to agree, and combining these independent measurements reduces charge misidentification to a negligible level.

The impact parameter requirements are $|d_0| < 0.2$ mm, $|d_0|/\sigma(d_0) < 3$, and $|z_0 \sin\theta| < 1.0$ mm. These cuts are chosen to be as tight as possible while maintaining a very high efficiency. Again the transverse impact parameter cuts primarily reject muons from heavy flavor decay, while the longitudinal impact parameter helps to protect against cosmic rays and beam backgrounds. After applying these cuts, the background from cosmic ray muons is found to be negligible.

Track isolation is applied, with different cuts depending on the muon p_{T}. For $p_{\mathrm{T}} < 100$ GeV, the requirement is ptcone40/$p_{\mathrm{T}} < 0.06$, while for $p_{\mathrm{T}} > 100$ GeV, the cut is ptcone40 $< (4+0.02\times p_{\mathrm{T}})$ GeV. The cut at higher p_{T} helps to reject background while maintaining high efficiency. Separation from jets of $\Delta R(\mu, \mathrm{jet}) > 0.4$ is required, with the jet selection described in Section 8.3.

The muon momentum measurement in MC is smeared by a few percent or less, depending on η, to reproduce the broader resolution observed in data.

8.2.1 Muon Efficiency

The efficiency of the muon requirements on impact parameters and isolation are computed using a tag-and-probe technique on $Z \to \mu\mu$, similar to electrons. Events with two opposite-sign muons are selected, and the invariant mass of the two muons is required to fulfill 81 GeV$< m(\mu\mu) < 101$ GeV. The tag muon is required to pass all requirements listed above for muons except the requirement that $\Delta R(\mu, jet) > 0.4$. The other muon acts as the probe.

The efficiency of the additional cuts from measurement in data is shown in Fig. 8.12 versus η and

$p_{\rm T}$. As a function of η, the total efficiency ranges from about 93–95%, with the largest inefficiency and η dependence coming from the track isolation requirement. As a function of $p_{\rm T}$, the efficiency increases from about 85% at 20 GeV to 97% at 60 GeV, dropping back to about 95% above 150 GeV. Again the track isolation cut shows the largest $p_{\rm T}$ dependence, and is intentionally tight at lower $p_{\rm T}$ to reject non-prompt background. The evolution of the efficiency at very high $p_{\rm T}$ is checked in simulation and shown in Fig. 8.13, which shows that the efficiency remains flat.

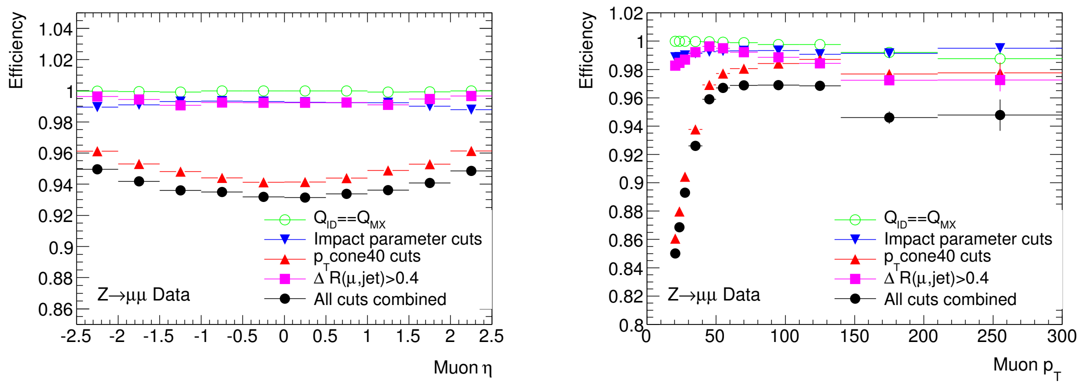

(a) (b)

Figure 8.12: Muon efficiency with respect to combined muons in data as a function of η (a) and $p_{\rm T}$ (b).

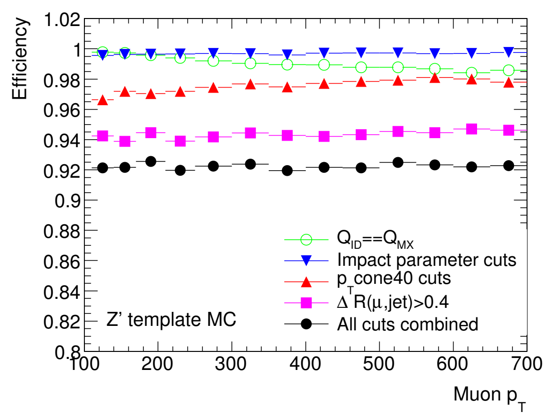

Figure 8.13: Muon efficiency versus $p_{\rm T}$ measured in MC using a simulated high-$p_{\rm T}$ sample.

The efficiencies are measured in a $Z \to \mu\mu$ MC sample as well, and the ratio of the data efficiency to the MC efficiency is taken as a scale factor to apply to be applied to MC. The resulting scale factors are shown in Fig. 8.14. The are flat in η, and versus $p_{\rm T}$, they range between about 0.97 and 0.99.

Due to poor statistics, the scale factor is assumed to be 0.99 above 110 GeV, and a 2% uncertainty is assigned to cover the observed deviations.

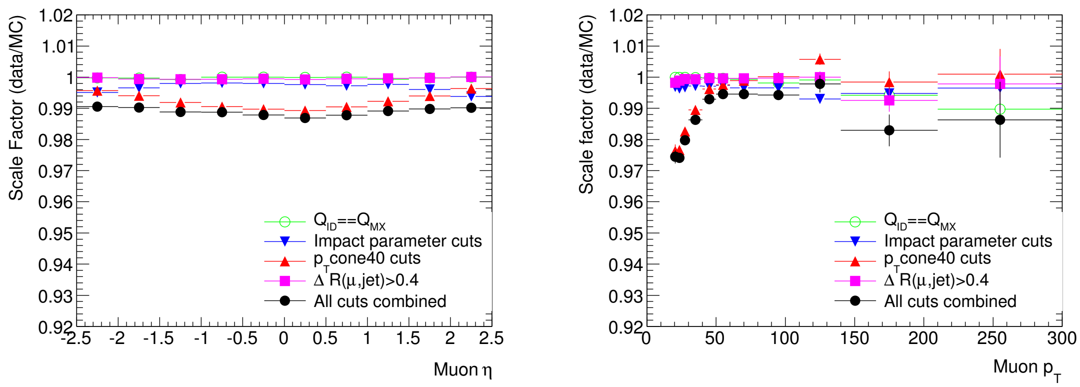

(a) (b)

Figure 8.14: Muon scale factors (efficiency in data divided by efficiency in MC) as a function of η (a) and p_{T} (b).

8.3 Jet Selection Details

Jet candidates are reconstructed from topological clusters in the calorimeter [89] using the anti-k_t algorithm [90] with a distance parameter of 0.4. Their energies are corrected for calorimeter non-compensation, energy loss in upstream material, and other instrumental effects. Furthermore, quality criteria are applied to remove reconstructed jets not arising from hard-scattering interactions [91]. Jets are required to have $p_{\mathrm{T}} > 25$ GeV, $|\eta| < 2.8$, and 75% of the momentum of the tracks within the jet must originate from the primary event vertex.

Electrons are also reconstructed as jet candidates, so any jet within a distance $\Delta R < 0.2$ of a candidate electron is discarded to avoid counting the electron as a jet. Electrons and muons are then required to be separated by $\Delta R > 0.4$ from any jet with $p_{\mathrm{T}} > 25$ GeV $+ 0.05 \times p_{\mathrm{T}}(\ell)$. Due to the overlap removal for electrons, this requirement has negligible impact, but for muons, it helps to reject non-prompt muons from hadronic decays.

8.4 Pair Selection

Pairs of leptons (ee, $e\mu$, $\mu\mu$) are formed from leptons fulfilling these requirements, with the leading and subleading p_{T} thresholds given above. At least one lepton is required to be matched to a trigger lepton which fired the single lepton trigger (within $\Delta R < 0.15$), and if this lepton is an electron, it is required to have $p_{\mathrm{T}} > 25$ GeV to be on the trigger efficiency plateau. In the $e\mu$ channel, electron tracks must not be within $\Delta R < 0.05$ of a muon track.

The invariant mass of the lepton pair, $m(\ell\ell)$, is required to be greater than 15 GeV to avoid low mass resonances. In the ee channel, the mass range $70 < m(ee) < 110$ GeV is also removed, with this used as a control region to measure the charge-flip background.

Lepton pairs are divided into like-sign (LS) and opposite-sign (OS), with the former constituting the signal region for this analysis and the latter being used as a control region. Further control regions are defined to validate the various background predictions; these are described in Chapter 9.

Chapter 9

Background Estimation

As outlined earlier in Chapter 6, the main backgrounds to this search come from SM sources of prompt like-sign (LS) leptons, charge-flips and conversions for electrons, and non-prompt leptons. Each of these is covered in detail below, along with the control regions in data used to validate the modeling of each.

9.1 Prompt Leptons

The prompt LS dilepton backgrounds are taken from MC, using the generators and normalizations described in Chapter 7. Although not directly used in the analysis, the regions with two prompt opposite-sign (OS) leptons provides a sanity check on the modeling of prompt backgrounds. They test the trigger and reconstruction efficiencies, as well as the lepton momentum scale and resolution. For the ee and $\mu\mu$ channels over the full mass range, and for the $e\mu$ channel at low mass, this control region is dominated by Z/γ^* production. At high mass in the $e\mu$ channel, $t\bar{t}$ production is the largest contribution. The total event yields for this control region are given in Table 9.1. The observed number of events in data is higher than the MC prediction by 3%, 4%, and 7% in the ee, $\mu\mu$, and $e\mu$ channels respectively, which is within the uncertainties assigned for the MC cross sections and luminosity.

The invariant mass distribution for each channel is shown in Fig. 9.1, and the p_{T} and η distributions of the leading and subleading leptons are shown for ee (Fig. 9.2), $\mu\mu$ (Fig. 9.3), and $e\mu$ (Fig. 9.4). The agreement in the shape of the mass distribution is good for the ee and $\mu\mu$ channels, while there is a deficit in the Drell-Yan prediction for the $e\mu$ channel. The lepton η shapes also agree well with prediction in the ee and $\mu\mu$ channel and fairly well in $e\mu$. There are some disagreements in the shapes of the p_{T} distributions in all three channels in regions dominated by Drell-Yan production, and these

Table 9.1: Observed and expected number of lepton pairs for the control region with opposite-sign, isolated leptons. The errors include both statistical and systematic uncertainties.

Process	Number of lepton pairs
ee	
Drell-Yan	932000 ± 61000
$t\bar{t}$	2720 ± 320
Non-prompt	1490 ± 64
WW	596 ± 76
WZ	840 ± 110
ZZ	519 ± 66
$W\gamma$	44.9 ± 8.5
$t\bar{t}W$	5.9 ± 3.0
$t\bar{t}Z$	9.5 ± 4.8
Total Prediction	938000 ± 62000
Observation in data	968973
$\mu\mu$	
Drell-Yan	1580000 ± 108000
$t\bar{t}$	3840^{+323}_{-423}
Non-prompt muons	1750 ± 563
WW	988 ± 128
WZ	1290 ± 166
ZZ	824 ± 106
$t\bar{t}W$	7.2 ± 3.6
$t\bar{t}Z$	12.0 ± 6.1
Sum of predictions	1590000 ± 109000
Observation in data	1655557
$e\mu$	
Drell-Yan	3525 ± 289
Non-prompt	489 ± 153
$t\bar{t}$	6473 ± 667
WW	1521 ± 186
WZ	214 ± 26
ZZ	53.0 ± 6.6
$W\gamma$	69.4 ± 13.4
Wt	694 ± 52
$t\bar{t}W$	13.3 ± 6.7
$t\bar{t}Z$	8.1 ± 4.1
Total of predictions	13060 ± 770
Observation in data	13979

are largely due to the Z-boson p_{T} spectrum being different in data and MC. The impact of correcting for this was found to be negligible in the LS signal region and so no correction is applied here.

Based on the kinematic distributions, the disagreement in the yield for the $e\mu$ channel stems mainly from an under-prediction of the Z/γ^* background, which is dominated by $Z \to \tau\tau$ in this control region. However, in the signal region, the contribution of $Z \to \tau\tau$ is small. There is a significantly larger contribution to the signal region from $Z\gamma$ (also classified as Drell-Yan production in this thesis), where the γ radiates from an initial-state quark or final-state lepton and subsequently converts to two electrons. The $Z\gamma$ process does not contribute significantly to the opposite-sign control region. Because of the different processes expected to contribute in the control and signal regions, no correction or systematic associated with the disagreement in the opposite-sign $e\mu$ control region is applied.

9.2 Charge-flips and Conversions

Standard Model sources of opposite-sign leptons, mainly Drell-Yan but also $W^{\pm}W^{\mp}$ and $t\bar{t}$ production, may contribute to the like-sign region if the charge of one of the leptons is incorrectly reconstructed. There are two primary methods by which this can occur.

The first, affecting only electrons, is due to material effects. A diagram of the bremsstrahlung process followed by a photon conversion is shown in Fig. 9.5. This can occur when a high-momentum photon is radiated through bremsstrahlung and converts into an e^+e^- pair. Electron candidates are rejected if they are associated with a reconstructed photon conversion vertex. However, for asymmetric conversions, sometimes only one of the tracks is reconstructed and its charge may be different from the charge of the original electron that radiated the photon.

The second source affects both electrons and muons and can occur for high-momentum tracks when the tracking detector is unable to determine the curvature of the track. This effect is significantly reduced for muons by the requirement that the charges measured in the ID and MS must agree, and for electrons, it is small compared to the material effects.

The following sections describe the measurement of the total charge-flip rate for electrons then muons, as well as the application of these rates to predict this background and its uncertainty.

9.2.1 Electron Charge-flips

The electron charge-flip background is predicted from MC by selecting LS pairs of electrons in Drell-Yan, $W^{\pm}W^{\mp}$, and $t\bar{t}$ MC samples. A scale factor is applied based on the η of the electron which has

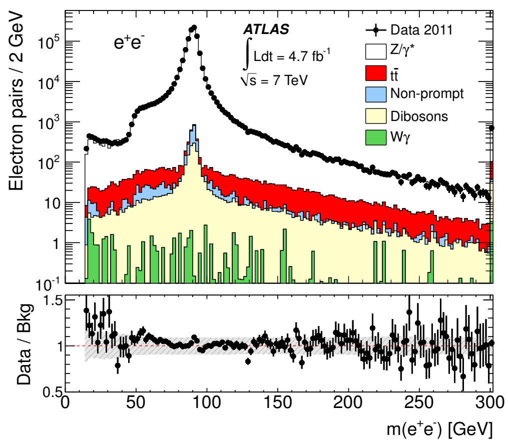

(a)

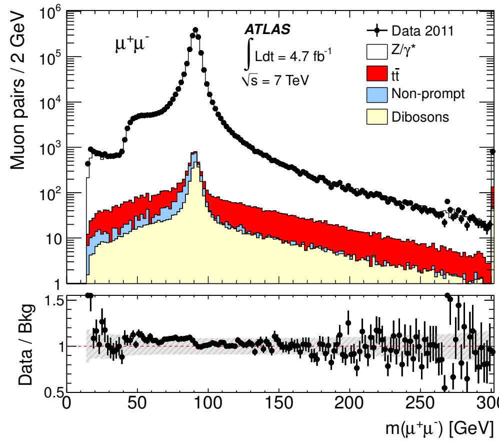

(b)

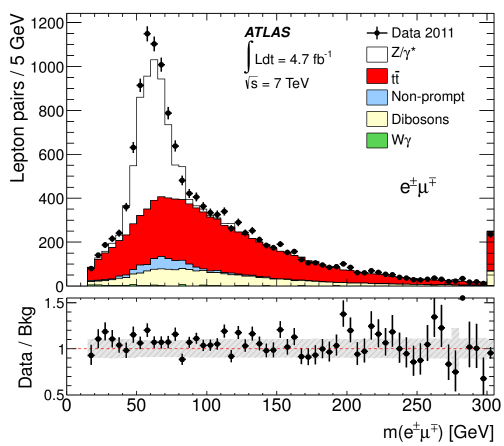

(c)

Figure 9.1: Invariant mass distributions for the control regions with isolated, opposite-sign (a) e^+e^-, (b) $\mu^+\mu^-$, and (c) $e^\pm\mu^\mp$ pairs. The data are shown as closed circles, and the stacked histograms represent the Standard Model predictions. The last bin is an overflow bin. The shaded band on the data / background ratio plots represents the systematic uncertainties due to the MC cross sections, luminosity, and lepton efficiencies.

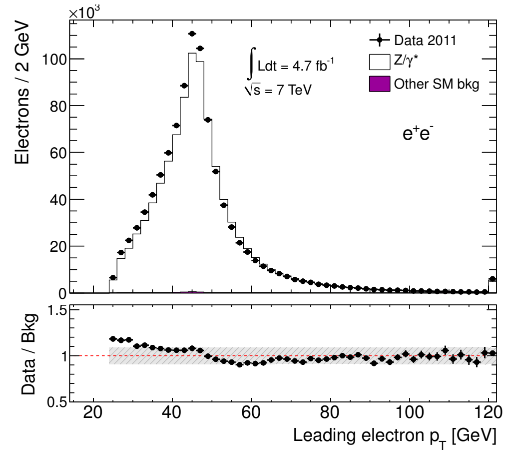

(a)

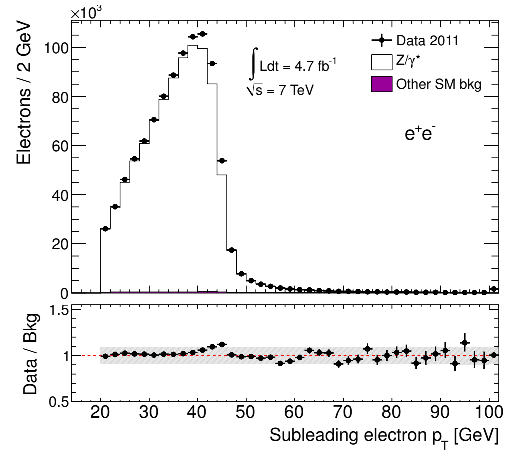

(b)

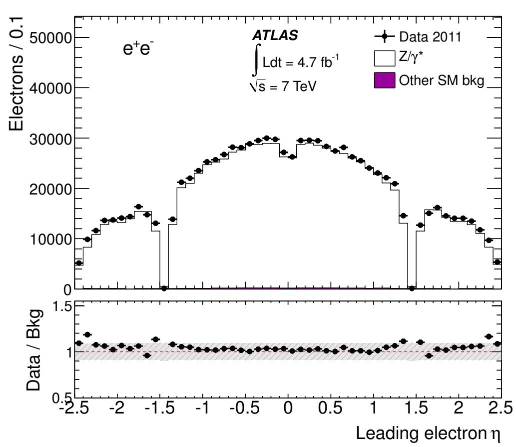

(c)

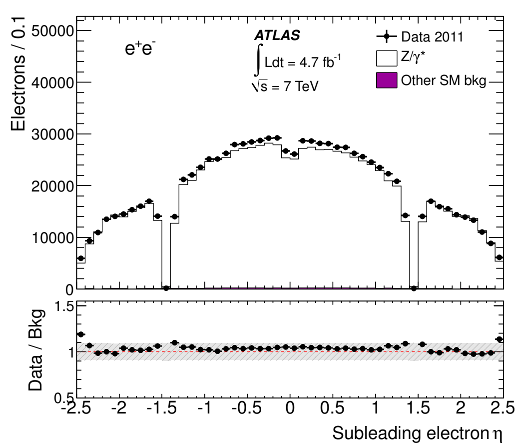

(d)

Figure 9.2: Distributions of (a) leading electron p_{T}, (b) subleading electron p_{T}, (c) leading electron η, and (d) subleading electron η for the $e^{\pm}e^{\mp}$ control region with two oppositely-charged isolated electrons. The last bin in the plots of p_{T} is an overflow bin. The shaded band on the data / background ratio plots represents the systematic uncertainties due to the MC cross sections, luminosity, and lepton efficiencies.

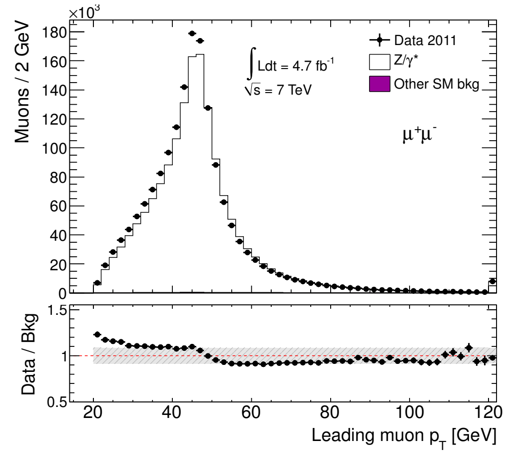

(a)

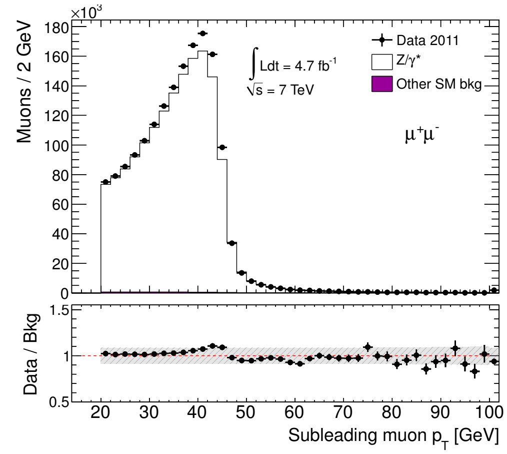

(b)

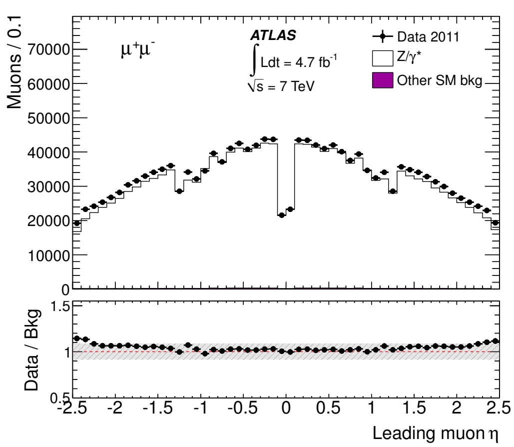

(c)

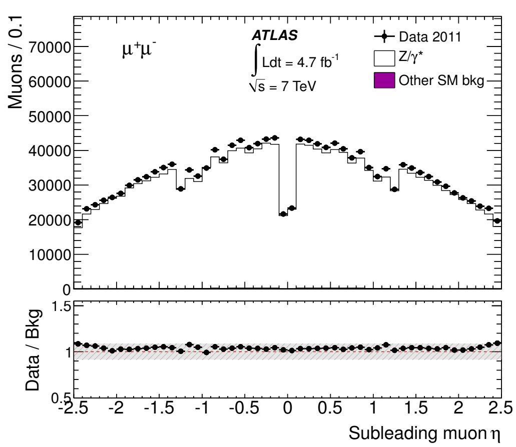

(d)

Figure 9.3: Distributions of (a) leading muon p_{T}, (b) subleading muon p_{T}, (c) leading muon η, and (d) subleading muon η for the $\mu^{\pm}\mu^{\mp}$ control region with two oppositely-charged isolated muons. The last bin in the plots of p_{T} is an overflow bin. The shaded band on the data / background ratio plots represents the systematic uncertainties due to the MC cross sections, luminosity, and lepton efficiencies.

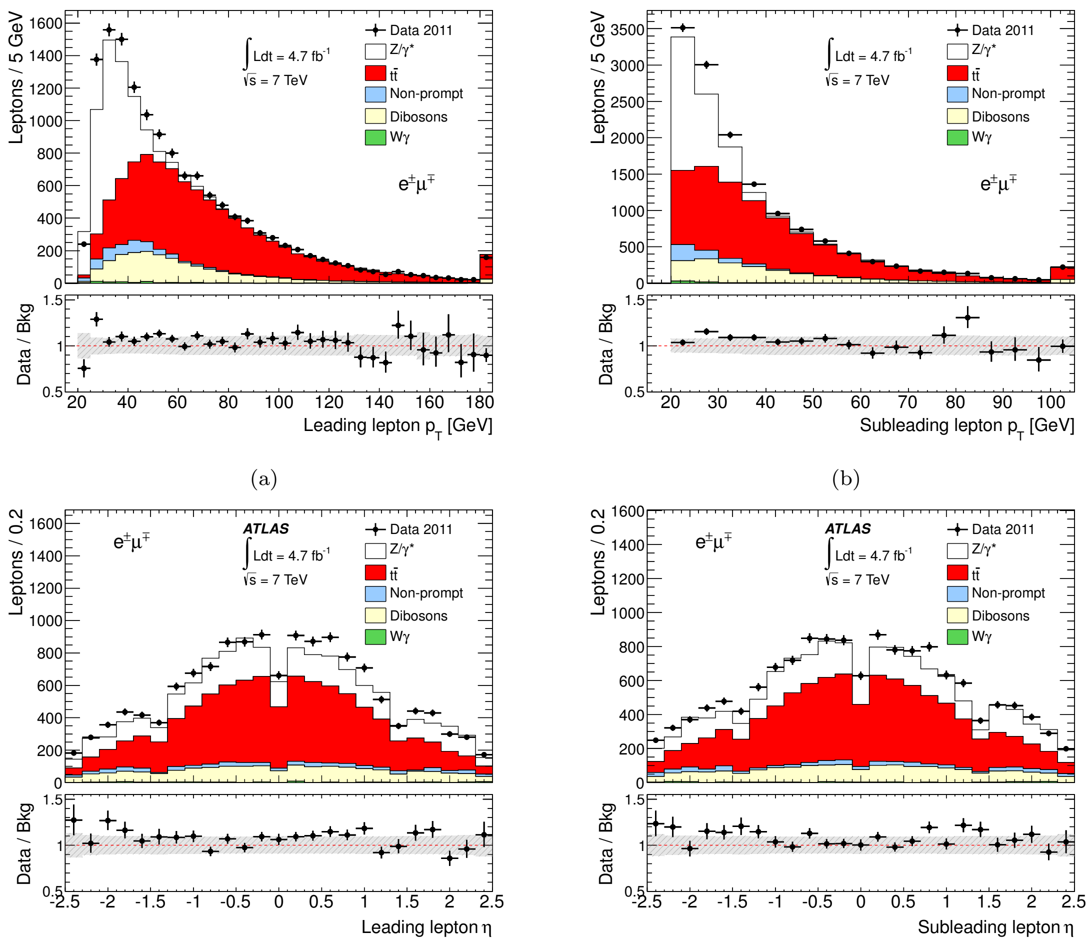

(a) (b) (c) (d)

Figure 9.4: Distributions of (a) leading lepton p_{T}, (b) subleading lepton p_{T}, (c) leading lepton η, and (d) subleading lepton η for the $e^{\pm}\mu^{\mp}$ control region with two oppositely-charged isolated leptons. The last bin in the plots of p_{T} is an overflow bin. The shaded band on the data / background ratio plots represents the systematic uncertainties due to the MC cross sections, luminosity, and lepton efficiencies.

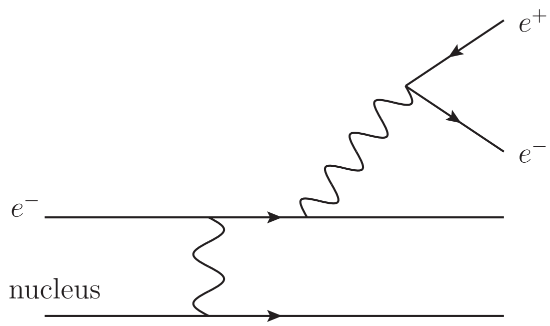

Figure 9.5: Diagram of the bremsstrahlung process followed by a photon conversion.

undergone a charge-flip, determined as described below as the ratio of the measured charge-flip rate in data to the rate in MC. The same factor is applied to backgrounds with prompt photons which convert to give electrons ($W\gamma$, $Z\gamma$) due to the similarity of the material interaction.

To understand the modeling of charge misidentification, the $Z \to ee$ peak in the like-sign $m(ee)$ distribution is used as a control region. The range $70 < m(ee) < 110$ GeV is removed from the signal region of the analysis, and data is compared with MC prediction in the smaller region $80 < m(ee) <$ 100 GeV, where charge-flip electrons from $Z \to ee$ dominate.

Three different methods are used to measure the charge-flip rate for the analysis selection, including both effects described in the previous section, following previous ATLAS like-sign analyses [25]. These are tag-and-probe (T&P), direct extraction, and a likelihood method, and each is described in more detail in Section 9.2.1.1 below. As material effects dominate the observed charge misidentification, the rates are extracted as a function of $|\eta|$ to track the change with the ID material. Additionally, the lepton η distributions vary for the OS dilepton processes which give rise to charge-flips, as shown in Fig. 9.6, making it important to correctly model the η dependence of this effect. Extraction as a function of p_{T} was also investigated but the information was limited due to poor statistics.

Closure tests are performed with the extracted rates. They are applied to the OS dielectron events in the $Z \to ee$ peak to predict the normalization of the LS $Z \to ee$ peak. This is done for both data and MC. Then scale factors are derived as a function of $|\eta|$, and these are applied to MC to predict LS $Z \to ee$ peak in data as a final validation step.

9.2.1.1 Charge-flip Rate Measurements

The following methods are used to measure the charge-flip rate in the $Z \to ee$ region.

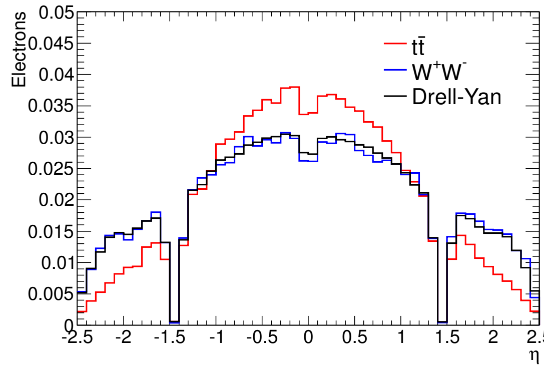

Figure 9.6: Electron η distributions for processes producing opposite-sign dileptons, all normalized to unity.

9.2.1.1.1 Tag-and-Probe This method is similar to the tag-and-probe described in Section 8.1.2. Events are selected with two electrons having invariant mass $80 < m(ee) < 100$ GeV, but no requirement is made on the charges of the electrons. Tag electrons must pass all analysis requirements and also have $|\eta| < 0.8$, as central electrons have the lowest charge-flip rate. The probe is required to pass the full analysis selection, and the number of like-sign events and opposite-sign events are evaluated for each η bin depending on the probe electron. Charge misidentification rates are then obtained in each $|\eta|$ bin i using:

$$\delta^i = \frac{N^i_{LS}}{N^i_{OS} + N^i_{LS}} \tag{9.1}$$

$$\epsilon^i = \delta^i - \epsilon^0 \tag{9.2}$$

where ϵ^i is the charge-flip rate for an electron from η bin i. Here the factor $\epsilon^0 = \frac{\delta^0}{2}$ is to correct for the tag electron charge-flip rate.

9.2.1.1.2 Direct Extraction The direct extraction method is similar to the tag-and-probe method, except both electrons from the Z peak mass range are required to be from the same $|\eta|$ bin to resolve the ambiguity of which one flipped charge. Thus the charge-flip rate for each bin is given by:

$$\epsilon^i = \frac{N^i_{LS}}{2N^i} \tag{9.3}$$

where $N^i = N^i_{OS} + N^i_{LS}$.

9.2.1.1.3 Likelihood Utilizing a likelihood with the charge-flip probabilities for both electrons allows all η combinations of electrons to be considered, maximizing the available statistics and minimizing any kinematic biases from the η restrictions of the previous methods. This method starts by assuming that the charge-flip rates for different $|\eta|$ regions are independent. Thus the mean number of expected LS events, N^{ij}_{LS}, in $|\eta|$ regions i and j as a function of the total number of events (opposite- and like-signed) N^{ij} is:

$$N^{ij}_{LS} = N^{ij}(\epsilon_i + \epsilon_j) \tag{9.4}$$

The Poisson probability to observe k events with a mean expected number of λ is:

$$f(k;\lambda) = \frac{\lambda^k e^{-\lambda}}{k!} \tag{9.5}$$

where here $\lambda = (\epsilon^i + \epsilon^j)N^{ij}$. A likelihood L is constructed from the product of the probabilities for all $|\eta|$ regions. Taking the negative log of this likelihood and simplifying, one obtains:

$$-lnL(\epsilon|N_{LS}, N) \approx \sum_{i,j} ln(N^{ij}(\epsilon^i + \epsilon^j))N^{ij}_{LS} - N^{ij}(\epsilon^i + \epsilon^j) \tag{9.6}$$

This function is then minimized to find the charge-flip rates and errors.

The electron charge-flip rates measured using these methods are shown in Table 9.2 for data and MC. The scale factors (SF) are also shown, defined as simply the data charge-flip rate over the MC charge-flip rate for a given $|\eta|$ bin. The measurements agree well in the central $|\eta|$ bins where they are essentially equivalent and use the same statistics, while they disagree in the highest $|\eta|$ bin with the largest charge-flip rate. The measured rates in data and MC with the likelihood method are shown also in Fig. 9.7.

Table 9.2: Electron charge-flip rates measured using the $Z \to ee$ peak in data and MC with the methods described in the text, together with the resulting scale factors. The errors shown are statistical only. The likelihood method is denoted by L.

Method	$\|\eta\| < 0.8$	$0.8 < \|\eta\| < 1.5$	$1.5 < \|\eta\| < 1.9$	$1.9 < \|\eta\| < 2.2$	$2.2 < \|\eta\| < 2.5$
T&P (Data)	$(1.3 \pm 0.2) \cdot 10^{-4}$	$(2.0 \pm 0.3) \cdot 10^{-4}$	$(1.2 \pm 0.1) \cdot 10^{-3}$	$(2.5 \pm 0.2) \cdot 10^{-3}$	$(4.4 \pm 0.4) \cdot 10^{-3}$
T&P (MC)	$(1.4 \pm 0.2) \cdot 10^{-4}$	$(2.9 \pm 0.3) \cdot 10^{-4}$	$(1.3 \pm 0.1) \cdot 10^{-3}$	$(2.3 \pm 0.2) \cdot 10^{-3}$	$(5.1 \pm 0.4) \cdot 10^{-3}$
Direct (Data)	$(1.3 \pm 0.2) \cdot 10^{-4}$	$(1.9 \pm 0.3) \cdot 10^{-4}$	$(2.0 \pm 0.3) \cdot 10^{-3}$	$(3.0 \pm 0.4) \cdot 10^{-3}$	$(9.1 \pm 0.9) \cdot 10^{-3}$
Direct (MC)	$(1.3 \pm 0.2) \cdot 10^{-4}$	$(2.2 \pm 0.3) \cdot 10^{-4}$	$(2.1 \pm 0.2) \cdot 10^{-3}$	$(3.1 \pm 0.3) \cdot 10^{-3}$	$(10.0 \pm 0.7) \cdot 10^{-3}$
L (Data)	$(1.2 \pm 0.2) \cdot 10^{-4}$	$(2.1 \pm 0.4) \cdot 10^{-4}$	$(1.6 \pm 0.2) \cdot 10^{-3}$	$(2.7 \pm 0.2) \cdot 10^{-3}$	$(5.8 \pm 0.4) \cdot 10^{-3}$
L (MC)	$(1.3 \pm 0.2) \cdot 10^{-4}$	$(2.7 \pm 0.3) \cdot 10^{-4}$	$(1.7 \pm 0.1) \cdot 10^{-3}$	$(3.0 \pm 0.2) \cdot 10^{-3}$	$(8.1 \pm 0.4) \cdot 10^{-3}$
T&P SF	0.87	0.67	0.93	1.07	0.85
Direct SF	0.87	0.88	0.97	0.96	0.91
L SF	0.86	0.75	0.94	0.90	0.71

The scale factors are also investigated as a function of p_{T} and are plotted versus $|\eta|$ and p_{T} in Fig. 9.8. The statistics when binning in p_{T} are very poor, but the results are consistent with a scale factor that is flat with p_{T}. This is reasonable given that the primary charge-flip effect is from material for the p_{T} range considered in this analysis, and the simulation modeling of material interactions should not change relative to data with p_{T}.

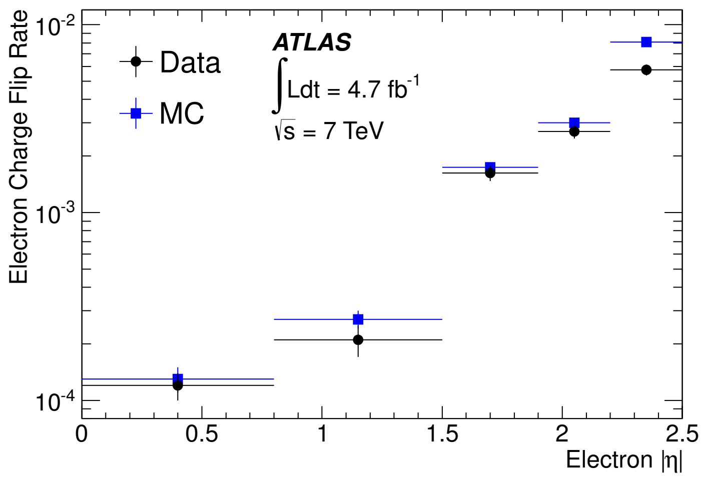

Figure 9.7: Electron charge-flip rate as function of electron η, measured in data and MC simulation using the likelihood method. The errors shown are statistical only.

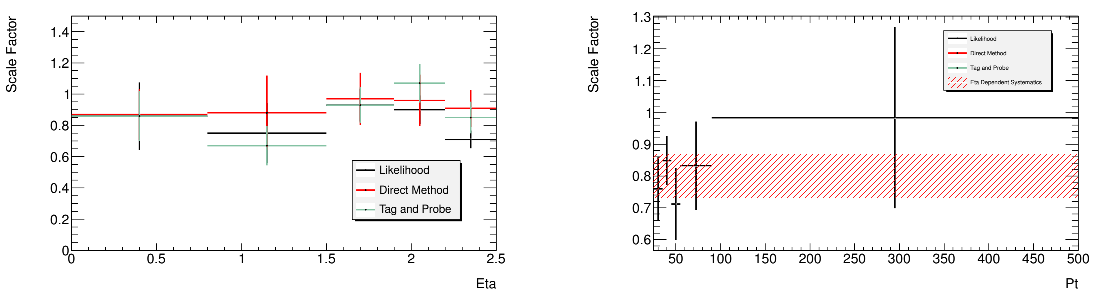

(a) (b)

Figure 9.8: Electron charge-flip scale factors derived in bins of $|\eta|$ (a) and p_{T} (b) using the three methods described in the text.

As shown below in the next section, the likelihood method gives the best closure results and is used to provide the nominal scale factors for the analysis. The uncertainty on these scale factors is taken to be the larger of the statistical error (dominant in most bins) or the smallest difference between the likelihood SF and either of the other method SFs in a given bin. The scale factors with full uncertainties are given in Table 9.3

Table 9.3: Electron charge-flip scale factors with full uncertainties used in this analysis, in bins of $|\eta|$.

Method	$|\eta| < 0.8$	$0.8 < |\eta| < 1.5$	$1.5 < |\eta| < 1.9$	$1.9 < |\eta| < 2.2$	$2.2 < |\eta| < 2.5$
Likelihood	0.86 ± 0.21	0.75 ± 0.19	0.94 ± 0.10	0.90 ± 0.09	0.71 ± 0.14

9.2.1.2 Charge-flip Validation

The first closure test performed applies the measured charge-flip rates to the OS pairs of electrons in the $Z \to ee$ mass window to predict the LS yield. This is done for data and MC, applying the rates measured in data back to data and likewise for MC. The results are shown in Fig. 9.9. One obvious feature is that the true LS events have invariant masses shifted to lower values than the OS events, due to the fact that charge-flips involve energy loss. (The mass peak can still be reconstructed reasonably well, however, because it uses the energy measurement from the calorimeter instead of the momentum measurement from the ID.) The likelihood method is seen to give the best overall results in terms of normalization.

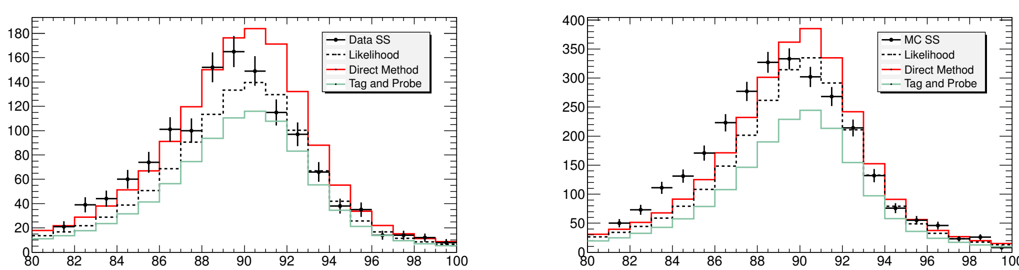

(a) Data closure test

(b) MC closure test

Figure 9.9: Closure tests for charge-flip rates in data (a) and MC (b).

The analysis scale factors in Table 9.3 are also applied to MC to predict the LS $Z \to ee$ peak in data. Comparisons of the predicted and observed kinematics are shown in Fig. 9.10. Better agreement is seen versus p_{T} compared to the opposite-sign control region in Fig. 9.2.

Table 9.4 shows the expected and observed number of events, using the non-prompt prediction from the nominal method after charge-flip correction (described below in Section 9.3.2). Data and prediction agree to about 4%, well within the systematics assessed for the charge-flip prediction. Results are also shown in Table 9.4 separately for e^+e^+ and e^-e^- pairs. A slight charge asymmetry is observed in this region, 1.12 ± 0.06 for e^+e^+/e^-e^- in data. This is well modeled by the MC in this region, where the charge asymmetry predicted is 1.17 ± 0.06.

Table 9.4: Observed and expected number of lepton pairs for the control region with like-sign, isolated electrons falling inside the Z mass window. The uncertainties on the predictions are statistical then systematic. Separate counts are also shown for e^+e^+ and e^-e^- pairs.

Process	Number of ee pairs
Like-sign ee Z mass window	
Non-prompt	34 ± 24
Charge-flips	$1349 \pm 24 \pm 230$
Prompt Electrons	$25 \pm 1 \pm 3$
Total Prediction	$1408 \pm 33 \pm 230$
Data	1470
Agreement	-0.3σ
Like-sign e^+e^+ Z mass window	
Non-prompt	25 ± 17
Charge-flips	$722 \pm 17 \pm 123$
Prompt Electrons	$16 \pm 1 \pm 2$
Total Prediction	$763 \pm 24 \pm 123$
Data	777
Agreement	-0.2σ
Like-sign e^-e^- Z mass window	
Non-prompt	9 ± 17
Charge-flips	$627 \pm 16 \pm 107$
Prompt Electrons	$10 \pm 1 \pm 1$
Total Prediction	$645 \pm 23 \pm 107$
Data	693
Agreement	-0.4σ

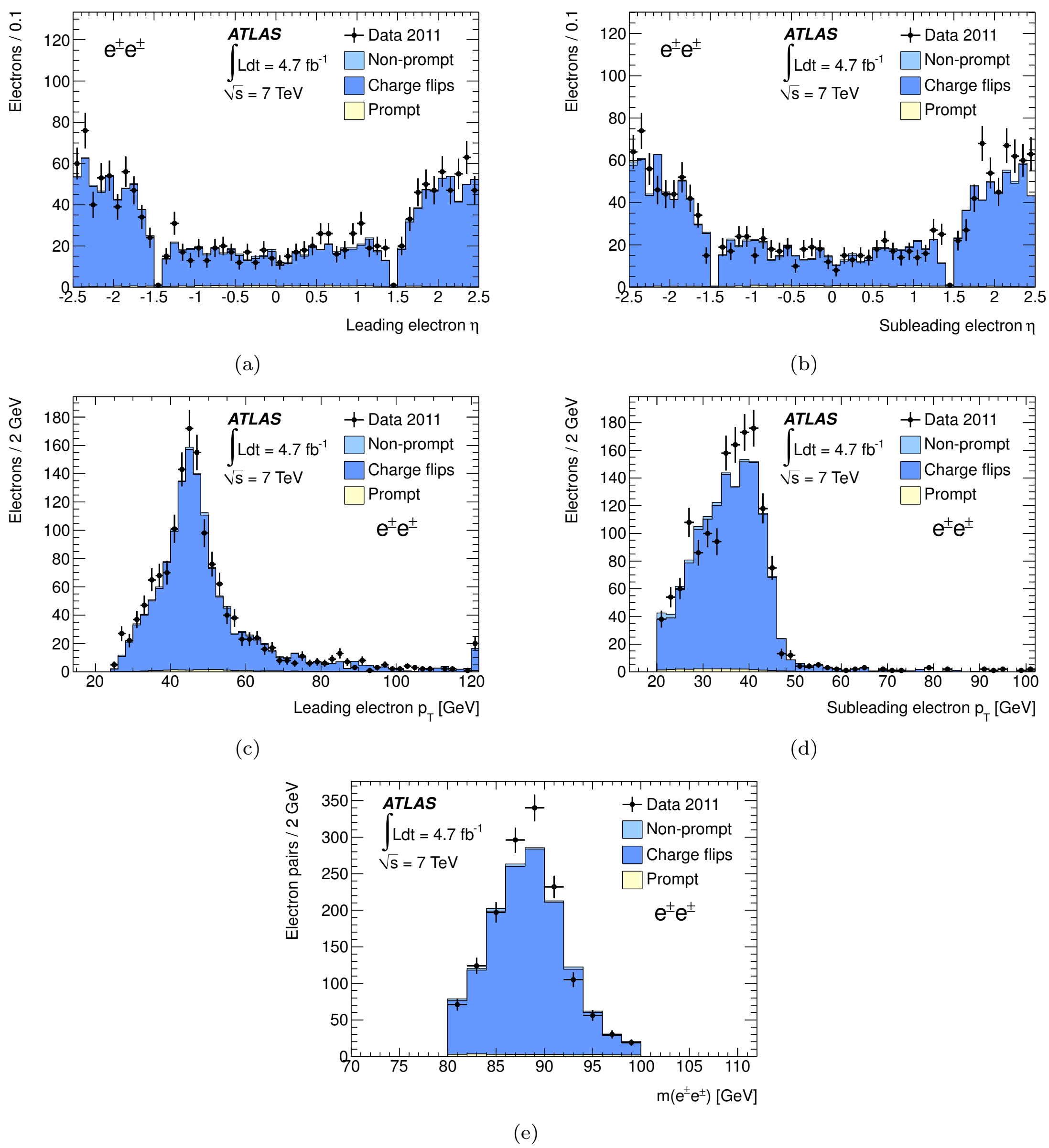

(a) (b) (c) (d) (e)

Figure 9.10: Distributions of (a) leading electron η, (b) subleading electron η, (c) leading electron p_{T}, (d) subleading electron p_{T}, and (e) invariant mass in the like-sign $Z \to ee$ peak control region with two isolated electrons. The last bin in the plots of p_{T} is an overflow bin.

9.2.2 Muon Charge-flips

For muons, the source of charge-flips would be high-momentum tracks when the tracking detector is unable to determine the curvature of the track, as they do not suffer the same material effects as electrons. Since the combined muon reconstruction is used and a requirement that the ID and the MS components have the same charge is placed, a charge-flip can only occur if both the ID and the MS track are misreconstructed.

Such misreconstruction is constrained directly using $Z \to \mu\mu$ candidates in data. The ID (MS) measurement is probed based on Z candidates selected based on the invariant mass using only the MS (ID) momentum. The invariant mass distribution for the ID- and MS-only reconstruction is shown in Fig. 9.11 for data and MC, demonstrating that each subsystem is able to independently reconstruct the $Z \to \mu\mu$ resonance peak.

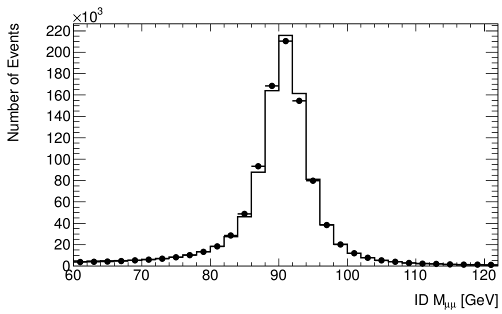

(a) ID only

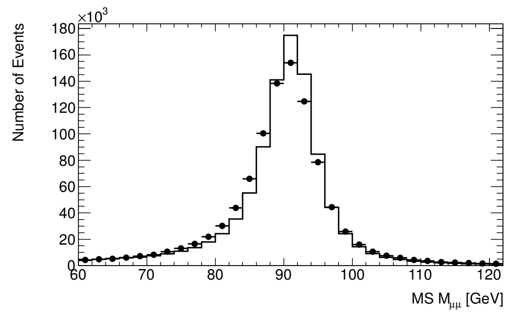

(b) MS only

Figure 9.11: Invariant mass distribution of dimuon events using only the ID (a) or MS (b) for reconstruction. The points show the data and the histogram the MC.

Z candidates are then selected based on the respective reconstructed mass in a range $76 < M_{\mu\mu} < 106$ GeV and requiring the two muons to be of opposite charge (again based only on the MS or the ID). The charge measurement of the other system can then be compared to that of the reference system used to select the Z candidates. This provides information about how often either of the systems misreconstructs the charge. In each event there are two muons that can be used as a probe to test the charge-flip.

The result of this measurement is shown in Fig. 9.12 for the MS and ID. In the MS, the charge misidentification fraction increases from about 10^{-4} at $p_{\mathrm{T}} = 50$ GeV to about 10% at $p_{\mathrm{T}} = 400$ GeV in data. In simulation it is typically a factor of two lower. The muons contributing to charge misidentification mostly come from the region $1.2 < |\eta| < 1.6$, as in this region the alignment and the instrumentation of the MS is not yet optimal. In this momentum range the charge misidentification

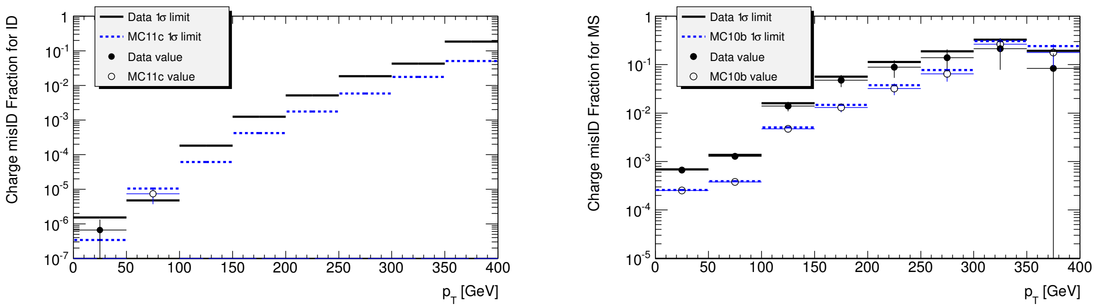

(a) ID only

(b) MS only

Figure 9.12: Charge-flip probability as function of muon p_{T} for the ID (a) and the MS (b). Shown are both the measurements and the upper limits at 67% confidence level.

rate in the ID is consistent with zero. Also shown is the upper limit at 67% confidence level (CL) for both data and MC. The upper limit is 18% at $p_{\mathrm{T}} \approx 375$ GeV for the ID and 38% for the MS. For these high p_{T} values, the limit is statistically limited and will improve in future iterations of this analysis. At lower p_{T} values, the limit is significantly lower.

An upper limit on the probability of reconstructing the charge of a combined muon incorrectly is given by the product of the individual charge mismeasurement probabilities since a requirement that both charges are the same is made in the muon selection. The product of the upper limits is shown in Fig. 9.13.

For the prediction of background due to charge-flips in the signal region, Monte Carlo is used to determine the central value. In practice it turns out that there is not a single charge-flipped MC event in the samples used with the analysis selection cuts. The systematic uncertainty is derived using the upper limit on the ID×MS charge-flip probability as measured in data, which is applied to the MC samples with two opposite-sign prompt muons.

9.3 Non-prompt Leptons

The non-prompt background, also sometimes called the fake background, includes lepton pairs where one or both of the leptons result from hadronic decay or misidentification. Processes contributing to this background include W+jet, Z+jet, QCD multijet (including $b\bar{b}$ and $c\bar{c}$), and $t\bar{t}$ production. Non-prompt electrons can arise from QCD jets due to hadrons misidentified as electrons, photon conversions, and semi-leptonic decays of heavy-flavor (b, c) quarks. For muons, the sources include semi-leptonic b- or c-hadron decays and muons from π and K mesons which decay in the detector volume (decay-in-flight). This background is determined from data, using the method described in

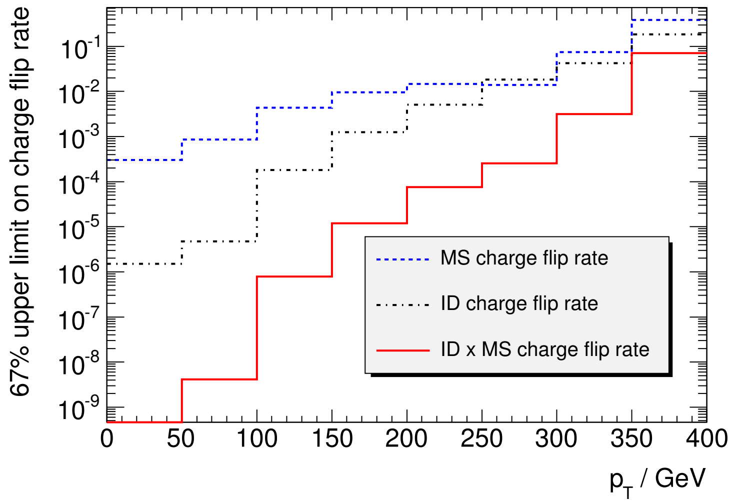

Figure 9.13: Charge-flip probability as function of muon p_T for the ID, the MS and the product of the two (ID$\times$MS). The limits are derived at 67% confidence level from data.

the following sections.

Section 9.3.1 describes the method used. Section 9.3.2 describes the specific implementation for electrons, while Section 9.3.3 describes the application to muons. Section 9.3.4 describes the data control regions used to validate these non-prompt predictions and shows the validation results.

9.3.1 Non-prompt Method

The non-prompt background is determined directly from data. For both electrons and muons, the determination relies on measuring a factor f (sometimes called the "fake factor") that is the ratio of the number of selected leptons satisfying the analysis selection criteria (N_S) to the number of leptons failing these selection criteria but passing a less stringent set of requirements, referred to as anti-selected leptons (N_A):

$$f \equiv \frac{N_S}{N_A} \tag{9.7}$$

The factor f is determined as a function of p_{T} and η in a data sample dominated by non-prompt leptons. Any contamination by prompt leptons in the selected or anti-selected sample is subtracted using MC simulation. The details of the anti-selected definitions and the regions used for measuring f depend on the lepton flavor and are described in more detail in the next sections.

A background prediction is derived from f using dilepton pairs where one or both leptons are anti-selected but pass all other event selection criteria. The non-prompt background prediction is then given by

$$N_{\text{non-prompt}} = \sum_{i=1}^{N_{A+S}} f(p_{\text{T}1}, \eta_1) + \sum_{i=1}^{N_{S+A}} f(p_{\text{T}2}, \eta_2) - \sum_{i=1}^{N_{A+A}} f(p_{\text{T}1}, \eta_1) f(p_{\text{T}2}, \eta_2), \tag{9.8}$$

where the sums are over the number of pairs, N_{A+S} (N_{S+A}), where the subleading (leading) lepton satisfies the selection criteria and the other lepton satisfies the anti-selection, or over the number of pairs where both leptons are anti-selected (N_{A+A}). The last term with both leptons anti-selected has a negative sign to avoid double counting of the background where both leptons are non-prompt. The prompt contributions to N_{A+S}, N_{S+A}, and N_{A+A} are subtracted based on MC predictions. The variables $p_{\text{T}1}$ and η_1 ($p_{\text{T}2}$ and η_2) refer to the kinematic properties of the leading (subleading) lepton.

Also described in the following sections are the systematic uncertainties associated with f for each lepton flavor. An assumption of this method is that the region used to derive f is similar in kinematics and composition to the region where f will be applied. Binning in p_{T} and η accounts for the lepton kinematics, but other differences can remain, especially in non-prompt composition. The systematic uncertainties for both electrons and muons attempt to quantify the effects of these differences.

9.3.2 Non-prompt Electrons

Non-prompt electrons can arise from light flavor (LF) QCD jets via charged hadrons reconstructed as electrons and photon conversions, typically from π^0 decays. Additionally, there are heavy flavor (HF) sources, semi-leptonic decays of b- and c-hadrons. These different sources have different signatures in the detector, which motivate the treatments below. Those from LF sources tend to fail electron ID and be non-isolated, while those from HF sources may pass electron ID (as they are real electrons), but they tend to be non-isolated and have larger transverse impact parameters due to the lifetime of the b quark.

9.3.2.1 Definitions

The primary handles used to separate non-prompt from prompt electrons are electron ID and $d_0/\sigma(d_0)$. The anti-selected definition requires candidates to pass all other cuts, plus some of the track quality cuts from *Tight*,[19] while failing electron *Medium* or the analysis cut on $d_0/\sigma(d_0)$. As the cuts in *Medium* are a subset of the cuts in *Tight*, reversing either *Medium* or the analysis $d_0/\sigma(d_0)$ cut creates a selection orthogonal to the numerator (analysis) selection.

[19]Specifically, a minimum number of hits are required in the silicon tracker, and a hit is required in the innermost pixel layer if the candidate track traversed an active pixel module.

This will be referred to as the "nominal anti-selection." Reversing electron ID collects the LF sources, while reversing $d_0/\sigma(d_0)$ captures HF sources. One weakness of this denominator, however, is that reversing $d_0/\sigma(d_0)$ also collects charge-flip electrons. The solution for this is discussed in Section 9.3.2.5.1.

9.3.2.2 Measurement of f

The factor f is measured in QCD dijet data samples, triggered with primary and supporting single electron triggers. Events are selected by requiring a specific trigger (with more details below) and requiring an away-side jet with $p_{\mathrm{T}} > 20$ GeV. Other than the p_{T} threshold, the jet selection is the same as described in Section 8.3. Electrons from prompt sources (W,Z) are largely removed by making the following requirements:

- reject events with two candidate electrons with invariant mass between 80 and 100 GeV
- reject events with two *Loose* electrons
- reject events where electron candidate and $E_{\mathrm{T}}^{\mathrm{miss}}$ have transverse mass $m_{\mathrm{T}} > 40$ GeV[20]

Residual contamination of prompt electrons is subtracted using MC, and a systematic uncertainty is assessed for this as described later.

As the selected and anti-selected electron samples are mutually exclusive, they need not come from the same trigger. Prescaled triggers[21] can be used if the relative effective prescale is taken into account. The advantage to doing this is more statistics: this allows using prescaled *Loose* supporting triggers for the anti-selected sample and the unprescaled primary electron triggers for the selected sample. In this case, Equation 9.7 becomes:

$$f \equiv \frac{N_S}{(\text{effective prescale}) \times N_A} \tag{9.9}$$

where the relative effective prescale between the two triggers is used.

Different triggers are also used in different p_{T} ranges, to take advantage of the available triggers. These triggers evolved throughout 2011 due to the changing luminosity conditions, as described in Table 7.1. Table 9.5 describes the trigger strategy used for each p_{T} range for measuring f.

Note that for the p_{T} range $20 < p_{\mathrm{T}} < 25$ GeV, only triggers from the early part of the 2011 run (ATLAS data periods B–J) are used, because the trigger thresholds increased in the later run periods.

[20] $m_{\mathrm{T}} = \sqrt{2 p_{\mathrm{T}}^{e} E_{\mathrm{T}}^{\mathrm{miss}} (1 - cos(\phi))}$, where ϕ is the angle between the transverse momentum of the electron and $E_{\mathrm{T}}^{\mathrm{miss}}$.

[21] For information on trigger prescales, see Section 4.5.

This treatment is justified by the fact that f is observed to be independent of run period, as shown in Fig. 9.14.

Table 9.5: Triggers used to collect selected and anti-selected single electron samples for measuring f, with threshold and identification requirements and prescales (PS). These triggers require an electron candidate with the specified p_{T} threshold and electron ID requirement. The trigger p_{T} thresholds used for the range $25 < p_{\mathrm{T}} < 100$ GeV evolved according to Table 7.1. The triggers used for the range $20 < p_{\mathrm{T}} < 25$ GeV were only active for the first part of 2011, so the effective prescales include the fraction of the total integrated luminosity collected during those periods.

	Selected Sample			Anti-selected Sample		
p_{T} range [GeV]	Threshold [GeV]	e ID	PS	Threshold [GeV]	e ID	PS
$20 < p_{\mathrm{T}} < 25$	20	*Medium*	2.75	20	*Loose*	242.0
$25 < p_{\mathrm{T}} < 100$	20–22	*Medium*	1.0	20–22	*Loose*	134.0
$100 < p_{\mathrm{T}} < 300$	80	*Loose*	1.0	80	*Loose*	1.0

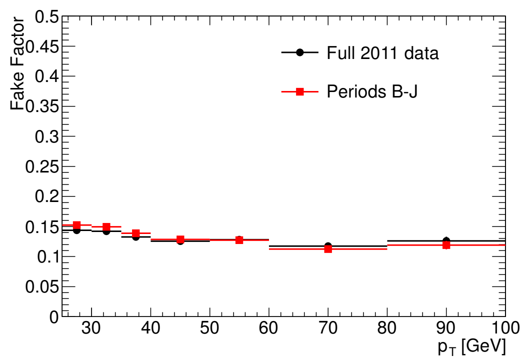

Figure 9.14: Electron fake factor f values vs p_{T}, comparing the triggers used for the full 2011 dataset with those from periods B–J.

The central values for f binned versus p_{T} and η are shown in Fig. 9.15. The factor f is relatively flat to slightly decreasing for $p_{\mathrm{T}} > 25$ GeV and increases at high η.

9.3.2.3 Application

To predict the non-prompt background in the signal region, the factor f is applied as described above in Section 9.3.1.

For the dielectron channel, the additional complication arises that the selection applied by the primary electron trigger used for the analysis (*Medium*) is tighter than the anti-selection requirement (*Loose*). This is not a problem for the $S + A$ region, where the leading electron can pass the trigger

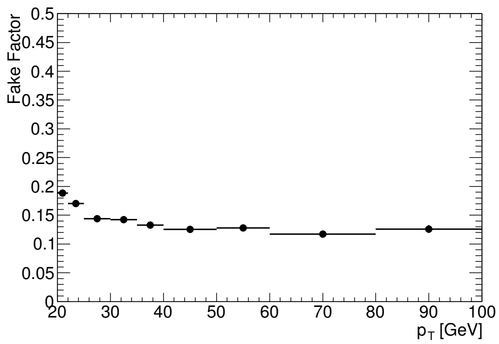

(a)

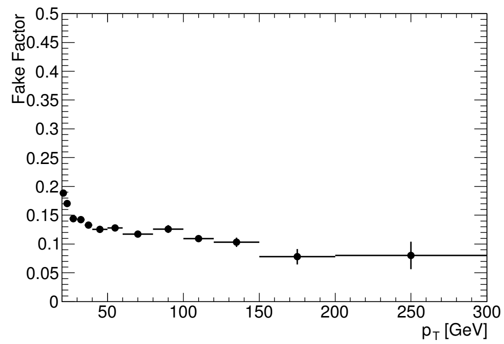

(b)

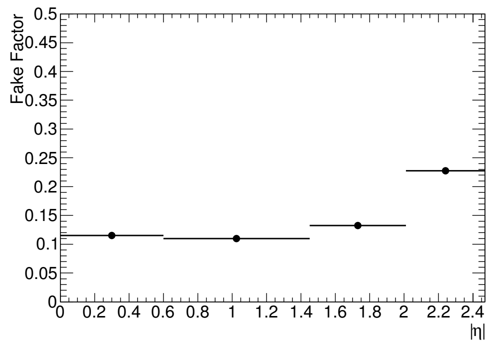

(c)

Figure 9.15: Electron fake factor f central value vs p_{T} (top) and η (bottom). Figure (a) shows a zoom of the low p_{T} region.

requirements. For the $A+S$ and $A+A$ regions, however, the leading electron cannot pass the trigger. In the $A+S$ region, the subleading electron would need to pass the trigger, but the efficiency for $p_{\mathrm{T}} < 25$ GeV is reduced. And in the $A+A$ region, neither electron can pass the analysis trigger.

To cover the full phase space in these regions, a trigger requiring two *Loose* electrons both with $p_{\mathrm{T}} > 20$ GeV is employed for the $A+S$ and $A+A$ regions. As is shown in Fig. 9.16, the trigger threshold at 20 GeV results in a bias (inefficiency) for candidates with $20 < p_{\mathrm{T}} < 22$ GeV. In the application of f, this bias is explicitly corrected by scaling up the prediction in that p_{T} bin.

9.3.2.4 Systematic Uncertainty on f

The following sources of systematic uncertainty from the measurement of f are considered:

- Statistical uncertainty on the data. The statistical uncertainty on the measurement of f is shown in Fig. 9.15.

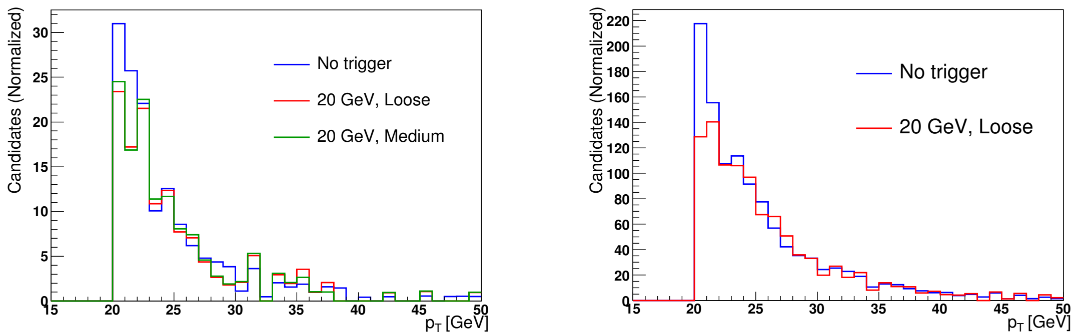

(a) (b)

Figure 9.16: Distribution of p_{T} for selected (a) and anti-selected (b) candidates with trigger requirements in dijet MC. The difference between no trigger requirement and requiring a trigger in the first p_{T} bins is interpreted as a trigger threshold bias.

- Uncertainty on the subtraction of prompt contamination. The prompt subtraction is varied by $\pm 10\%$ to assess this. This number is somewhat arbitrary but is chosen to cover luminosity ($\sim 4\%$) and cross section ($\sim 7\%$) uncertainties. This variation is shown in Fig. 9.17.

- Uncertainty due to jet kinematics. This is assessed by varying of away side jet p_{T} requirement. As dijet events tend to be balanced in p_{T}, this acts as a proxy for the near side jet p_{T}. This variation is shown in Fig. 9.18.

- Uncertainty due to trigger bias from trigger p_{T} threshold. This is evaluated in a dijet MC sample by comparing the objects passing the numerator and denominator selections before and after trigger requirements, as shown in Fig. 9.16. A bias of 28% is seen for $20 < p_{\mathrm{T}} < 22$ GeV. Although this bias will partially cancel in f (because both the selected and anti-selected samples are biased in the same direction), to be conservative the full bias on the selection is taken as an uncertainty.

- Uncertainty due to variation in light quark jet versus gluon jet fakes. This was investigated in a dijet MC sample, and the components are seen to have the same value of f within statistical errors, as shown in Fig. 9.19. No additional uncertainty is assigned for this.

The total systematic uncertainty bands for f are shown in Fig. 9.20 and a breakdown for each p_{T} bin is given in Table 9.6. For candidates with $p_{\mathrm{T}} > 300$ GeV, the value of f from the highest p_{T} bin is used with an uncertainty of 100%.

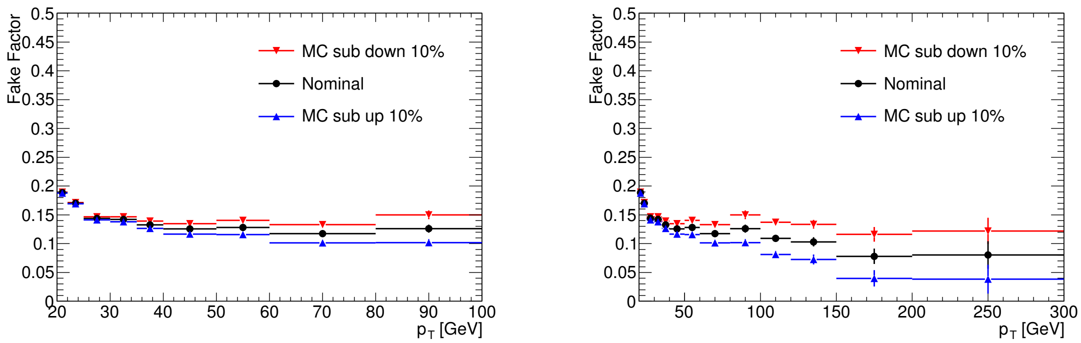

(a) (b)

Figure 9.17: Electron fake factor f versus p_{T} with 10% variation on prompt MC subtraction. Figure (a) shows a zoom of the low p_{T} region.

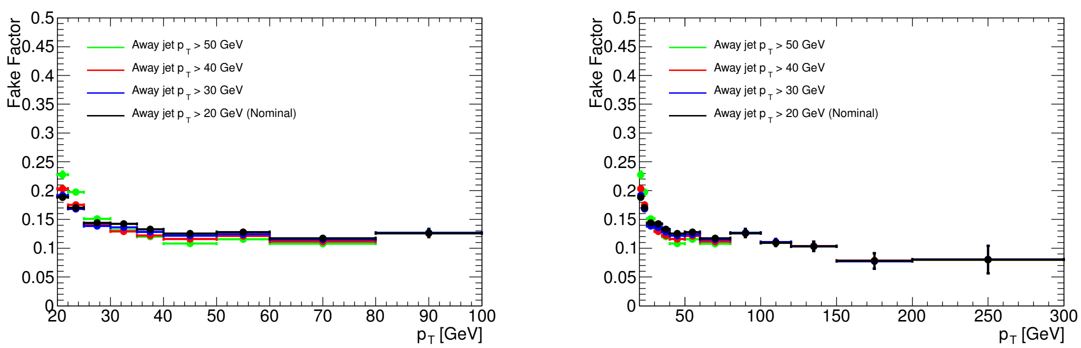

(a) (b)

Figure 9.18: Electron fake factor f versus p_{T} with away side jet p_{T} requirement variation. Figure (a) shows a zoom of the low p_{T} region.

9.3.2.5 Other Systematic Uncertainties

Other sources of systematic uncertainty considered are due to light flavor versus heavy flavor composition and overlap between the fake and charge-flip predictions. Instead of evaluating these as uncertainties on the fake factors themselves, they are evaluated by comparing total fake predictions for the signal region, as described below.

9.3.2.5.1 Overlap with Charge-flips Because the nominal fake denominator definition for electrons includes a reversed cut on $d_0/\sigma(d_0)$, charge-flip electrons can enter the denominator sample. This is not an issue for deriving the fake factors, because the dijet region used is dominated by true

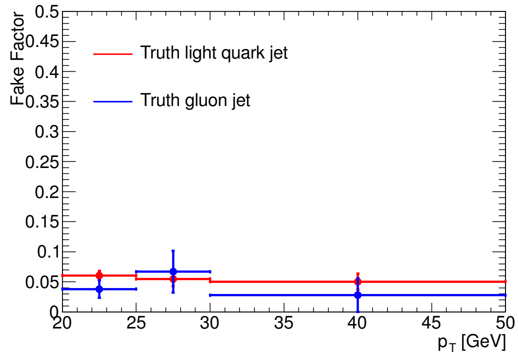

Figure 9.19: Electron fake factors f in dijet MC, for candidates coming from light quark jets and gluon jets.

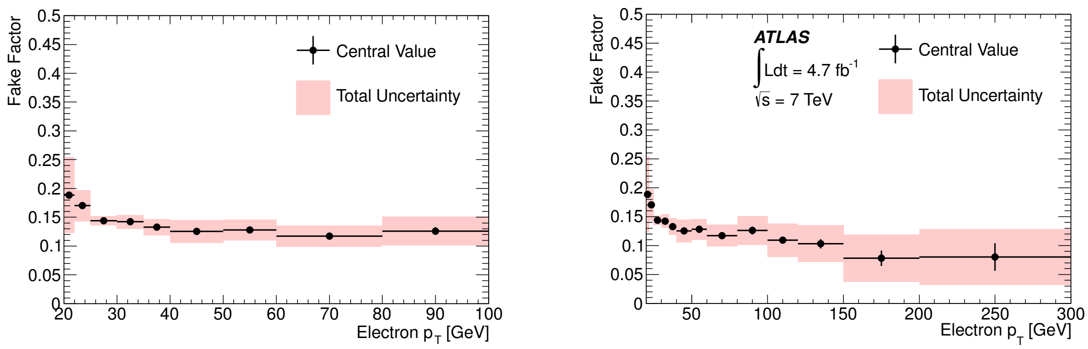

(a) (b)

Figure 9.20: Electron fake factor f versus p_{T} with full statistical plus systematic errors from derivation. Figure (a) shows a zoom of the low p_{T} region.

non-prompt electrons, and residual prompt contamination (including charge-flip) is subtracted out. This is however a concern when predicting the signal region, as the dilepton selection will enhance the number of charge-flips in the $S + A$, $A + S$, and $A + A$ regions used for the non-prompt prediction.

The overlap between the non-prompt and charge-flip predictions is studied in the like-sign Z peak region ($80 < m(ee) < 100$ GeV), and a correction for the non-prompt estimate is derived. It has an 11% impact on the non-prompt prediction in the signal region. The central value is corrected and the full correction of 11% is taken as a systematic uncertainty. More details can be found in Appendix A.1.

Table 9.6: Electron fake factor f central values and uncertainties in bins of p_{T}, averaging over η. Only uncertainties from the measurement of f are shown here.

p_T Bin [GeV]	Cent Val	Tot Err	Stat Err	Prompt Sub	Away Jet Var	Trig Bias
[20, 22]	0.189	34.8%	0.7%	0.4%	20.7%	28.0%
[22, 25]	0.170	15.9%	0.6%	0.5%	15.9%	0.0%
[25, 30]	0.144	5.4%	0.5%	1.9%	5.0%	0.0%
[30, 35]	0.142	8.3%	0.7%	3.1%	7.7%	0.0%
[35, 40]	0.133	10.8%	1.0%	4.9%	9.6%	0.0%
[40, 50]	0.126	15.7%	1.1%	7.3%	13.8%	0.0%
[50, 60]	0.128	13.9%	1.9%	9.7%	9.8%	0.0%
[60, 80]	0.117	15.8%	2.5%	13.4%	8.0%	0.0%
[80, 100]	0.126	19.9%	5.4%	19.1%	0.5%	0.0%
[100, 120]	0.109	26.1%	5.3%	25.6%	0.5%	0.0%
[120, 150]	0.103	30.7%	7.8%	29.7%	0.2%	0.0%
[150, 200]	0.078	52.0%	17.2%	49.1%	0.3%	0.0%
[200, 300]	0.080	60.3%	29.8%	52.4%	0.5%	0.0%
[300, ...]	0.080	100%	-	-	-	-

9.3.2.5.2 Light/Heavy Flavor Composition As they are not explicitly treated separately, the light flavor (LF) versus heavy flavor (HF) composition of the non-prompt background sample could impact the prediction. This would require the true fake factors for non-prompt electrons from LF and HF to be different, and it would also further require that the relative composition of these two components is different between the dijet sample where f is derived and the dilepton sample where it is applied to predict the non-prompt background.

To assess the size of this effect, an alternative method was developed with separate factors f for LF and HF. Separation is achieved by using the b-tagging weight of the reconstructed jet near the electron candidate. This method is used to predict non-prompt-dominated data control regions to gain confidence that it is working properly, then it is applied to the signal region. Good agreement with the nominal prediction is seen, at the level of 4% or better.

The HF/LF separation method relies on an assumption of b-tagging efficiency from MC for candidates after the numerator selections. This efficiency is varied and the signal region predicted again, and the largest differences seen between the varied HF/LF separation method and nominal method are taken as a systematic uncertainty. This results in an uncertainty of 4–20% on the signal region prediction, depending on the dilepton invariant mass requirement. More details can be found in Appendix A.2.

9.3.3 Non-prompt Muons

The main sources of non-prompt muons are heavy flavor (HF) semi-leptonic decays of b- and c-hadrons, with a smaller component from decay-in-flight of light flavor (LF) mesons. Non-prompt muons tend to not be isolated, and muons from HF decays often have large transverse impact parameters. These features are exploited in the muon non-prompt estimate described below.

9.3.3.1 Definitions

The primary variables used to discriminate non-prompt from prompt muons are the transverse impact parameter d_0 and track isolation. Anti-selected muons are required to pass the analysis muon selection described in Section 8.2, except that they are required to fail the track isolation cut and instead pass a looser track isolation requirement of ptcone40/$p_{\mathrm{T}} < 1.0$. Anti-selected muons must still pass the requirement of separation from the closest jet by $\Delta R > 0.4$.

9.3.3.2 Measurement of f

The factor f is determined from data using control samples enhanced in non-prompt muons. In order to mimic the signal region as closely as possible, f is determined from dimuon events, selected using a trigger which requires two muons both with $p_{\mathrm{T}} > 10$ GeV. This lower-threshold trigger allows derivation of f for low-p_{T} muons. For the signal region both muons must have $p_{\mathrm{T}} > 20$ GeV. However, some control regions use muon pairs where the p_{T} cut is loosened to 10 GeV for the subleading muon for increased statistics.

Both events with like-sign and opposite-sign muon pairs are used. The invariant mass of the dimuon pair is required to be larger than 15 GeV to avoid low mass resonances, and for opposite-sign pairs, the range $60 < m(\mu^+\mu^-) < 120$ GeV is removed to avoid large prompt contamination from Drell-Yan production.

Among the selected dimuon events, all muons satisfying a modified muon definition are used for determining f. Non-prompt muons are selected by reversing and loosening the impact parameter cuts, requiring $|d_0| < 10$ mm and $|d_0|/\sigma(d_0) > 5$ to further reduce the prompt contamination.

Any remaining prompt muon contamination from W/Z+jets and $t\bar{t}$ is removed based on MC estimates. The prompt contamination is negligible at low p_{T} but becomes large at higher p_{T}. The factor f before and after subtraction of prompt contamination is shown in Fig. 9.21.

Using MC simulated events, a dependence is observed of f on the impact parameter significance. The factor f is determined from data using muons with $|d_0|/\sigma(d_0) > 5$ and $|d_0| < 10$ mm, while muons in the signal region are required to have $|d_0|/\sigma(d_0) < 3$ and $|d_0| < 0.2$ mm. A correction

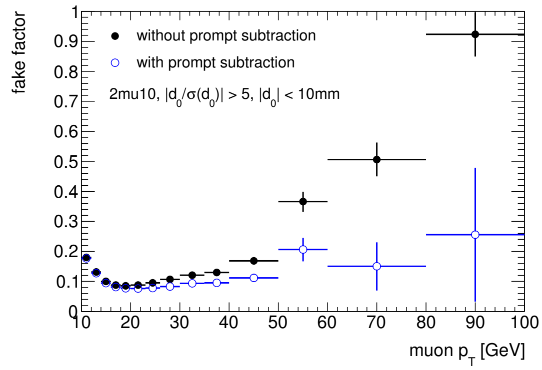

Figure 9.21: Fake factor f before and after subtraction of prompt contributions from W/Z+jets and $t\bar{t}$.

is made for the difference in f between muons with high and low impact parameter significance by deriving a scale factor from $b\bar{b}/c\bar{c}$ MC (contributions from other sources such as $t\bar{t}$ and W+jets are negligible). As no significant p_{T} dependence is observed, the scale factor is derived using muons with $p_{\mathrm{T}} > 10$ GeV in dimuon events with $m(\mu\mu) > 15$ GeV. Figure 9.22 shows the scale factor and the ratio for pass to fail impact parameter significance as a function of muon p_{T} for f, and a flat value of 1.34 is taken.

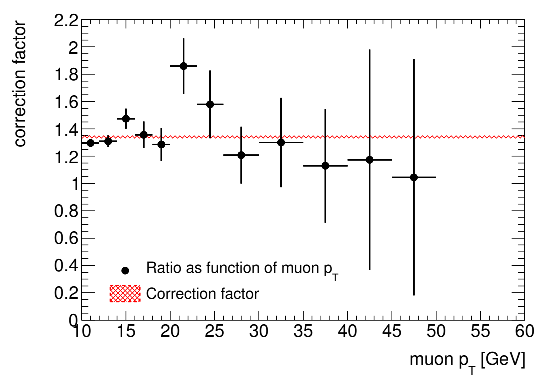

Figure 9.22: Ratio of fake factor f for muons with low impact parameter significance to f for muons with high impact parameter significance for MC. The red line shows the resulting correction factor.

The factors f are shown in Fig. 9.23 as a function of muon p_{T} and η after applying the correction factor from high to low impact parameter significance. The factor f increases significantly for muon $p_{\mathrm{T}} < 1/0.06 \sim 17$ GeV as a consequence of the isolation variable definition (only tracks with $p_{\mathrm{T}} >$ 1 GeV are used).

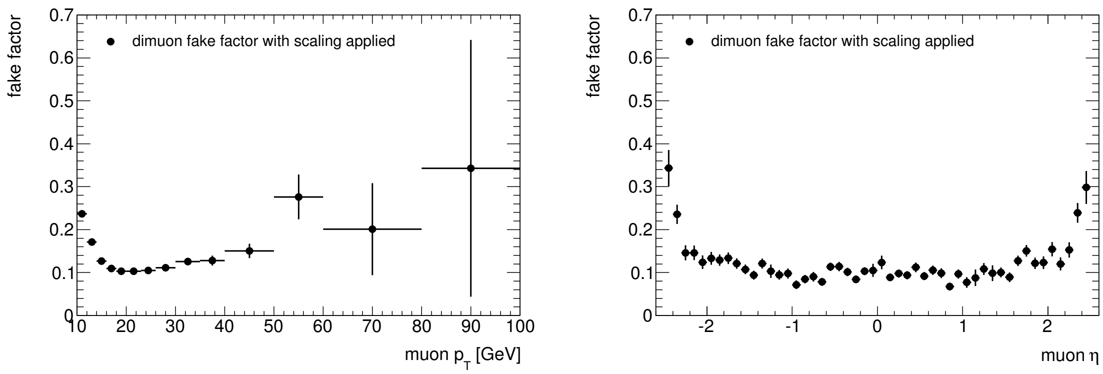

(a) (b)

Figure 9.23: Fake factor f as function of muon p_{T} and η after applying correction factor for high vs low impact parameter significance.

Since a fairly linear dependence of f is observed for muon $p_{\mathrm{T}} > 20$ GeV, a parametrization is used to overcome the low statistics for muon $p_{\mathrm{T}} > 50$ GeV. A first-order polynomial is fitted for muon $20 < p_{\mathrm{T}} < 100$ GeV. For lower p_{T} values the statistics are good and f is not parametrized. The fitted parametrization for the $20 < p_{\mathrm{T}} < 100$ GeV region is $0.05920 + 0.00197 \times p_{\mathrm{T}}(\mu)$. For $p_{\mathrm{T}} > 100$ GeV, where there are no statistics in data, f is assumed flat with 100% uncertainty. This assumption is justified by the change in the track isolation cut at 100 GeV, which loosens more slowly as a function of p_{T} in this region.

9.3.3.3 Systematic Uncertainty on *f*

Several effects are taken into account when determining the systematic uncertainty on f:

- Statistical uncertainty on the data (from limited statistics of anti-selected objects particularly at high muon p_{T}). This is given directly from data and ranges between $\pm 0.5 - 87\%$. For muon $p_{\mathrm{T}} > 100$ GeV, the statistics are very limited and a $\pm 100\%$ systematic uncertainty is assigned.
- Uncertainty on the subtraction of prompt contamination. This source of systematic uncertainty is determined by varying the MC prediction by $\pm 10\%$ which covers cross section and luminosity uncertainties. The resulting uncertainty ranges between $\pm 0.2\%$ (for $p_{\mathrm{T}} \sim 10$ GeV) to $\pm 27\%$ (for $p_{\mathrm{T}} \sim 100$ GeV).
- Uncertainty associated with the correction factor from low to high impact parameter significance. The full value of the correction is taken as an uncertainty, $\pm 34\%$.

- Uncertainty associated with non-prompt muons from heavy-flavor vs light-flavor. The non-prompt muon composition in data is estimated using a variable sensitive to the measured momentum loss between the Inner Detector and Muon Spectrometer. For LF mesons which decay outside the ID volume to produce muons, the distribution of this variable has a characteristic tail. Taking the shape of this variable from MC, an estimate of the LF and HF composition in data is performed. The difference in f between these sources is estimated in MC, and this allows estimating a $\pm15\%$ uncertainty on f in data.

Table 9.7 shows the systematic uncertainty in bins of muon p_{T} for the different sources together with the central value and the total error, and Fig. 9.24 shows f versus p_{T} with the total systematic uncertainty and linear parametrization.

Table 9.7: Muon fake factor f central values and uncertainties in bins of p_{T}, averaging over η.

p_{T} bin (GeV)	Cent Val	Total Err	Stat Err	Prompt Sub	$d_0/\sigma(d_0)$	LF/HF
[10, 12]	0.237	37.2%	0.5%	0.2%	34.0%	15.0%
[12, 14]	0.171	37.2%	0.8%	0.3%	34.0%	15.0%
[14, 16]	0.127	37.2%	1.2%	0.6%	34.0%	15.0%
[16, 18]	0.110	37.2%	1.6%	0.8%	34.0%	15.0%
[18, 20]	0.103	37.2%	2.3%	1.1%	34.0%	15.0%
[20, 23]	0.102	37.3%	2.3%	1.5%	34.0%	15.0%
[23, 26]	0.107	37.4%	3.5%	2.2%	34.0%	15.0%
[26, 30]	0.114	37.5%	4.5%	2.8%	34.0%	15.0%
[30, 35]	0.123	37.7%	5.4%	3.0%	34.0%	15.0%
[35, 40]	0.133	38.4%	8.9%	3.6%	34.0%	15.0%
[40, 50]	0.148	39.1%	11.2%	5.0%	34.0%	15.0%
[50, 60]	0.168	42.4%	18.9%	7.8%	34.0%	15.0%
[60, 80]	0.197	69.3%	53.2%	24.1%	34.0%	15.0%
[80, 100]	0.236	98.6%	87.3%	26.9%	34.0%	15.0%
[100, ...]	0.256	100%	-	-	-	-

9.3.4 Non-prompt Validation

Control regions enhanced in non-prompt leptons are selected in data to validate the non-prompt background estimates. Due to the inclusive nature of this analysis, there are no event level cuts which can be inverted to select these regions, so instead lepton selection requirements are loosened or inverted. An intermediate isolation selection is defined, where leptons are required to fail the analysis isolation cuts but pass a cut on the same variable 4 GeV looser. Because the analysis isolation cut has been failed, this selection is explicitly orthogonal to the analysis selection.

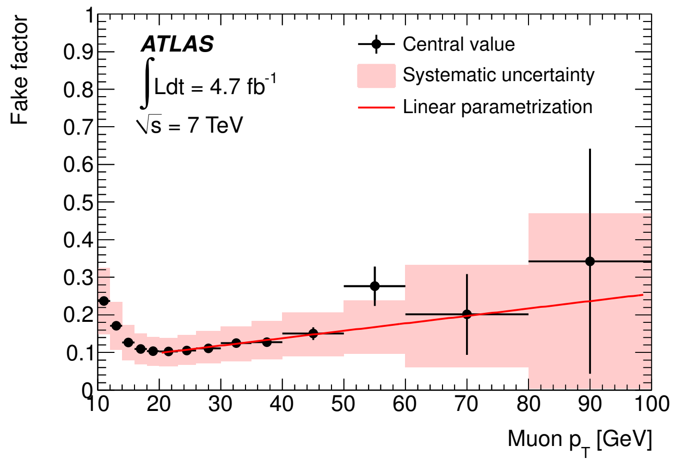

Figure 9.24: Fake factor f central value and combined total systematic uncertainty.

For muons, either the impact parameter is loosened or intermediate isolation is required. For electrons, intermediate isolation is used, and electron PID is also loosened in some regions to get more statistics. In others, electron ID is reversed. For these alternate selections, separate fake factors f are computed following the same method described in the above sections, replacing the "selected" definition with the relevant requirements.

Some of the regions are presented in Figures 9.25–9.27, which show the dilepton invariant mass for regions enhanced in non-prompt background, with the selections described in the captions. In total, 8, 5, and 4 regions are investigated in the $e^{\pm}e^{\pm}$, $\mu^{\pm}\mu^{\pm}$, and $e^{\pm}\mu^{\pm}$ channels respectively. In most of these regions, the data agree with prediction within the uncertainty on the non-prompt background. The largest deviations correspond to 1.2σ, 1.6σ, and 1.4σ in the $e^{\pm}e^{\pm}$, $\mu^{\pm}\mu^{\pm}$, and $e^{\pm}\mu^{\pm}$ channels respectively, including statistical and systematic errors, and given the large number of regions checked, these deviations are considered acceptable.

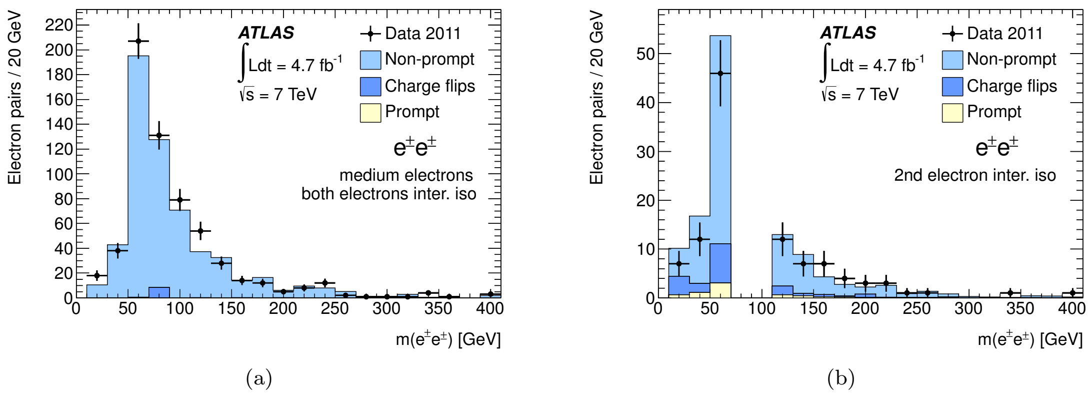

Figure 9.25: Invariant mass distributions for different $e^{\pm}e^{\pm}$ control regions enhanced in non-prompt lepton background. Figure (a) shows like-sign *Medium* electron pairs where both electrons satisfy intermediate isolation criteria. Figure (b) shows like-sign *Tight* electron pairs where the leading electron is fully isolated and the subleading electron satisfies intermediate isolation criteria. The last bin is an overflow bin.

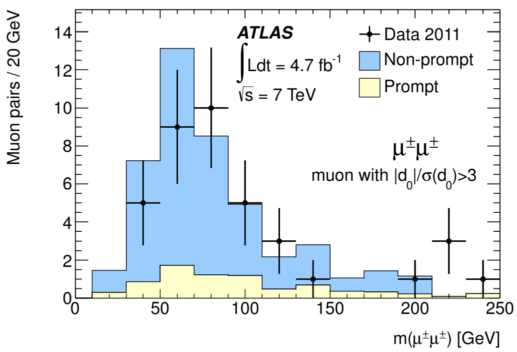

(a)

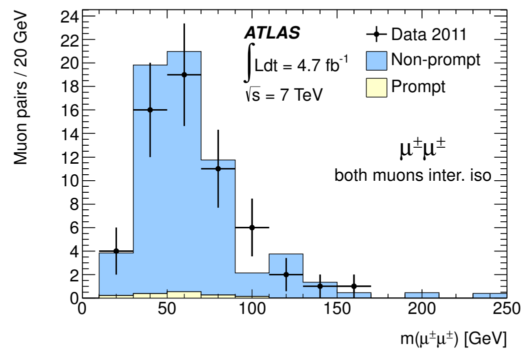

(b)

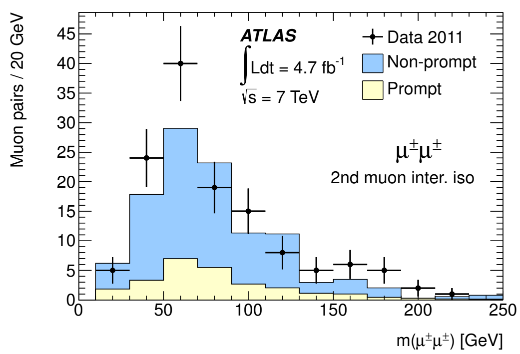

(c)

Figure 9.26: Invariant mass distributions for different $\mu^{\pm}\mu^{\pm}$ control regions enhanced in non-prompt lepton background. Figure (a) shows like-sign muon pairs, requiring $|d_0|/\sigma(d_0) > 3$ for ≥ 1 muon. Figure (b) shows like-sign muon pairs where both muons satisfy intermediate isolation criteria. Figure (c) shows like-sign muon pairs where the leading muon is fully isolated and the subleading muon satisfies intermediate isolation criteria. The last bin is an overflow bin.

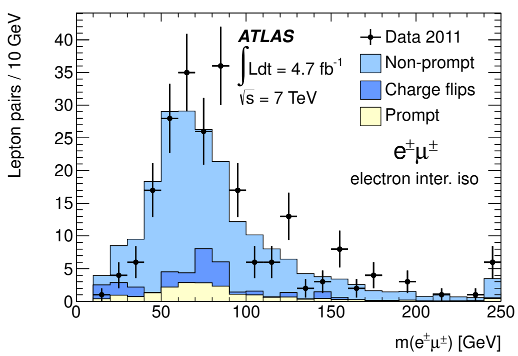

(a)

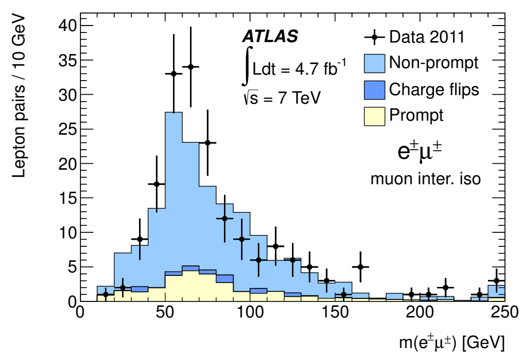

(b)

Figure 9.27: Invariant mass distributions for $e^{\pm}\mu^{\pm}$ control regions enhanced in non-prompt lepton background. Figure (a) shows like-sign $e\mu$ pairs where the electron is intermediately isolated and the muon is fully isolated. Figure (b) shows like-sign $e\mu$ pairs where the electron is fully isolated and the muon is intermediately isolated. The last bin is an overflow bin.

Chapter 10

Systematic Uncertainties

Several systematic effects can change the signal acceptance and background estimate, and the sources of these are described in the following sections. Table 10.1 summarizes the effects, with the processes whose predicted yields are affected by each source and the sizes of the uncertainties. Systematic uncertainties on different physics processes due to a given source are assumed to be 100% correlated.

10.1 Prompt Lepton Uncertainties

There are several systematic uncertainties on the estimated acceptance for signal as well as background processes involving prompt leptons. The uncertainties described below are assigned to all processes whose yields are estimated from MC, but not to data-driven predictions.

10.1.1 Lepton Identification Efficiency

The uncertainty on the lepton identification efficiency is largely taken from measurements by the ATLAS combined performance groups, which provide efficiencies and uncertainties for lepton reconstruction and identification, as well as trigger efficiencies and uncertainties for the triggers used in this analysis. The additional selection criteria described in Chapter 8 have associated uncertainties discussed below.

10.1.1.1 Electron Identification Efficiency

The uncertainties on the electron reconstruction and *Tight* identification efficiencies are estimated by the ATLAS electron/photon (e/gamma) combined performance group using primarily a tag-and-probe method on electrons from $Z \to ee$ [52]. For reconstruction, the uncertainties range from ±0.6–1.2%

depending on η, while for *Tight*, the uncertainties range from about ± 0.5–5% depending on both p_{T} and η.

Efficiency scale factors for the additional cuts used in this analysis (impact parameters and isolation) were evaluated using $Z \to ee$ tag-and-probe as described in Section 8.1.2. An additional systematic uncertainty of $\pm 1\%$ per electron to cover p_{T} and pileup dependence is assigned.

The impact on the number of expected events in the ee signal region for the backgrounds predicted from MC is ± 2–3% for reconstruction and *Tight* identification and $\pm 2\%$ for the additional cuts. In the $e\mu$ signal region, the effect is ± 1–2% for reconstruction and *Tight* ID and $\pm 1\%$ for the additional cuts.

10.1.1.2 Electron Identification in Fast Simulation

Some of the signal samples used in this analysis to calculate acceptance were simulated with the ATLAS fast simulation, AtlFastII. Studies were done comparing full simulation and AtlFastII by simulating a $H^{\pm\pm}H^{\mp\mp} \to \ell^{\pm}\ell^{\pm}\ell^{\mp}\ell^{\mp}$ sample with a mass of 300 GeV using each. Comparisons of the lepton kinematics show good agreement, and separate data/MC scale factors were derived in Section 8.1.2 differing from full simulation by about 1%. However, after all corrections are applied to the MC samples a 2% relative difference in efficiency per electron is observed between the 300 GeV $H^{\pm\pm}H^{\mp\mp}$ samples with full simulation and AtlFastII. The bulk of this disagreement was found to come from the data/MC scale factor for *Tight* identification at high electron p_{T}, and this disagreement is taken as an uncertainty ($\pm 2\%$ per electron).

10.1.1.3 Muon Identification Efficiency

The uncertainty on the muon reconstruction and identification efficiency, including the track quality requirements in the ID, is estimated by the ATLAS muon combined performance group using a tag-and-probe method on muons from $Z \to \mu\mu$ [92]. The uncertainty on the efficiency for these cuts depends on the η and p_{T} of the muon, and is generally $< 1\%$. This results in a $\pm 0.6\%$ uncertainty in the $\mu\mu$ signal region yield and a $\pm 0.3\%$ uncertainty for the $e\mu$ channel.

In addition to these standard quality cuts, this analysis imposes requirements on the impact parameter and the isolation. The efficiencies of these requirements are determined via the tag-and-probe method described in Section 8.2.1. Differences between data and MC of up to 2.5% are observed, depending on the p_{T} of the muon (see Fig. 8.14). The scale factors are applied to all Monte Carlo samples, and the full size of the scale factor is assessed as a systematic uncertainty. The p_{T} dependence of the scale factor is taken into account. The uncertainty of the signal region yield thus slightly depends on the process considered, since the p_{T} spectrum of the muons is process-dependent. The largest uncertainties observed are $\pm 2.4\%$ in the $\mu\mu$ channel and $\pm 1.3\%$ in the $e\mu$ channel, and this uncertainty is assigned to all prompt background processes. For signal processes, a higher uncertainty is observed due to the generally higher p_{T} of the muons. A systematic uncertainty of $\pm 2\%$ per muon is applied for these, with a total effect of $\pm 4\%$ in the $\mu\mu$ channel and $\pm 2\%$ in the $e\mu$ channel.

10.1.2 Lepton Momentum Measurement

The uncertainty in the momentum scale of the leptons results in an uncertainty on the number of events with two leptons passing the p_{T} and dilepton invariant mass cuts outlined in Chapter 8. Again, the ATLAS combined performance groups provide uncertainties on the momentum measurement [52, 93], and the differences in the signal region yields assessed are using systematically varied momentum measurements.

10.1.2.1 Muon Momentum Measurement

Due to the good momentum resolution of low p_{T} muons, the effect on the expected contributions in the signal region is very small, maximally 0.1%. A symmetric $\pm 0.1\%$ uncertainty is assigned for this effect for the $\mu\mu$ and $e\mu$ channels.

10.1.2.2 Electron Energy Measurement

The e/gamma group provides recommendations for energy scale and resolution variations. These variations result in uncertainties of generally up to $\pm 3.5\%$ for all backgrounds taken from MC in the ee channel. The exceptions are in the highest mass regions ($m > 300$ GeV), where the MC statistics are poor. As these variations can change the number of MC events passing the analysis selections, coupled with the low statistics, they end up having impacts of up to $\pm 10\%$ in the ee channel. The numbers in Table 10.1 reflect the effect only in bins with relatively high MC statistics. The impact on signal efficiency for the models considered is very small for each of these effects, $\pm 0.1\%$ or less.

10.1.3 Trigger Efficiency

The uncertainty on both the muon and electron trigger scale factors is estimated to be $< 1\%$ by the ATLAS electron and muon trigger groups [94, 95]. The resulting uncertainty on the yield in the signal region is smaller, since there are two leptons that can pass the trigger requirement. The uncertainty is evaluated to be $\pm 0.7\%$ for the $\mu\mu$ channel, $\pm 0.4\%$ or less for the $e\mu$ channel, and $\pm 0.2\%$ or less for the ee channel.

10.1.4 Integrated Luminosity

The total uncertainty on the integrated luminosity is taken to be ±3.9%, following [96].

10.2 Background Estimate Uncertainties

The following uncertainties are specific to the different background sources.

10.2.1 Like-sign Prompt Lepton Backgrounds

The prompt acceptance uncertainties defined above are also assigned to the prompt like-sign Standard Model backgrounds since they are estimated from MC. In addition, the uncertainty in the processes' production cross sections will affect the predicted yield of these backgrounds.

For WZ and ZZ production, an uncertainty of ±10% is estimated due to higher-order corrections by varying the renormalization and factorization scales by a factor of two. The uncertainty due to the parton distribution functions (PDFs) is evaluated using the eigenvectors provided by the CTEQ10 set [86] of PDFs using the prescription given in [12]. The difference between the central cross-section values obtained using this PDF set and that obtained with the MRST2008NLO PDFs [84] is also added in quadrature. This procedure gives a conservative estimate of the PDF uncertainty on the cross section of ±7%. For $t\bar{t}W$, $t\bar{t}Z$ and $W^{\pm}W^{\pm}$ production a normalization uncertainty of ±50% is assigned [66, 69].

10.2.2 Charge-flip Uncertainty

The details of the charge misidentification for electrons are described in Section 9.2.1, and the η-dependent scale factors and corresponding systematic uncertainties are listed in Table 9.3. In general the limited statistics drive this uncertainty.

Uncertainties on the production cross sections of the contributing processes are also considered. The PDF uncertainties for Z/γ^* and $t\bar{t}$ are computed using the MSTW2008 NNLO PDF sets [97] and the renormalization and factorization scales are varied by factors of two to derive the uncertainties due to higher-order QCD corrections. For Z/γ^*, an additional systematic uncertainty is attributed to electroweak corrections [72]. The total uncertainties on the Z/γ^* and $t\bar{t}$ cross sections are ±7% and +10/−11%, respectively. The $W^{\pm}W^{\mp}$ cross-section uncertainty is determined using the same scale and PDF variations as for WZ and ZZ, yielding a total uncertainty of ±12%.

The details for muons and the associated systematic are described in Section 9.2.2. The central value of the contribution from charge-flip background to the $\mu\mu$ signal region is estimated using

Monte Carlo samples and is found to be negligible. The systematic uncertainty is derived using the upper limit on the charge-flip probability as measured in data, which is applied to the MC samples with two opposite-sign prompt muons, yielding 4.9 events for $m(\mu\mu) > 15$ GeV and 1.7 events for $m(\mu\mu) > 400$ GeV.

10.2.3 Photons Reconstructed as Electrons

The process $W\gamma$, where the photon is reconstructed as an electron, is estimated from MC. As the underlying physics is the same as electron charge-flips (a material interaction where a photon converts to be reconstructed as an electron) the scale factor and uncertainty from the electron charge-flip background is applied to this process as well. This is conservative as charge-flips require an additional material interaction (brem emission) on top of a photon conversion reconstructed as an electron. This results in an uncertainty of ±12–18% on the signal region predictions of this background for the ee and $e\mu$ channels. The production cross section normalization and uncertainty for the $W\gamma$ process are taken from an ATLAS measurement [79], resulting in an uncertainty of ±14%.

10.2.4 Non-prompt Backgrounds

The systematic uncertainties on the non-prompt electron and muon backgrounds are derived in Sections 9.3.2.4–9.3.2.5 and 9.3.3.3. The total uncertainty for each encompass uncertainties in deriving the fake factors f as well as differences in non-prompt composition between the regions where f is derived compared to the regions where it is applied. For muons, all uncertainties are given as uncertainties on f, while for electrons, some uncertainties are given on f and others (the charge-flip overlap and light/heavy flavor composition) come from comparisons of alternate predictions in the signal region. In the $e\mu$ channel the electron and muon fake factor uncertainties are varied simultaneously.

The resulting uncertainty on the non-prompt background is evaluated separately in each mass bin where we set a limit. In the ee channel, it ranges from around ±15% for $m(ee) > 15$ GeV to ±40% for $m(ee) > 400$ GeV. For the $\mu\mu$ channel, it ranges from around ±34% for $m(\mu\mu) > 15$ GeV to ±100% for $m(\mu\mu) > 300$ GeV. In the $e\mu$ channel, it ranges from ±20% for $m(e\mu) > 15$ GeV to ±35% for $m(e\mu) > 400$ GeV.

10.2.5 Monte Carlo and Control Region Statistical Uncertainties

An additional source of systematic uncertainty is the limited statistics available in the MC samples and the data control samples used for the background predictions, with the values summarized in Table 10.1. These uncertainties are especially large in the high-mass bins.

Table 10.1: Sources of systematic uncertainty and their effect on predicted yields in the signal region for each individual channel followed by the sources common to all channels. The relative uncertainties give the impact on the relevant backgrounds only, not on the sum of all backgrounds. For instance, in the ee channel, the charge-flip scale factor uncertainty has a ±15–17% effect on the charge-flip background only. The range in numbers reflects their relative impact in different bins of invariant mass.

Channel	Source of uncertainty	Processes affected	Effect on prediction
ee	e reco, ID, trigger eff	Signal, Prompt, Charge-flips	±3–4%
	e energy scale, resolution		±0–5%
	Non-prompt region stats	Non-prompt	±12–100%
	e fake factor uncertainty		±14–40%
	e non-prompt/charge-flip		±11–25%
	e non-prompt LF/HF		±4–20%
	e charge-flip SF	Charge-flips	±15–17%
	γ reconstructed as e	$W\gamma$	±15–18%
	MC statistics	Prompt	±2–26%
		$W\gamma$	±14–100%
	e fastsim eff at high p_T	Signal	±4%
$\mu\mu$	μ ID, isolation, trigger eff	Signal, Prompt	±2.5–4.0%
	μ momentum measurement		±0.1%
	Non-prompt region stats	Non-prompt	±6–100%
	Fake factor uncertainty		±34–100%
	μ charge-flip rate	Charge-flips	4.9–1.7 events
	MC statistics	Prompt	±2–26%
$e\mu$	e reco, ID, trigger eff	Signal, Prompt, Charge-flips	±1.6–2.1%
	e energy scale, resolution		±1%
	μ ID, isolation, trigger eff	Signal, Prompt	±1.6–2.2%
	μ momentum measurement		±0.1%
	Non-prompt region stats	Non-prompt	±4–48%
	e/μ fake factor uncertainty		±20–35%
	e non-prompt/charge-flip		±18%
	e non-prompt LF/HF		±5–30%
	e charge-flip SF	Charge-flips	±14–17%
	γ reconstructed as e	$W\gamma$	±12–18%
	MC statistics	Prompt	±2–26%
		$W\gamma$	±14-100%
	e fastsim eff at high p_T	Signal	±2%
all	Luminosity	Signal, Prompt, Charge-flips	±3.9%
	Cross section	Drell-Yan	±7%
		WW, ZZ	±12%
		WZ	±12–15%
		$t\bar{t}$	+10/-11%
		$W^{\pm}W^{\pm}$, $t\bar{t}W$, $t\bar{t}Z$	±50%
		$W\gamma$	±14%
	MC statistics	Signal	±3%

Chapter 11

Results

The predicted numbers of background pairs are compared to the observed numbers of like-sign lepton pairs in Table 11.1. For the $e^{\pm}e^{\pm}$ final state, about 30% of the background is from prompt leptons in all mass bins, while for the $e^{\pm}\mu^{\pm}$ final state it is about 50%. The rest arises from leptons from non-prompt leptons or charge-flips. For the $\mu^{\pm}\mu^{\pm}$ final state, the prompt background constitutes about 83% of the total background for $m(\mu^{\pm}\mu^{\pm}) > 15$ GeV, rising to nearly 100% of the total background for $m(\mu^{\pm}\mu^{\pm}) > 400$ GeV. The overall uncertainty on the background is about $\pm 15\%$ at low mass and $\pm 30\%$ at high mass.

Table 11.2 shows the data compared to the background expectation separately for $\ell^{+}\ell^{+}$ and $\ell^{-}\ell^{-}$ events for each channel. The background is higher for the $\ell^{+}\ell^{+}$ final state due to the larger cross section in pp collisions for W^{+} than W^{-} bosons produced in association with γ, Z, or hadrons.

The level of agreement between the data and the background expectation is evaluated using $1-\mathrm{CL}_b$ [98], defined as the one-sided probability of the background-only hypothesis to fluctuate up to at least the number of observed events. Statistical and systematic uncertainties and their correlations are fully considered for this calculation. The largest upward deviation, observed for $m(\mu^{-}\mu^{-}) > 100$ GeV, occurs about 8% of the time in background-only pseudo-experiments for this mass bin. The statistical method used is described in more detail in Section 12.1.

Figure 11.1 shows the dilepton invariant mass spectra for the $e^{\pm}e^{\pm}$, $e^{\pm}\mu^{\pm}$, and $\mu^{\pm}\mu^{\pm}$ final states, while Figs. 11.2–11.4 shows the lepton p_{T} and η for each final state. Good agreement with the background expectation is observed for all three channels. Then the dilepton invariant mass spectra for each channel and each charge selection are shown in Figs. 11.5–11.6, and the lepton p_{T} and η for the charge-separated selections are shown in Figs. 11.7–11.12. In general, good agreement is observed in the $\ell^{+}\ell^{+}$ regions, while in the $\ell^{-}\ell^{-}$ regions, the data is larger than prediction for each channel though the effect is not statistically significant.

Table 11.1: Expected and observed numbers of pairs of isolated like-sign leptons for various cuts on the dilepton invariant mass, $m(\ell^\pm\ell^\pm)$. The uncertainties shown are the quadratic sum of the statistical and systematic uncertainties. The prompt background contribution includes the WZ, ZZ, $W^\pm W^\pm$, $t\bar{t}W$, and $t\bar{t}Z$ processes. When zero events are predicted, the uncertainty corresponds to the 68% CL upper limit on the prediction.

Sample	Number of electron pairs with $m(e^\pm e^\pm)$				
	> 15 GeV	> 100 GeV	> 200 GeV	> 300 GeV	> 400 GeV
Prompt	101 ± 13	56.3 ± 7.2	14.8 ± 2.0	4.3 ± 0.7	1.4 ± 0.3
Non-prompt	75 ± 21	28.8 ± 8.6	5.8 ± 2.5	$0.5^{+0.8}_{-0.5}$	$0.0^{+0.2}_{-0.0}$
Charge-flips and conversions	170 ± 33	91 ± 16	22.1 ± 4.4	8.0 ± 1.7	3.4 ± 0.8
Sum of backgrounds	346 ± 44	176 ± 21	42.8 ± 5.7	12.8 ± 2.1	4.8 ± 0.9
Data	329	171	38	10	3
	Number of muon pairs with $m(\mu^\pm\mu^\pm)$				
	> 15 GeV	> 100 GeV	> 200 GeV	> 300 GeV	> 400 GeV
Prompt	205 ± 26	90 ± 11	21.8 ± 2.8	5.8 ± 0.9	2.2 ± 0.4
Non-prompt	42 ± 14	12.1 ± 4.6	1.0 ± 0.6	$0.0^{+0.3}_{-0.0}$	$0.0^{+0.3}_{-0.0}$
Charge-flips	$0.0^{+4.9}_{-0.0}$	$0.0^{+2.5}_{-0.0}$	$0.0^{+1.8}_{-0.0}$	$0.0^{+1.7}_{-0.0}$	$0.0^{+1.7}_{-0.0}$
Sum of backgrounds	247^{+30}_{-29}	102 ± 12	$22.8^{+3.4}_{-2.9}$	$5.8^{+1.9}_{-0.9}$	$2.2^{+1.7}_{-0.4}$
Data	264	110	29	6	2
	Number of lepton pairs with $m(e^\pm\mu^\pm)$				
	> 15 GeV	> 100 GeV	> 200 GeV	> 300 GeV	> 400 GeV
Prompt	346 ± 43	157 ± 20	36.6 ± 4.7	10.8 ± 1.5	3.9 ± 0.6
Non-prompt	151 ± 47	45 ± 13	9.2 ± 4.1	2.6 ± 1.1	1.0 ± 0.6
Charge-flips and conversions	142 ± 28	33 ± 7	10.5 ± 2.8	2.9 ± 1.2	2.2 ± 1.1
Sum of backgrounds	639 ± 71	235 ± 25	56.4 ± 7.0	16.3 ± 2.3	7.0 ± 1.4
Data	658	259	61	17	7

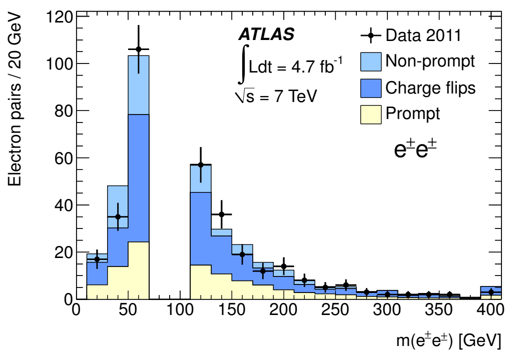

(a)

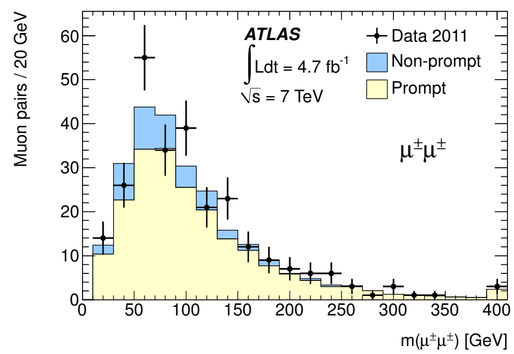

(b)

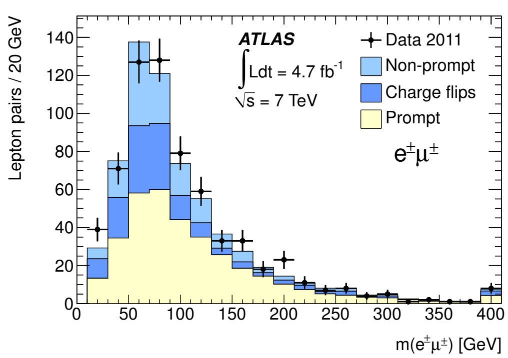

(c)

Figure 11.1: Invariant mass distributions for (a) $e^{\pm}e^{\pm}$, (b) $\mu^{\pm}\mu^{\pm}$, and (c) $e^{\pm}\mu^{\pm}$ pairs passing the full event selection. The data are shown as closed circles. The stacked histograms represent the backgrounds composed of pairs of prompt leptons from SM processes, pairs with at least one non-prompt lepton, and for the electron channels, backgrounds arising from charge misidentification and photon conversions. Events in the ee channel with invariant masses between 70 GeV and 110 GeV are excluded because of the large background from charge misidentification in $Z \to e^{\pm}e^{\mp}$ decays. The last bin is an overflow bin.

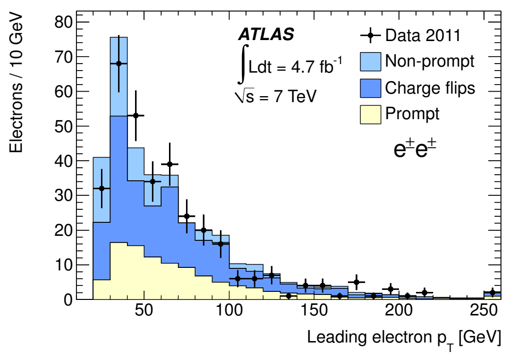

(a)

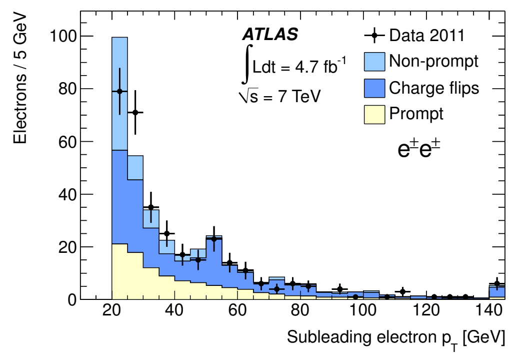

(b)

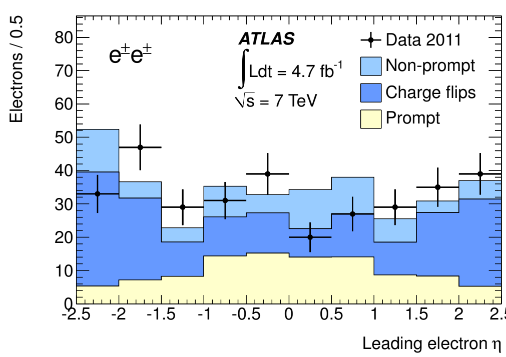

(c)

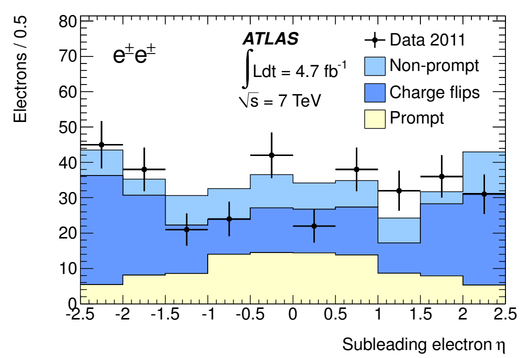

(d)

Figure 11.2: Distributions of (a) leading electron p_{T}, (b) subleading electron p_{T}, (c) leading electron η, and (d) subleading electron η for $e^{\pm}e^{\pm}$ pairs passing the full event selection. The data are shown as closed circles, and the stacked histograms represent the background predictions. The last bin in the plots of p_{T} is an overflow bin.

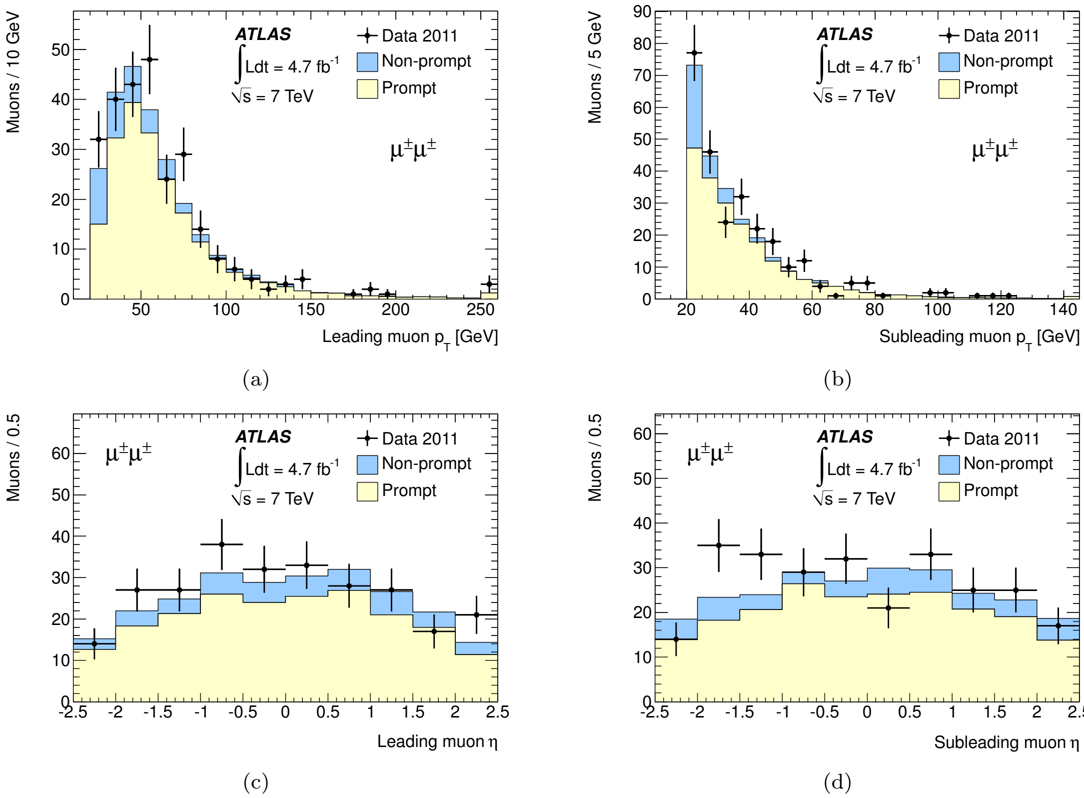

Figure 11.3: Distributions of (a) leading muon p_{T}, (b) subleading muon p_{T}, (c) leading muon η, and (d) subleading muon η for $\mu^{\pm}\mu^{\pm}$ pairs passing the full event selection. The data are shown as closed circles, and the stacked histograms represent the background predictions. The last bin in the plots of p_{T} is an overflow bin.

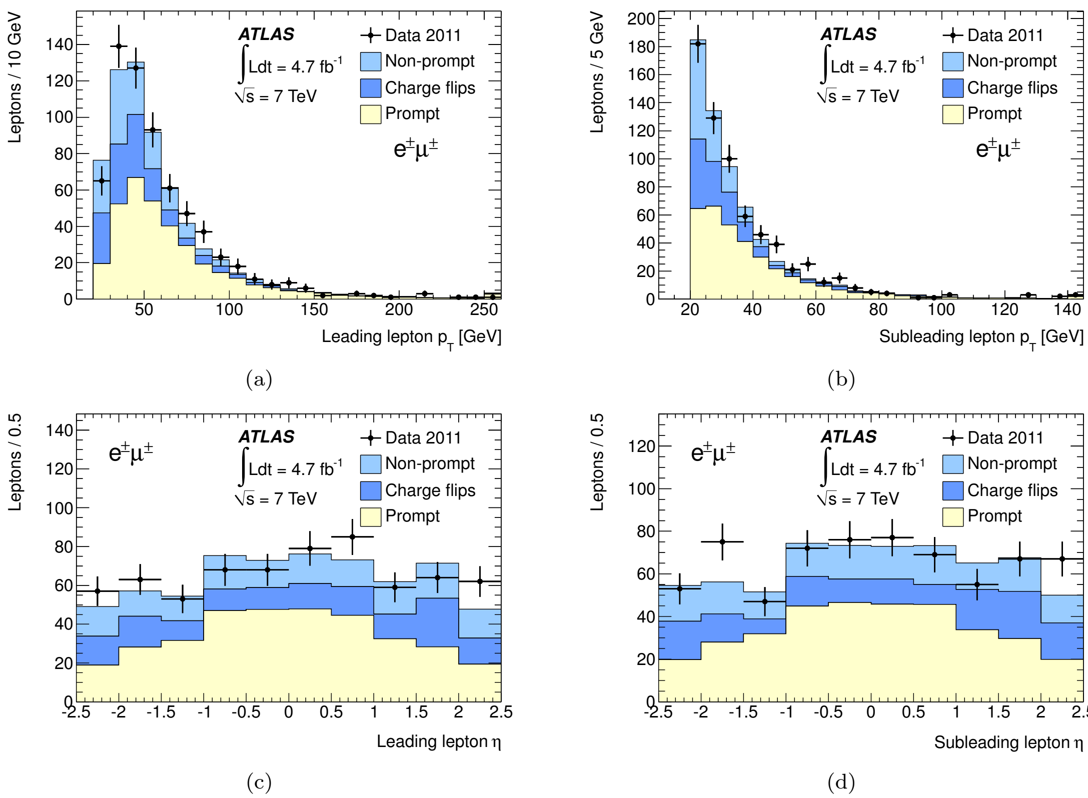

Figure 11.4: Distributions of (a) leading lepton p_{T}, (b) subleading lepton p_{T}, (c) leading lepton η, and (d) subleading lepton η for $e^{\pm}\mu^{\pm}$ pairs passing the full event selection. The data are shown as closed circles, and the stacked histograms represent the background predictions. The last bin in the plots of p_{T} is an overflow bin.

Table 11.2: Expected and observed numbers of positively- and negatively-charged lepton pairs for different lower limits on the dilepton invariant mass, $m(\ell^\pm\ell^\pm)$. The uncertainties shown are the quadratic sum of the statistical and systematic uncertainties.

Sample	Number of lepton pairs with $m(\ell^\pm\ell^\pm)$				
	> 15 GeV	> 100 GeV	> 200 GeV	> 300 GeV	> 400 GeV
	e^+e^+ pairs				
Sum of backgrounds	208 ± 28	112 ± 14	28.6 ± 4.0	8.5 ± 1.4	3.3 ± 0.7
Data	183	93	26	6	1
	e^-e^- pairs				
Sum of backgrounds	138 ± 21	63.3 ± 8.5	14.2 ± 2.3	4.4 ± 0.8	$1.54^{+0.4}_{-0.3}$
Data	146	78	12	4	2
	$\mu^+\mu^+$ pairs				
Sum of backgrounds	147 ± 17	$63.7^{+7.7}_{-7.6}$	$14.5^{+2.1}_{-1.9}$	$4.1^{+1.1}_{-0.6}$	$1.6^{+0.9}_{-0.3}$
Data	144	60	16	4	2
	$\mu^-\mu^-$ pairs				
Sum of backgrounds	100 ± 12	$38.4^{+5.0}_{-4.8}$	$8.3^{+1.5}_{-1.2}$	$1.7^{+0.9}_{-0.3}$	$0.6^{+0.9}_{-0.1}$
Data	120	50	13	2	0
	$e^+\mu^+$ pairs				
Sum of backgrounds	381 ± 42	142 ± 15	33.8 ± 5.3	9.8 ± 1.5	4.2 ± 0.9
Data	375	149	39	9	4
	$e^-\mu^-$ pairs				
Sum of backgrounds	259 ± 31	93 ± 10	22.6 ± 3.0	6.5 ± 1.3	2.9 ± 1.0
Data	283	110	22	8	3

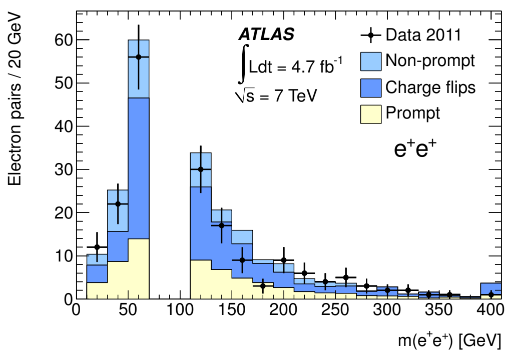

(a)

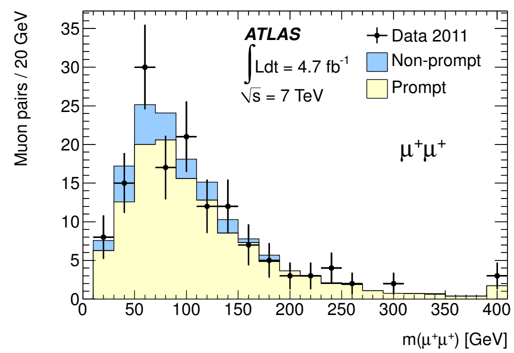

(b)

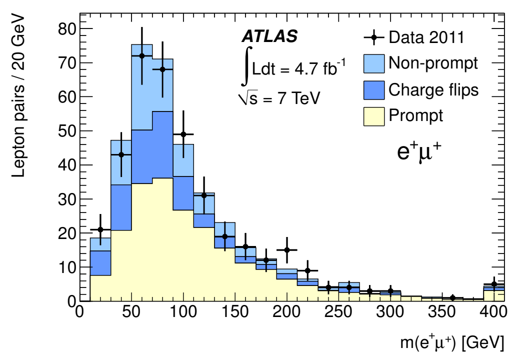

(c)

Figure 11.5: Invariant mass distributions for (a) e^+e^+, (b) $\mu^+\mu^+$, and (c) $e^+\mu^+$ pairs passing the full event selection. The data are shown as closed circles, and the stacked histograms represent the background predictions. The last bin is an overflow bin.

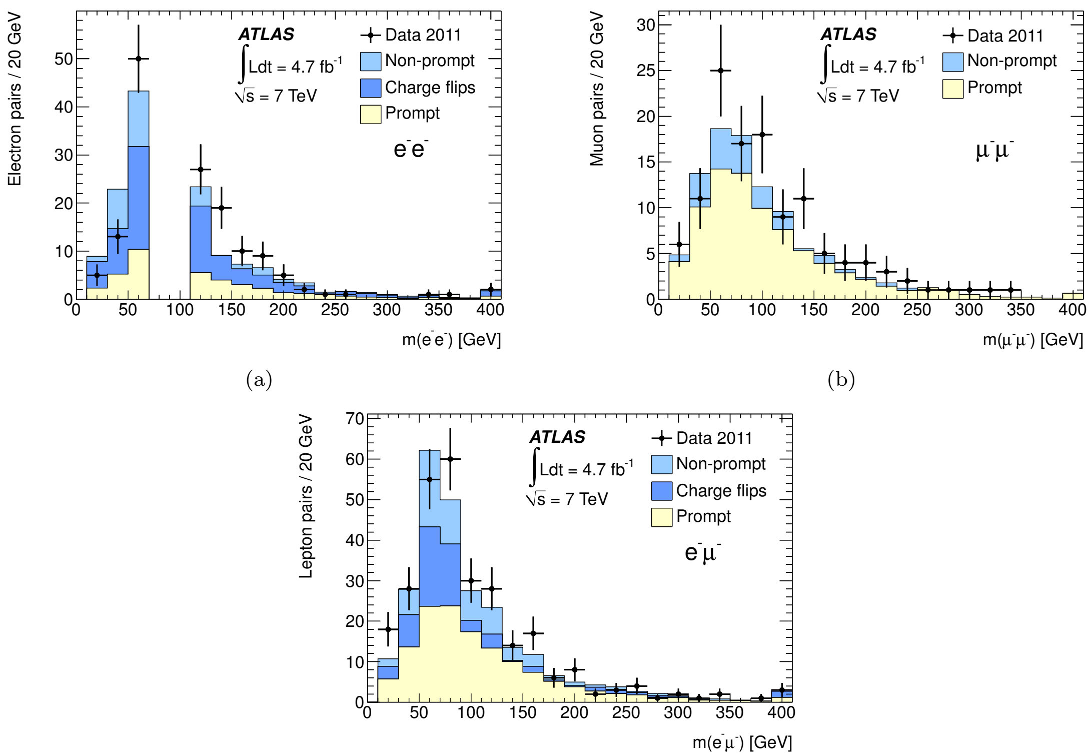

(a) (b) (c)

Figure 11.6: Invariant mass distributions for (a) e^-e^-, (b) $\mu^-\mu^-$, and (c) $e^-\mu^-$ pairs passing the full event selection. The data are shown as closed circles, and the stacked histograms represent the background predictions. The last bin is an overflow bin.

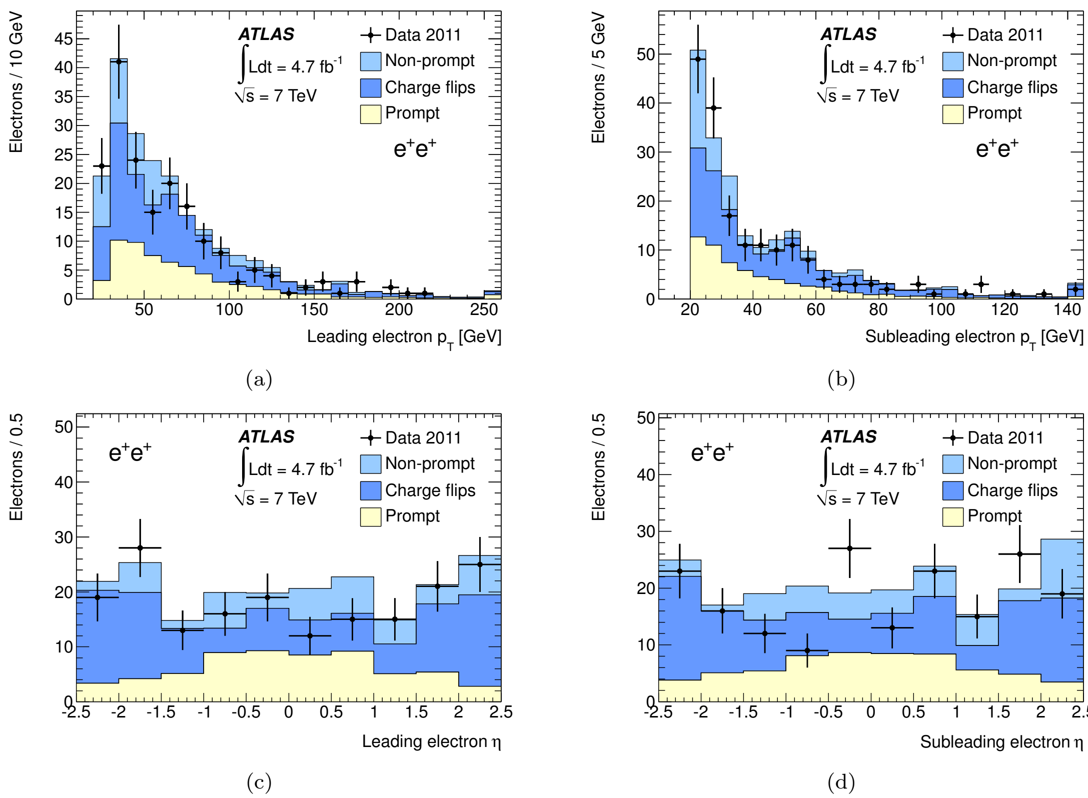

Figure 11.7: Distributions of (a) leading electron p_{T}, (b) subleading electron p_{T}, (c) leading electron η, and (d) subleading electron η for the e^+e^+ signal region. The last bin in the plots of p_{T} is an overflow bin.

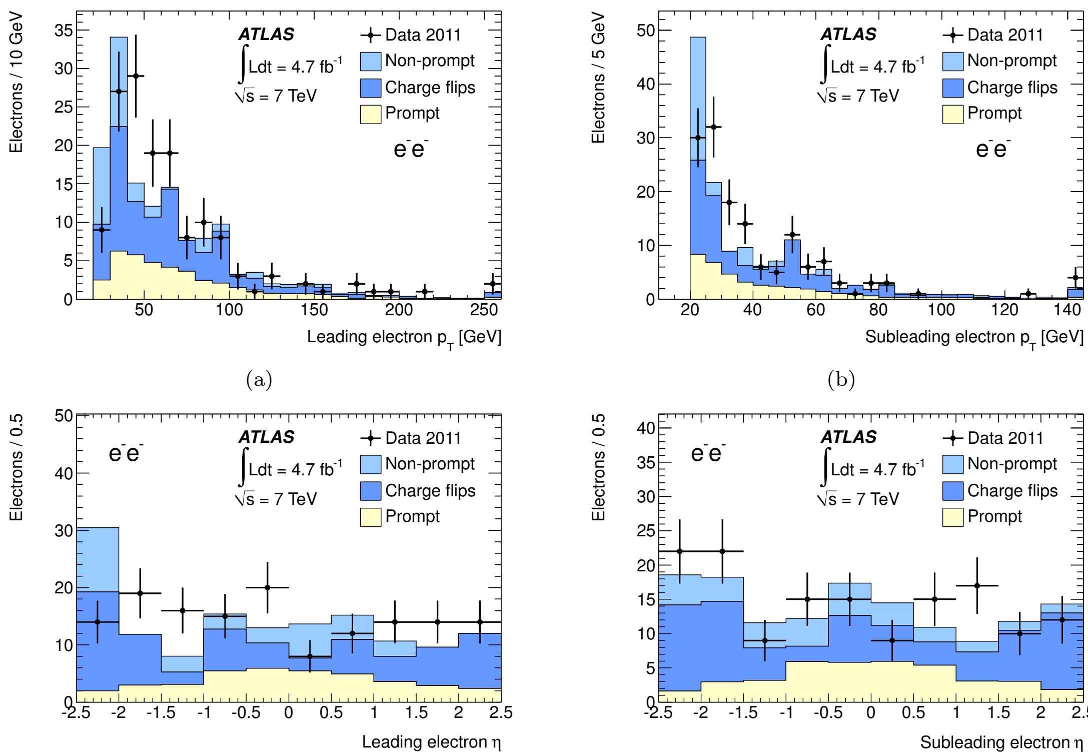

(a) (b) (c) (d)

Figure 11.8: Distributions of (a) leading electron p_{T}, (b) subleading electron p_{T}, (c) leading electron η, and (d) subleading electron η for the e^-e^- signal region. The last bin shown in the plots of p_{T} is an overflow bin.

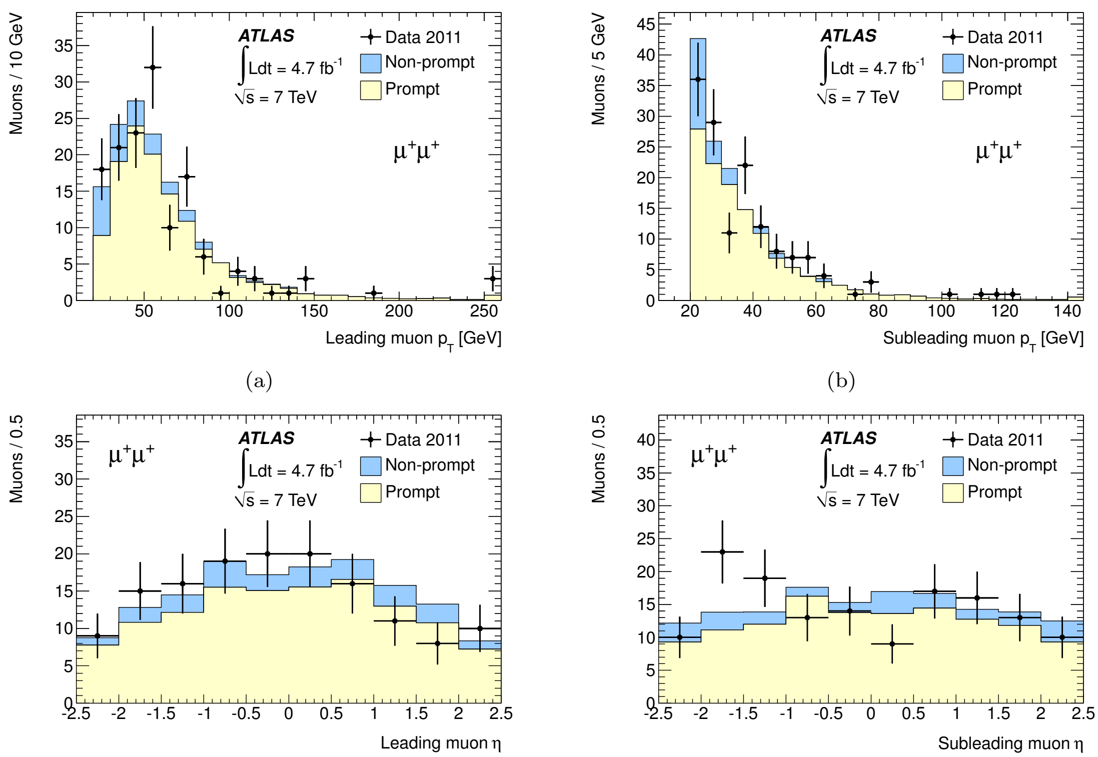

(a) (b) (c) (d)

Figure 11.9: Distributions of (a) leading muon p_{T}, (b) subleading muon p_{T}, (c) leading muon η, and (d) subleading muon η for the $\mu^+\mu^+$ signal region. The last bin in the plots of p_{T} is an overflow bin.

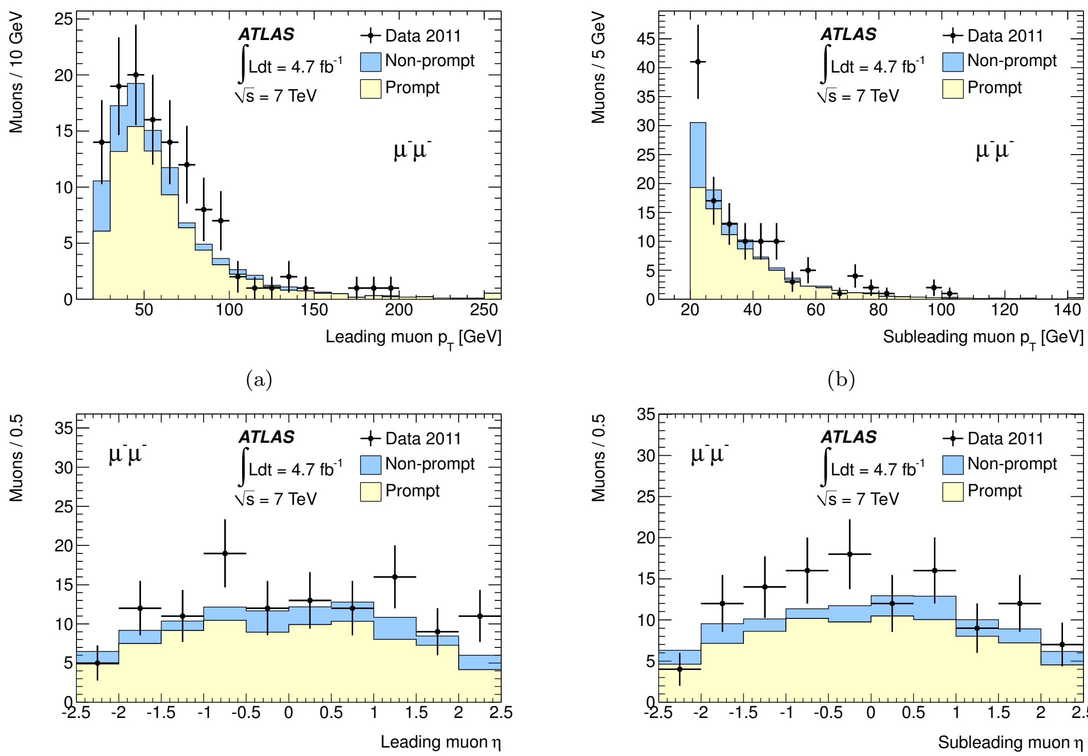

(a) (b) (c) (d)

Figure 11.10: Distributions of (a) leading muon p_{T}, (b) subleading muon p_{T}, (c) leading muon η, and (d) subleading muon η for the $\mu^-\mu^-$ signal region. The last bin shown in the plots of p_{T} is an overflow bin.

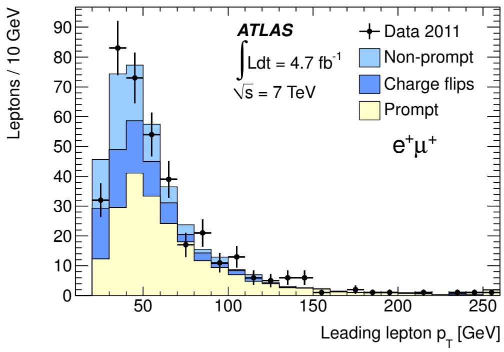

(a)

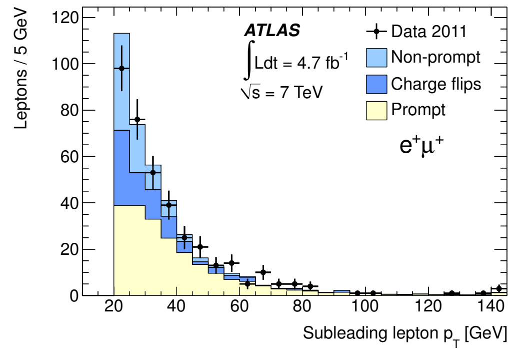

(b)

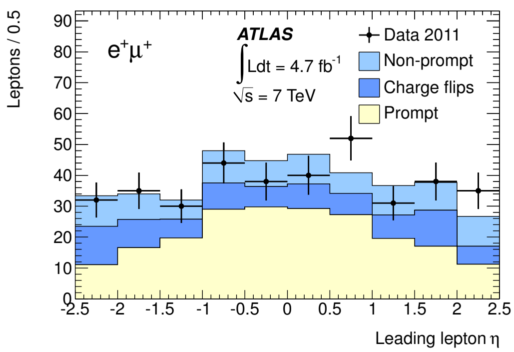

(c)

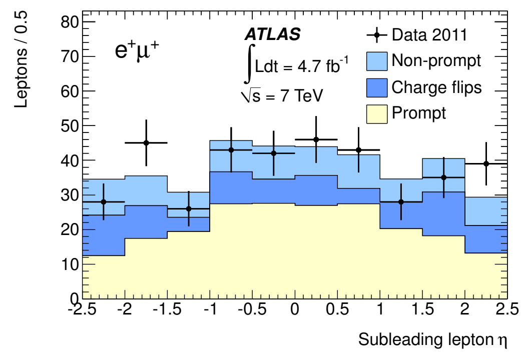

(d)

Figure 11.11: Distributions of (a) leading lepton p_{T}, (b) subleading lepton p_{T}, (c) leading lepton η, and (d) subleading lepton η for the $e^{+}\mu^{+}$ signal region. The last bin in the plots of p_{T} is an overflow bin.

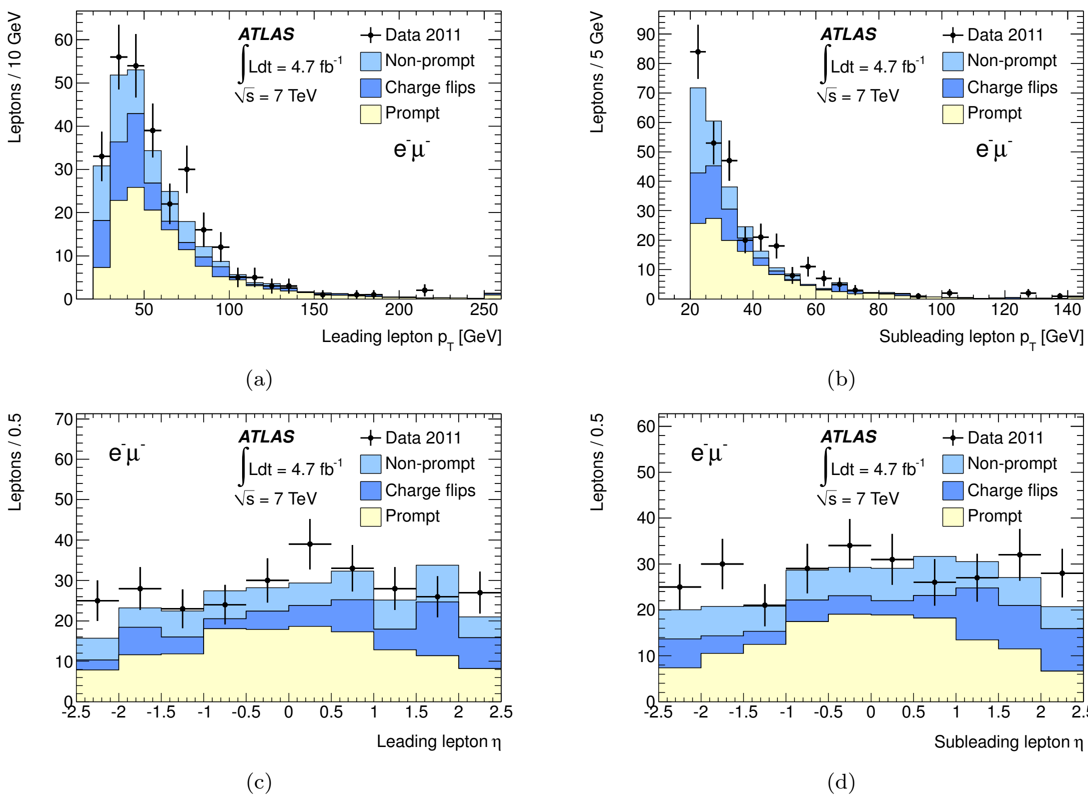

Figure 11.12: Distributions of (a) leading lepton p_{T}, (b) subleading lepton p_{T}, (c) leading lepton η, and (d) subleading lepton η for the $e^-\mu^-$ signal region. The last bin shown in the plots of p_{T} is an overflow bin.

Chapter 12

Model-Independent Cross Section Limits

12.1 Statistical Formalism

The CL_s method [98, 99] used in this analysis, also called the modified frequentist confidence level, is a ratio of two frequentist quantities. The numerator is CL_{s+b}, which quantifies the probability for finding the observed data given an expectation of signal plus background. The denominator is CL_b, which does the same with an expectation of background only. Writing this explicitly:

$$\mathrm{CL}_s \equiv \frac{\mathrm{CL}_{s+b}}{\mathrm{CL}_b} \tag{12.1}$$

The CL_{s+b} approach is a pure frequentist construction, but it has the undesirable property that if the observed data fluctuates lower than the expected background, it can be used to exclude any hypothesis at the considered confidence level (CL, usually taken to be 95%), even those to which the experiment should not have sensitivity. The CL_s approach of dividing by CL_b effectively penalizes experiments in the case of low sensitivity, and $\mathrm{CL}_s \geq \mathrm{CL}_{s+b}$, implying that the limit set is less stringent. The implementation of these methods is summarized in this section, and the following sections describe each step in more detail.

The first step in the CL_{s+b} method is constructing a likelihood for the number of observed events. This depends on the number of expected signal and background events, as well as typically on some systematic uncertainties on these numbers, called "nuisance parameters." A signal strength parameter, μ, is also introduced, simply a multiplicative factor for the expected number of signal events, which will allow this number to be scanned over. Once the likelihood is constructed, a test statistic is defined from it. This is taken to be a ratio of likelihoods: the likelihood to observe some number of events given a new physics hypothesis, H_1, divided by the likelihood given a null hypothesis, H_0.[22]

[22]This choice of test statistic is shown to be optimal by the Neyman-Pearson lemma [100].

In ATLAS, the H_0 hypothesis is taken to be the one which best describes the data, while in the LEP experiments, for instance, it was taken to be the background-only hypothesis.

For a given value of μ, pseudoexperiments are generated by choosing random values for the number of observed events and the nuisance parameters, using the likelihood as a probability density function (PDF). The test statistic is evaluated for each pseudoexperiment, creating a distribution of test statistic values. From this distribution and the value of the test statistic for the observed number of events, a p-value is computed, the probability to have observed a number of data events which is equally or less consistent with the given hypothesis (including a specific value of μ). This gives CL_{s+b}, and repeating the same procedure for background-only ($\mu = 0$) pseudoexperiments yields CL_b. Then Equation 12.1 can be used to compute CL_s.

By varying μ and repeating the pseudoexperiments, p-values are created for different values of μ, and from this ensemble one finds the value of μ corresponding to the desired value of CL_s. Using the actual number of observed events throughout this procedure gives what is called the observed limit.

The expected limit, defined as the limit that would be set if the data were due only to background, is an important quantity for estimating the sensitivity of a search. For each value of μ, the above procedure is applied to a set of simulated experiments, where the observed number of events in each simulated experiment is generated using a background-only hypothesis. This yields a distribution where the median value is the expected limit and from which the uncertainty bands can be computed.

12.1.1 Likelihood Definition

The simplest likelihood for a counting experiment, as is done in this search, is a Poisson distribution for the number of expected events given the expected signal and background counts. The Poisson distribution is:

$$P(k;\lambda) = \frac{e^{-\lambda}\lambda^k}{k!} \tag{12.2}$$

where k is the (observed) number of events and λ is the (expected) mean of the distribution. As a likelihood for the number of events given signal and background expectations:

$$L(N;\mu) = P(N;\mu \cdot s_{exp} + b_{exp}) \tag{12.3}$$

where N is the number of events, s_{exp} is the expected number of signal events, b_{exp} is the expected background, and μ is the signal strength as defined above. Here s_{exp} and b_{exp} are taken to be fixed numbers, while μ is a variable.

A more generic likelihood can be written which takes into account systematic uncertainties on s_{exp}

or b_{exp}. Assuming these systematic uncertainties are Gaussian, then the following can be written:

$$L(N, \boldsymbol{\Theta}; \mu, \boldsymbol{\theta}) = P(N; \mu \cdot s_{exp} \cdot \nu_s(\boldsymbol{\theta}) + b_{exp} \cdot \nu_b(\boldsymbol{\theta})) \cdot G(\boldsymbol{\theta}; \boldsymbol{\Theta}, 1) \tag{12.4}$$

Here, $\boldsymbol{\theta}$ is a vector of the nuisance parameters representing systematic uncertainties, and $\boldsymbol{\Theta}$ is a vector of "auxiliary measurements" or "global variables" which are measured, for instance in side-bands, and are used to constrain the systematic uncertainties. The function $G(\boldsymbol{\theta}; \boldsymbol{\Theta}, 1)$ represents a product of Gaussian functions with means $\boldsymbol{\Theta}$ and width 1 as parameters, and evaluated at $\boldsymbol{\theta}$ (for each nuisance parameter $\theta^i \in \boldsymbol{\theta}$). The functions $\nu_s(\boldsymbol{\theta})$ and $\nu_b(\boldsymbol{\theta})$ are "response functions" relating the nuisance parameters to the signal and background counts.

As a concrete example of a response function [101], suppose that there are two systematic uncertainties which can affect the expected background, on the cross section and on the acceptance, with corresponding nuisance parameters θ^{xsec} and θ^{acc}. If the values of these relative uncertainties are known (and symmetric), denoted Δ_{xsec} and Δ_{acc}, then the response function could be written as:

$$\nu_b(\boldsymbol{\theta}) = \nu_b(\theta^{xsec}, \theta^{acc}) = (1 + \mathrm{sign}(\theta^{xsec}) \cdot \Delta_{xsec})^{|\theta^{xsec}|} \cdot (1 + \mathrm{sign}(\theta^{acc}) \cdot \Delta_{acc})^{|\theta^{acc}|} \tag{12.5}$$

with constraint functions:

$$G(\boldsymbol{\theta}; \boldsymbol{\Theta}, 1) = G(\theta^{xsec}; \Theta^{xsec}, 1) \cdot G(\theta^{acc}; \Theta^{acc}, 1) \tag{12.6}$$

The means of the constraint Gaussians are the global observables Θ^{xsec} and Θ^{acc}. In the case of the observed data, if there are no side-bands to constrain these systematics, these will be 0. Then for example, the case $\theta^{xsec} = 1$ and $\theta^{acc} = 0$ would correspond to a upward fluctuation of the expected background by one standard deviation in the cross section uncertainty. Note here that the Δ_i are fixed numbers, while the θ^i and Θ^i are variables which are varied during the process of calculating the limit described below.

12.1.2 Test Statistic Definition

As mentioned above, for discriminating between hypotheses H_1 (new physics) and H_0 (null hypothesis), the optimal test statistic is:

$$q(N) \equiv \frac{L(N, \boldsymbol{\Theta}_{obs}; H_1)}{L(N, \boldsymbol{\Theta}_{obs}; H_0)} \tag{12.7}$$

For ATLAS searches, typically "profiling" is used to constrain the values of the nuisance parameters using the observed data [102] (and potentially side-band measurements, though not in this analysis). This removes the $\boldsymbol{\theta}$ dependence of the test statistic q. The vector of values $\boldsymbol{\Theta}_{obs}$ represents the evaluation points of the constraints from global observables. In this analysis, no side-bands are used so these are 0 for data but varied in pseudoexperiments as described below.

The hypothesis H_1 selects a fixed value for μ and maximizes $L(N, \mathbf{\Theta}_{obs}; \mu, \boldsymbol{\theta})$ by varying $\boldsymbol{\theta}$, obtaining a value $\hat{\hat{\boldsymbol{\theta}}}(\mu)$, which is called the conditional maximum likelihood estimator (MLE). The hypothesis H_0 is taken as the one which best matches the observed data. The likelihood $L(N, \mathbf{\Theta}_{obs}; \mu, \boldsymbol{\theta})$ is maximized varying both μ and $\boldsymbol{\theta}$, obtaining values $\hat{\mu}$ and $\hat{\boldsymbol{\theta}}$, with $\hat{\boldsymbol{\theta}}$ called the unconditional MLE.

Physical constraints are imposed on the test statistic: $\hat{\mu}$ is required to be non-negative to avoid a negative signal contribution. For $\hat{\mu} < 0$, μ is fixed to 0 and the likelihood is maximized to obtain $\hat{\hat{\boldsymbol{\theta}}}(0)$. Since $\hat{\mu}$ corresponds to the null hypothesis, μ is required to be larger than $\hat{\mu}$, and the test statistic is defined to be 0 for $\hat{\mu} > \mu$. Finally, the logarithm is taken of the likelihood ratio to ease computation, which is allowed since the logarithm is a monotonic function. The final test statistic is:

$$q(N;\mu) = \begin{cases} -2\ln\left(L(N, \mathbf{\Theta}_{obs}; \mu, \hat{\hat{\boldsymbol{\theta}}}(\mu))/L(N, \mathbf{\Theta}_{obs}; 0, \hat{\hat{\boldsymbol{\theta}}}(0))\right), & \text{if } \hat{\mu} < 0 \\ -2\ln\left(L(N, \mathbf{\Theta}_{obs}; \mu, \hat{\hat{\boldsymbol{\theta}}}(\mu))/L(N, \mathbf{\Theta}_{obs}; \hat{\mu}, \hat{\boldsymbol{\theta}})\right), & \text{if } 0 \le \hat{\mu} \le \mu \\ 0, & \text{if } \hat{\mu} > \mu \end{cases} \tag{12.8}$$

12.1.3 Pseudoexperiments and Observed Limit

To compute the confidence levels that are used to set limits, pseudoexperiments are employed to sample the distribution of the test statistic q for a given choice of μ, called $f(q_\mu)$. The fixed value of μ will be denoted μ_{fixed}. The likelihood $L(N, \mathbf{\Theta}; \mu_{fixed}, \hat{\hat{\boldsymbol{\theta}}}(\mu_{fixed}))$ is used as a PDF to generate values of N and $\mathbf{\Theta}$ for each pseudoexperiment. The values $\hat{\hat{\boldsymbol{\theta}}}(\mu_{fixed})$ come from maximizing $L(N_{obs}, \mathbf{\Theta}_{obs}; \mu_{fixed}, \boldsymbol{\theta})$, i.e. with N and $\mathbf{\Theta}$ fixed to the observed values in data.

The value of q_μ evaluated using N_{obs} and $\mathbf{\Theta}_{obs}$, called q_{obs}, falls somewhere in this distribution $f(q_\mu)$. To find the p-value of this observed point, the probability given the expected signal and background to find an excess as large or larger than N_{obs}, the integral of $f(q_\mu)$ is taken:

$$\mathrm{CL}_{s+b} \equiv P(q \ge q_{obs}; \mu_{fixed}) = \int_{q_{obs}}^{\infty} f(q)dq \tag{12.9}$$

This p-value is specific to the chosen value of μ_{fixed} used to generate the pseudoexperiments, as indicated in the equation. A signal hypothesis (i.e. value of μ_{fixed}) is excluded at the 95% CL if one finds that $\mathrm{CL}_{s+b} < \alpha$, where $\alpha = 0.05$. To find the observed 95% CL exclusion limit for μ using CL_{s+b}, one would choose different values of μ_{fixed} and repeat the pseudoexperiments for each μ_{fixed} value until finding $\alpha = 0.05$.

To compute CL_s, CL_b must also be computed. Pseudoexperiments are generated as above, but this time using $\mu = 0$ to reflect the background-only case, and $\hat{\hat{\boldsymbol{\theta}}}(0)$ from maximizing $L(N_{obs}, \mathbf{\Theta}_{obs}; 0, \boldsymbol{\theta})$ is used. Thus the PDF used to generate values of N and $\boldsymbol{\Theta}$ is $L(N, \boldsymbol{\Theta}; 0, \hat{\hat{\boldsymbol{\theta}}}(0))$. Again the distribution $f(q_0)$ is formed, then CL_b is calculated as:

$$\mathrm{CL}_b \equiv 1 - P(q \leq q_{obs}; \mu_{fixed}) = 1 - \int_{-\infty}^{q_{obs}} f(q)dq \tag{12.10}$$

where $P(q \leq q_{obs}; \mu_{fixed})$ is the p-value of the background-only hypothesis. Note that $f(q_0)$ does not depend here on μ_{fixed} since it comes from background-only pseudoexperiments, but the observed test-statistic value q_{obs} does depend on μ_{fixed}.

Then CL_s is computed using Equation 12.1 for each μ_{fixed}, and similarly to CL_{s+b}, a μ_{fixed} value is excluded at the 95% CL if one finds that $\mathrm{CL}_s < 0.05$. Thus one must iterate μ to find the value excluded at 95% CL, called μ_{up}^{95}.

12.1.4 Expected Limit and Uncertainty Bands

The calculation of the expected limits proceeds similarly to the procedure described in the previous section. There is one additional step at the beginning: first simulated experiments are generated using $L(N, \boldsymbol{\Theta}; 0, \hat{\hat{\boldsymbol{\theta}}}(0))$ as the PDF, where $\hat{\hat{\boldsymbol{\theta}}}(0)$ has been optimized using the observed data N_{obs}. For each simulated experiment, the generated values N_{gen} and $\boldsymbol{\Theta}_{gen}$ are used instead of N_{obs} and $\boldsymbol{\Theta}_{obs}$ in the procedure described in Section 12.1.3 to evaluate μ_{up}^{95}. A distribution $g(\mu_{up}^{95})$ is then formed from the set of simulated experiments. The median of this distribution is the expected limit, and to find the uncertainty bands corresponding to 68% and 95% deviations from the expected limit, the distribution $g(\mu_{up}^{95})$ is integrated accordingly.

12.2 Limits on Number of Events

As no significant deviations from SM expectations are observed in the signal regions considered for this analysis, upper limits are placed on contributions due to processes from physics beyond the SM. Limits are derived independently in each final state and mass bin shown in tables 11.1 and 11.2. The 95% CL upper limit on the number of events, N_{up}^{95}, is determined using the CL_s method described in the previous section.[23] For the inclusive $\ell^{\pm}\ell^{\pm}$ final states, the upper limit ranges from 168 pairs for $m(e^{\pm}\mu^{\pm}) > 15$ GeV to 4.8 pairs for $m(\mu^{\pm}\mu^{\pm}) > 400$ GeV.

[23] The limit on signal strength, μ_{up}^{95}, which comes out of the limit procedure described in Section 12.1, is converted to a number of events, called here N_{up}^{95}.

12.3 Fiducial Cross Section Limits

The limit on the number of lepton pairs can be translated to an upper limit on the cross section measured in a given region of phase space (referred to here as the fiducial region), σ^{95}_{fid}, via

$$\sigma^{95}_{\text{fid}} = \frac{N^{95}_{up}}{\varepsilon_{\text{fid}} \cdot \mathcal{L}_{\text{int}}} \tag{12.11}$$

where ε_{fid} is the efficiency for detecting events within the fiducial region and $\mathcal{L}_{\text{int}}$ is the integrated luminosity of 4.7 fb^{-1}.

The fiducial region definition is based on MC generator information such that it is independent of the ATLAS detector environment, and the definition is chosen to both mirror the analysis criteria applied after ATLAS reconstruction and also minimize differences in ε_{fid} among potential signal models. The primary sources of different lepton pair efficiencies in potential signal models are the p_{T} dependence of the lepton identification efficiency and the isolation efficiency, which depends on the hadronic activity in the events. The chosen definition as well as observed values of ε_{fid} for various models are given in the following sections, followed by the resulting cross section limits σ^{95}_{fid}.

12.3.1 Fiducial Definition

The lepton p_{T} and η cuts and the dilepton invariant mass cuts in the fiducial definition are the same as those applied at the reconstruction level. These cuts serve to reduce the dependence of ε_{fid} on the lepton kinematics. To emulate the impact parameter requirements imposed in the analysis, electrons or muons are selected as stable particles that originate from a W or Z boson, from a τ lepton, or from an exotic new particle (e.g. a $H^{\pm\pm}$ or a right-handed W).

The track isolation requirements are also emulated at the fiducial level to reduce the dependence of ε_{fid} on the level of hadronic activity in the events. The generator-level track isolation, $p_{\text{T}}^{cone\Delta R_{iso}}$, is defined as the scalar sum of all stable charged particles with $p_{\text{T}} > 1$ GeV in a cone of size ΔR_{iso} around the electron or muon, excluding the lepton itself. The same requirements are placed on this variable as the reconstructed track isolation. The calorimeter isolation variable used for electrons is dominated by calorimeter noise for prompt electrons. Thus it is not well reproduced at the generator level and is not emulated here. The requirement on $\Delta R(\ell, \text{jet}) > 0.4$ was also investigated and found to make a small impact on ε_{fid}, so it is not applied.

The fiducial definition for the leptons is summarized in Table 12.1. In addition to these, the analysis requirements are imposed on the lepton charges and the dilepton invariant mass for each final state, requiring $m(\ell^{\pm}\ell^{\pm}) > 15$ GeV and for $e^{\pm}e^{\pm}$ excluding the mass range 70–110 GeV.

Table 12.1: Summary of requirements on generated leptons in the fiducial region. The definition of the isolation variable, $p_{\mathrm{T}}^{cone\Delta R_{iso}}$, is given in the text. In addition to these, the analysis requirements are imposed on the lepton charges and the dilepton invariant mass for each final state.

	Electron requirement	Muon requirement
Leading lepton p_{T}	$p_{\mathrm{T}} > 25$ GeV	$p_{\mathrm{T}} > 20$ GeV
Sub-leading lepton p_{T}	$p_{\mathrm{T}} > 20$ GeV	$p_{\mathrm{T}} > 20$ GeV
Lepton η	$\lvert\eta\rvert < 1.37$ or $1.52 < \lvert\eta\rvert < 2.47$	$\lvert\eta\rvert < 2.5$
Isolation	$p_{\mathrm{T}}^{cone0.3}/p_{\mathrm{T}} < 0.1$	$p_{\mathrm{T}}^{cone0.4}/p_{\mathrm{T}} < 0.06$ and $p_{\mathrm{T}}^{cone0.4} < 4\text{ GeV} + 0.02 \times p_{\mathrm{T}}$

12.3.2 Fiducial Efficiencies

The fiducial efficiency, ε_{fid} is defined as the fraction of lepton pairs passing the fiducial selection described above that also satisfy the experimental selection criteria described in Chapter 8. In order to set a model independent limit, ε_{fid} should ideally be stable across a number of potential signal models. To check this, ε_{fid} has been calculated for the following models:

- Pair production and leptonic decay of doubly charged Higgs bosons. A number of different values for $m(H^{\pm\pm})$ were used. These samples represent topologies with little activity outside the isolated leptons.
- A single sample of pair production of a like-sign right-handed top quark ($t_R t_R$) through a flavor-changing neutral Z' boson.
- Pair production of heavy down-type quarks (d_4) which both subsequently decay into tW. Samples with $m(d_4)$ = 300, 350, 400, 450 and 500 GeV were utilized. With many final state jets, this model is used as an example of a busy topology.
- Single production of a right-handed W_R boson which subsequently decays into a lepton and a Majorana neutrino (N_R), with the neutrino further decaying into a lepton and jet (see Fig. 2.5). A number of samples with various masses for W_R and N are utilized. This topology is used as it includes jets, sometimes near leptons, as well as isolated leptons in its final state.

The motivations for each of these models are described in more detail in Section 2.4.

The calculated values of ε_{fid} for these models with various requirements on the dilepton invariant mass are shown in Tables 12.2–12.4 for each channel. The largest variation is observed in the $e^{\pm}e^{\pm}$ channel, where ε_{fid} ranges between about 43% to 67%. This is largely due to the p_{T}-dependent efficiency of the *Tight* electron ID requirement, which varies by about 15% over the relevant p_{T} range, increasing at higher p_{T} [52]. There is unfortunately no way to emulate these requirements at the fiducial level to mitigate this dependence. In the $\mu^{\pm}\mu^{\pm}$ channel the observed variation is smaller, about 59% to 72%, and the variation in the $e^{\pm}\mu^{\pm}$ channel is intermediate between these, about 55% to 71%. The efficiencies are also checked separately for $\ell^{+}\ell^{+}$ and $\ell^{-}\ell^{-}$ pairs, and the results are consistent with the charge inclusive case.

12.3.2.1 Fiducial Leakage

Another consideration in the choice of a fiducial definition is the fiducial leakage, the efficiency of selecting events at the reconstruction level which fall outside the MC generator fiducial region. It is defined here as the number of pairs that passed analysis selection cuts, but not the fiducial cuts, divided by the number of pairs that passed the analysis cuts irrespective of whether they passed the fiducial cuts. A high leakage value would mean that the fiducial definition is excluding events that the analysis should actually be sensitive to.

This leakage is computed on for the same signal models as $\varepsilon_{\mathrm{fid}}$, with the results shown in Tables 12.5–12.7. The leakage values range from about 2–9% for the $e^{\pm}e^{\pm}$ channel, 0.2–6% for $\mu^{\pm}\mu^{\pm}$, and 1–8% for $e^{\pm}\mu^{\pm}$. The largest leakage values come from models with low-p_{T} leptons and substantial hadronic activity. Separating into $\ell^{+}\ell^{+}$ and $\ell^{-}\ell^{-}$ pairs gives consistent results.

12.3.3 Cross Section Limits

Given the observed variation in $\varepsilon_{\mathrm{fid}}$, the lowest value of $\varepsilon_{\mathrm{fid}}$ is chosen in each channel to set conservative model-independent cross section limits. Equation 12.11 is used to compute the 95% CL upper limits on the fiducial cross section for like-sign lepton pair production beyond the SM. The expected and observed limits are given in Table 12.8 for each channel and mass threshold considered as well as the signal regions separated into $\ell^{+}\ell^{+}$ and $\ell^{-}\ell^{-}$ pairs. For the regions with $\ell^{\pm}\ell^{\pm}$ pairs, the observed cross section limits range from 64.1 fb for $m(e^{\pm}\mu^{\pm}) > 15$ GeV to 1.7 fb for $m(\mu^{\pm}\mu^{\pm}) > 400$ GeV. The expected and observed limits for all regions considered are also shown in Figs. 12.1–12.3.

Table 12.2: Fiducial efficiency ε_{fid} (%) in the $e^{\pm}e^{\pm}$ final state for several potential signal models. The uncertainties are statistical. Entries listed as "n/a" have too few lepton pairs in that bin to form a meaningful selection efficiency. Due to the exclusion of the mass range $70 < m(ee) < 110$ GeV, the $e^{\pm}e^{\pm}$ channel is not sensitive to the $H^{\pm\pm}$ with mass 100 GeV. The lowest observed efficiency value, used in the analysis, is highlighted in bold face.

	Fiducial efficiency (%)			
Model	$m > 15$ GeV	$m > 100$ GeV	$m > 200$ GeV	$m > 300$ GeV
$H^{\pm\pm}$ ($m = 50$ GeV)	**43.4 ± 1.5**	n/a	n/a	n/a
$H^{\pm\pm}$ ($m = 100$ GeV)	n/a	n/a	n/a	n/a
$H^{\pm\pm}$ ($m = 150$ GeV)	57.8 ± 1.1	58.4 ± 1.1	n/a	n/a
$H^{\pm\pm}$ ($m = 200$ GeV)	60.1 ± 1.0	60.4 ± 1.1	n/a	n/a
$H^{\pm\pm}$ ($m = 250$ GeV)	61.0 ± 1.0	61.2 ± 1.0	63.5 ± 1.1	n/a
$H^{\pm\pm}$ ($m = 300$ GeV)	62.0 ± 1.0	62.2 ± 1.0	64.2 ± 1.1	n/a
$H^{\pm\pm}$ ($m = 350$ GeV)	61.8 ± 1.3	61.9 ± 1.3	63.9 ± 1.4	66.2 ± 1.5
$H^{\pm\pm}$ ($m = 400$ GeV)	62.3 ± 1.0	62.4 ± 1.0	63.6 ± 1.1	65.5 ± 1.1
$H^{\pm\pm}$ ($m = 1000$ GeV)	62.9 ± 1.1	62.9 ± 1.1	63.2 ± 1.1	64.0 ± 1.1
$t_R t_R$	50.5 ± 1.5	50.8 ± 1.5	52.3 ± 1.8	55.0 ± 2.1
d_4 (300 GeV)	47.9 ± 2.5	52.2 ± 3.3	50.7 ± 7.2	n/a
d_4 (350 GeV)	50.0 ± 2.7	54.0 ± 3.3	58.9 ± 6.2	n/a
d_4 (400 GeV)	52.5 ± 2.3	56.5 ± 2.8	62.4 ± 5	62.5 ± 9.7
d_4 (450 GeV)	50.7 ± 2.4	53.4 ± 2.8	59.2 ± 4.7	57.8 ± 8.2
d_4 (500 GeV)	51.3 ± 1.8	54.0 ± 2.1	60.2 ± 3.4	60.9 ± 5.6
W_R ($m(W_R) = 800$ GeV, $m(N_R) = 100$ GeV)	57.6 ± 2.3	57.7 ± 2.3	58.2 ± 2.4	60.1 ± 2.7
W_R ($m(W_R) = 800$ GeV, $m(N_R) = 300$ GeV)	61.8 ± 1.4	62.2 ± 1.5	63.5 ± 1.6	64.4 ± 1.8
W_R ($m(W_R) = 800$ GeV, $m(N_R) = 500$ GeV)	62.2 ± 1.9	62.5 ± 2.0	63.7 ± 2.2	66.4 ± 2.8
W_R ($m(W_R) = 1000$ GeV, $m(N_R) = 200$ GeV)	57.6 ± 2.0	57.7 ± 2.0	58.5 ± 2.1	59.5 ± 2.2
W_R ($m(W_R) = 1000$ GeV, $m(N_R) = 500$ GeV)	63.4 ± 2.0	63.5 ± 2.0	64.9 ± 2.1	66.3 ± 2.4
W_R ($m(W_R) = 1000$ GeV, $m(N_R) = 800$ GeV)	60.2 ± 2.8	60.5 ± 2.8	61.6 ± 3.1	62.8 ± 3.9
W_R ($m(W_R) = 1200$ GeV, $m(N_R) = 200$ GeV)	60.8 ± 2.1	60.7 ± 2.1	61.0 ± 2.1	62.5 ± 2.3
W_R ($m(W_R) = 1200$ GeV, $m(N_R) = 600$ GeV)	65.1 ± 2.0	65.3 ± 2.0	66.2 ± 2.1	67.2 ± 2.2
W_R ($m(W_R) = 1200$ GeV, $m(N_R) = 1000$ GeV)	63.8 ± 2.0	64.3 ± 2.0	65.2 ± 2.2	65.4 ± 2.6
W_R ($m(W_R) = 1500$ GeV, $m(N_R) = 300$ GeV)	61.5 ± 2.0	61.6 ± 2.0	62.3 ± 2.1	63.4 ± 2.1
W_R ($m(W_R) = 1500$ GeV, $m(N_R) = 800$ GeV)	65.3 ± 1.9	65.4 ± 1.9	65.8 ± 2.0	66.5 ± 2.1
W_R ($m(W_R) = 1500$ GeV, $m(N_R) = 1300$ GeV)	63.6 ± 1.9	63.8 ± 2.0	64.0 ± 2.1	65.0 ± 2.4

Table 12.3: Fiducial efficiency ε_{fid} (%) in the $\mu^{\pm}\mu^{\pm}$ final state for several potential signal models. The uncertainties are statistical. Entries listed as "n/a" have too few lepton pairs in that bin to form a meaningful selection efficiency. The lowest observed efficiency value, used in the analysis, is highlighted in bold face.

	Fiducial efficiency (%)			
Model	$m > 15$ GeV	$m > 100$ GeV	$m > 200$ GeV	$m > 300$ GeV
$H^{\pm\pm}$ ($m = 50$ GeV)	72.9 ± 2.0	n/a	n/a	n/a
$H^{\pm\pm}$ ($m = 100$ GeV)	71.1 ± 1.3	n/a	n/a	n/a
$H^{\pm\pm}$ ($m = 150$ GeV)	69.1 ± 1.1	70.7 ± 1.2	n/a	n/a
$H^{\pm\pm}$ ($m = 200$ GeV)	66.7 ± 1.1	67.6 ± 1.1	n/a	n/a
$H^{\pm\pm}$ ($m = 250$ GeV)	66.2 ± 1.0	66.9 ± 1.1	69.1 ± 1.1	n/a
$H^{\pm\pm}$ ($m = 300$ GeV)	65.3 ± 1.0	65.7 ± 1.0	67.6 ± 1.1	n/a
$H^{\pm\pm}$ ($m = 350$ GeV)	63.5 ± 1.3	63.8 ± 1.3	65.2 ± 1.4	67.7 ± 1.5
$H^{\pm\pm}$ ($m = 400$ GeV)	62.6 ± 1.0	62.8 ± 1.0	64.1 ± 1.0	66.0 ± 1.1
$H^{\pm\pm}$ ($m = 1000$ GeV)	**59.2 ± 1.0**	59.3 ± 1.0	59.5 ± 1.0	60.0 ± 1.0
$t_R t_R$	61.3 ± 2.0	61.1 ± 2.1	62.0 ± 2.4	63.2 ± 3.0
d_4 (300 GeV)	68.2 ± 2.8	69.5 ± 4	72.4 ± 9.2	n/a
d_4 (350 GeV)	65.4 ± 2.9	68 ± 3.9	68.4 ± 7.1	n/a
d_4 (400 GeV)	65.3 ± 2.5	66.6 ± 3.2	67.7 ± 5.4	69.9 ± 9.8
d_4 (450 GeV)	64.4 ± 2.7	64.5 ± 3.3	71.6 ± 5.9	71.5 ± 9.8
d_4 (500 GeV)	64.1 ± 2.0	65.4 ± 2.4	67.5 ± 3.7	69.3 ± 6.2
W_R ($m(W_R) = 800$ GeV, $m(N_R) = 100$ GeV)	66.6 ± 2.9	66.7 ± 2.9	66.8 ± 3.0	66.2 ± 3.4
W_R ($m(W_R) = 800$ GeV, $m(N_R) = 300$ GeV)	67.6 ± 1.5	67.7 ± 1.5	68.4 ± 1.6	68.6 ± 1.8
W_R ($m(W_R) = 800$ GeV, $m(N_R) = 500$ GeV)	68.4 ± 2.0	68.6 ± 2.1	69.0 ± 2.3	67.7 ± 2.8
W_R ($m(W_R) = 1000$ GeV, $m(N_R) = 200$ GeV)	65.5 ± 2.2	65.6 ± 2.2	65.9 ± 2.3	66.4 ± 2.4
W_R ($m(W_R) = 1000$ GeV, $m(N_R) = 500$ GeV)	66.8 ± 2.0	67.0 ± 2.0	67.6 ± 2.1	68.0 ± 2.3
W_R ($m(W_R) = 1000$ GeV, $m(N_R) = 800$ GeV)	65.1 ± 2.8	65.2 ± 2.8	66.0 ± 3.2	65.9 ± 3.9
W_R ($m(W_R) = 1200$ GeV, $m(N_R) = 200$ GeV)	64.7 ± 2.3	64.7 ± 2.3	65.2 ± 2.4	65.5 ± 2.5
W_R ($m(W_R) = 1200$ GeV, $m(N_R) = 600$ GeV)	65.9 ± 2.0	66.0 ± 2.0	66.4 ± 2.1	67.1 ± 2.2
W_R ($m(W_R) = 1200$ GeV, $m(N_R) = 1000$ GeV)	65.7 ± 2.0	66.1 ± 2.0	66.9 ± 2.2	67.5 ± 2.6
W_R ($m(W_R) = 1500$ GeV, $m(N_R) = 300$ GeV)	63.5 ± 2.1	63.5 ± 2.1	64.1 ± 2.1	64.6 ± 2.2
W_R ($m(W_R) = 1500$ GeV, $m(N_R) = 800$ GeV)	65.0 ± 1.9	65.1 ± 1.9	65.6 ± 2.0	65.8 ± 2.1
W_R ($m(W_R) = 1500$ GeV, $m(N_R) = 1300$ GeV)	65.8 ± 2.0	66.1 ± 2.0	66.5 ± 2.2	66.7 ± 2.5

Table 12.4: Fiducial efficiency ε_{fid} (%) in the $e^{\pm}\mu^{\pm}$ final state for several potential signal models. The uncertainties are statistical. Entries listed as "n/a" have too few lepton pairs in that bin to form a meaningful selection efficiency. The lowest observed efficiency value, used in the analysis, is highlighted in bold face.

	Fiducial efficiency (%)			
Model	$m > 15$ GeV	$m > 100$ GeV	$m > 200$ GeV	$m > 300$ GeV
$H^{\pm\pm}$ ($m = 50$ GeV)	**55.2 ± 2.4**	n/a	n/a	n/a
$H^{\pm\pm}$ ($m = 100$ GeV)	58.4 ± 1.5	n/a	n/a	n/a
$H^{\pm\pm}$ ($m = 150$ GeV)	60.3 ± 1.4	64.6 ± 1.5	n/a	n/a
$H^{\pm\pm}$ ($m = 200$ GeV)	60.1 ± 1.3	62.5 ± 1.4	n/a	n/a
$H^{\pm\pm}$ ($m = 250$ GeV)	60.1 ± 1.3	61.8 ± 1.3	67.8 ± 1.6	n/a
$H^{\pm\pm}$ ($m = 300$ GeV)	60.7 ± 1.3	61.9 ± 1.3	66.4 ± 1.5	n/a
$H^{\pm\pm}$ ($m = 350$ GeV)	59.8 ± 1.6	60.6 ± 1.6	64.9 ± 1.8	69.0 ± 2.1
$H^{\pm\pm}$ ($m = 400$ GeV)	60.0 ± 1.2	60.7 ± 1.3	64.5 ± 1.4	68.1 ± 1.6
$H^{\pm\pm}$ ($m = 1000$ GeV)	56.9 ± 1.2	57.0 ± 1.2	57.9 ± 1.2	59.5 ± 1.3
$t_R t_R$	57.7 ± 1.3	58.2 ± 1.3	59.8 ± 1.5	61.0 ± 1.9
d_4 (300 GeV)	56.2 ± 1.7	59.5 ± 2.4	61.7 ± 5.8	n/a
d_4 (350 GeV)	59.7 ± 1.9	61.6 ± 2.5	64.8 ± 4.9	68.3 ± 9.8
d_4 (400 GeV)	58.5 ± 1.6	60.6 ± 2.0	62.3 ± 3.5	64.5 ± 6.6
d_4 (450 GeV)	58.6 ± 1.8	61.3 ± 2.2	66.0 ± 3.8	71.3 ± 6.7
d_4 (500 GeV)	58.4 ± 1.3	60.4 ± 1.6	61.9 ± 2.4	65.5 ± 4.1
W_R ($m(W_R) = 800$ GeV, $m(N_R) = 100$ GeV)	62.3 ± 1.5	62.2 ± 1.5	62.9 ± 1.6	63.6 ± 1.7
W_R ($m(W_R) = 800$ GeV, $m(N_R) = 300$ GeV)	67.9 ± 1.2	67.9 ± 1.2	68.7 ± 1.3	69.4 ± 1.5
W_R ($m(W_R) = 800$ GeV, $m(N_R) = 500$ GeV)	67.7 ± 1.2	68.1 ± 1.2	69.0 ± 1.4	69.0 ± 1.6
W_R ($m(W_R) = 1000$ GeV, $m(N_R) = 200$ GeV)	65.1 ± 1.3	65.2 ± 1.3	65.4 ± 1.3	66.4 ± 1.4
W_R ($m(W_R) = 1000$ GeV, $m(N_R) = 500$ GeV)	67.9 ± 1.2	68.1 ± 1.2	68.7 ± 1.3	69.1 ± 1.4
W_R ($m(W_R) = 1000$ GeV, $m(N_R) = 800$ GeV)	68.9 ± 1.2	69.2 ± 1.2	70.4 ± 1.4	71.0 ± 1.7
W_R ($m(W_R) = 1200$ GeV, $m(N_R) = 200$ GeV)	65.0 ± 1.3	65.0 ± 1.3	65.2 ± 1.3	65.5 ± 1.4
W_R ($m(W_R) = 1200$ GeV, $m(N_R) = 600$ GeV)	68.8 ± 1.2	68.8 ± 1.2	69.1 ± 1.2	69.4 ± 1.3
W_R ($m(W_R) = 1200$ GeV, $m(N_R) = 1000$ GeV)	67.4 ± 1.2	67.8 ± 1.2	68.3 ± 1.3	68.4 ± 1.5
W_R ($m(W_R) = 1500$ GeV, $m(N_R) = 300$ GeV)	66.3 ± 1.2	66.5 ± 1.3	66.7 ± 1.3	67.2 ± 1.3
W_R ($m(W_R) = 1500$ GeV, $m(N_R) = 800$ GeV)	68.1 ± 1.2	68.2 ± 1.2	68.5 ± 1.2	68.8 ± 1.2
W_R ($m(W_R) = 1500$ GeV, $m(N_R) = 1300$ GeV)	68.1 ± 1.2	68.2 ± 1.2	68.8 ± 1.3	69.4 ± 1.4

Table 12.5: Leakage (%) outside the fiducial region in the $e^{\pm}e^{\pm}$ final state for several potential signal models. The uncertainties are statistical.

	Efficiency outside fiducial region (%)			
Model	$m > 15$ GeV	$m > 100$ GeV	$m > 200$ GeV	$m > 300$ GeV
$H^{\pm\pm}$ ($m = 50$ GeV)	4.7 ± 0.6	n/a	n/a	n/a
$H^{\pm\pm}$ ($m = 100$ GeV)	n/a	n/a	n/a	n/a
$H^{\pm\pm}$ ($m = 150$ GeV)	3.8 ± 0.3	3.8 ± 0.3	n/a	n/a
$H^{\pm\pm}$ ($m = 200$ GeV)	2.6 ± 0.2	2.6 ± 0.2	n/a	n/a
$H^{\pm\pm}$ ($m = 250$ GeV)	2.1 ± 0.2	2.1 ± 0.2	4.4 ± 0.3	n/a
$H^{\pm\pm}$ ($m = 300$ GeV)	2.1 ± 0.2	2.1 ± 0.2	3.3 ± 0.2	n/a
$H^{\pm\pm}$ ($m = 350$ GeV)	1.4 ± 0.2	1.4 ± 0.2	2.1 ± 0.2	5.9 ± 0.4
$H^{\pm\pm}$ ($m = 400$ GeV)	2.0 ± 0.2	2.0 ± 0.2	2.4 ± 0.3	4.1 ± 0.3
$H^{\pm\pm}$ ($m = 1000$ GeV)	2.5 ± 0.2	2.5 ± 0.2	2.5 ± 0.2	2.4 ± 0.2
$t_R t_R$	5.5 ± 0.6	5.3 ± 0.6	6.4 ± 0.7	6.9 ± 0.8
d_4 (300 GeV)	8.9 ± 1.3	7.0 ± 1.4	n/a	n/a
d_4 (350 GeV)	4.9 ± 1.0	3.1 ± 0.9	n/a	n/a
d_4 (400 GeV)	5.2 ± 0.8	4.5 ± 0.8	6.5 ± 1.6	n/a
d_4 (450 GeV)	6.3 ± 1.0	6.4 ± 1.1	5.8 ± 1.5	n/a
d_4 (500 GeV)	4.4 ± 0.6	4.2 ± 0.6	4.6 ± 1.0	8.2 ± 2.1
W_R ($m(W_R) = 800$ GeV, $m(N_R) = 100$ GeV)	3.6 ± 0.6	3.6 ± 0.6	4.0 ± 0.7	5.2 ± 0.8
W_R ($m(W_R) = 800$ GeV, $m(N_R) = 300$ GeV)	3.4 ± 0.3	3.4 ± 0.3	3.5 ± 0.4	5.2 ± 0.5
W_R ($m(W_R) = 800$ GeV, $m(N_R) = 500$ GeV)	2.7 ± 0.4	2.5 ± 0.4	3.8 ± 0.5	5.3 ± 0.7
W_R ($m(W_R) = 1000$ GeV, $m(N_R) = 200$ GeV)	3.6 ± 0.5	3.6 ± 0.5	4.0 ± 0.6	4.6 ± 0.6
W_R ($m(W_R) = 1000$ GeV, $m(N_R) = 500$ GeV)	2.2 ± 0.4	2.2 ± 0.4	3.0 ± 0.4	3.2 ± 0.5
W_R ($m(W_R) = 1000$ GeV, $m(N_R) = 800$ GeV)	3.1 ± 0.6	3.1 ± 0.6	4.4 ± 0.8	7.1 ± 1.3
W_R ($m(W_R) = 1200$ GeV, $m(N_R) = 200$ GeV)	4.6 ± 0.6	4.7 ± 0.6	5.0 ± 0.6	5.3 ± 0.7
W_R ($m(W_R) = 1200$ GeV, $m(N_R) = 600$ GeV)	2.3 ± 0.4	2.3 ± 0.4	2.8 ± 0.4	3.4 ± 0.5
W_R ($m(W_R) = 1200$ GeV, $m(N_R) = 1000$ GeV)	2.7 ± 0.4	2.7 ± 0.4	4.0 ± 0.5	5.5 ± 0.7
W_R ($m(W_R) = 1500$ GeV, $m(N_R) = 300$ GeV)	4.3 ± 0.5	4.3 ± 0.5	4.4 ± 0.5	5.3 ± 0.6
W_R ($m(W_R) = 1500$ GeV, $m(N_R) = 800$ GeV)	2.6 ± 0.4	2.6 ± 0.4	3.0 ± 0.4	3.4 ± 0.4
W_R ($m(W_R) = 1500$ GeV, $m(N_R) = 1300$ GeV)	2.2 ± 0.4	2.2 ± 0.4	3.5 ± 0.5	3.9 ± 0.6

Table 12.6: Leakage (%) outside the fiducial region in the $\mu^\pm\mu^\pm$ final state for several potential signal models. The uncertainties are statistical.

	Efficiency outside fiducial region (%)			
Model	$m > 15$ GeV	$m > 100$ GeV	$m > 200$ GeV	$m > 300$ GeV
$H^{\pm\pm}$ ($m = 50$ GeV)	3.2 ± 0.4	n/a	n/a	n/a
$H^{\pm\pm}$ ($m = 100$ GeV)	1.3 ± 0.2	n/a	n/a	n/a
$H^{\pm\pm}$ ($m = 150$ GeV)	1.0 ± 0.1	1.1 ± 0.1	n/a	n/a
$H^{\pm\pm}$ ($m = 200$ GeV)	0.8 ± 0.1	0.8 ± 0.1	n/a	n/a
$H^{\pm\pm}$ ($m = 250$ GeV)	0.5 ± 0.1	0.5 ± 0.1	0.7 ± 0.1	n/a
$H^{\pm\pm}$ ($m = 300$ GeV)	0.5 ± 0.1	0.5 ± 0.1	0.6 ± 0.1	n/a
$H^{\pm\pm}$ ($m = 350$ GeV)	0.3 ± 0.1	0.2 ± 0.1	0.2 ± 0.1	0.4 ± 0.1
$H^{\pm\pm}$ ($m = 400$ GeV)	0.5 ± 0.1	0.4 ± 0.1	0.5 ± 0.1	0.5 ± 0.1
$H^{\pm\pm}$ ($m = 1000$ GeV)	0.3 ± 0.1	0.3 ± 0.1	0.4 ± 0.1	0.3 ± 0.1
$t_R t_R$	2.0 ± 0.4	2.2 ± 0.4	2.6 ± 0.5	3.9 ± 0.7
d_4 (300 GeV)	2.6 ± 0.5	4.2 ± 0.9	n/a	n/a
d_4 (350 GeV)	2.6 ± 0.6	3.1 ± 0.8	n/a	n/a
d_4 (400 GeV)	2.1 ± 0.4	2.4 ± 0.6	5.5 ± 1.5	n/a
d_4 (450 GeV)	2.5 ± 0.5	3.3 ± 0.7	n/a	n/a
d_4 (500 GeV)	2.0 ± 0.3	1.9 ± 0.4	n/a	6.1 ± 1.7
W_R ($m(W_R) = 800$ GeV, $m(N_R) = 100$ GeV)	2.9 ± 0.6	2.8 ± 0.6	3.5 ± 0.6	4.1 ± 0.8
W_R ($m(W_R) = 800$ GeV, $m(N_R) = 300$ GeV)	0.7 ± 0.1	0.7 ± 0.1	1.1 ± 0.2	1.5 ± 0.2
W_R ($m(W_R) = 800$ GeV, $m(N_R) = 500$ GeV)	0.7 ± 0.2	0.9 ± 0.2	1.4 ± 0.3	2.5 ± 0.5
W_R ($m(W_R) = 1000$ GeV, $m(N_R) = 200$ GeV)	1.4 ± 0.3	1.3 ± 0.3	1.7 ± 0.3	1.8 ± 0.4
W_R ($m(W_R) = 1000$ GeV, $m(N_R) = 500$ GeV)	0.8 ± 0.2	0.8 ± 0.2	1.3 ± 0.3	1.2 ± 0.3
W_R ($m(W_R) = 1000$ GeV, $m(N_R) = 800$ GeV)	0.6 ± 0.3	0.6 ± 0.3	1.4 ± 0.4	3.3 ± 0.8
W_R ($m(W_R) = 1200$ GeV, $m(N_R) = 200$ GeV)	1.5 ± 0.3	1.5 ± 0.3	1.5 ± 0.3	2.0 ± 0.4
W_R ($m(W_R) = 1200$ GeV, $m(N_R) = 600$ GeV)	0.5 ± 0.2	0.5 ± 0.2	0.7 ± 0.2	1.0 ± 0.3
W_R ($m(W_R) = 1200$ GeV, $m(N_R) = 1000$ GeV)	0.6 ± 0.2	0.7 ± 0.2	1.0 ± 0.3	2.5 ± 0.5
W_R ($m(W_R) = 1500$ GeV, $m(N_R) = 300$ GeV)	0.8 ± 0.2	0.7 ± 0.2	0.8 ± 0.2	1.1 ± 0.3
W_R ($m(W_R) = 1500$ GeV, $m(N_R) = 800$ GeV)	0.2 ± 0.1	0.2 ± 0.1	0.3 ± 0.1	0.7 ± 0.2
W_R ($m(W_R) = 1500$ GeV, $m(N_R) = 1300$ GeV)	0.8 ± 0.2	1.0 ± 0.2	1.4 ± 0.3	2.4 ± 0.4

Table 12.7: Leakage (%) outside the fiducial region in the $e^{\pm}\mu^{\pm}$ final state for several potential signal models. The uncertainties are statistical.

	Efficiency outside fiducial region (%)			
Model	$m > 15$ GeV	$m > 100$ GeV	$m > 200$ GeV	$m > 300$ GeV
$H^{\pm\pm}$ ($m = 50$ GeV)	4.9 ± 0.8	n/a	n/a	n/a
$H^{\pm\pm}$ ($m = 100$ GeV)	2.8 ± 0.3	n/a	n/a	n/a
$H^{\pm\pm}$ ($m = 150$ GeV)	2.1 ± 0.3	2.6 ± 0.3	n/a	n/a
$H^{\pm\pm}$ ($m = 200$ GeV)	2.3 ± 0.3	2.5 ± 0.3	n/a	n/a
$H^{\pm\pm}$ ($m = 250$ GeV)	2.0 ± 0.2	2.3 ± 0.3	3.4 ± 0.3	n/a
$H^{\pm\pm}$ ($m = 300$ GeV)	2.2 ± 0.2	2.2 ± 0.2	2.9 ± 0.3	n/a
$H^{\pm\pm}$ ($m = 350$ GeV)	2.0 ± 0.3	2.1 ± 0.3	2.3 ± 0.3	4.0 ± 0.5
$H^{\pm\pm}$ ($m = 400$ GeV)	2.8 ± 0.3	2.8 ± 0.3	3.0 ± 0.3	4.2 ± 0.4
$H^{\pm\pm}$ ($m = 1000$ GeV)	4.7 ± 0.4	4.7 ± 0.4	4.7 ± 0.4	4.7 ± 0.4
$t_R t_R$	3.1 ± 0.3	3.3 ± 0.3	4.6 ± 0.4	5.5 ± 0.6
d_4 (300 GeV)	5.1 ± 0.5	6.3 ± 0.8	7.1 ± 2.0	n/a
d_4 (350 GeV)	3.5 ± 0.5	4.2 ± 0.6	4.8 ± 1.3	n/a
d_4 (400 GeV)	2.9 ± 0.4	3.9 ± 0.5	6.1 ± 1.1	7.9 ± 2.3
d_4 (450 GeV)	3.0 ± 0.4	3.4 ± 0.5	3.8 ± 0.9	n/a
d_4 (500 GeV)	2.7 ± 0.3	3.2 ± 0.4	5.7 ± 0.7	7.6 ± 1.3
W_R ($m(W_R) = 800$ GeV, $m(N_R) = 100$ GeV)	4.0 ± 0.4	4.0 ± 0.4	4.2 ± 0.4	5.8 ± 0.5
W_R ($m(W_R) = 800$ GeV, $m(N_R) = 300$ GeV)	1.9 ± 0.2	1.9 ± 0.2	2.6 ± 0.2	3.9 ± 0.3
W_R ($m(W_R) = 800$ GeV, $m(N_R) = 500$ GeV)	1.4 ± 0.2	1.5 ± 0.2	2.7 ± 0.3	4.0 ± 0.4
W_R ($m(W_R) = 1000$ GeV, $m(N_R) = 200$ GeV)	2.1 ± 0.2	2.2 ± 0.2	2.5 ± 0.2	3.0 ± 0.3
W_R ($m(W_R) = 1000$ GeV, $m(N_R) = 500$ GeV)	1.6 ± 0.2	1.6 ± 0.2	2.0 ± 0.2	3.3 ± 0.3
W_R ($m(W_R) = 1000$ GeV, $m(N_R) = 800$ GeV)	1.6 ± 0.2	1.8 ± 0.2	2.7 ± 0.2	4.7 ± 0.4
W_R ($m(W_R) = 1200$ GeV, $m(N_R) = 200$ GeV)	3.0 ± 0.3	3.0 ± 0.3	3.0 ± 0.3	3.2 ± 0.3
W_R ($m(W_R) = 1200$ GeV, $m(N_R) = 600$ GeV)	1.4 ± 0.2	1.5 ± 0.2	1.9 ± 0.2	2.4 ± 0.2
W_R ($m(W_R) = 1200$ GeV, $m(N_R) = 1000$ GeV)	1.2 ± 0.1	1.3 ± 0.2	2.3 ± 0.2	3.5 ± 0.3
W_R ($m(W_R) = 1500$ GeV, $m(N_R) = 300$ GeV)	2.7 ± 0.2	2.7 ± 0.2	2.7 ± 0.2	3.0 ± 0.3
W_R ($m(W_R) = 1500$ GeV, $m(N_R) = 800$ GeV)	1.7 ± 0.2	1.8 ± 0.2	2.0 ± 0.2	2.3 ± 0.2
W_R ($m(W_R) = 1500$ GeV, $m(N_R) = 1300$ GeV)	1.3 ± 0.2	1.4 ± 0.2	2.0 ± 0.2	3.2 ± 0.3

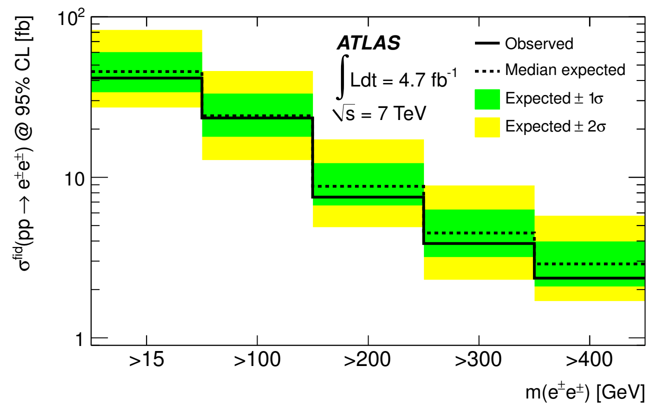

(a) $e^{\pm}e^{\pm}$ channel

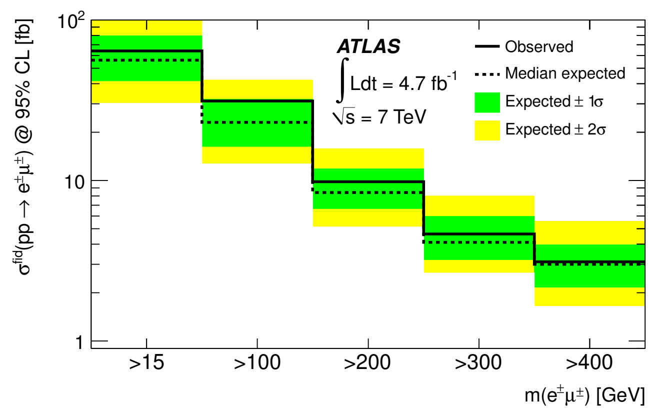

(b) $e^{\pm}\mu^{\pm}$ channel

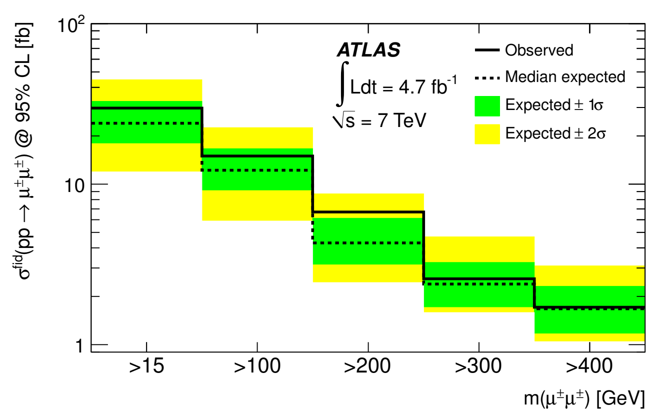

(c) $\mu^{\pm}\mu^{\pm}$ channel

Figure 12.1: 95% CL upper limits on the fiducial cross section for new physics contributing to the fiducial region for (a) $e^{\pm}e^{\pm}$, (b) $e^{\pm}\mu^{\pm}$, and (c) $\mu^{\pm}\mu^{\pm}$ pairs.

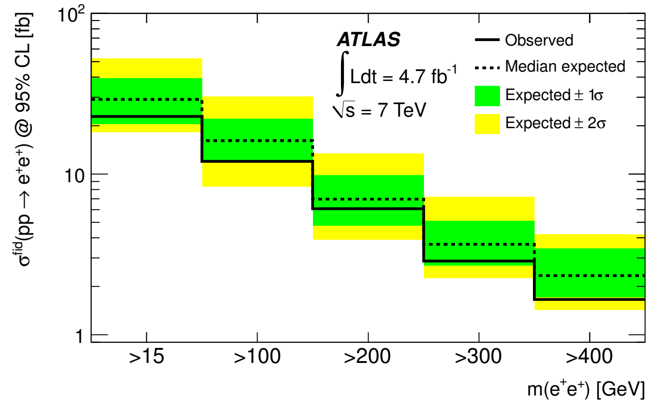

(a) e^+e^+ channel

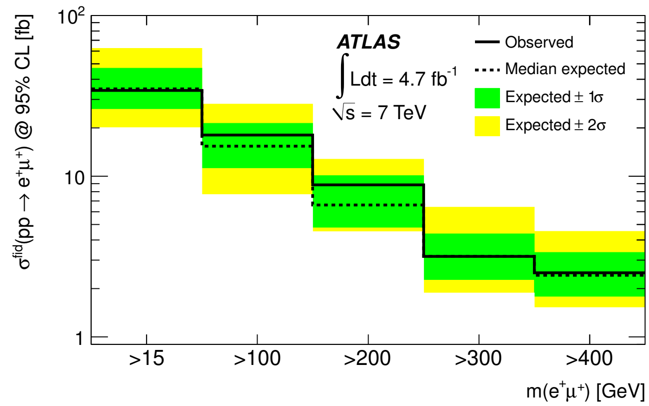

(b) $e^+\mu^+$ channel

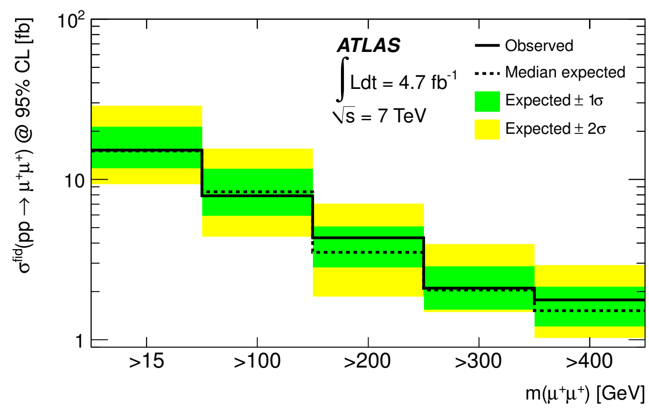

(c) $\mu^+\mu^+$ channel

Figure 12.2: 95% CL upper limits on the fiducial cross section for new physics contributing to the fiducial region for (a) e^+e^+, (b) $e^+\mu^+$, and (c) $\mu^+\mu^+$ pairs.

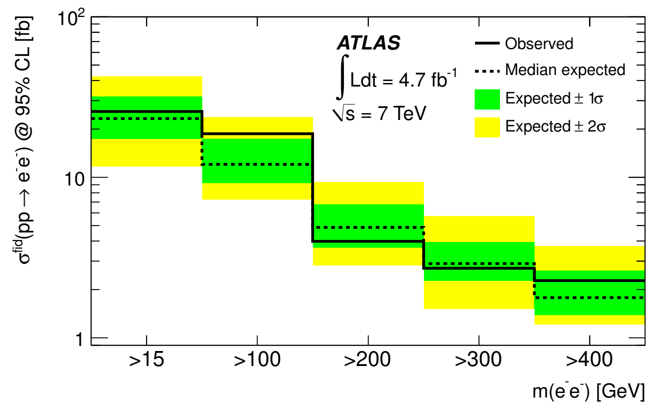

(a) e^-e^- channel

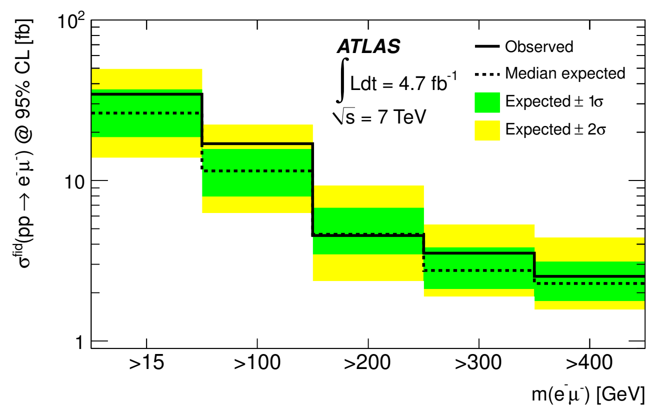

(b) $e^-\mu^-$ channel

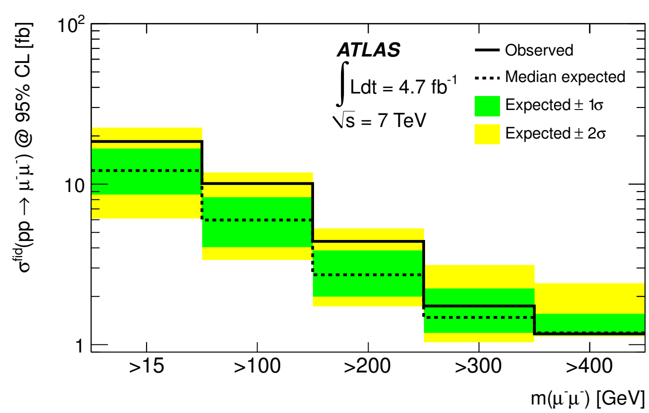

(c) $\mu^-\mu^-$ channel

Figure 12.3: 95% CL upper limits on the fiducial cross section for new physics contributing to the fiducial region for (a) e^-e^-, (b) $e^-\mu^-$, and (c) $\mu^-\mu^-$ pairs.

Table 12.8: Upper limits at 95% CL on the fiducial cross section for $\ell^{\pm}\ell^{\pm}$ pairs from non-SM physics. The expected limits and their 1σ uncertainties are given, as well as the observed limits in data, for the ee, $e\mu$, and $\mu\mu$ final states inclusively and separated by charge.

	95% CL upper limit [fb]					
Mass range	expected	observed	expected	observed	expected	observed
	$e^{\pm}e^{\pm}$		$e^{\pm}\mu^{\pm}$		$\mu^{\pm}\mu^{\pm}$	
$m > 15$ GeV	$45.5^{+14.5}_{-11.5}$	41.5	$56.2^{+23.3}_{-14.5}$	64.1	$24.0^{+8.9}_{-6.0}$	29.8
$m > 100$ GeV	$24.1^{+8.9}_{-6.2}$	23.4	$23.0^{+9.1}_{-6.7}$	31.2	$12.2^{+4.5}_{-3.0}$	15.0
$m > 200$ GeV	$8.8^{+3.4}_{-2.1}$	7.5	$8.4^{+3.4}_{-1.7}$	9.8	$4.3^{+1.8}_{-1.1}$	6.7
$m > 300$ GeV	$4.5^{+1.8}_{-1.3}$	3.9	$4.1^{+1.8}_{-0.9}$	4.6	$2.4^{+0.9}_{-0.7}$	2.6
$m > 400$ GeV	$2.9^{+1.1}_{-0.8}$	2.4	$3.0^{+1.0}_{-0.8}$	3.1	$1.7^{+0.6}_{-0.5}$	1.7
	$e^{+}e^{+}$		$e^{+}\mu^{+}$		$\mu^{+}\mu^{+}$	
$m > 15$ GeV	$29.1^{+10.2}_{-8.6}$	22.8	$34.9^{+12.2}_{-8.6}$	34.1	$15.0^{+6.1}_{-3.3}$	15.2
$m > 100$ GeV	$16.1^{+5.9}_{-4.3}$	12.0	$15.4^{+5.9}_{-4.1}$	18.0	$8.4^{+3.2}_{-2.4}$	7.9
$m > 200$ GeV	$7.0^{+2.9}_{-2.2}$	6.1	$6.6^{+3.5}_{-1.8}$	8.8	$3.5^{+1.6}_{-0.7}$	4.3
$m > 300$ GeV	$3.7^{+1.4}_{-1.0}$	2.9	$3.2^{+1.2}_{-0.9}$	3.2	$2.0^{+0.8}_{-0.5}$	2.1
$m > 400$ GeV	$2.3^{+1.1}_{-0.6}$	1.7	$2.4^{+0.9}_{-0.6}$	2.5	$1.5^{+0.6}_{-0.3}$	1.8
	$e^{-}e^{-}$		$e^{-}\mu^{-}$		$\mu^{-}\mu^{-}$	
$m > 15$ GeV	$23.2^{+8.6}_{-5.8}$	25.7	$26.2^{+10.6}_{-7.6}$	34.4	$12.1^{+4.5}_{-3.5}$	18.5
$m > 100$ GeV	$12.0^{+5.3}_{-2.8}$	18.7	$11.5^{+4.2}_{-3.5}$	16.9	$6.0^{+2.3}_{-1.9}$	10.1
$m > 200$ GeV	$4.9^{+1.9}_{-1.2}$	4.0	$4.6^{+2.1}_{-1.2}$	4.5	$2.7^{+1.1}_{-0.7}$	4.4
$m > 300$ GeV	$2.9^{+1.0}_{-0.6}$	2.7	$2.7^{+1.1}_{-0.6}$	3.5	$1.5^{+0.8}_{-0.3}$	1.7
$m > 400$ GeV	$1.8^{+0.8}_{-0.4}$	2.3	$2.3^{+0.8}_{-0.5}$	2.5	$1.2^{+0.4}_{-0.0}$	1.2

Chapter 13

Limits on Doubly-Charged Higgs Production

The same dataset and selection can be used to perform a dedicated search for a narrow doubly-charged resonance decaying to leptons. The benchmark model used to set limits is the doubly-charged Higgs boson described in Section 2.4.1. There are two main differences between this search and the limits described in the previous chapter: a scan is performed in narrow mass bins corresponding to the detector resolution to exploit the resonance topology, and the acceptance numbers are taken directly from simulated samples of doubly-charged Higgs boson pair production with no need for a fiducial definition. The uncertainties are evaluated in the same way as described in Chapter 10, except here they are evaluated in the narrow mass bins used for the search.

Section 13.1 describes the specifics of this search stemming from the doubly-charged Higgs boson signature, including the mass binning and signal acceptance. Section 13.2 compares the observed data with the predicted backgrounds and expected yield. Section 13.3 uses this information to set limits on the cross section times branching ratio for doubly-charged Higgs production, and Section 13.4 translates these into limits on $m(H^{\pm\pm})$ making assumptions on the branching ratio to leptons.

13.1 Doubly-Charged Higgs Signal

The simulated samples used to evaluate the signal acceptance for this search are described in Chapter 7. The cross section is normalized to NLO using calculations at $\sqrt{s} = 7$ TeV from the author of [103]. Doubly-charged Higgs bosons can couple to either left-handed or right-handed fermions. In left-right symmetric models (described in Section 2.4.1.2), the two cases are distinguished and denoted $H_L^{\pm\pm}$ and $H_R^{\pm\pm}$. The cross section for $H_L^{\pm\pm}H_L^{\mp\mp}$ production is about 2.5 times larger than that for $H_R^{\pm\pm}H_R^{\mp\mp}$ production due to different couplings to the Z boson [103].

13.1.1 Invariant Mass Binning

The intrinsic width of the $H^{\pm\pm}$ resonance peak is narrow for the mass range considered, and the width of the reconstructed mass peak is consequently dominated by the detector resolution, described in Section 5.1 for electrons and Section 5.2 for muons. The reconstructed mass peaks in simulation for the $e^{\pm}e^{\pm}$ and $\mu^{\pm}\mu^{\pm}$ channels for a $H^{\pm\pm}$ with mass 300 GeV are shown in Fig. 13.1.

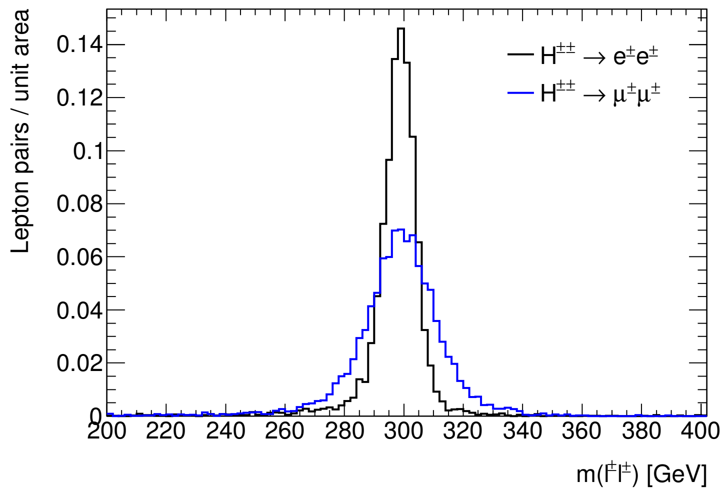

Figure 13.1: Simulated invariant-mass distributions for a $H^{\pm\pm}$ boson with a mass of 300 GeV, decaying to $e^{\pm}e^{\pm}$ (black curve) and $\mu^{\pm}\mu^{\pm}$ (blue curve), respectively. Each distribution is normalized to unit area.

The size of the invariant-mass bins used for this search depend on the hypothesized $H^{\pm\pm}$ mass. They are chosen to maximize the expected sensitivity of the analysis, using the significance defined as:

$$\sqrt{2((s+b)\cdot\ln(1+s/b)-s)} \tag{13.1}$$

where s is the number of expected signal events and b is the number of predicted background events. This is the asymptotic expression for the expected significance of a counting experiment in the limit of a large number of expected events in data $(s+b)$ and no systematic uncertainties, derived in [102].[24] The significance depends weakly on the mass bin size for sizes close to the detector resolution.

For the $e^{\pm}e^{\pm}$ channel, the mass bins are defined as $\pm 0.04 \times m(H^{\pm\pm})$. For the $\mu^{\pm}\mu^{\pm}$ channel, to account for the degrading resolution at high mass, the bins are defined as:

$$\pm\,(0.06 \times m(H^{\pm\pm}) + 0.7 \cdot 10^{-4} \times m(H^{\pm\pm})^2) \tag{13.2}$$

[24] In [102], it is shown that this asymptotic formula performs well at predicting the significance of an experiment even in the low statistics case of a few events expected in data.

which corresponds to about a 6% (9%) window for m($H^{\pm\pm}$) = 50 (500) GeV. Since the search sensitivity depends mildly on small differences in the mass bin width, the same bin width is used in the $e^{\pm}\mu^{\pm}$ as the $\mu^{\pm}\mu^{\pm}$ channel for simplicity.

13.1.2 Signal Acceptance

The total acceptance times efficiency for $H^{\pm\pm}$ bosons to pass the full analysis selection (ε_{tot}) is shown in Fig. 13.2 for the simulated $H^{\pm\pm}$ mass points. For each channel, the denominator used to calculate ε_{tot} is the number of true simulated $H^{\pm\pm} \to \ell^{\pm}\ell^{\pm}$ decays to the lepton flavor pair of interest. The numerator is the number of reconstructed lepton pairs passing the full analysis selection, including the mass bin requirement described above.

To interpolate between the simulated $H^{\pm\pm}$ mass points, ε_{tot} is fitted for each channel by an empirical piecewise functional form, also shown in Fig. 13.2. For the $e^{\pm}e^{\pm}$ channel, the following function is used:

$$\varepsilon_{tot}(m) = \begin{cases} p_0(1 - e^{-(m-p_1)/p_2}), & \text{if } m < 300 \text{ GeV} \\ p_3 + p_4 m, & \text{if } 300 \leq m < 500 \text{ GeV} \\ p_5, & \text{if } m \geq 500 \text{ GeV} \end{cases} \tag{13.3}$$

with the values of the parameters p_i given in Table 13.1. The empirical fit agrees with the predicted efficiency within statistical errors for every simulated mass point, so no additional uncertainty is assessed due to this interpolation function.

Table 13.1: Fitted parameter values for Equation 13.3, which gives $\varepsilon_{tot}(m)$ for the $e^{\pm}e^{\pm}$ channel.

Parameter	Value
p_0	$4.95 \cdot 10^{-1}$
p_1	$3.02 \cdot 10^{+1}$
p_2	8.85
p_3	$4.01 \cdot 10^{-1}$
p_4	$2.50 \cdot 10^{-4}$
p_5	$5.26 \cdot 10^{-1}$

For the $\mu^{\pm}\mu^{\pm}$ channel, a similar piecewise function is used for the interpolation between simulated $H^{\pm\pm}$ mass points:

$$\varepsilon_{tot}(m) = \begin{cases} p_0(1 - e^{-(m-p_1)/p_2}), & \text{if } m < 300 \text{ GeV} \\ p_3 - p_4 m, & \text{if } m \geq 300 \text{ GeV} \end{cases} \tag{13.4}$$

with the values of the parameters p_i given in Table 13.2. Also for the $\mu^\pm\mu^\pm$ case, the empirical fit agrees with the predicted efficiency within statistical errors for every simulated mass point, so no additional uncertainty is assessed due to the interpolation function.

Table 13.2: Fitted parameter values for Equation 13.4, which gives $\varepsilon_{tot}(m)$ for the $\mu^\pm\mu^\pm$ channel.

Parameter	Value
p_0	$5.17 \cdot 10^{-1}$
p_1	$3.04 \cdot 10^{+1}$
p_2	$3.98 \cdot 10^{+1}$
p_3	$5.36 \cdot 10^{-1}$
p_4	$7.60 \cdot 10^{-5}$

And similarly for the $e^\pm\mu^\pm$ channel:

$$\varepsilon_{tot}(m) = \begin{cases} p_0(1 - e^{-(m-p_1)/p_2}), & \text{if } m < 500 \text{ GeV} \\ p_3, & \text{if } m \geq 500 \text{ GeV} \end{cases} \tag{13.5}$$

with the values of the parameters p_i given in Table 13.3. The empirical fit again agrees with the predicted efficiency within statistical errors for every simulated mass point.

Table 13.3: Fitted parameter values for Equation 13.5, which gives $\varepsilon_{tot}(m)$ for the $e^\pm\mu^\pm$ channel.

Parameter	Value
p_0	$5.34 \cdot 10^{-1}$
p_1	$3.08 \cdot 10^{+1}$
p_2	$6.31 \cdot 10^{+1}$
p_3	$5.36 \cdot 10^{-1}$

The acceptance times efficiency to reconstruct a $H^{\pm\pm}$ boson in the selected mass windows is about 27% for the $e^\pm e^\pm$, 36% for the $e^\pm\mu^\pm$, and 43% for the $\mu^\pm\mu^\pm$ channel for $m(H^{\pm\pm}) = 100$ GeV. For $m(H^{\pm\pm}) = 400$ GeV it is about 50% for all three final states.

13.1.3 Systematic Uncertainties

The prompt lepton systematic uncertainties described in Section 10.1 are all evaluated for their impacts on the doubly-charged Higgs boson signal acceptance. The samples are simulated with

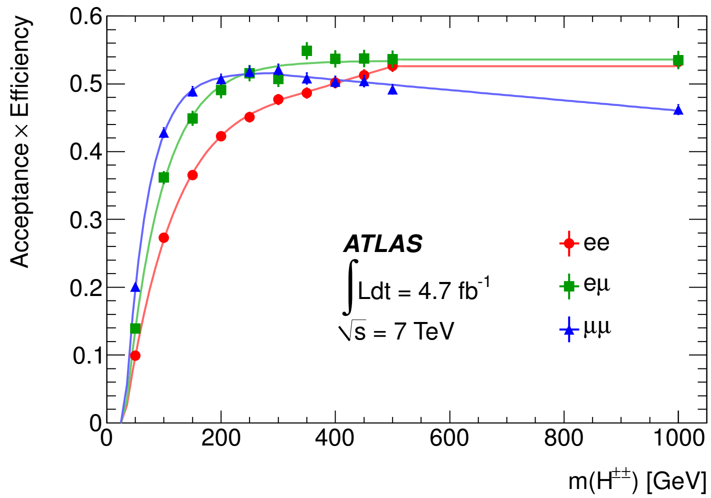

Figure 13.2: Total acceptance times efficiency vs simulated $H^{\pm\pm}$ mass for the $e^{\pm}e^{\pm}$, $e^{\pm}\mu^{\pm}$, and $\mu^{\pm}\mu^{\pm}$ channels, fitted with piecewise empirical functions used for interpolation. The decrease in the acceptance times efficiency in the $\mu^{\pm}\mu^{\pm}$ channel at high mass is primarily due to the requirement that the dimuon mass falls within a certain range around $m(H^{\pm\pm})$. The size of this range has been chosen to give optimal search sensitivity.

ATLAS fast simulation, so the uncertainty for electron identification in fast simulation is applied. An additional acceptance uncertainty of $\pm1.6\%$ is estimated from the parton distribution functions by using the uncertainties provided by the MSTW 2008 90% CL set [97] and following the prescription of [12], added in quadrature to the difference between the central value of this set and the CTEQ6L1 PDF set.

13.2 Results

The number of observed events is compared to the expected background and signal yields in each narrow mass bin, with no significant discrepancies observed. A comparison of the observed data and predicted background yields for a selection of mass bins is presented in Tables 13.4-13.6 for each channel. The predicted and observed invariant mass distributions for each channel are shown in Fig. 13.3, along with the expected contributions for $H^{\pm\pm}$ bosons at various masses with 100% branching ratio to the channel presented.

Table 13.4: Expected and observed numbers of like-sign electron pairs for various bins in invariant mass, $m(e^{\pm}e^{\pm})$. The uncertainties shown include the statistical and systematic components.

Bin center [GeV]	50	150	250	360	460	560
Non-prompt	5.6 ± 3.4	2.3 ± 1.4	1.1 ± 0.7	0.3 ± 0.3	$0.0^{+0.2}_{-0.0}$	$0.0^{+0.2}_{-0.0}$
Charge flips and conversions	9.5 ± 4.3	7.6 ± 1.8	$2.7^{+1.4}_{-0.7}$	1.5 ± 0.6	$0.5^{+1.2}_{-0.1}$	0.5 ± 0.2
Prompt	4.0 ± 0.6	5.2 ± 0.8	2.2 ± 0.4	0.8 ± 0.2	0.2 ± 0.1	0.2 ± 0.1
Sum of Backgrounds	19.1 ± 5.6	15.1 ± 2.5	$6.0^{+1.6}_{-1.1}$	2.5 ± 0.7	$0.7^{+1.2}_{-0.1}$	$0.6^{+0.3}_{-0.2}$
Data	18	17	7	3	1	0

Table 13.5: Expected and observed numbers of like-sign muon pairs for various bins in invariant mass, $m(\mu^{\pm}\mu^{\pm})$. The uncertainties shown include the statistical and systematic components.

Bin center [GeV]	50	150	250	360	460	560
Non-prompt	2.3 ± 0.9	1.7 ± 0.9	0.4 ± 0.4	0.1 ± 0.1	$0.0^{+0.3}_{-0.0}$	$0.0^{+0.3}_{-0.0}$
Charge flips	$0^{+0.00005}_{-0.0}$	$0^{+0.03}_{-0.0}$	$0^{+0.04}_{-0.0}$	$0^{+0.02}_{-0.0}$	$0^{+0.1}_{-0.0}$	$0^{+0.1}_{-0.0}$
Prompt	9.1 ± 1.3	12.5 ± 1.7	5.7 ± 0.8	1.9 ± 0.3	0.8 ± 0.2	0.4 ± 0.1
Sum of backgrounds	11.4 ± 1.6	14.2 ± 1.9	6.1 ± 0.9	1.9 ± 0.3	$0.8^{+0.4}_{-0.2}$	$0.4^{+0.3}_{-0.1}$
Data	13	16	8	1	1	1

Table 13.6: Expected and observed numbers of like-sign $e\mu$ pairs for various bins in invariant mass, $m(e^{\pm}\mu^{\pm})$. The uncertainties shown include the statistical and systematic components.

Bin center [GeV]	50	150	250	360	460	560
Non-prompt	9.6 ± 4.4	7.4 ± 3.3	3.6 ± 1.7	1.0 ± 0.6	0.6 ± 0.5	0.1 ± 0.2
Charge flips and conversions	15.4 ± 6.7	5.1 ± 1.6	3.1 ± 1.3	0.2 ± 0.1	0.7 ± 0.5	1.2 ± 0.9
Prompt	13.2 ± 1.8	22.6 ± 2.9	9.0 ± 1.2	2.9 ± 0.5	1.5 ± 0.3	1.0 ± 0.2
Sum of backgrounds	38.2 ± 8.3	35.1 ± 4.7	15.7 ± 2.5	4.0 ± 0.7	2.8 ± 0.8	2.3 ± 1.0
Data	31	35	14	4	5	0

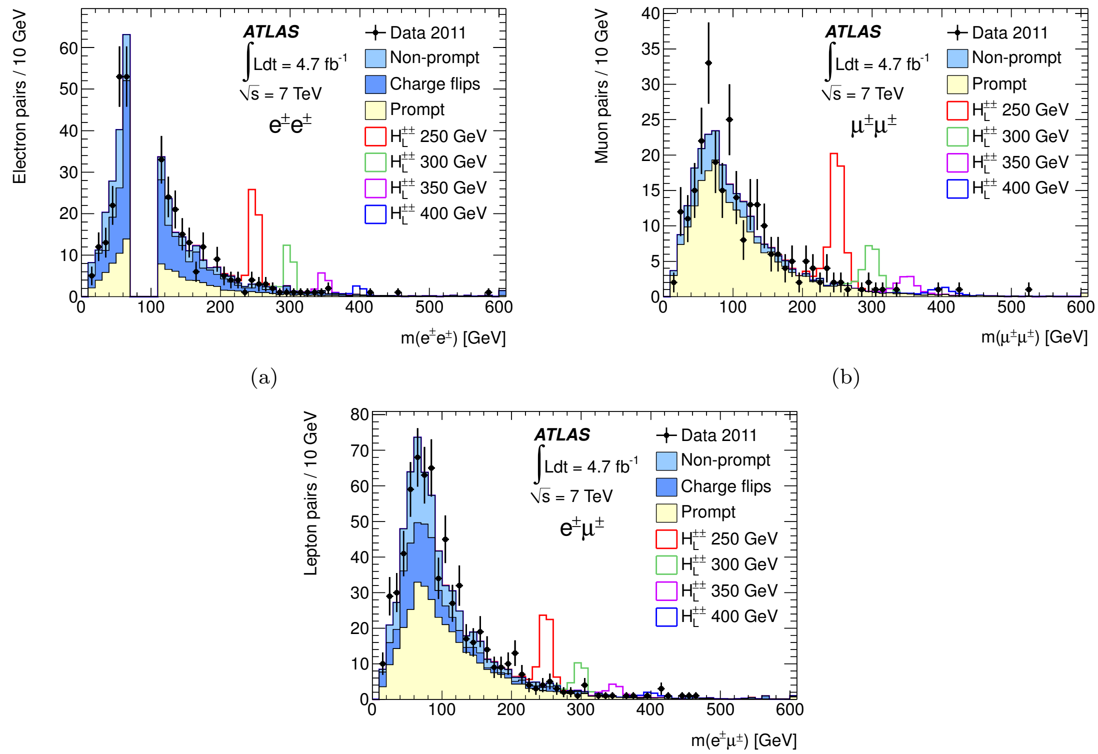

Figure 13.3: Invariant mass distributions for (a) $e^{\pm}e^{\pm}$, (b) $\mu^{\pm}\mu^{\pm}$, and (c) $e^{\pm}\mu^{\pm}$ pairs passing the full event selection. The data are shown as filled circles. The stacked histograms represent the backgrounds composed of pairs of prompt leptons from SM processes, pairs with at least one non-prompt lepton, and for the electron channels, backgrounds arising from charge misidentification and conversions. The open histograms show the expected signal from simulated $H_L^{\pm\pm}$ samples, assuming a 100% branching ratio to the decay channel considered and coupling to left-handed fermions. The last bin is an overflow bin. The data and SM predictions shown are the same as in Fig. 11.1.

13.3 Cross Section Limits

Since no significant discrepancy is observed between data and the background prediction, the data are used to derive upper cross-section limits on pair production of doubly-charged Higgs bosons. Using the mass bins described in Section 13.1.1, 95% CL limits are placed as function of the hypothesized $H^{\pm\pm}$ mass.

This analysis aims to constrain the $H^{\pm\pm}H^{\mp\mp}$ process. However, the analysis counts lepton pairs, and two pairs per event can contribute. The translation between number of events with pair produced $H^{\pm\pm}$ bosons and number of lepton pairs is done as follows. The cross section for pair production of

$H^{\pm\pm}$ bosons, σ_{HH}, is given by:

$$\sigma_{HH} = \frac{N_{HH}}{\mathcal{L}_{\text{int}}}, \tag{13.6}$$

where N_{HH} is the true number of events containing a pair of $H^{\pm\pm}$ bosons and $\mathcal{L}_{\text{int}}$ is the integrated luminosity. N_{HH} is then related to the number of $H^{\pm\pm}$ bosons decaying to a certain decay channel with a branching ratio (BR), N_H, via $N_H = 2 \cdot BR \cdot N_{HH}$. It follows that

$$\sigma_{HH} \cdot BR = \frac{N_H}{2 \cdot \mathcal{L}_{\text{int}}}. \tag{13.7}$$

The number of true $H^{\pm\pm}$ bosons is related to the number of reconstructed $H^{\pm\pm}$ bosons: $N_H^{rec} = N_H \cdot \varepsilon_{tot}$, where ε_{tot} is the acceptance times efficiency to detect a single $H^{\pm\pm}$ boson. The cross section times branching ratio is thus finally given by

$$\sigma_{HH} \cdot BR = \frac{N_H^{rec}}{2 \cdot \varepsilon_{tot} \cdot \mathcal{L}_{\text{int}}}. \tag{13.8}$$

Limits on the cross section of pair production of doubly charged Higgs bosons are derived with the CL$_s$ method described in Section 12.1. The expected and observed upper cross section limits at 95% CL times the branching ratio to the considered channel are shown in Fig. 13.4.

13.4 Mass Limits

Using the theoretical $H^{\pm\pm}$ pair-production cross sections, the limits on $H^{\pm\pm} \to \ell^{\pm}\ell^{\pm}$ production cross section are converted to mass limits. The theoretical cross section curves can be seen in Fig. 13.4 for left and right-handed $H^{\pm\pm}$ bosons, assuming 100% branching fraction to the relevant channel. An uncertainty of 10% on the theoretical cross sections is assumed.

These same limits can be interpreted as limits on the branching fraction of $H^{\pm\pm} \to \ell^{\pm}\ell^{\pm}$ versus $H^{\pm\pm}$ mass. These 95% CL limits are displayed in Fig. 13.5 for $H_L^{\pm\pm}$ and $H_R^{\pm\pm}$ and summarized in Table 13.7 for a few choices of the branching fractions.

Assuming 100% branching fraction to the channel of interest, mass limits of 409, 398, and 375 GeV are observed for $H_L^{\pm\pm}$ in the $e^{\pm}e^{\pm}$, $\mu^{\pm}\mu^{\pm}$, and $e^{\pm}\mu^{\pm}$ channels respectively. These limits are comparable to those set by a dedicated CMS search using final states with three or more leptons [15]. For pair production of $H_L^{\pm\pm}$ and assuming 100% branching ratios, CMS set limits of 382, 395, and 391 GeV in the $e^{\pm}e^{\pm}$, $\mu^{\pm}\mu^{\pm}$, and $e^{\pm}\mu^{\pm}$ channels respectively.

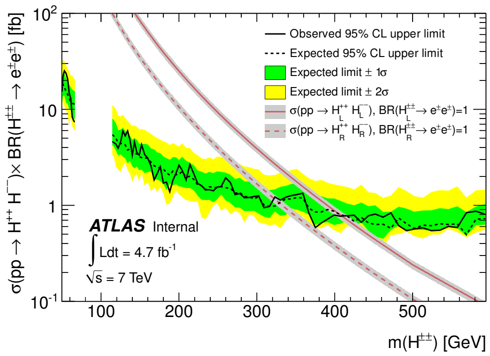

(a)

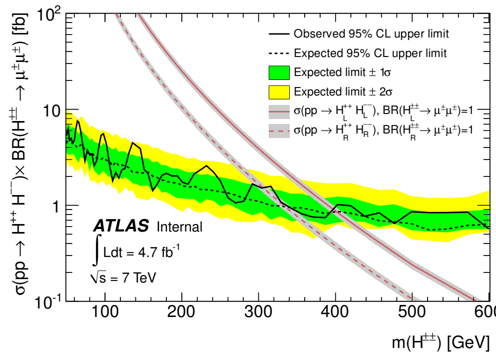

(b)

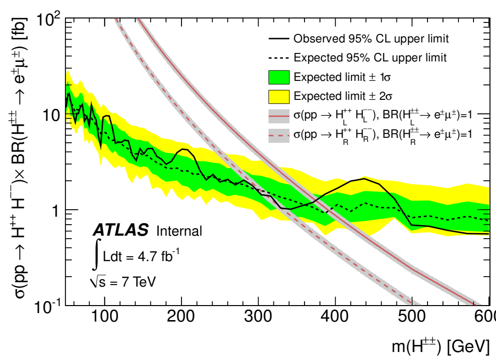

(c)

Figure 13.4: Upper limit at 95% CL on the cross section times branching ratio for pair production of $H^{\pm\pm}$ bosons decaying to (a) $e^{\pm}e^{\pm}$, (b) $\mu^{\pm}\mu^{\pm}$, and (c) $e^{\pm}\mu^{\pm}$ pairs. The observed and median expected limits are shown along with the 1σ and 2σ variations in the expected limits. In the range $70 < m(H^{\pm\pm}) < 110$ GeV, no limit is set in the $e^{\pm}e^{\pm}$ channel. Also shown are the theoretical predictions at next-to-leading order for the $pp \to H^{\pm\pm}H^{\mp\mp}$ cross section for $H_L^{\pm\pm}$ and $H_R^{\pm\pm}$ bosons. The variation from bin to bin in the expected limits is due to fluctuations in the background yields derived from small MC samples.

Table 13.7: Lower mass limits at 95% CL on $H^{\pm\pm}$ bosons decaying to $e^{\pm}e^{\pm}$, $\mu^{\pm}\mu^{\pm}$, or $e^{\pm}\mu^{\pm}$ pairs. Mass limits are derived assuming branching ratios to a given decay mode of 100%, 33%, 22%, or 11%. Both expected and observed limits are given.

$\mathrm{BR}(H_L^{\pm\pm} \to \ell^{\pm}\ell'^{\pm})$	95% CL lower limit on $m(H_L^{\pm\pm})$ [GeV]					
	$e^{\pm}e^{\pm}$		$\mu^{\pm}\mu^{\pm}$		$e^{\pm}\mu^{\pm}$	
	exp.	obs.	exp.	obs.	exp.	obs.
100%	407	409	401	398	392	375
33%	318	317	317	290	279	276
22%	274	258	282	282	250	253
11%	228	212	234	216	206	190
$\mathrm{BR}(H_R^{\pm\pm} \to \ell^{\pm}\ell'^{\pm})$	95% CL lower limit on $m(H_R^{\pm\pm})$ [GeV]					
	$e^{\pm}e^{\pm}$		$\mu^{\pm}\mu^{\pm}$		$e^{\pm}\mu^{\pm}$	
	exp.	obs.	exp.	obs.	exp.	obs.
100%	329	322	335	306	303	310
33%	241	214	247	222	220	195
22%	203	199	223	212	194	187
11%	160	151	184	176	153	151

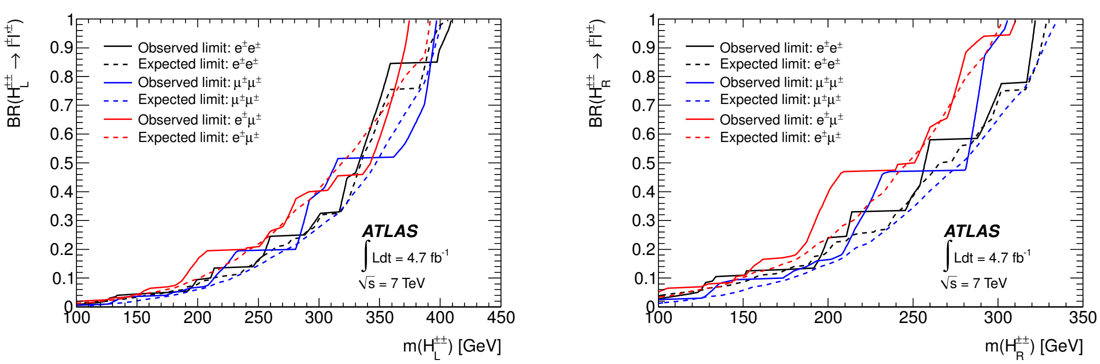

(a) (b)

Figure 13.5: The mass limits as function of the branching ratio for the $H^{\pm\pm}$ decaying to $e^{\pm}e^{\pm}$, $e^{\pm}\mu^{\pm}$, and $\mu^{\pm}\mu^{\pm}$ for (a) $H_L^{\pm\pm}$ and (b) $H_R^{\pm\pm}$ bosons. Shown are both the observed limits (solid lines) and the expected limits (dashed lines). The stepping behavior, where the same mass limit is valid for a range of branching ratios, results from fluctuations in the observed cross-section limits shown in Fig. 13.4.

Chapter 14

Potential Extensions

Several potential improvements could be made to the analyses described here, some of which will be adopted for a similar search using the 2012 ATLAS dataset of pp collisions at $\sqrt{s} = 8$ TeV.

The first is adding new signal regions with requirements on the hadronic activity or missing energy in the event. For hadronic activity, cuts on either the number of QCD jets above a reasonable p_{T} threshold or a scale sum of jet p_{T} (often called H_T) could be used to enhance sensitivity to final states with multiple jets. Models producing top quarks, like like-sign top production or fourth generation down-type quarks (d_4) decaying to tW, would benefit. A cut on $E_{\mathrm{T}}^{\mathrm{miss}}$ would improve sensitivity to models with neutrinos or new non-interacting particles in the final state, like $d_4 \to tW$.

Reducing backgrounds would improve sensitivity. The backgrounds from diboson production of $W^{\pm}Z$ and ZZ could be suppressed by vetoing events containing an opposite-sign same-flavor lepton pair consistent with the Z mass. In the channels with electrons, the charge-flip background is large. Improving the electron charge determination could reduce this background. For example, in [104], the CMS collaboration uses three different methods to measure the electron charge and requires that they all agree. These include the curvature measurement of the standard track fit, the curvature from a bremsstrahlung fit, and a method drawing a line between the cluster position in the calorimeter and the track segment in the pixel detector and examining the other hits in the tracking detector. Something like the latter could be investigated for ATLAS to see if it yields improvement.

The fiducial cross sections from Section 12.3, with the fiducial region definition and fiducial efficiencies, are an attempt to provide sufficient information for theorists to apply the limits to other processes of interest. However, the observed variation in fiducial efficiencies among potential signal models makes this less than optimal, and most of the difference comes from the differences in lepton p_{T} spectra among models coupled with the p_{T}-dependence of the analysis efficiency for leptons. A solution to this is to publish the lepton efficiency curves directly, as is done in [104] and other searches by the CMS collaboration and is starting to be done in some ATLAS searches. This should be done in the next incarnation of this inclusive like-sign dilepton search for ATLAS.

Finally, repeating this search when the LHC run resumes in 2015 at $\sqrt{s}$ = 13–14 TeV will be inherently exciting. With a large increase in the center-of-mass energy, new phenomena may come into reach, and inclusive searches like this one are essential in ensuring that new hints are not overlooked.

Chapter 15

Conclusions

This thesis began by describing the Standard Model of particle physics, some of the many outstanding questions surrounding it, and some of the proposed extensions that this search would be sensitive to through like-sign dilepton final states. It overviewed the experiment used for this analysis, the ATLAS detector at the Large Hadron Collider, then detailed how leptons are reconstructed and identified in ATLAS, forming the foundations of this search.

This search then looked inclusively for anomalous production of two prompt, isolated leptons with the same electric charge, using a data sample corresponding to 4.7 fb^{-1} of integrated luminosity collected in 2011 at $\sqrt{s} = 7$ TeV. Pairs of high-p_{T} leptons ($e^{\pm}e^{\pm}$, $e^{\pm}\mu^{\pm}$, and $\mu^{\pm}\mu^{\pm}$) were selected, with no requirements on additional leptons, hadronic activity, or missing transverse energy. The dilepton invariant mass distribution was examined for any deviation from the Standard Model expectation. No excess was found, and upper limits on the production of like-sign lepton pairs due to contributions from physics beyond the Standard Model were placed as a function of the dilepton mass within a fiducial region close to the experimental selection criteria. The 95% confidence level upper limits on the cross section of anomalous $e^{\pm}e^{\pm}$, $e^{\pm}\mu^{\pm}$, or $\mu^{\pm}\mu^{\pm}$ production ranged between 1.7 fb and 64.1 fb depending on the dilepton mass and flavor combination. Using the fiducial definition, these limits can be applied to any model producing final states including like-sign lepton pairs.

The same data were interpreted in the context of a search for a narrow doubly-charged resonance, using the doubly-charged Higgs boson as a benchmark model. Again, no significant deviations from Standard Model expectations were found. The masses of doubly-charged Higgs bosons were constrained depending on the branching ratio into these leptonic final states. Assuming pair production, coupling to left-handed fermions, and a branching ratio of 100% for each final state, masses below 409 GeV, 375 GeV, and 398 GeV were excluded for $e^{\pm}e^{\pm}$, $e^{\pm}\mu^{\pm}$, and $\mu^{\pm}\mu^{\pm}$, respectively.

Although no new phenomena were observed in this search, the model-independent nature of the cross section limits allow them to apply to a broad range of models, helping to incrementally restrict the available phase space for physics beyond the Standard Model. Inclusive searches like this one help to ensure that hints of new physics are not overlooked by searches tailored to specific models. Updates of this search using $\sqrt{s} = 8$ TeV and then $\sqrt{s} = 13$–14 TeV collisions will carry on this inclusive approach, further exploring this interesting signature for new phenomena.

Appendix A

Non-prompt Electron Uncertainties

This appendix details the systematic uncertainties on the non-prompt electron background, first considering the overlap with the charge-flip prediction in Section A.1 then covering issues related to light and heavy flavor composition in Section A.2.

A.1 Non-prompt Background Overlap with Charge-flips

Because the nominal non-prompt anti-selection definition for electrons includes a reversed cut on $d_0/\sigma(d_0)$, charge-flip electrons can enter the anti-selected sample. This is not an issue for deriving the fake factors f, because the dijet region used is dominated by true non-prompt electrons, and residual prompt contamination (including charge-flip) is subtracted out. This is however a concern when predicting the signal region, as the dilepton selection will enhance the number of charge-flips in the $S + A$, $A + S$, and $A + A$ regions used for the non-prompt prediction.

The overlap between the non-prompt and charge-flip predictions is studied in the like-sign $Z \to ee$ peak region ($80 < m(ee) < 100$ GeV), and a correction for the non-prompt estimate is derived.

A.1.1 Non-prompt Prediction in Like-sign Z Peak

To estimate the correct number of fakes in the like-sign $Z \to ee$ peak, the same non-prompt prediction method is used with an alternate anti-selection. Instead of allowing candidates to fail $d_0/\sigma(d_0)$, this denominator allows the candidate to be instead intermediately isolated, using the same intermediate isolation requirement described in Section 9.3.4. This anti-selection definition will be referred to as the "interiso anti-selection." This definition is seen to have very little overlap with the charge-flips, and so is used to provide a better estimate of the non-prompt contribution in the like-sign Z peak region. The non-prompt predictions from the nominal and interiso anti-selections for this region are shown in Table A.1. As can be seen by comparing the first two lines, the nominal anti-selection appears to significantly overestimate the actual number of non-prompt electrons in this region. A correction for this is applied, as described in the next section.

Table A.1: Non-prompt predictions for the like-sign $Z \to ee$ peak region using different denominators and corrections, as described in the text. The last column shows the agreement of the total prediction with data. 1470 events are observed in data, and 1374 events are predicted by MC. The errors shown are statistical only.

Method	Non-prompt prediction	Agreement of total prediction
Nominal anti-sel	227 ± 24	8.9%
Interiso anti-sel	24 ± 2	-4.9%
Nominal anti-sel w/ charge-flip cor	35 ± 24	-4.2%

A.1.2 Correction for Charge-flip Overlap

In the application of the fake factor method, to predict the background in a given region, the prompt MC backgrounds (as well as charge-flips) are subtracted out of the $S+A$, $A+S$, and $A+A$ regions. The problem of charge-flips appearing in the non-prompt prediction is thus a problem of MC not perfectly modeling the charge-flip contribution to these anti-selected regions; if it did, the charge-flips would already be subtracted out.

As described in Section 9.2.1, a charge-flip scale factor is derived to account for MC mismodeling of the charge-flips. The scale factor is for the numerator (analysis) selection, however, and may not be appropriate for the anti-selection with a reversed $d_0/\sigma(d_0)$ cut. To account for the charge-flip correction in the non-prompt prediction, an additional, flat scale factor is derived to apply to the charge-flips in the anti-selected regions.

This scale factor is chosen by looking at the anti-selected regions used for the non-prompt prediction in the like-sign Z peak. The charge-flip contributions to these regions are scaled up to arrive at the non-prompt prediction given by the interiso anti-selection in Table A.1. The non-prompt prediction region breakdown is given in Table A.2. The third column contains the numbers which will be weighted up. An additional scale factor of 10% is found to give good agreement, resulting in the prediction in the last line of Table A.1.

A.1.3 Impact on Signal Region Prediction

The impact of this correction is smaller in the signal region as it is not so dominated by charge-flips. Table A.3 shows the prediction in the signal region for the nominal anti-selection before and

Table A.2: Non-prompt prediction regions for the like-sign Z peak region using the nominal anti-selection. $S + A$ etc refer to pairs of electrons, where S is a selected object, A is an anti-selected object, the first is the leading, and the second is the subleading. The fake factors f have already been applied in the numbers presented.

Region	Data (weighted by f)	MC Charge-flips (weighted by f)	Contrib. to non-prompt
$S + A$	1246	1118	128
$A + S$	932	828	104
$A + A$	21	15	-6

after this charge-flip correction as well as the interiso anti-selection prediction. The full charge-flip correction is taken as a systematic uncertainty, so 16%, and the nominal anti-selection with the charge-flip correction is taken for the central value of the non-prompt prediction. (The exact value of the correction and uncertainty depend on the dilepton pair invariant mass threshold, as with all other uncertainties.)

Table A.3: Non-prompt predictions for the signal region using different anti-selections and corrections, as described in the text. The last column shows the difference from the nominal anti-selection prediction without a correction applied. The errors are statistical only.

Method	Non-prompt prediction	Diff from Nominal
Nominal anti-sel	89 ± 9	-
Interiso anti-sel	89 ± 2	-
Nominal anti-sel w/ charge-flip cor	75 ± 9	-16%

The shape of the background prediction is also checked. In the LS Z peak mass region, the contamination due to charge-flips produces a characteristic Z peak shape in the non-prompt prediction using the nominal anti-selection, as seen in Fig. A.1. This shape is not seen in the non-prompt prediction using the interiso anti-selection as the charge-flip contamination is small. The mass shape of the charge-flips is not modeled well by MC in the anti-selection regions, and as a result, applying the non-prompt correction results in the distorted mass shape seen inside the Z peak region[25]. However, as this figure also shows, the shape of the nominal anti-selection prediction and the interiso prediction agree well outside the Z peak, where the charge-flip correction is a smaller effect.

[25]The negative bins in the non-prompt prediction inside the Z peak region are again an artifact of the poor modeling of the charge-flips in the anti-selection regions. Because the MC predictions for charge-flips are subtracted from data, if the peak is broader in MC (as it appears to be in the anti-selection regions) some bins can become negative. This is especially the case after the correction, which is effectively constraining the integral in the mass range $80 < m(ee) < 100$ GeV to yield $\sim$25 events. The mass shape inside the Z peak is not explicitly used anywhere in the analysis, and the prediction outside the Z peak remains positive. Also, as long as the non-prompt prediction is integrated over a suitably large mass range, it yields a sensible (positive) value.

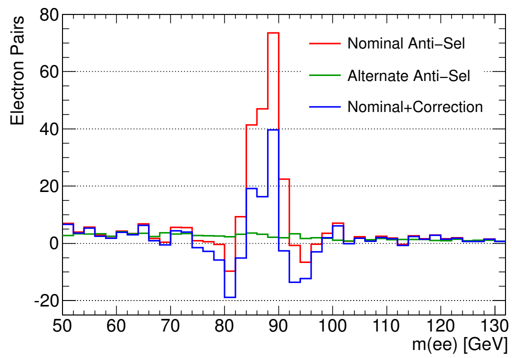

Figure A.1: Non-prompt predictions for like-sign electron pairs, including the Z peak, using the methods described in the text. The nominal anti-selection gives a distorted shape inside the Z peak region but agrees well with the interiso anti-selection prediction outside.

The interiso anti-selection described in this section, while more robust against charge-flips, is not taken as the central value for the analysis as it is expected that the total systematics will be larger. The intermediate isolation requirement makes it more sensitive to event topology and jet kinematics. Figure A.2 shows the fake factors f for this definition and their dependence on the away side jet kinematics, which is significantly larger than the nominal anti-selection (Fig. 9.18).

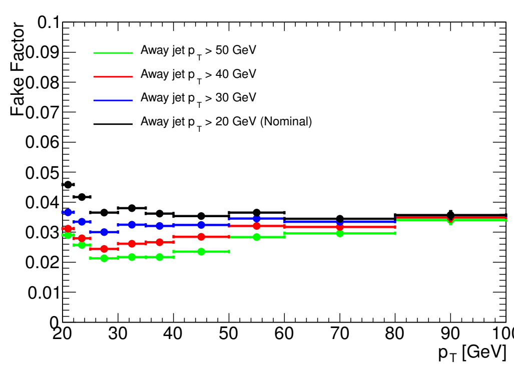

Figure A.2: Electron fake factor f for the interiso anti-selection versus p_{T} with away side jet p_{T} requirement variation.

A.2 Non-prompt Light/Heavy Flavor Composition

To assess the impact of the light flavor (LF) versus heavy flavor (HF) composition of the non-prompt background sample for electrons, an alternative method was developed. This method also uses fake factors f as described in Section 9.3.1. The selected and anti-selected definitions are the same as in the nominal method, described in Section 9.3.2.1, and the same data samples are used to measure the fake factors f, described in Section 9.3.2.2. The difference is that the alternative method described here incorporates b-tagging information to attempt to separate the LF and HF components of the non-prompt background. This alternative method will be used to cross check the non-prompt prediction in the signal region and as such, full systematics for this method are not evaluated.

A.2.1 MV1 b-tagger

A b-tagging algorithm uses information about the tracks associated to a given jet to try to determine if it is likely to have originated from a b-quark as opposed to a light-flavor quark. The typical information used includes displaced (secondary) vertex reconstruction as well as the impact parameters of the tracks relative to the primary interaction vertex.

The MV1 b-tagging algorithm used here is the recommended algorithm from the ATLAS flavor tagging performance group [105]. This algorithm is based on a neural network using the output weights of the JetFitter+IP3D, IP3D and SV1 algorithms as input. For the non-prompt method described here, the idea is to use the b-tag weight of the jet overlapping with an electron candidate to try to classify it as a light or heavy flavor non-prompt electron.[26]

A complication arises in that the b-tagging efficiency is correlated with the identification cuts on the electron candidate. Not surprisingly, the cuts which are most effective at rejecting heavy flavor background (track isolation and $d_0/\sigma(d_0)$) are the most correlated with the b-tagging weight, as they cut on the same information used by the b-tagging algorithms (tracks for secondary vertices, impact parameters).

The MV1 b-tagging weight is plotted for the overlapping jet for true HF electrons passing the selected and anti-selected requirements in Fig. A.3, from $b\bar{b}$ electron-filtered MC. Typically b-like jets receive a high MV1 weight. As seen in the figure, for the anti-selection (which reverses the cut on $d_0/\sigma(d_0)$), there is a large peak at high MV1, but for the analysis selection, this peak is substantially reduced.

From JF17 dijet MC, a cut on MV1 weight > 0.9 is nevertheless quite pure in HF electrons, with a purity of about 90% or larger for both selected and anti-selected electrons. Taking this cut value, the efficiency for selecting true HF electrons is shown as a function of the electron candidate p_{T} and η in Fig. A.4. The efficiency is fairly flat as a function of p_{T} but shows dependence on η. For the method described below, the efficiency is taken as flat vs p_{T} using a linear fit (the dashed lines in

[26] Similar to Section 8.3, the closest jet to an electron candidate with $\Delta R < 0.2$ is taken as the "overlapping" jet.

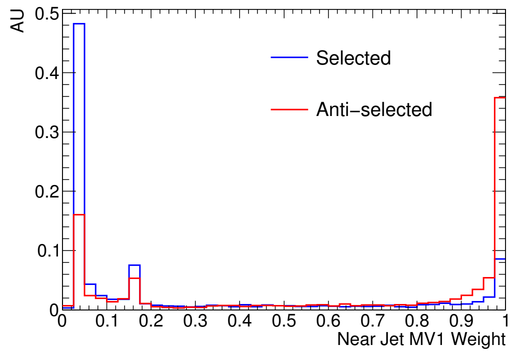

Figure A.3: MV1 b-tagging weight shapes for the jet overlapping with electron candidates, for true HF electrons in $b\bar{b}$ electron-filtered MC.

Fig. A.4a) while the η dependence is used.

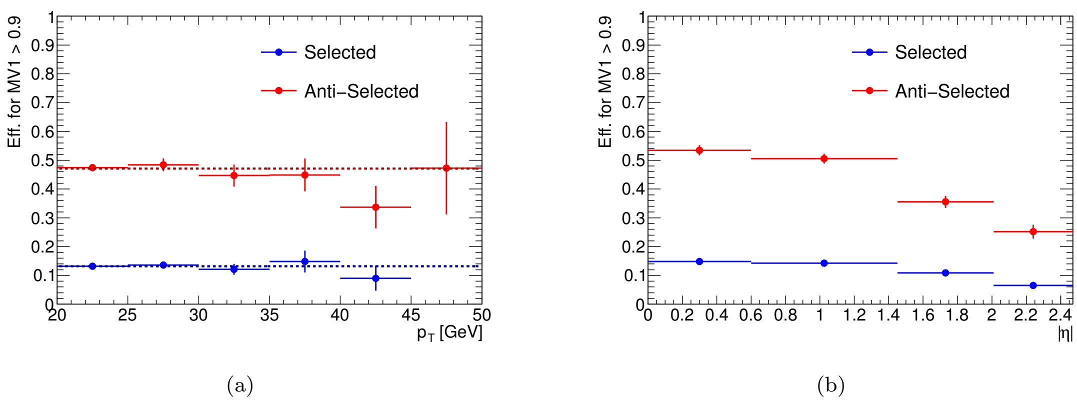

Figure A.4: MC efficiency for cutting on MV1 weight > 0.9 for the overlapping jet, for true HF electrons in $b\bar{b}$ electron-filtered MC. This is plotted versus electron candidate p_{T} (a) and η (b) for the selected and anti-selected requirements. The dashed lines in the plot versus p_{T} are a linear fit to the points.

By assuming (i) that the requirement of MV1 weight > 0.9 selects a pure sample of HF electrons and (ii) the efficiency for a true HF electron to pass the requirement of MV1 weight > 0.9, one can estimate the total number of true HF electrons in a non-prompt-dominated data control region. This information will be used to derive "true" HF and LF fake factors.

A.2.2 Definitions and Measurement of f

First the following quantities are defined, which will be used in deriving the fake factors:

- S_{tag}, A_{tag}: the number of selected/anti-selected candidates with the overlapping jet passing MV1 weight > 0.9
- S_{notag}, A_{notag}: the number of selected/anti-selected candidates with the overlapping jet failing MV1 weight > 0.9
- ε_{tag}: the MC efficiency for a true HF electron passing the selected requirements to also have the overlapping jet passing MV1 weight > 0.9. As seen in Fig. A.4, this number is $\sim$13% for these requirements.

Then the following are defined:

$$S_{HF} \equiv \frac{S_{tag}}{\varepsilon_{tag}}, \quad S_{LF} = S_{tot} - S_{HF} \tag{A.1}$$

where S_{HF} and S_{LF} are the estimated numbers of true HF and LF electrons in the numerator selection. Effectively, the number of true HF electrons is estimated by scaling up the pure HF sample S_{tag} by ε_{tag}. As seen in the previous section, ε_{tag} is small ($\sim$13%), so this scaling is large. Then the remaining selected candidates which are not HF are considered to be LF.

These can be used to derive what will be called the "true" HF and LF fake factors:

$$f_{HF} \equiv \frac{S_{HF}}{A_{tag}}, \quad f_{LF} \equiv \frac{S_{LF}}{A_{notag}} \tag{A.2}$$

These factors use the A_{tag} selection, which is fairly pure in HF electrons, to predict the number of true HF electrons in the selected sample, and the A_{notag} selection, which is dominated by LF, to predict the true number of LF electrons. This idea is similar to binning the fake factor in two bins of b-tagging weight, as is done in some analyses. The main difference here is the efficiency correction applied to the selected sample, to account for the fact that the MV1 b-tagging efficiency is low after the analysis electron selection.

If the fake factors were simply computed by binning both the selected and anti-selected samples in bins of MV1 weight > 0.9 and MV1 weight ≤ 0.9 (i.e. using S_{tag}/A_{tag} and S_{notag}/A_{notag}), the result would be the red points in Fig. A.5. Using instead the definitions of the "true" HF and LF fake factors from Eq. A.2, one gets the blue points. Since $S_{HF} > S_{tag}$, the "true" fake factors have larger values than the red points in Fig. A.5a, and likewise since $S_{LF} < S_{notag}$, the "true" fake factors are smaller than the red points in Fig. A.5b.

As seen in Fig. A.5a, the fake factor is allowed to be larger than 1. This simply means that when it is used to predict the background to the signal region, the region to which the fake factor will be applied has fewer statistics than the ultimate prediction for the signal region. It is entirely analogous to applying a weight greater than 1 to a MC sample for which the generated luminosity is smaller than the data sample being considered.

The HF fake factor, in blue in Fig. A.5a, falls off quickly with p_T. In Fig. A.5b, the difference between the red and blue points is negligible above 40 GeV, which can be interpreted as meaning that the HF background (and explicit treatment of it) are irrelevant above 40 GeV.

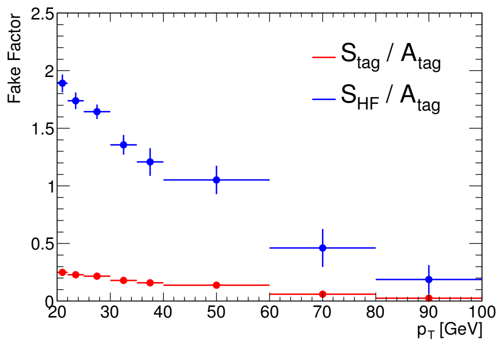

(a)

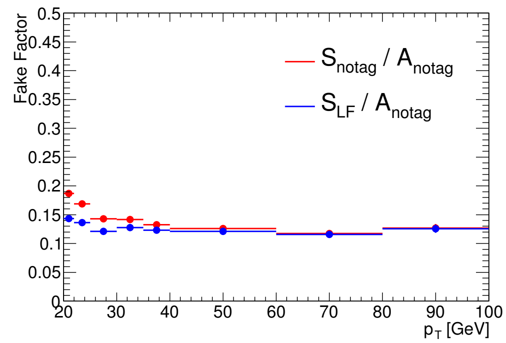

(b)

Figure A.5: Electron fake factors f versus p_T computed using the definitions in the text. The blue points are interpreted as the "true" HF (a) and LF (b) fake factors.

A.2.3 Application

The fake factors using f_{HF} and f_{LF} are applied in essentially the same way as is described in Section 9.3.1. The only difference is that the MV1 b-tagging weight of the overlapping jet is checked for denominator objects. If the MV1 weight is greater than 0.9, f_{HF} is applied; otherwise f_{LF} is applied.

A.2.4 Results

This LF/HF method is used to predict the same dielectron non-prompt control regions in data as are described in Section 9.3.4, and the results are consistent with those of the nominal method. The LF/HF method is then used to compare predictions with the nominal method in the signal region. The resulting predictions are again in very good agreement.

As this LF/HF method relies on the assumption of ε_{tag} from MC, this number was varied to see the impact on the signal region prediction. Variations by a factor of 2 were considered, chosen fairly arbitrarily to be large (compared to up to 20% uncertainty on the efficiency for identifying b-quark jets with the MV1 algorithm [106]). These variations resulted in changes of the signal region prediction by up to about 4%. The results are displayed in Table A.4. Restricting to higher invariant mass, deviations up to 20% are observed. The largest of these variations for each invariant mass threshold are taken as a (symmetric) systematic uncertainty on the non-prompt background prediction.

Table A.4: Signal region non-prompt predictions for the alternate LF/HF method and variations described in the text. Errors shown are statistical only.

Method	Variation	Signal region prediction	Diff from nominal
Nominal	-	75 ± 9	-
LF/HF	-	73 ± 10	-2.6%
LF/HF	ε_{tag} up by 2x	74 ± 9	-1.4%
LF/HF	ε_{tag} down by 2x	72 ± 13	-4.2%

A.2.5 Discussion

In the nominal non-prompt prediction, where non-prompt LF and HF electrons are not treated separately, differences between these two categories would lead to a systematic error in predicting the non-prompt background only if two conditions were true. This would require the true fake factors for non-prompt electrons from LF and HF to be different, and it would also further require that the relative composition of these two components is different between the dijet sample where f is derived and the dilepton sample where it is applied to predict the non-prompt background.

To illustrate this concretely, consider the truth level fake factors for LF and HF, denoted F_{LF} and F_{HF} (to distinguish them from the measured values above). Then suppose one wants to measure a single fake factor f_{meas} as in the nominal non-prompt method. Table A.5 shows some hypothetical cases depending on F_{LF}, F_{HF}, and the non-prompt composition in the dijet and dilepton regions. The first line shows the case of $F_{LF} = F_{HF}$, where the relative compositions become irrelevant. The second line shows the case where the relative LF/HF compositions are the same in each region, and the difference between F_{LF} and F_{HF} becomes irrelevant. The last two lines show cases where F_{LF} and F_{HF} differ as well as the compositions in the different regions. In those cases, biases appear in the total non-prompt prediction. Of course, measuring and applying f_{LF} and f_{HF} separately could minimize these biases.

In light of this discussion, the observation that the LF/HF method presented in this section arrives at essentially the same non-prompt prediction as the nominal method establishes confidence that the background composition does not produce a large systematic effect. Since the measured values of f_{LF} and f_{HF} differ significantly, the likely explanation is that the background composition is in fact fairly similar between the dijet region and the dilepton region. This may be because HF electrons are heavily suppressed in both cases due to the selections employed.

Table A.5: Some hypothetical examples to illustrate the impact of LF/HF composition on the non-prompt background prediction. In each region, "LF frac" and "HF frac" are the fractions of true non-prompt electrons originating from each source. The value f_{meas} comes from measuring f in the dijet region, while f_{eff} (effective fake factor) is what one would measure in the dilepton region. The bias on the total non-prompt prediction is given by simply $(f_{eff} - f_{meas})/f_{eff}$.

		Dijet Region			Dilepton Region			
F_{LF}	F_{HF}	LF frac	HF frac	f_{meas}	LF frac	HF frac	f_{eff}	Bias on pred.
0.1	0.1	80%	20%	0.1	20%	80%	0.1	0%
0.1	0.5	80%	20%	0.18	80%	20%	0.18	0%
0.1	0.5	80%	20%	0.18	70%	30%	0.22	-18%
0.1	0.5	80%	20%	0.18	20%	80%	0.42	-57%

Bibliography

[1] ATLAS Collaboration, G. Aad et al., *Search for anomalous production of prompt like-sign lepton pairs at sqrt(s) = 7 TeV with the ATLAS detector*, arXiv:1210.4538 [hep-ex]. 1

[2] ATLAS Collaboration, G. Aad et al., *Search for doubly-charged Higgs bosons in like-sign dilepton final states at sqrt(s) = 7 TeV with the ATLAS detector*, arXiv:1210.5070 [hep-ex]. 1

[3] S. Glashow, *Partial Symmetries of Weak Interactions*, Nucl.Phys. **2**2 (1961) 579–588. 2.1

[4] S. Weinberg, *A Model of Leptons*, Phys.Rev.Lett. **1**9 (1967) 1264–1266. 2.1

[5] A. Salam, *Weak and Electromagnetic Interactions*, Conf.Proc. **C**680519 (1968) 367–377. 2.1

[6] ATLAS Collaboration, G. Aad et al., *Observation of a new particle in the search for the Standard Model Higgs boson with the ATLAS detector at the LHC*, Phys.Lett.B (2012) , arXiv:1207.7214 [hep-ex]. 2.1.1.1

[7] CMS Collaboration, S. Chatrchyan et al., *Observation of a new boson at a mass of 125 GeV with the CMS experiment at the LHC*, Phys.Lett.B (2012) , arXiv:1207.7235 [hep-ex]. 2.1.1.1

[8] C. T. Hill and E. H. Simmons, *Strong dynamics and electroweak symmetry breaking*, Phys.Rept. **3**81 (2003) 235–402, arXiv:hep-ph/0203079 [hep-ph]. 2.1.1.2

[9] W. Alberico and S. Bilenky, *Neutrino oscillations, masses and mixing*, Phys.Part.Nucl. **3**5 (2004) 297–323, arXiv:hep-ph/0306239 [hep-ph]. 2.1.1.3

[10] M. Nebot, J. F. Oliver, D. Palao, and A. Santamaria, *Prospects for the Zee-Babu Model at the CERN LHC and low energy experiments*, Phys.Rev. **D**77 (2008) 093013, arXiv:0711.0483 [hep-ph]. 2.1.1.3, 2.4.1.4

[11] Particle Data Group, J. Beringer et al., *Review of Particle Physics*, Phys. Rev. D **8**6 (2012) 010001. 2.1.1.4, 2.4.1

[12] J. M. Campbell, J. Huston, and W. Stirling, *Hard Interactions of Quarks and Gluons: A Primer for LHC Physics*, Rept.Prog.Phys. **7**0 (2007) 89, arXiv:hep-ph/0611148 [hep-ph]. 2.2, 10.2.1, 13.1.3

[13] V. Rentala, W. Shepherd, and S. Su, *A Simplified Model Approach to Same-sign Dilepton Resonances*, Phys.Rev. **D**84 (2011) 035004, arXiv:1105.1379 [hep-ph]. 2.4.1, 2.4.1, 2.4.1.1, 7

[14] ATLAS Collaboration, G. Aad et al., *Search for anomalous production of prompt like-sign muon pairs and constraints on physics beyond the Standard Model with the ATLAS detector*, Phys.Rev. **D**85 (2012) 032004, arXiv:1201.1091 [hep-ex]. 2.4.1

[15] CMS Collaboration, S. Chatrchyan et al., *A search for a doubly-charged Higgs boson in pp collisions at sqrt(s) = 7 TeV*, arXiv:1207.2666 [hep-ex]. 2.4.1, 13.4

[16] K. Huitu and J. Maalampi, *The Higgs sector of a supersymmetric left-right model*, Phys.Lett. **B**344 (1995) 217–224, arXiv:hep-ph/9410342 [hep-ph]. 2.4.1.2

[17] M. Schmaltz and D. Tucker-Smith, *Little Higgs review*, Ann.Rev.Nucl.Part.Sci. **5**5 (2005) 229–270, arXiv:hep-ph/0502182 [hep-ph]. 2.4.1.3

[18] A. Zee, *Quantum Numbers of Majorana Neutrino Masses*, Nucl.Phys. **B**264 (1986) 99. 2.4.1.4

[19] K. Babu, *Model of 'Calculable' Majorana Neutrino Masses*, Phys.Lett. **B**203 (1988) 132. 2.4.1.4

[20] CDF Collaboration, T. Aaltonen et al., *Forward-Backward Asymmetry in Top Quark Production in $p\bar{p}$ Collisions at sqrts* $= 1.96$ *TeV*, Phys.Rev.Lett. **1**01 (2008) 202001, arXiv:0806.2472 [hep-ex]. 2.4.2

[21] S. Jung, H. Murayama, A. Pierce, and J. D. Wells, *Top quark forward-backward asymmetry from new t-channel physics*, Phys.Rev. **D**81 (2010) 015004, arXiv:0907.4112 [hep-ph]. 2.4.2

[22] D0 Collaboration, V. M. Abazov et al., *Forward-backward asymmetry in top quark-antiquark production*, Phys.Rev. **D**84 (2011) 112005, arXiv:1107.4995 [hep-ex]. 2.4.2

[23] CMS Collaboration, S. Chatrchyan et al., *Measurement of the charge asymmetry in top-quark pair production in proton-proton collisions at sqrt(s) = 7 TeV*, Phys.Lett. **B**709 (2012) 28–49, arXiv:1112.5100 [hep-ex]. 2.4.2

[24] J. Aguilar-Saavedra and M. Perez-Victoria, *No like-sign tops at Tevatron: Constraints on extended models and implications for the t tbar asymmetry*, Phys.Lett. **B**701 (2011) 93–100, arXiv:1104.1385 [hep-ph]. 2.4.2, 7

[25] ATLAS Collaboration, G. Aad et al., *Search for same-sign top-quark production and fourth-generation down-type quarks in pp collisions at sqrt(s) = 7 TeV with the ATLAS detector*, JHEP **1**204 (2012) 069, arXiv:1202.5520 [hep-ex]. 2.4.2, 9.2.1

[26] CMS Collaboration, S. Chatrchyan et al., *Search for new physics in events with same-sign dileptons and b-tagged jets in pp collisions at sqrt(s) = 7 TeV*, arXiv:1205.3933 [hep-ex]. 2.4.2, 2.4.5

[27] O. Eberhardt, A. Lenz, A. Menzel, U. Nierste, and M. Wiebusch, *Status of the fourth fermion generation before ICHEP2012: Higgs data and electroweak precision observables*, arXiv:1207.0438 [hep-ph]. 2.4.3

[28] A. Atre, M. Carena, T. Han, and J. Santiago, *Heavy Quarks Above the Top at the Tevatron*, Phys.Rev. **D**79 (2009) 054018, arXiv:0806.3966 [hep-ph]. 2.4.3

[29] ATLAS Collaboration, G. Aad et al., *Search for heavy vector-like quarks coupling to light quarks in proton-proton collisions at sqrt(s) = 7 TeV with the ATLAS detector*, Phys.Lett. **B**712 (2012) 22–39, arXiv:1112.5755 [hep-ex]. 2.4.3

[30] ATLAS Collaboration, G. Aad et al., *Search for down-type fourth generation quarks with the ATLAS detector in events with one lepton and hadronically decaying W bosons*, Phys.Rev.Lett. **109** (2012) 032001, arXiv:1202.6540 [hep-ex]. 2.4.3

[31] ATLAS Collaboration, G. Aad et al., *Search for pair production of a new quark that decays to a Z boson and a bottom quark with the ATLAS detector*, Phys.Rev.Lett. **1**09 (2012) 071801, arXiv:1204.1265 [hep-ex]. 2.4.3

[32] CMS Collaboration, S. Chatrchyan et al., *Search for heavy bottom-like quarks in 4.9 inverse femtobarns of pp collisions at sqrt(s) = 7 TeV*, JHEP **1**205 (2012) 123, arXiv:1204.1088 [hep-ex]. 2.4.3

[33] CMS Collaboration, S. Chatrchyan et al., *Search for a Vector-like Quark with Charge 2/3 in t + Z Events from pp Collisions at sqrt(s) = 7 TeV*, Phys.Rev.Lett. **1**07 (2011) 271802, arXiv:1109.4985 [hep-ex]. 2.4.3

[34] R. N. Mohapatra and G. Senjanovic, *Neutrino Masses and Mixings in Gauge Models with Spontaneous Parity Violation*, Phys.Rev. **D**23 (1981) 165. 2.4.4

[35] A. Ferrari, J. Collot, M.-L. Andrieux, B. Belhorma, P. de Saintignon, et al., *Sensitivity study for new gauge bosons and right-handed Majorana neutrinos in pp collisions at s = 14-TeV*, Phys.Rev. **D**62 (2000) 013001. 2.4.4

[36] F. del Aguila, S. Bar-Shalom, A. Soni, and J. Wudka, *Heavy Majorana Neutrinos in the Effective Lagrangian Description: Application to Hadron Colliders*, Phys.Lett. **B**670 (2009) 399–402, arXiv:0806.0876 [hep-ph]. 2.4.4, 7

[37] ATLAS Collaboration, G. Aad et al., *Search for heavy neutrinos and right-handed W bosons in events with two leptons and jets in pp collisions at sqrt(s) = 7 TeV with the ATLAS detector*, Eur.Phys.J. **C**72 (2012) 2056, arXiv:1203.5420 [hep-ex]. 2.4.4

[38] S. P. Martin, *A Supersymmetry primer*, arXiv:hep-ph/9709356 [hep-ph]. 2.4.5

[39] ATLAS Collaboration, G. Aad et al., *Search for direct slepton and gaugino production in final states with two leptons and missing transverse momentum with the ATLAS detector in pp collisions at sqrt(s) = 7 TeV*, arXiv:1208.2884 [hep-ex]. 2.4.5

[40] ATLAS Collaboration, G. Aad et al., *Search for direct production of charginos and neutralinos in events with three leptons and missing transverse momentum in sqrt(s) = 7 TeV pp collisions with the ATLAS detector*, arXiv:1208.3144 [hep-ex]. 2.4.5

[41] CMS Collaboration, S. Chatrchyan et al., *Search for new physics with same-sign isolated dilepton events with jets and missing transverse energy*, Phys.Rev.Lett. **1**09 (2012) 071803, arXiv:1205.6615 [hep-ex]. 2.4.5

[42] CMS Collaboration, S. Chatrchyan et al., *Search for anomalous production of multilepton events in pp collisions at sqrt(s)=7 TeV*, JHEP **1**206 (2012) 169, arXiv:1204.5341 [hep-ex]. 2.4.5

[43] L. Evans and P. Bryant, *LHC Machine*, JINST **3** (2008) S08001. 3, 5.1.3.2.2

[44] CERN, *oai:cds.cern.ch:1424362. Chamonix 2012 Workshop on LHC Performance*. CERN, Geneva, 2012. 3.2

[45] ATLAS Collaboration, G. Aad et al., *The ATLAS Experiment at the CERN Large Hadron Collider*, JINST **3** (2008) S08003. 4.1

[46] Atlas Collaboration, G. Aad et al., *Performance of the ATLAS Trigger System in 2010*, Eur.Phys.J. **C**72 (2012) 1849, arXiv:1110.1530 [hep-ex]. 4.1

[47] ATLAS TRT Collaboration, E. Abat et al., *The ATLAS TRT barrel detector*, JINST **3** (2008) P02014. 4.2.1

[48] ATLAS TRT Collaboration, E. Abat et al., *The ATLAS TRT end-cap detectors*, JINST **3** (2008) P10003. 4.2.1

[49] ATLAS TRT Collaboration, E. Abat et al., *The ATLAS TRT electronics*, JINST **3** (2008) P06007. 4.2.1.1

[50] D. Huffman, *A Method for the Construction of Minimum-Redundancy Codes*, Proceedings of the IRE **4**0 (1952) no. 9, 1098 –1101. 4.2.1.1.2

[51] S. Fratina, M. Hance, M. Newcomer, D. Olivito, R. Van Berg, et al., *The ATLAS transition radiation detector (TRT) Fast-OR trigger*, . 4.2.1.1.4

[52] ATLAS Collaboration, G. Aad et al., *Electron performance measurements with the ATLAS detector using the 2010 LHC proton-proton collision data*, Eur.Phys.J. **C**72 (2012) 1909, arXiv:1110.3174 [hep-ex]. 5.1, 5.1, 10.1.1.1, 10.1.2, 12.3.2

[53] ATLAS Collaboration, *Improved electron reconstruction in ATLAS using the Gaussian Sum Filter-based model for bremsstrahlung*, ATLAS-CONF-2012-47, 2012. 5.1.1

[54] R. Fruhwirth, *Application of Kalman filtering to track and vertex fitting*, Nucl.Instrum.Meth. **A**262 (1987) 444–450. 5.1.1

[55] ATLAS Collaboration, *Particle Identification Performance of the ATLAS Transition Radiation Tracker*, ATLAS-CONF-2011-128, 2011. 5.1.2

[56] ATLAS Collaboration, *Performance of primary vertex reconstruction in proton-proton collisions at sqrt(s) = 7 TeV in the ATLAS experiment*, ATLAS-CONF-2010-069, 2010. 15

[57] Atlas Collaboration, G. Aad et al., *Measurement of the inclusive isolated prompt photon cross section in pp collisions at sqrt(s) = 7 TeV with the ATLAS detector*, Phys.Rev. **D**83 (2011) 052005, arXiv:1012.4389 [hep-ex]. 5.1.3.2.2

[58] ATLAS Collaboration, G. Aad et al., *Expected Performance of the ATLAS Experiment - Detector, Trigger and Physics*, arXiv:0901.0512 [hep-ex]. 5.2

[59] J.-F. Arguin, K. Hamano, A. Hawkins, B. Heinemann, M. Hurwitz, E. Lytken, D. Olivito, N. Rodd, L. Skinnari, and E. Thomson, *Search for anomalous production of prompt like-sign lepton pairs and constraints on physics beyond the Standard Model*, ATL-COM-PHYS-2012-529, 2012. 6

[60] J.-F. Arguin, K. Hamano, A. Hawkins, B. Heinemann, M. Hurwitz, E. Lytken, D. Olivito, N. Rodd, L. Skinnari, and E. Thomson, *Search for doubly charged Higgs bosons in like-sign dilepton final states with the ATLAS detector*, ATL-COM-PHYS-2012-1247, 2012. 6

[61] T. Gleisberg, S. Hoeche, F. Krauss, M. Schonherr, S. Schumann, et al., *Event generation with SHERPA 1.1*, JHEP **0**902 (2009) 007, arXiv:0811.4622 [hep-ph]. 7

[62] J. Alwall, M. Herquet, F. Maltoni, O. Mattelaer, and T. Stelzer, *MadGraph 5 : Going Beyond*, JHEP **1**106 (2011) 128, arXiv:1106.0522 [hep-ph]. 7

[63] T. Sjostrand, S. Mrenna, and P. Z. Skands, *PYTHIA 6.4 Physics and Manual*, JHEP **0**605 (2006) 026, arXiv:hep-ph/0603175 [hep-ph]. 7

[64] J. M. Campbell, R. K. Ellis, and C. Williams, *Vector boson pair production at the LHC*, JHEP **1**107 (2011) 018, arXiv:1105.0020 [hep-ph]. 7

[65] J. M. Campbell and R. K. Ellis, *$t\bar{t}W^{+-}$ production and decay at NLO*, JHEP **1**207 (2012) 052, arXiv:1204.5678 [hep-ph]. 7

[66] A. Lazopoulos, T. McElmurry, K. Melnikov, and F. Petriello, *Next-to-leading order QCD corrections to $t\bar{t}Z$ production at the LHC*, Phys.Lett. **B**666 (2008) 62–65, arXiv:0804.2220 [hep-ph]. 7, 10.2.1

[67] M. Garzelli, A. Kardos, C. Papadopoulos, and Z. Trocsanyi, *Z0 - boson production in association with a top anti-top pair at NLO accuracy with parton shower effects*, Phys.Rev. **D**85 (2012) 074022, arXiv:1111.1444 [hep-ph]. 7

[68] A. Kardos, Z. Trocsanyi, and C. Papadopoulos, *Top quark pair production in association with a Z-boson at NLO accuracy*, Phys.Rev. **D**85 (2012) 054015, arXiv:1111.0610 [hep-ph]. 7

[69] B. Jager, C. Oleari, and D. Zeppenfeld, *Next-to-leading order QCD corrections to W+ W+ jj and W- W- jj production via weak-boson fusion*, Phys.Rev. **D**80 (2009) 034022, arXiv:0907.0580 [hep-ph]. 7, 10.2.1

[70] T. Melia, K. Melnikov, R. Rontsch, and G. Zanderighi, *Next-to-leading order QCD predictions for W^+W^+jj production at the LHC*, JHEP **1**012 (2010) 053, arXiv:1007.5313 [hep-ph]. 7

[71] R. Hamberg, W. van Neerven, and T. Matsuura, *A Complete calculation of the order $\alpha - s^2$ correction to the Drell-Yan K factor*, Nucl.Phys. **B**359 (1991) 343–405. 7

[72] ATLAS Collaboration, G. Aad et al., *Search for high-mass resonances decaying to dilepton final states in pp collisions at a center-of-mass energy of 7 TeV with the ATLAS detector*, arXiv:1209.2535 [hep-ex]. 7, 10.2.2

[73] C. Carloni Calame, G. Montagna, O. Nicrosini, and A. Vicini, *Precision electroweak calculation of the charged current Drell-Yan process*, JHEP **0**612 (2006) 016, arXiv:hep-ph/0609170 [hep-ph]. 7

[74] C. Carloni Calame, G. Montagna, O. Nicrosini, and A. Vicini, *Precision electroweak calculation of the production of a high transverse-momentum lepton pair at hadron colliders*, JHEP **0**710 (2007) 109, arXiv:0710.1722 [hep-ph]. 7

[75] S. Frixione and B. R. Webber, *Matching NLO QCD computations and parton shower simulations*, JHEP **0**206 (2002) 029, arXiv:hep-ph/0204244 [hep-ph]. 7

[76] G. Corcella, I. Knowles, G. Marchesini, S. Moretti, K. Odagiri, et al., *HERWIG 6: An Event generator for hadron emission reactions with interfering gluons (including supersymmetric processes)*, JHEP **0**101 (2001) 010, arXiv:hep-ph/0011363 [hep-ph]. 7

[77] M. Aliev, H. Lacker, U. Langenfeld, S. Moch, P. Uwer, et al., *HATHOR: HAdronic Top and Heavy quarks crOss section calculatoR*, Comput.Phys.Commun. **1**82 (2011) 1034–1046, arXiv:1007.1327 [hep-ph]. 7

[78] M. L. Mangano, M. Moretti, F. Piccinini, R. Pittau, and A. D. Polosa, *ALPGEN, a generator for hard multiparton processes in hadronic collisions*, JHEP **0**307 (2003) 001, arXiv:hep-ph/0206293 [hep-ph]. 7

[79] ATLAS Collaboration, G. Aad et al., *Measurement of W gamma and Z gamma production cross sections in pp collisions at sqrt(s) = 7 TeV and limits on anomalous triple gauge couplings with the ATLAS detector*, arXiv:1205.2531 [hep-ex]. 7, 10.2.3

[80] R. Mohapatra and J. C. Pati, *A Natural Left-Right Symmetry*, Phys.Rev. **D**11 (1975) 2558. 7

[81] Q.-H. Cao, D. McKeen, J. L. Rosner, G. Shaughnessy, and C. E. Wagner, *Forward-Backward Asymmetry of Top Quark Pair Production*, Phys.Rev. **D**81 (2010) 114004, arXiv:1003.3461 [hep-ph]. 7

[82] J. Aguilar-Saavedra, *Effective four-fermion operators in top physics: A Roadmap*, Nucl.Phys. **B**843 (2011) 638–672, arXiv:1008.3562 [hep-ph]. 7

[83] J. Pumplin, D. Stump, J. Huston, H. Lai, P. M. Nadolsky, et al., *New generation of parton distributions with uncertainties from global QCD analysis*, JHEP **0**207 (2002) 012, arXiv:hep-ph/0201195 [hep-ph]. 7

[84] A. Sherstnev and R. Thorne, *Parton Distributions for LO Generators*, Eur.Phys.J. **C**55 (2008) 553–575, arXiv:0711.2473 [hep-ph]. 7, 10.2.1

[85] P. M. Nadolsky, H.-L. Lai, Q.-H. Cao, J. Huston, J. Pumplin, et al., *Implications of CTEQ global analysis for collider observables*, Phys.Rev. **D**78 (2008) 013004, arXiv:0802.0007 [hep-ph]. 7

[86] M. Guzzi, P. Nadolsky, E. Berger, H.-L. Lai, F. Olness, et al., *CT10 parton distributions and other developments in the global QCD analysis*, arXiv:1101.0561 [hep-ph]. 7, 10.2.1

[87] ATLAS Collaboration, G. Aad et al., *The ATLAS Simulation Infrastructure*, Eur.Phys.J. **C**70 (2010) 823–874, arXiv:1005.4568 [physics.ins-det]. 7

[88] GEANT4, S. Agostinelli et al., *GEANT4: A Simulation toolkit*, Nucl.Instrum.Meth. **A**506 (2003) 250–303. 7

[89] W. Lampl, S. Laplace, D. Lelas, P. Loch, H. Ma, et al., *Calorimeter clustering algorithms: Description and performance*, . 8.3

[90] M. Cacciari, G. P. Salam, and G. Soyez, *The Anti-k(t) jet clustering algorithm*, JHEP **0**804 (2008) 063, arXiv:0802.1189 [hep-ph]. 8.3

[91] ATLAS Collaboration, G. Aad et al., *Jet energy measurement with the ATLAS detector in proton-proton collisions at sqrt(s) = 7 TeV*, arXiv:1112.6426 [hep-ex]. 8.3

[92] ATLAS Collaboration, *Muon reconstruction efficiency in reprocessed 2010 LHC proton-proton collision data recorded with the ATLAS detector*, ATLAS-CONF-2011-063, 2011. 10.1.1.3

[93] ATLAS Collaboration, *ATLAS Muon Momentum Resolution in the First Pass Reconstruction of the 2010 p-p Collision Data at sqrt(s)=7 TeV*, ATLAS-CONF-2011-046, 2011. 10.1.2

[94] ATLAS Collaboration, *Performance of the ATLAS Electron and Photon Trigger in p-p Collisions at sqrt(s) = 7 TeV in 2011*, ATLAS-CONF-2012-048, 2011. 10.1.3

[95] ATLAS Collaboration, *Performance of the ATLAS muon trigger in 2011*, ATLAS-CONF-2012-099, 2011. 10.1.3

[96] ATLAS Collaboration, *Luminosity Determination in pp Collisions at sqrt(s) = 7 TeV using the ATLAS Detector in 2011*, ATLAS-CONF-2011-116, 2011. 10.1.4

[97] A. Martin, W. Stirling, R. Thorne, and G. Watt, *Parton distributions for the LHC*, Eur.Phys.J. **C**63 (2009) 189–285, arXiv:0901.0002 [hep-ph]. 10.2.2, 13.1.3

[98] A. L. Read, *Presentation of search results: The CL(s) technique*, J.Phys. **G**28 (2002) 2693–2704. 11, 12.1

[99] T. Junk, *Confidence level computation for combining searches with small statistics*, Nucl.Instrum.Meth. **A**434 (1999) 435–443, arXiv:hep-ex/9902006 [hep-ex]. 12.1

[100] J. Neyman and E. S. Pearson, *On the Problem of the Most Efficient Tests of Statistical Hypotheses*, Phil. Trans. R. Soc. Lond. **A**231 (1933) no. 694-706, 289–337. 22

[101] K. Cranmer, G. Lewis, L. Moneta, A. Shibata, and W. Verkerke, *HistFactory: A tool for creating statistical models for use with RooFit and RooStats.*, CERN-OPEN-2012-016, 2012. 12.1.1

[102] G. Cowan, K. Cranmer, E. Gross, and O. Vitells, *Asymptotic formulae for likelihood-based tests of new physics*, Eur.Phys.J. **C**71 (2011) 1–19. 12.1.2, 13.1.1, 24

[103] M. Muhlleitner and M. Spira, *Note on doubly charged Higgs pair production at hadron colliders*, Phys.Rev. **D**68 (2003) 117701, arXiv:hep-ph/0305288 [hep-ph]. 13.1

[104] CMS Collaboration, S. Chatrchyan et al., *Search for new physics with same-sign isolated dilepton events with jets and missing transverse energy at the LHC*, JHEP **1**106 (2011) 077, arXiv:1104.3168 [hep-ex]. 14

[105] ATLAS Collaboration, *Commissioning of the ATLAS high-performance b-tagging algorithms in the 7 TeV collision data*, ATLAS-CONF-2011-102, 2011. A.2.1

[106] ATLAS Collaboration, *Measurement of the b-tag Efficiency in a Sample of Jets Containing Muons with 5 fb*$^{-1}$ *of Data from the ATLAS Detector*, ATLAS-CONF-2012-043, 2012. A.2.4